Dipl.-Ing. Manuel Eibinger, BSc

A detailed view on enzymatic cellulose deconstruction: In situ real time visualization of cellulases and auxiliary activities on the cellulose surface

DISSERTATION

zur Erlangung des akademischen Grades

Doktor der technischen Wissenschaften

eingereicht an der

Technischen Universität Graz

Betreuer

Univ.-Prof. Dipl.-Ing. Dr.techn. Bernd Nidetzky

Institute of Biotechnology and Biochemical Engineering

Graz, Mai 2017

EIDESSTATTLICHE ERKLÄRUNG

Ich erkläre an Eides statt, dass ich die vorliegende Arbeit selbstständig verfasst, andere als die angegebenen Quellen/Hilfsmittel nicht benutzt, und die den benutzten Quellen wörtlich und inhaltlich entnommenen Stellen als solche kenntlich gemacht habe. Das in TUGRAZonline hochgeladene Textdokument ist mit der vorliegenden Dissertation identisch.

AFFIDAVIT

I declare that I have authored this thesis independently, that I have not used other than the declared sources/ resources, and that I have explicitly indicated all material which has been quoted either literally or by content from the sources used. The text document uploaded to TUGRAZonline is identical to the present doctoral dissertation.

Datum / Date	Unterschrift / Signature

Danksagung

Die hier vorliegende Arbeit wäre nicht ohne die Mithilfe von zahlreichen Menschen, denen ich zu tiefstem Dank verpflichtet bin, möglich gewesen.

An erster Stelle danke ich Prof. Bernd Nidetzky, der mir trotz holprigem Start, die Möglichkeit gab an diesem vielfältigen und fordernden Thema zu arbeiten. Er erlaubte und förderte meine wissenschaftliche Entwicklung auf zahlreichen Gebieten, und leitete mich stets mit Geduld durch den wissenschaftlichen Alltag.

Besonderer Dank geht an Ass. Prof. Harald Plank, der als Leiter des AFM Teams ein unverzichtbarer Teil des Cellulose-Projekts war. Auch gebührt großer Dank meinem langjährigen wissenschaftlichen Weggefährten Thomas Ganner, da er als Kollege und Freund gleichermaßen mitverantwortlich für den großen Erfolg des Projektes ist.

Ich möchte mich auch bei allen Studenten, in deren Betreuung ich involviert war, im Besonderen bei Karin Sigl, Saverio Danubio und Thomas Zahel, bedanken, deren Arbeit, Expertise und Hingabe ein weiteres Kernelement für die hier vorliegende Arbeit war. Ebenfalls möchte ich allen Studenten unter der wissenschaftlichen Führung von Harald und Thomas, aber im besonderen Jürgen Sattelkow, für ihren Einsatz im Zuge des Projektes danken.

Hervorheben möchte ich auch die Bedeutung des guten Arbeitsklimas am Institut und die draus resultierende Motivation im, nicht immer leichten, Forschungsalltag. Stellvertretend für meine Kollegen, von denen ich vielen freundschaftlich verbunden bin, möchte ich Alexander Gutmann, Ass. Prof. Regina Kratzer, Vera Novy und Zdenek Petrasek erwähnen.

Großer Dank gilt auch meinem größtenteils „fachfremden“ Freundeskreis, der in all den Jahren ein essentieller Rückhalt für mich war.

Zum Abschluss möchte ich meiner Familie, im Besonderen meinen Eltern Martina Ceru-Eibinger und Peter Ceru, danken ohne deren Unterstützung diese Arbeit nicht möglich gewesen wäre.

Abstract

Lignocellulosic biomass represents an abundant renewable resource for sustainable production of fuels and commodity chemicals. Its main constituent cellulose is a water-insoluble linear polysaccharide composed of several hundred or more β-1,4-linked D-glucosyl units. Multiple chains are organized spatially into a densely packed material referred as crystalline cellulose and more disordered parts are usually called amorphous cellulose. In contrast to amorphous regions, crystalline cellulose is highly recalcitrant to depolymerization. Thus, complete deconstruction of cellulose to fermentable sugars requires the cooperative action of various cellulolytic enzymes and remains up to the present day a major obstacle for an economically viable process.

A key feature of the enzymatic deconstruction of cellulose is the interdependence of physical cellulose disruption and hydrolysis kinetics. This markedly dynamic process occurs on various scales but is yet poorly understood. We prepared a mixed amorphous-crystalline cellulosic model substrate (MACS), which exposes a completely smooth surface and applied it for kinetic analysis of cellulase action. Employing a complete *Trichoderma* sp. cellulase system and its main cellulolytic components (CBH I, CBH II, EG) combined kinetic and atomic force microscopy (AFM) studies were used to examine surface structural dynamics and key determinates of the overall efficiency were identified. Later on the dynamic features of cellulose surface degradation by cellulases acting in synergy were reproduced in a spatiotemporal stochastic model in good agreement with evidence from previously obtained visualization experiments.

In recent years, the reinforcement of existing cellulase preparations by auxiliary activities and accessory proteins has attracted considerable attention.

Most prominent auxiliary activity is the lytic polysaccharide monooxygenase (LPMO), which employs a unique principle of cellulose degradation through O_2 dependent oxidative polysaccharide chain cleavage. When applied in combination with cellulases, LPMO appears to constitute an important factor of the efficiency of enzymatic lignocellulose deconstruction. Using AFM, we analyzed in real time dynamic features of the interaction of a C1' oxidizing LPMO from *Neurospora crassa* with the surface of a crystalline cellulose substrate and its impact on hydrolytic enzymes. Activity and fibrillation on crystalline cellulose was shown and critical features of surface morphology for LPMO/cellulase synergy were recognized.

A well-known accessory protein is *Trichoderma reesei* swollenin (*Tr*Swo1). *Tr*Swo1 is thought to induce structural changes in the substrate via physical interactions with the cellulosic surface and therefore believed to facilitate the enzymatic hydrolysis by cellulases. We obtained *Tr*Swo1 through overexpression in the native host. Its binding to cellulose, hemicellulose and lignin was characterized; AFM and WAXS were used to analyze results of action of swollenin on different cellulosic materials. Thus, direct insights into the interaction and impact of *Tr*Swo1 on the cellulosic surface were obtained.

Zusammenfassung

Lignocellulose ist ein häufig vorkommender und erneuerbare Rohstoff, welcher für die Produktion von nachhaltigen Treibstoffen und Plattformchemikalien genutzt werden kann. Der Hauptbestandteil, Cellulose, ist ein lineares wasserunlösliches Polysacharid, welches aus hunderten β-1,4-verknüfpten D-glucosyl Einheiten besteht. Oft sind mehrere Polysacharidketten räumlich in dicht gepackten kristallinen Bündeln organisiert, welche hochresistent gegenüber Depolymerisierung sind. Bereiche mit reduzierter Ordnung werden üblicherweise als „amorph" bezeichnet und sind, im Vergleich dazu, leichter abbaubar. Daher verlangt die komplette Depolymerisierung von Cellulose zu fermentierbaren Zuckern, eine kooperative Interaktion von zahlreichen cellulolytischen Enzymen. Dieser Prozess ist bis zum heutigen Tage nicht ökonomisch gewinnbringend durchführbar.

Ein Schlüsselcharakteristikum der enzymatischen Cellulosehydrolyse ist die wechselseitige Abhängigkeit des physischen Zusammenbruchs der Cellulose und der Hydrolysekinetik. Dieser bedeutende und bemerkenswert dynamische Prozess ist auf mehreren Größenordnung zu beobachten, aber nach wie vor schlecht verstanden. Wir stellten ein gemischt kristallin-amorphes Modelsubstrat (MACS) her, welches eine nanoflache Oberfläche besitzt und nutzten es für die kinetische Analyse der Cellulosehydrolyse. Wir untersuchten ein typisches Cellulasesystem (von *Trichoderma sp.*) sowie dessen isolierte Hauptaktivitäten (CBH, CBH II, EG). Eine Kombination aus Hydrolysestudien und Rasterkraftmikroskopie (AFM) erlaubte es Schlüsselparameter für die Effizienz des kompletten Cellulasesystems zu bestimmen. Später wurden die dynamischen Elemente des beobachteten Prozesses durch ein spatiotemporales Model, im guten Einklang mit den vorher erhaltenen Daten von AFM Experimenten, rekonstruiert.

In den letzten Jahren haben sogenannte „auxiliary activities" und „accessory proteins", als Zusatz in Cellulasepräparationen, an großer Bedeutung gewonnen. Das wohl bekannteste Beispiel ist die lytische Polysacharidmonooxygenase (LPMO), welche Polysacharidketten in Gegenwart von O_2 oxidativ spalten kann. In Kombination mit hydrolytischen Cellulasen, scheinen LPMOs ein integraler Faktor für die effiziente Depolymerisierung von Cellulose zu sein. Wir untersuchten eine C1‘ oxidierende LPMO von *Neurospora crassa* und deren Einfluss auf die Celluloseoberfläche und Cellulasen mittels AFM. Dabei konnte LPMO – Aktivität auf kristalliner Cellulose sowie die daraus resultierende Fibrillierung beobachtet werden. Diese Erkenntnisse erlaubten uns essentielle strukturelle Elemente, an Celluloseoberflächen, für die synergistische Interaktion zwischen Hydrolasen und LPMOs zu identifizieren.

Ein weiteres bekanntes Beispiel ist das „accessory protein" Swollenin (*Tr*Swo1), welches aus *Trichoderma reesei* stammt. Es wird angenommen, dass *Tr*Swo1via physischer Interaktion mit der Celluloseoberfläche in der Lage ist strukturelle Veränderungen herbeizuführen, welche wiederrum die enzymatische Depolymerisation von Cellulose erleichtern. Wir produzierten *Tr*Swo1 in seinem nativen Wirt und charakterisierten seine Bindung an Cellulose, Lignin und Hemicellulose. Darüber hinaus wurden AFM und WAXS Messungen durchgeführt um die Wirkung von *Tr*Swo1 auf verschiedenen Cellulosen zu analysieren. So konnten Erkenntnisse über die direkte Interaktion sowie den Effekt von *Tr*Swo1 auf die Celluloseoberfläche gewonnen werden.

Contents

Dissecting and Reconstructing Synergism: In situ visualization of cooperativity among cellulases ..1

Surface structural dynamics of enzymatic cellulose degradation, revealed by combined kinetic and atomic force microscopy studies 14

Tunable mixed amorphous–crystalline cellulose substrates (MACS) for dynamic degradation studies by atomic force microscopy in liquid environments 36

Cellulose Surface Degradation by a Lytic Polysaccharide Monooxygenase and Its Effect on Cellulase Hydrolytic Efficiency 50

Cellular automata modeling depicts degradation of cellulosic material by a cellulase system with single-molecule resolution 61

Functional characterization of the native swollenin from *Trichoderma reesei*: study of its possible role as C1 factor of enzymatic lignocellulose conversion.....82

Single molecule study of oxidative enzymatic deconstruction of cellulose.....102

Complete list of peer reviewed publications & oral presentations.....127

Dissecting and Reconstructing Synergism:
In situ visualization of cooperativity among cellulases

⌘ *Author's Choice*

THE JOURNAL OF BIOLOGICAL CHEMISTRY VOL. 287, NO. 52, pp. 43215–43222, December 21, 2012

Dissecting and Reconstructing Synergism

IN SITU VISUALIZATION OF COOPERATIVITY AMONG CELLULASES[*] [S]

Received for publication, September 15, 2012, and in revised form, October 24, 2012 Published, JBC Papers in Press, November 1, 2012, DOI 10.1074/jbc.M112.419952

Thomas Ganner[‡§1], **Patricia Bubner**[¶1], **Manuel Eibinger**[¶1], **Claudia Mayrhofer**[§], **Harald Plank**[‡§2], **and Bernd Nidetzky**[¶3]

From the [‡]*Institute for Electron Microscopy and Fine Structure Research, Graz University of Technology, Steyrergasse 17, A-8010 Graz, Austria, the* [§]*Center for Electron Microscopy, Steyrergasse 17, A-8010 Graz, Austria, and the* [¶]*Institute of Biotechnology and Biochemical Engineering, Graz University of Technology, Petersgasse 12, A-8010 Graz, Austria*

Background: Synergistic interplay of cellulases is key for efficiency of cellulose hydrolysis.
Results: *In situ* observation of individual and synergistic action of endo- and exo-cellulases on a polymorphic cellulose substrate reveals specificity of individual enzyme components for crystalline or amorphous regions.
Conclusion: Cellulase synergism is governed by mesoscopic morphological characteristics of the cellulose substrate.
Significance: Advanced knowledge basis for rational optimization of cellulose saccharification.

Cellulose is the most abundant biopolymer and a major reservoir of fixed carbon on earth. Comprehension of the elusive mechanism of its enzymatic degradation represents a fundamental problem at the interface of biology, biotechnology, and materials science. The interdependence of cellulose disintegration and hydrolysis and the synergistic interplay among cellulases is yet poorly understood. Here we report evidence from *in situ* atomic force microscopy (AFM) that delineates degradation of a polymorphic cellulose substrate as a dynamic cycle of alternating exposure and removal of crystalline fibers. Direct observation shows that chain-end-cleaving cellobiohydrolases (CBH I, CBH II) and an internally chain-cleaving endoglucanase (EG), the major components of cellulase systems, take on distinct roles: EG and CBH II make the cellulose surface accessible for CBH I by removing amorphous-unordered substrate areas, thus exposing otherwise embedded crystalline-ordered nanofibrils of the cellulose. Subsequently, these fibrils are degraded efficiently by CBH I, thereby uncovering new amorphous areas. Without prior action of EG and CBH II, CBH I was poorly active on the cellulosic substrate. This leads to the conclusion that synergism among cellulases is morphology-dependent and governed by the cooperativity between enzymes degrading amorphous regions and those targeting primarily crystalline regions. The surface-disrupting activity of cellulases therefore strongly depends on mesoscopic structural features of the substrate: size and packing of crystalline fibers are key determinants of the overall efficiency of cellulose degradation.

Lignocellulosic plant biomass is generally considered as the most promising renewable feedstock for sustainable bioproduction of transportation fuels and commodity chemicals. A bioeconomy built on lignocellulose utilization offers compelling advantages: reduced dependence on crude oil, decreased carbon dioxide emission, productive use of agricultural, forestal, and municipal waste, and elimination of "food *versus* fuel" concerns which arise from the use of an edible raw material (1–4). The critical bottleneck in the development of bioconversion applications, however, remains the production of soluble sugars from cellulose (5). Chemically, cellulose, which constitutes the main polysaccharide component of plant biomass, is a linear β-(1,4)-linked D-glucose homopolymer (6–9). The complex structural organization of cellulose imparts it a pronounced resistance to chemical and enzymatic degradation into soluble hydrolysis products (6, 8): depending on its source, cellulose consists of varying amounts of highly ordered (*i.e.* crystalline) regions and such of lower order, referred to as amorphous cellulose, and additionally, it can be intertwined with hemicellulose and lignin (9, 10). Cellulases are highly proficient catalysts for the hydrolysis of β-glycosidic linkages in isolated, soluble short-chain fragments of the cellulose. By contrast, hydrolysis rates of the natural insoluble substrate often decrease dramatically at later stages of hydrolysis (11–14). Therefore, many attempts have been made to enhance the intrinsic efficiency of cellulases (6, 15) and various types of cellulose pretreatment have been developed with the aim of maximizing substrate accessibility and reactivity toward enzymatic hydrolysis (6, 16). The actual source of this limitation, however, be it the enzymes, the substrate, or both, is a fundamentally unsolved puzzle (14). Identifying the limiting factors by achieving a deeper mechanistic understanding of enzymatic cellulose degradation is pivotal for advancing biomass-to-fuel process development (5–7).

Comprehension of cellulase activity on the cellulose surface has turned out to be remarkably difficult, essentially because of two main complexities: firstly, natural cellulase systems are a

* This work was supported by the Austrian Science Fund FWF (Grant P 24156-B21, to B. N.).
⌘ *Author's Choice*—Final version full access.
[S] This article contains supplemental Figs. S1–S3 and Videos S1–S3.
[1] These authors contributed equally to this work.
[2] To whom correspondence may be addressed: Institute for Electron Microscopy and Fine Structure Research, Graz University of Technology, Steyrergasse 17, A-8010 Graz, Austria. Tel.: +43-(316)-873-8821; Fax: +43-(316)-873-811596; E-mail: harald.plank@felmi-zfe.at.
[3] To whom correspondence may be addressed: Institute of Biotechnology and Biochemical Engineering, Graz University of Technology, Petersgasse 12, A-8010 Graz, Austria. Tel.: +43-(316)-873–8400; Fax: +43-(316)-873-108401; E-mail: bernd.nidetzky@tugraz.at.

multi-component mixture of at least two basic types of enzyme activity: chain-end-cleaving cellobiohydrolase (CBH)[4] and internally chain-cleaving endoglucanase (EG). CBH enzymes are additionally distinguished according to their preference for hydrolysis of the cellulose chain from either the reducing (CBH I) or the non-reducing end (CBH II) (12, 17–19). Another highly distinctive feature of the action of CBH and EG is their synergy in the hydrolysis of insoluble cellulose: a combination of the three enzymes is much more active in terms of soluble sugar release than it would be expected from the sum of the individual activities (12, 17, 18, 20–22). Although the molecular structure and function of the enzymes are known (23–25) and synergism has been extensively studied (12, 17, 20, 22, 26–28), the distinct roles of the single enzymes in cellulose degradation are unclear. Secondly, cellulose is polymorphic at several levels of its structural organization, which leads to a spatial variation in crystallinity and hence to resistance toward hydrolysis (6, 29). With the molecular determinants of the hydrolytic chain cleavage being well understood, the factors affecting the hydrolysis rate most are presumably associated with substrate morphology (28, 30, 31). Mechanistic questions of cellulase synergy will therefore only become tractable when adequate visualization on a nano- and mesoscale is applied to a suitable cellulosic substrate. The cellulose surface exhibits a large amount of meso- and microscopic heterogeneity, thus complicating visualization of surface degradation events at the requisite nanometer scale. Morphological characteristics of the substrate will moreover change with conversion (10, 17). One way of dealing with cellulose polymorphism is by using a highly crystalline model substrate thus reducing the structural complexity. This has proven to be particularly successful in the application of AFM in order to study the mode of action of CBH I, which is able to bind to and degrade crystalline cellulose (12, 32). Recent studies visualized single CBH I molecules moving unidirectionally along accessible lanes on the surface of crystalline cellulose, which is consistent with the proposed processivity of cellulose chain degradation by this enzyme (28, 33). The strictly crystalline *Valonia* cellulose employed in these studies is a suitable model substrate for CBH I, but does not allow direct observation of CBH II (34). EG, which hardly releases soluble sugars from crystalline cellulose (17, 32), is likely to present a similar problem. Considering the key importance of CBH II and EG for full cellulase activity on real-life cellulose substrates, it is pivotal to expand mesoscale visualization to a polymorphic (*i.e.* mixed amorphous-crystalline) cellulose preparation.

EXPERIMENTAL PROCEDURES

Cellulase Preparation and Characterization—All materials were purchased of the highest purity available from Carl Roth (Karlsruhe, Germany) unless stated otherwise. The complete cellulase system of *Trichoderma reesei* mutant SVG 17 was produced and stored as previously described (7). Pure preparations of β-glucosidase (BGL) from *Aspergillus niger* and CBH I and EG, both from *T. longibrachiatum*, were purchased from Megazyme (Dublin, Ireland). *T. longibrachiatum* is closely related to *T. reesei* and its CBH I and EG are isofunctional and structurally analogous to the respective *T. reesei* enzymes (35, 36). Recombinant *T. reesei* CBH II, obtained by heterologous expression in *Pichia pastoris*, was a gift from Anton Glieder (Institute of Molecular Biotechnology, Graz University of Technology). The absence of relevant cross-contaminations by other cellulolytic activities in these preparations was verified by employing the well-established carboxymethyl cellulose (CMC) and 4-methylumbelliferyl-β-D-cellobioside (MUF-cellobioside) assays (30, 37, 38). Reducing sugars were measured using the 3,5-dinitrosalicylic acid (DNS) assay (39).

Generally, a 50 mM sodium citrate buffer (pH 5.0) was used for all experiments in this study unless stated otherwise. Using the filter paper unit (FPU) assay as recommended by the IUPAC (39), the activity of the complete cellulase system was determined as 2.1 FPU/mg. We measured the protein concentration of the complete cellulase system according to Bradford (40), employing Roti®-Quant and Roti®-Nanoquant assays (both from Carl Roth, Karlsruhe, Germany) standardized with BSA. The concentration of pure enzyme preparations was determined via their intrinsic UV absorbance at a wavelength of 280 nm using a Nanodrop 1000 Spectrometer (Thermo Fisher Scientific Inc., Walham, MA). The respective molar extinction coefficients were calculated using ProtParam (41): ϵ_{CBHI} = 88250 $M^{-1}cm^{-1}$; ϵ_{CBHII} = 97665 $M^{-1}cm^{-1}$; ϵ_{EG} = 74940 $M^{-1}cm^{-1}$.

Polymorphic Cellulose and Specimen Preparation—The cellulosic substrate employed in this study was prepared and characterized as previously described (7). The protocol involves dissolution of the microcrystalline cellulose Avicel (Sigma-Aldrich) in ionic liquid. We used 1-butyl-3-methylimidazolium chloride (BMIMCl, Sigma-Aldrich). The resulting transparent gel was subjected to a fractional dehydration with ethanol (30% to absolute). This procedure removed the residual ionic liquid, leaving a pure and polymorphic cellulosic substrate (7).

To generate a stationary substrate for AFM studies, we embedded the substrate in epoxy resin without employing elevated temperatures or pressure. The absence of epoxy material diffusion into the substrate was confirmed previously (7). To prepare a nano-flat specimen surface, the epoxy-embedded substrate was first pre-cut with an Ultracut UCT ultramicrotome (Leica Microsystems, Wetzlar, Germany), then, the substrate was allowed to swell in buffer for one hour. The wet specimen was finally cut again to receive a nano-flat surface with a root-mean-squared (RMS) roughness of 10–15 nm.

Enzymatic Hydrolysis Studies—All hydrolysis experiments were conducted in triplicate at 50 °C, pH 5.0, in buffer. The cellulosic substrate concentration was 7.2 mg/ml in a total volume of 350 μl. Enzyme loadings were the same as in the respective AFM experiments: 3.6 $mg/g_{substrate}$ (complete system), 36 $mg/g_{substrate}$ (CBH I and EG) and 1.3 $g/g_{substrate}$ (CBH II). Sample tubes were centrifuged for 1 min at 10,000 rpm at defined breakpoints. The supernatant was heated to 95 °C for 7 min to terminate cellulase activity, and then again centrifuged for 1

[4] The abbreviations used are: CBH, cellobiohydrolase; AFM, atomic force microscopy; BGL, β-glucosidase; BMIMCl, 1-butyl-3-methylimidazolium chloride; CMC, carboxymethyl cellulose; DNS, 3,5-dinitrosalicylic acid; EG, endoglucanase; FPU, filter paper unit; MUF-cellobioside, methylumbelliferyl-β-D-cellobioside; MS, mass spectrometry; RMS, root-mean-squared.

min at 10,000 rpm. The reducing sugars were determined in the resulting supernatant by means of the DNS assay (30).

For the hydrolysis experiment probing cellulase synergism, the cellulosic substrate concentration was 1 mg/ml in a total volume of 1 ml of buffer. To prevent inhibition by accumulating cellobiose, 1 unit of BGL was added. The setup was designed to resemble the AFM synergism experiment at 20 °C: in the beginning, solely EG (9 mg/$g_{substrate}$) was present. CBH II (320 mg/$g_{substrate}$) was added after 160 min and CBH I (9 mg/$g_{substrate}$) after 280 min total reaction time. After 350 min, the reaction was stopped. Samples were drawn accordingly, treated as described above and the amount of reducing sugars was determined.

In Situ AFM Observation, Data Collection, and Analyses—For the *in situ* AFM measurements at 20 °C in buffer a commercial Dimension 3100 AFM equipped with a Hybrid scan head, a liquid cell tip holder, and Nanoscope IVa controller (Bruker AXS, Santa Barbara) was used. Imaging was performed with a TR400PSA cantilever (Olympus Probes, Tokyo, Japan) in TappingMode®. A laboratory-built liquid cell featuring an injection valve was used for specimen mounting. Scan rates, set points, and drive amplitudes were chosen accordingly to guarantee stable scanning with the lowest energy dissipation possible. During image recording we gave careful consideration to avoiding tip related artifacts by permanently evaluating side wall angles and morphological features of the surface.

Initially, AFM reference images of the specimen surface were recorded in buffer (3 ml) and areas for continuous *in situ* observation were selected. Suitable areas featured one larger, characteristic crystalline region, which served as a marker. Then, the respective enzyme solution was added, and the dynamics of the enzymatic degradation were recorded continuously. The protein loadings used were 3.6 mg/$g_{substrate}$ for the complete cellulase system, 36 mg/$g_{substrate}$ for EG and CBH I, and 1.3 g/$g_{substrate}$ for CBH II. These loadings were chosen after preliminary studies showed a good time-dependent resolution of activity for the settings of our AFM experiments. For the hydrolysis experiment probing cellulase synergism, solely EG (9 mg/$g_{substrate}$) was present in the beginning. CBH II (320 mg/$g_{substrate}$) was added after 160 min and CBH I (9 mg/$g_{substrate}$) after 280 min total reaction time. After 350 min, the reaction was stopped. 1 unit of BGL was present in the reaction solution to prevent inhibition by accumulating cellobiose.

Image processing and detailed analysis was performed with NanoScope Analysis 1.20 (Build R1Sr3.64571, Veeco Instruments Inc.) and Gwyddion (Gwyddion 2.25). Data analysis of depth evolution and degradation velocity was done in OriginLab 8.5 (OriginLab Corp, Northampton).

We analyzed the vertical degradation quantitatively by evaluating multiple points on the surface and tracking their change over time using large crystallites as a reference. Careful post-processing of the images allowed for measuring the depth of a distinct point in reference to a crystallite on each of 18 images which were taken in distinct time intervals. Evaluation of the height difference per time allowed to calculate the degradation velocity at different positions on the substrate. Evidence for two distinct velocities was found through statistical evaluation of velocities and double peak fitting.

RESULTS AND DISCUSSION

A Mesoscopic View on Synergistic Degradation of Polymorphic Cellulose—Here we present a study on the cellulolytic degradation of a representative mixed amorphous-crystalline cellulose (7). We prepared the substrate by incomplete dissolution of Avicel in an ionic liquid and subsequent removal of the solvent. The supramolecular structure of the resulting polymorphic cellulose exhibits an amorphous cellulose matrix in which larger crystallites (100 nm-10 μm) and smaller fibrils (width: ≤15 nm; length: 100–300 nm) are embedded randomly as schematically shown in supplemental Fig. S1. Overall, 30% of the substrate consists of crystallites and small crystalline fibrils. The primarily amorphous character of the cellulose preparation was reported previously (7). The surface roughness in liquid environments was lower than 10 nm, as determined by using AFM in a liquid cell. As previously confirmed, the respective crystalline phases are predominantly made of cellulose I (7), which is the main allomorph of natural cellulose in higher plants (42). This substrate is well suited for drawing conclusions to natural and pretreated biomass cellulose because it features amorphous as well as crystalline regions of allomorph I. Furthermore, it fulfills the requirements for a comprehensive analysis of cellulase synergy by AFM: it is sufficiently flat and it features crystalline and amorphous regions which make a suitable substrate for the diverse cellulases.

A Complete Cellulase System Preferentially Degrades the Amorphous Regions of the Polymorphic Substrate to Bare Crystalline Regions—First of all, we aimed at visualizing the mesoscopic structural consequences of exposure of the polymorphic substrate to the synergistic degradation by a complete cellulase system *in situ*. We used a complete cellulase preparation from the cellulolytic fungus *Trichoderma reesei*, which contains CBH I (60%), CBH II (20%), and EG (12%) as its major enzyme components (17, 19, 33). Enzymatic attack resulted in a considerable volume degradation of the polymorphic substrate in dependence of the incubation time (Fig. 1, *A* and *B*). After 4 h, the height differed up to 700 nm compared with the start of the reaction (Fig. 1*B*). Eventually, the cellulose surface was completely rugged with the large crystallite marker remaining (Fig. 1*A*). This implies that the bulk of the amorphous material had been degraded (Fig. 1*A*). *In situ* AFM imaging shows that homogeneous substrate areas, corresponding to amorphous cellulose, are degraded to bare crystalline nanofibrils and crystallite surfaces with a defined and highly ordered structure (crystalline cellulose), comparable to AFM images of crystalline model substrates and fibrils (28, 43). Generally, we observed that large crystallites were degraded extremely slowly. Therefore, they were used as markers for the scan area and to follow height changes over time. This is reflected in the graph in Fig. 1*B* where the surface evolution is illustrated by superimposition of time-resolved section profiles: while the material at the side of the crystallites is removed and leads to the formation of cavities, the crystallite itself remains unchanged.

Interestingly, in time-resolved AFM sequences we observed that small cellulose fibrils (width: ≤15 nm) appeared and were degraded in an alternating manner (Fig. 1*D*; supplemental Videos S1 and S2). At first, these fibrils were polished from cover-

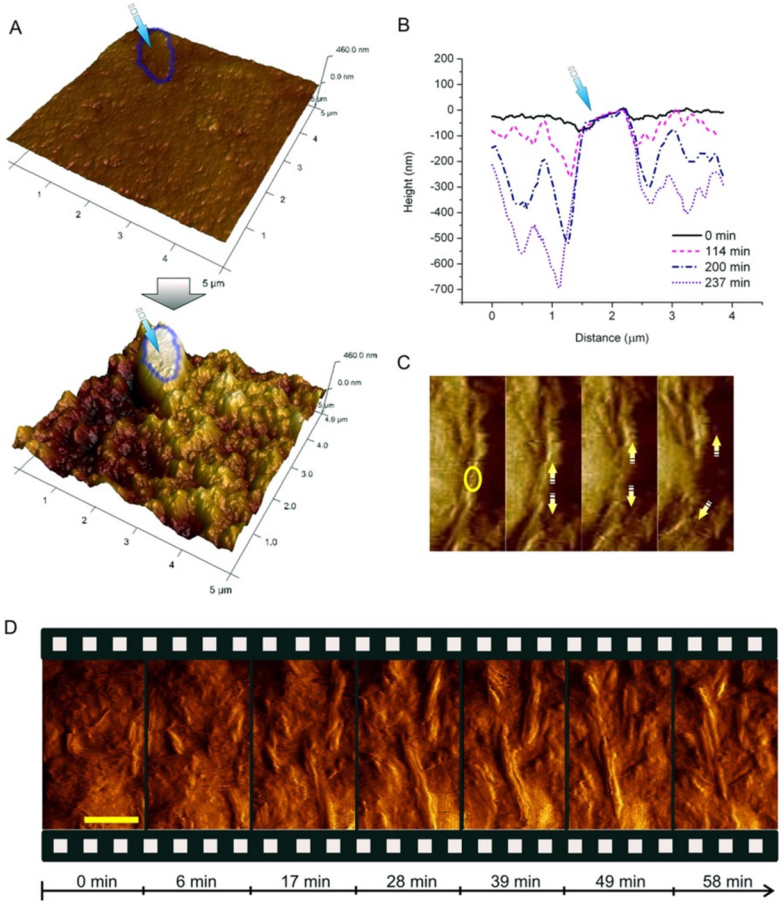

FIGURE 1. ***In situ* observation of the synergistic degradation of polymorphic cellulose by the complete cellulase system of *T. reesei*.** *A*, substrate surface at the beginning of (t = 0 min) and after incubation (t = 237 min) with the complete cellulase system. A typical large crystallite, which was used as a marker for height change during degradation, is indicated. The substrate around it is degraded, while the crystallite itself remains virtually unaltered (see also supplemental Video S2). *B*, section profiles of the area shown in *B* reflect the volumetric degradation with time. Relative to the marker, the substrate around it was degraded up to 700 nm in 237 min. *C*, *in situ* observation of a defect (*circle*) being introduced into a fibril. Subsequently, the fibril is attacked and degraded from both new ends of the generated defect (*arrows*). *D*, snapshots along the time course of cellulose degradation (see also supplemental Video S1) show initial degradation of amorphous regions (17 min). Previously buried crystalline fibrils appear (28 min) and are quickly degraded in a processive manner starting at their ends as well as at previously introduced defects (49 min). The scale bar represents 100 nm.

ing amorphous material. Subsequently, they were degraded rapidly. This leads to the conclusion that cellulases remove amorphous material surrounding the crystalline fibrils first, and then degrade the fibrils to uncover subjacent amorphous material again. Fibrils are degraded in various ways: primarily by thinning starting from the side walls, but also by shortening starting from fibril tips and introduction of defects in the middle of the fibrils (Fig. 1, *C* and *D*; supplemental Videos S1 and S2). As soon as a new defect was generated (Fig. 1*C*, *circle* in the *left panel*), degradation proceeded rapidly from the two new ends thus produced (Fig. 1*C*, *arrows*). Eventually, the fibril was degraded quickly (Fig. 1*C*; supplemental Video S1). However, in contrast to the smaller crystalline fibrils (width: ≤15 nm; length: 100–300 nm), the large crystallites (100 nm-10 μm) remained unchanged. This is probably due to a majority of the cellulase binding sites being buried within the crystal, which would impede enzymatic attack. The thin fibrils, by contrast, exhibit easily accessible cellulase binding sites at their ends and therefore are quickly attacked as soon as they are bared from the amorphous matrix.

We analyzed vertical degradation quantitatively by evaluating multiple points on the surface and tracking their change over time. Strikingly, we thus found evidence for two distinct degradation velocities (supplemental Fig. S2). This corroborates what we observed in the AFM images: once bared, small crystalline fibrils are degraded significantly faster (3.8 ± 0.2 nm/min) than the residual amorphous matrix (0.7 ± 0.2 nm/min). Taking into account that large crystallites are degraded infinitely slower, this leads to the practically important conclusion that the retarding effect of cellulose crystallin-

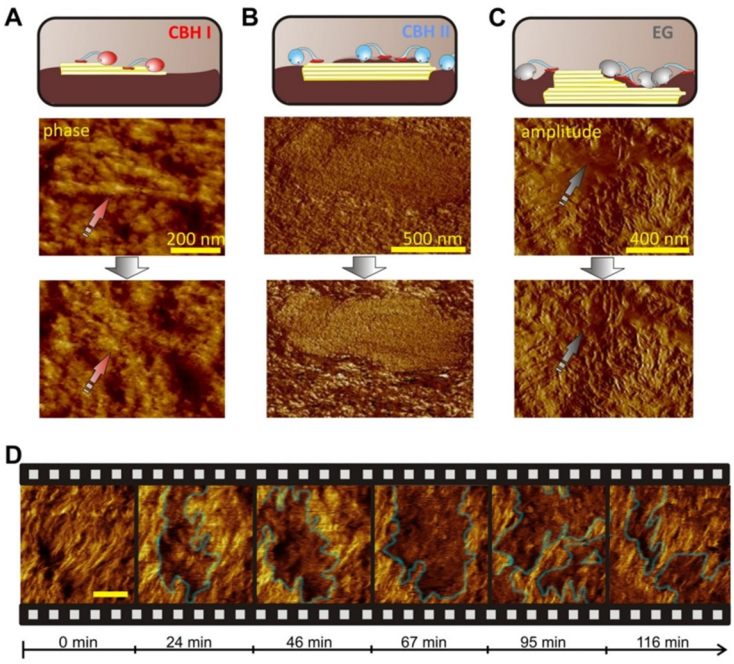

FIGURE 2. **Dissecting synergism: *in situ* observation of single enzymes.** *A*, CBH I degrades small fibrils (phase image). *B*, CBH II polishes the surface of a large crystallite by removing amorphous cellulose (phase image). *Right*: (*C*), an example of EG polishing which leads to a highly defined fibrillar surface (amplitude image). *D*, "clustering" effect of CBH II in a phase image sequence (see also supplemental Video S3). The scale bar represents 100 nm.

ity on the reaction rate is strongly dependent on crystal size and shape and the accessibility of binding sites at crystals.

CBH II and EG Efficiently Remove Amorphous Cellulose and Polish Crystalline Regions for CBH I Attack—Consequently, the next question was how each of the major cellulase enzymes contributes to the mesoscopic destruction of the cellulose as observed with the complete system. Therefore, we dissected the synergistic action of the complete system by separate *in situ* imaging and analysis of its major individual activities: CBH I, CBH II, and EG. In contrast to the complete cellulase system, neither of the single enzymes caused the massive volumetric degradation as observed in the complete cellulase system. With each of the individual cellulases, the surface roughness was only modestly increased and no volume loss was observed, despite the high loadings used: the amount of CBH I, CBH II, and EG used corresponded to 17 times, 1800 times, and 83 times their respective relative abundance in the experiment with the complete system. These loadings were chosen with respect to a suitable time-dependent resolution of their activity in our AFM experiments.

Each of the enzymes produced a remarkably distinct pattern of cellulose surface disruption (Fig. 2, *A–C*). We observed that EG, which has been shown to preferably attack amorphous cellulose (31, 43, 44), efficiently degraded amorphous regions of the specimen. Thus, EG action caused gradual exposure of well-defined crystalline nanofibrils ("polishing"), which were previously covered by amorphous material. The crystalline fibrils themselves were not attacked by EG. This is exemplified by selected AFM images (Fig. 2*C*), where an amorphous spot (Fig. 2*C*, *arrow*) is polished by EG and thus cellulose of higher order is bared: in the second image, the previously blurry surface is highly defined. Interestingly, treatment with CBH II caused a similar polishing effect in combination with clustering of the enzymes. Generally, CBH II enzymes are known to be essential in deconstruction of crystalline cellulose (12, 31, 45). However, it has been proposed from indirect biochemical data that CBH II also degrades amorphous cellulose (45). We here show direct and conclusive evidence on the specificity of this enzyme for amorphous areas. In the AFM image shown in Fig. 2*B*, a large crystallite is at first buried beneath amorphous material. CBH II polishes it from amorphous material and the result is a defined crystallite surface visible in the second image. Additionally, we observed the appearance of CBH II "clusters" using AFM phase imaging, which allows a clear distinction between materials with different characteristics (*e.g.* cellulose and enzymes). In the AFM phase images these clusters are visible as darker cloud-like areas (Fig. 2*D*; supplemental Video S3). Initially, they bound to areas that did not exhibit a defined surface structure. Then, the clusters removed the amorphous cellulose to leave behind a more defined (*i.e.* crystalline) area (Fig. 2*B*; supplemental Video S3). However, in contrast to EG, and despite its observed distinct preference for amorphous cellulose, CBH II was bi-specific and also showed minor degradation of crystalline cellulose, observable as slight shortening of the fibrils. Accompanying biochemical studies of the substrate saccharification showed that EG and CBH II reached almost 60% conver-

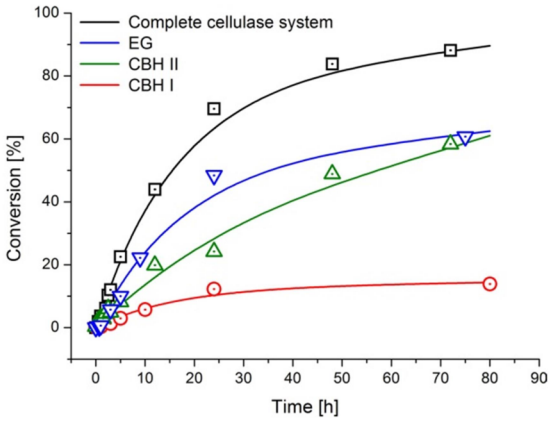

FIGURE 3. **Conversion *versus* time profiles of the complete cellulase system and the single cellulases used in this study.** The highest degree of conversion is achieved by the synergistic action of the complete cellulase system (3.6 mg/$g_{substrate}$). When solely CBH I (36 mg/$g_{substrate}$) is present, the hydrolysis rate declines at a pronouncedly lower degree of conversion. CBH II (1.3 g/$g_{substrate}$) and EG (36 mg/$g_{substrate}$) show a pronounced preference for the amorphous regions, which is reflected in a higher overall conversion of the primarily amorphous substrate as compared with CBH I.

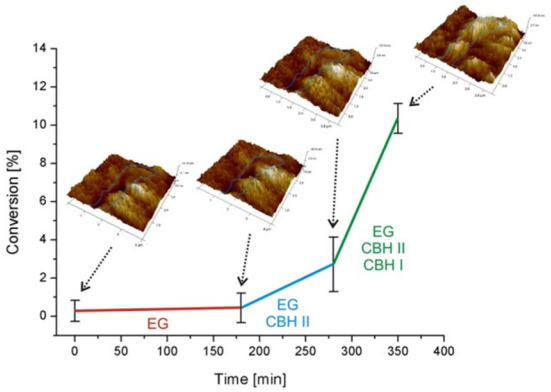

FIGURE 4. **Reconstructing synergism, substrate degradation with sequential addition of single cellulases.** This biochemical study of synergism shows how synergism becomes effective after addition of CBH I, which boosts the hydrolysis rate on the polymorphic substrate. The AFM image insets depict changes of the substrate along the reaction timeline. Rapid synergistic degradation and consequential three-dimensional disruption of the substrate does not happen until all three cellulases (EG, CBH II, and CBH I) are present.

sion (Fig. 3). This is in good agreement with the relative abundance of amorphous cellulose in our specimen (7).

Notably, EG and CBH I behaved as monospecific cellulases, showing complementary substrate preference for amorphous and crystalline cellulose, respectively. The surface roughness stayed constant during CBH I treatment (RMS roughness: 10.6 ± 0.5 nm). The AFM images in Fig. 2*A* depict the selective degradation of a small crystalline fibril (arrow). CBH I was exclusively active toward such small crystalline nanofibrils (≤ 10 nm width) on the surface (Fig. 2*A*), but did neither attack the surrounding amorphous material nor fibrils coated with amorphous material. Accordingly, sugar release by CBH I became stalled at low conversion (≤ 14%), this supposedly is the moment when the limited amount of accessible crystalline fibrils on the surface has been degraded (Fig. 3). This implies that, in order to degrade crystalline cellulose, CBH I requires helpers, which remove the amorphous layers beforehand. Overall, the absence of synergism renders single cellulases incapable of rapid and complete three-dimensional degradation of polymorphic cellulose. Accordingly, biochemical studies showed that synergistic degradation of the polymorphic substrate by the complete cellulase system resulted in 90% conversion (Fig. 3).

A Combination of EG, CBH II, and CBH I Enables Reconstruction of Synergism as Observed in the Complete System—While we observed considerable volumetric degradation with the complete cellulase system, this was not the case with the dissected single activities although we used them at significantly higher loadings compared with their abundance in the complete system. In the single enzyme experiments, CBH I only degraded small crystalline fibrils, which were exposed on the surface. The main effect of CBH II and EG was to polish crystalline regions by removing amorphous material covering those. In that way, CBH II and EG would prepare crystalline regions for CBH I attack. Accordingly, a mixture of solely EG and CBH II should not result in a significant rate acceleration or increase in volumetric degradation. Only when CBH I is added to these two, complete synergism would be re-established and boost the rate. In order to test this hypothesis, we added EG, CBH II, and CBH I in a controlled manner (Fig. 4). We also provided a sufficient amount of BGL to prevent inhibition by cellobiose (14, 17, 30). As expected, the pre-incubation of the substrate with EG led to minor hydrolysis through removal of some amorphous material. Subsequently, we added CBH II, which aided in the removal of amorphous cellulose, and besides it slowly started degrading the small crystalline fibrils, which had been exposed by foregoing EG action. In contrast to the single enzyme experiments, we now also observed a beginning volume loss and an increase in surface roughness from 12 nm to 16 nm RMS roughness. Over time, large crystalline areas, which were not attacked, became prevalent on the surface due to removal of the amorphous matrix. The rate of sugar release was enhanced 4-fold as a consequence of the synergy between EG and CBH II (Fig. 4). Finally, we added CBH I which immediately caused a massive degradation of both amorphous and crystalline areas of the cellulose. Large crystallites were unaltered, and small crystalline fibrils were degraded instantly upon being bared. RMS roughness and total volume loss increased significantly over time. Accordingly, we noted a 6-fold increase in the hydrolysis rate after addition of CBH I (Fig. 4). The presence of CBH I enhances the degradation of small fibrils in particular. As a consequence, we observed alternating appearance and disappearance of fibrils on the cellulose surface, as it was the case with the complete cellulase system (supplemental Video S1). Globally, the performance of the three-component enzyme mixture on the cellulose surface was identical to that of the complete cellulase system: large cellulose crystals were degraded more slowly than surrounding areas featuring small fibrils embedded in amorphous material.

The Rate of Enzymatic Cellulose Degradation Is Dependent on Substrate Morphology—Our results show that the appearance of large crystallites hardly changed as they were attacked

slowly, probably due to the fact that most of the cellulase binding sites were buried inside the crystal and hence not accessible to the enzymes. Exposed small crystalline fibrils, by contrast, were degraded faster even than amorphous regions through synergistic interaction of the cellulases (supplemental Fig. S2 and Video S1). This seemingly contradictory observation can be explained by size and shape of the crystallites in the respective substrates. There are various reasons for the slower degradation of big crystallites: the tight packing of the cellulose fibrils generally prevents interception and limits accessibility, cellulase binding sites might be buried inside the crystal, and traffic jams among surface-bound enzymes impede mobility and cause unproductive binding (22, 28).

Synergism among Cellulases Is Morphology-dependent and Dominated by Cooperativity between Enzymes Degrading Amorphous Cellulose and Those Degrading Crystalline Cellulose—We here demonstrated that synergism among cellulases is based upon the cooperation between those enzymes primarily attacking amorphous regions and those preferring crystalline areas: while EG and CBH II are utterly efficient in removing amorphous material, they show no (EG) or only marginal (CBH II) activity on crystalline cellulose (supplemental Fig. S3). Conversely, CBH I has a pronounced preference for regions of higher order, but is dependent on having these made accessible by EG and CBH II. A recent mechanistic study (30) found evidence that the rates of complexation of CBH and accessible chain ends are low but are significantly enhanced by presence of EG, which was reported to amplify CBH activity (30, 31). Moreover, the study authors assume a morphology-influenced synergy, meaning that other cellulases aid in removal of obstacles, which might impede CBH. This is in good agreement with several other *in vitro* and *in silico* studies (28, 30, 31, 46–48). According to the *in situ* visualization presented here, these obstacles are amorphous regions covering the substrate of CBH I, *i.e.* crystalline cellulose. We showed that CBH I efficiently degrades crystalline nanofibrils, which have easily accessible chain ends as compared with the large crystallites, where lots of chain ends might be buried within. Recently it was reported that amorphous regions of bacterial cellulose caused CBH I processivity to halt (31). In the polymorphic substrate used in our study, the majority of the nanofibrils are enclosed in the amorphous matrix of the substrate and hence inaccessible for CBH I. This is also reflected in the low activity of CBH I on the polymorphic substrate: when the surface-exposed nanofibrils are degraded, its activity stalls (Fig. 3). Accordingly, when the obstacles are removed by EG and CBH II, it is mainly CBH I that boosts the hydrolysis rate (Fig. 4).

Both CBH I and the bi-specific CBH II lack the ability to efficiently degrade crystalline cellulose unless other cellulases are present (Fig. 3; supplemental Fig. S2). Hence, cooperativity between an endo-exo system (EG and CBH II), which prepares the cellulose, and an exo-cellulase (CBH I) is pivotal, and this morphology-dependent synergy therefore constitutes the primary synergism. We showed that the three major cellulase components EG, CBH II, and CBH I are sufficient to reconstruct the synergism that can be observed for the complete cellulase system. Therefore, these three are the main cellulolytic enzymes of a system, which is ideally adapted for degradation of crystalline cellulosic substrates.

The degradation of crystalline regions once they are bared is furthermore strongly dependent on the size and shape of these areas. Aspect ratio, packing, and accessibility of free chain ends are responsible for the rapid degradation of small crystalline fibrils as compared with the cumbersome attack on the large crystallites (Figs. 1 and 2). It is conceivable, that the nanofibrils have easily accessible chain ends and allow for rapid processive degradation as shown in Fig. 1 and supplemental Video S1. This relatively rapid degradation of small crystalline fibrils explains the puzzling observations made in a number of other studies, which showed that crystallinity did not increase substantially with enzymatic conversion in some cellulose substrates while it did in others (12, 21).

Dependent on its source and possible pretreatment, biomass cellulose contains amorphous and crystalline regions to a variable extent (10). The polymorphic substrate we used is typical for a substrate with amorphous and crystalline regions of varying size. Our study visualizes that morphology is the main determinant of cellulase synergism. The finding that synergy among cellulases is dependent on substrate morphology furthermore explains why synergism between cellulases was observed on some substrates but not on others (49). Hence, enzyme mixtures for efficient saccharification of biomass need to be adapted for the morphology of their respective substrate.

Acknowledgments—We thank Karin Longus for producing the complete cellulase system; Gregor Trimmel for characterization of the substrate; Anton Glieder for the kind gift of CBH II; Ferdinand Hofer for discussions; and Dominika Stiger for commenting on the manuscript.

REFERENCES

1. Farrell, A. E., Plevin, R. J., Turner, B. T., Jones, A. D., O'Hare, M., and Kammen, D. M. (2006) Ethanol can contribute to energy and environmental goals. *Science* **311,** 506–508
2. Graham-Rowe, D. (2011) Agriculture: Beyond food versus fuel. *Nature* **474,** S6–8
3. Hill, J., Polasky, S., Nelson, E., Tilman, D., Huo, H., Ludwig, L., Neumann, J., Zheng, H., and Bonta, D. (2009) Climate change and health costs of air emissions from biofuels and gasoline. *Proc. Natl. Acad. Sci. U.S.A.* **106,** 2077–2082
4. Schmer, M. R., Vogel, K. P., Mitchell, R. B., and Perrin, R. K. (2008) Net energy of cellulosic ethanol from switchgrass. *Proc. Natl. Acad. Sci. U.S.A.* **105,** 464–469
5. Lynd, L. R., Laser, M. S., Bransby, D., Dale, B. E., Davison, B., Hamilton, R., Himmel, M., Keller, M., McMillan, J. D., Sheehan, J., and Wyman, C. E. (2008) How biotech can transform biofuels. *Nat. Biotechnol.* **26,** 169–172
6. Himmel, M. E., Ding, S. Y., Johnson, D. K., Adney, W. S., Nimlos, M. R., Brady, J. W., and Foust, T. D. (2007) Biomass recalcitrance: engineering plants and enzymes for biofuels production. *Science* **315,** 804–807
7. Bubner, P., Dohr, J., Plank, H., Mayrhofer, C., and Nidetzky, B. (2012) Cellulases dig deep: In situ observation of the mesoscopic structural dynamics of enzymatic cellulose degradation. *J. Biol. Chem.* **287,** 2759–2765
8. Chundawat, S. P., Bellesia, G., Uppugundla, N., da Costa Sousa, L., Gao, D., Cheh, A. M., Agarwal, U. P., Bianchetti, C. M., Phillips, G. N., Jr., Langan, P., Balan, V., Gnanakaran, S., and Dale, B. E. (2011) Restructuring crystalline cellulose hydrogen bond network enhances its depolymerization rate. *J. Am. Chem. Soc.* **133,** 11163–11174
9. Jarvis, M. (2003) Chemistry: cellulose stacks up. *Nature* **426,** 611–612

10. Klemm, D., Heublein, B., Fink, H. P., and Bohn, A. (2005) Cellulose: fascinating biopolymer and sustainable raw material. *Angew. Chem. Int. Ed. Engl.* **44,** 3358–3393
11. Bansal, P., Hall, M., Realff, M. J., Lee, J. H., and Bommarius, A. S. (2009) Modeling cellulase kinetics on lignocellulosic substrates. *Biotechnol. Adv.* **27,** 833–848
12. Lynd, L. R., Weimer, P. J., van Zyl, W. H., and Pretorius, I. S. (2002) Microbial cellulose utilization: fundamentals and biotechnology. *Microbiol. Mol. Biol. Rev.* **66,** 506–577
13. Yang, B., Willies, D. M., and Wyman, C. E. (2006) Changes in the enzymatic hydrolysis rate of Avicel cellulose with conversion. *Biotechnol. Bioeng.* **94,** 1122–1128
14. Levine, S. E., Fox, J. M., Blanch, H. W., and Clark, D. S. (2010) A mechanistic model of the enzymatic hydrolysis of cellulose. *Biotechnol. Bioeng.* **107,** 37–51
15. Becker, D., Braet, C., Brumer, H., 3rd, Claeyssens, M., Divne, C., Fagerström, B. R., Harris, M., Jones, T. A., Kleywegt, G. J., Koivula, A., Mahdi, S., Piens, K., Sinnott, M. L., Ståhlberg, J., Teeri, T. T., Underwood, M., and Wohlfahrt, G. (2001) Engineering of a glycosidase Family 7 cellobiohydrolase to more alkaline pH optimum: the pH behaviour of *Trichoderma reesei* Cel7A and its E223S/A224H/L225V/T226A/D262G mutant. *Biochem. J.* **356,** 19–30
16. Blanch, H. W., Simmons, B. A., and Klein-Marcuschamer, D. (2011) Biomass deconstruction to sugars. *Biotechnol. J.* **6,** 1086–1102
17. Zhang, Y. H., and Lynd, L. R. (2004) Toward an aggregated understanding of enzymatic hydrolysis of cellulose: noncomplexed cellulase systems. *Biotechnol. Bioeng.* **88,** 797–824
18. Boisset, C., Fraschini, C., Schülein, M., Henrissat, B., and Chanzy, H. (2000) Imaging the enzymatic digestion of bacterial cellulose ribbons reveals the endo character of the cellobiohydrolase Cel6A from *Humicola insolens* and its mode of synergy with cellobiohydrolase Cel7A. *Appl. Environ. Microbiol.* **66,** 1444–1452
19. Goyal, A., Ghosh, B., and Eveleigh, D. (1991) Characteristics of Fungal Cellulases. *Biores. Technol.* **36,** 37–50
20. Nidetzky, B., Steiner, W., Hayn, M., and Claeyssens, M. (1994) Cellulose hydrolysis by the cellulases from *Trichoderma reesei*: a new model for synergistic interaction. *Biochem. J.* **298,** 705–710
21. Bansal, P., Vowell, B. J., Hall, M., Realff, M. J., Lee, J. H., and Bommarius, A. S. (2012) Elucidation of cellulose accessibility, hydrolysability and reactivity as the major limitations in the enzymatic hydrolysis of cellulose. *Bioresour. Technol.* **107,** 243–250
22. Väljamäe, P., Sild, V., Nutt, A., Pettersson, G., and Johansson, G. (1999) Acid hydrolysis of bacterial cellulose reveals different modes of synergistic action between cellobiohydrolase I and endoglucanase I. *Eur. J. Biochem./FEBS* **266,** 327–334
23. Divne, C., Stahlberg, J., Reinikainen, T., Ruohonen, L., Pettersson, G., Knowles, J. K., Teeri, T. T., and Jones, T. A. (1994) The three-dimensional crystal structure of the catalytic core of cellobiohydrolase I from *Trichoderma reesei*. *Science* **265,** 524–528
24. Koivula, A., Reinikainen, T., Ruohonen, L., Valkeajarvi, A., Claeyssens, M., Teleman, O., Kleywegt, G. J., Szardenings, M., Rouvinen, J., Jones, T. A., and Teeri, T. T. (1996) The active site of *Trichoderma reesei* cellobiohydrolase II: the role of tyrosine 169. *Protein Eng. Des. Sel.* **9,** 691–699
25. Kleywegt, G. J., Zou, J. Y., Divne, C., Davies, G. J., Sinning, I., Ståhlberg, J., Reinikainen, T., Srisodsuk, M., Teeri, T. T., and Jones, T. A. (1997) The crystal structure of the catalytic core domain of endoglucanase I from *Trichoderma reesei* at 3.6 Å resolution, and a comparison with related enzymes. *J. Mol. Biol.* **272,** 383–397
26. Henrissat, B., Driguez, H., Viet, C., and Schülein, M. (1985) Synergism of cellulases from *Trichoderma reesei* in the degradation of cellulose. *Nat. Biotechnol.* **3,** 722–726
27. Hu, J., Arantes, V., and Saddler, J. N. (2011) The enhancement of enzymatic hydrolysis of lignocellulosic substrates by the addition of accessory enzymes such as xylanase: is it an additive or synergistic effect? *Biotechnol. Biofuels* **4,** 36
28. Igarashi, K., Uchihashi, T., Koivula, A., Wada, M., Kimura, S., Okamoto, T., Penttilä, M., Ando, T., and Samejima, M. (2011) Traffic jams reduce hydrolytic efficiency of cellulase on cellulose surface. *Science* **333,** 1279–1282
29. Sturcová, A., His, I., Apperley, D. C., Sugiyama, J., and Jarvis, M. C. (2004) Structural details of crystalline cellulose from higher plants. *Biomacromolecules* **5,** 1333–1339
30. Fox, J. M., Levine, S. E., Clark, D. S., and Blanch, H. W. (2012) Initial- and processive-cut products reveal cellobiohydrolase rate limitations and the role of companion enzymes. *Biochemistry* **51,** 442–452
31. Jalak, J., Kurašhin, M., Teugjas, H., and Väljamäe, P. (2012) Endo-exo synergism in cellulose hydrolysis revisited. *J. Biol. Chem.* **287,** 28802–28815
32. Medve, J., Karlsson, J., Lee, D., and Tjerneld, F. (1998) Hydrolysis of microcrystalline cellulose by cellobiohydrolase I and endoglucanase II from Trichoderma reesei: adsorption, sugar production pattern, and synergism of the enzymes. *Biotechnol. Bioeng.* **59,** 621–634
33. Liu, Y. S., Baker, J. O., Zeng, Y., Himmel, M. E., Haas, T., and Ding, S. Y. (2011) Cellobiohydrolase hydrolyzes crystalline cellulose on hydrophobic faces. *J. Biol. Chem.* **286,** 11195–11201
34. Igarashi, K., Koivula, A., Wada, M., Kimura, S., Penttilä, M., and Samejima, M. (2009) High speed atomic force microscopy visualizes processive movement of *Trichoderma reesei* cellobiohydrolase I on crystalline cellulose. *J. Biol. Chem.* **284,** 36186–36190
35. Kubicek, C. P., Bolzlbauer, U. M., Kovacs, W., Mach, R. L., Kuhls, K., Lieckfeldt, E., Borner, T., and Samuels, G. J. (1996) Cellulase formation by species of *Trichoderma* sect. *Longibrachiatum* and of *Hypocrea* spp. with anamorphs referable to *Trichoderma* sect. *Longibrachiatum*. *Fungal Genet. Biol.* **20,** 105–114
36. Druzhinina, I. S., Komon-Zelazowska, M., Ismaiel, A., Jaklitsch, W., Mullaw, T., Samuels, G. J., and Kubicek, C. P. (2012) Molecular phylogeny and species delimitation in the section *Longibrachiatum* of *Trichoderma*. *Fungal Genet. Biol.* **49,** 358–368
37. Marx, M.-C., Wood, M., and Jarvis, S. C. (2001) A microplate fluorimetric assay for the study of enzyme diversity in soils. *Soil Biol. Biochem.* **33,** 1633–1640
38. Josefsson, P., Henriksson, G., and Wågberg, L. (2008) The physical action of cellulases revealed by a quartz crystal microbalance study using ultrathin cellulose films and pure cellulases. *Biomacromolecules* **9,** 249–254
39. Ghose, T. K. (1987) Measurement of Cellulase Activities. *Pure Appl. Chem.* **59,** 257–268
40. Bradford, M. M. (1976) A rapid and sensitive method for the quantitation of microgram quantities of protein utilizing the principle of protein-dye binding. *Anal. Biochem.* **72,** 248–254
41. Gasteiger, E., Hoogland, C., Gattiker, A., Duvaud, S., Wilkins, M. R., Appel, R. D., and Bairoch, A. (2005) in *The Proteomics Protocols Handbook* (Walker, J. M., ed), Humana Press
42. Lee, I., Evans, B. R., and Woodward, J. (2000) The mechanism of cellulase action on cotton fibers: evidence from atomic force microscopy. *Ultramicroscopy* **82,** 213–221
43. Wang, J., Quirk, A., Lipkowski, J., Dutcher, J. R., Hill, C., Mark, A., and Clarke, A. J. (2012) Real-Time Observation of the Swelling and Hydrolysis of a Single Crystalline Cellulose Fiber Catalyzed by Cellulase 7B from *Trichoderma reesei*. *Langmuir* **28,** 9664–9672
44. Nieves, R. A., Ellis, R. P., Todd, R. J., Johnson, T. J., Grohmann, K., and Himmel, M. E. (1991) Visualization of *Trichoderma reesei* cellobiohydrolase I and endoglucanase I on aspen cellulose by using monoclonal antibody-colloidal gold conjugates. *Appl. Environ. Microbiol.* **57,** 3163–3170
45. Koivula, A., Kinnari, T., Harjunpää, V., Ruohonen, L., Teleman, A., Drakenberg, T., Rouvinen, J., Jones, T. A., and Teeri, T. T. (1998) Tryptophan 272: an essential determinant of crystalline cellulose degradation by *Trichoderma reesei* cellobiohydrolase Cel6A. *FEBS Lett.* **429,** 341–346
46. Zhou, W., Xu, Y., and Schüttler, H.-B. (2010) Cellulose Hydrolysis in Evolving Substrate Morphologies III: Time-Scale Analysis. *Biotech. Bioeng.* **107,** 224–234
47. Cruys-Bagger, N., Elmerdahl, J., Praestgaard, E., Tatsumi, H., Spodsberg, N., Borch, K., and Westh, P. (2012) Pre-steady-state kinetics for hydrolysis of insoluble cellulose by cellobiohydrolase Cel7A. *J. Biol. Chem.* **287,** 18451–18458
48. Kurasin, M., and Väljamäe, P. (2011) Processivity of cellobiohydrolases is limited by the substrate. *J. Biol. Chem.* **286,** 169–177
49. Mansfield, S. D., Mooney, C., and Saddler, J. N. (1999) Substrate and enzyme characteristics that limit cellulose hydrolysis. *Biotechnol. Prog.* **15,** 804–816

Supplemental Information

Dissecting and reconstructing synergism - *in situ* visualization of cooperativity among cellulases

Thomas Ganner, Patricia Bubner, Manuel Eibinger, Claudia Mayrhofer, Harald Plank & Bernd Nidetzky

Supplemental Figures

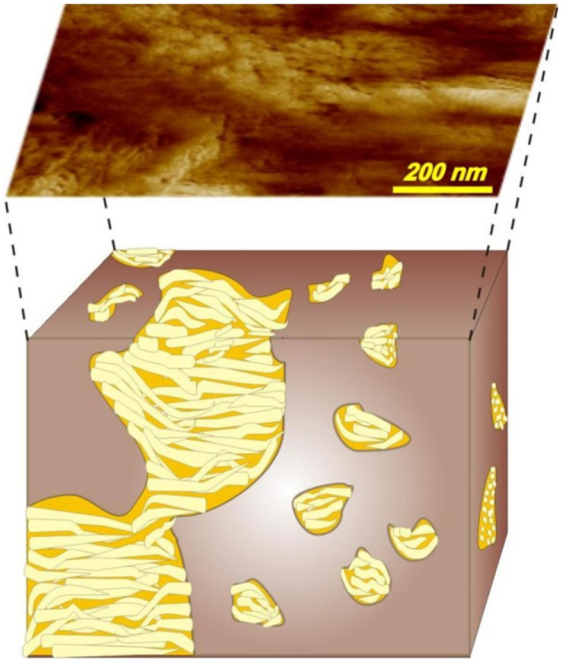

Fig. S1. Illustration of the cellulosic substrate superimposed with an AFM surface image of the substrate. The polymorphic substrate contains larger crystallites (100 nm-10 µm) and smaller fibrils (diameter: 7-12 nm; length: 100-300 nm) which are randomly distributed in an amorphous cellulose matrix. The specimen was prepared with a surface roughness of 10 nm or smaller in a liquid environment.

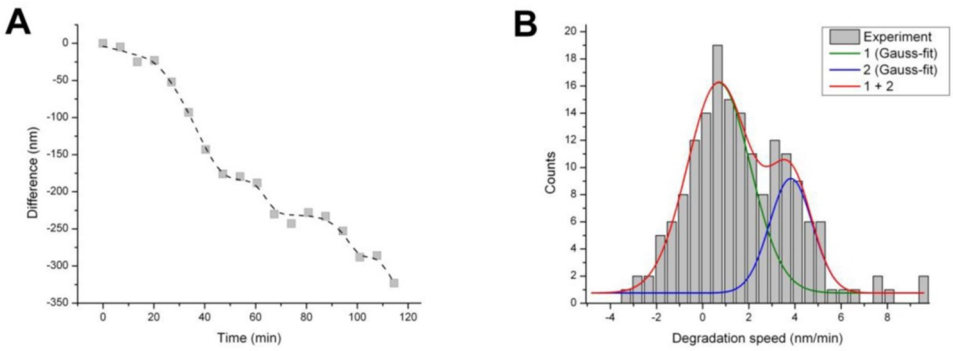

Fig. S2. Quantitative analysis of vertical degradation: evidence for two distinct degradation velocities. (A) Alternating fast and slow degradation velocity exemplified at one out of several points observed. **(B)** By evaluating multiple points on the surface and tracking their change over time we found strong evidence for two distinct velocities. This is in accordance with our overall observation that small crystalline fibrils are degraded even faster (3.8 ± 0.2 nm/min) than amorphous regions (0.7 ± 0.2 nm/min).

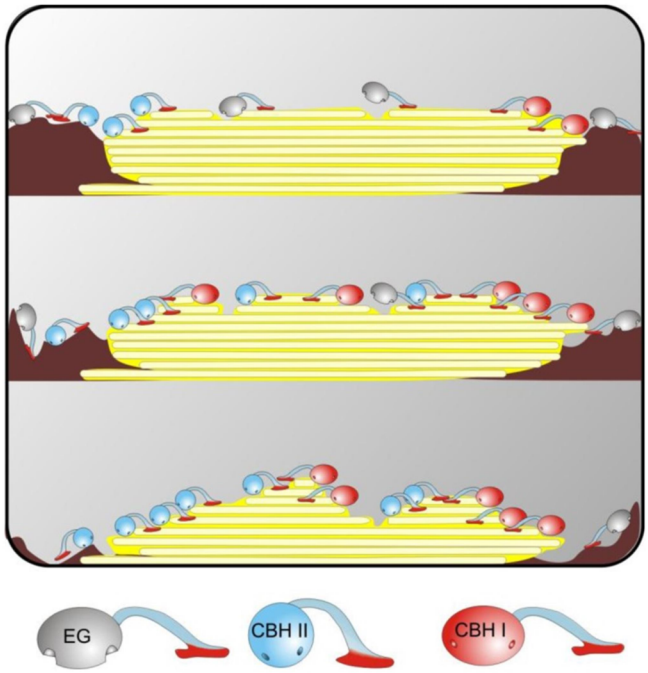

Fig. S3. Model of synergistic cellulose degradation. Illustration of the synergistic degradation of a substrate containing amorphous and crystalline regions based on the AFM observations in this study. red: CBH I; blue: CBH II; gray: EG.

Supplemental Video Captions:

Video S1. The complete cellulase system of *T. reesei* degrades a polymorphic cellulose (see also Fig. 1D). This video shows how a complete cellulase system of T. reesei degrades a polymorphic cellulose as imaged using AFM. The structural dynamics can be followed: initially, the amorphous regions are degraded. As a result, fibers are exposed and then quickly degraded in a processive manner.

Video S2. Three-dimensional superimposition of cellulose degradation by the complete cellulase system (see also Fig. 1A). In this video, recorded AFM images are superimposed

allowing to follow the degradation three-dimensionally with time (t=0-237 min). A typical large crystallite, which was used as a marker for height change during degradation, can be seen. The substrate around it is degraded, while the crystallite itself remains virtually unaltered.

Video S3. CBH II clustering and polishing. This video is a phase image sequence which shows CBH II clustering and polishing of the surface of a large crystallite by removing amorphous cellulose. When the clusters disappear, a more defined surface is left behind.

Surface structural dynamics of enzymatic cellulose degradation, revealed by combined kinetic and atomic force microscopy studies

the FEBS Journal

Surface structural dynamics of enzymatic cellulose degradation, revealed by combined kinetic and atomic force microscopy studies

Manuel Eibinger[1], Patricia Bubner[1,*], Thomas Ganner[2,3], Harald Plank[2,3] and Bernd Nidetzky[1]

1 Institute of Biotechnology and Biochemical Engineering, Graz University of Technology, Austria
2 Institute for Electron Microscopy and Fine Structure Research, Graz University of Technology, Austria
3 Center for Electron Microscopy, Graz University of Technology, Austria

Keywords
adsorption; atomic force microscopy; cellulase; cellulose morphology; hydrolysis kinetics

Correspondence
B. Nidetzky, Institute of Biotechnology and Biochemical Engineering, Petersgasse 12, A-8010 Graz, Austria
Fax: +43 316 873 8434
Tel: +43 316 873 8400
E-mail: bernd.nidetzky@tugraz.at
H. Plank, Institute for Electron Microscopy and Fine Structure Research, Graz University of Technology, Steyrergasse 17, A-8010 Graz, Austria
Fax: +43 316 811594
Tel: +43 316 873 8821
E-mail: harald.plank@tugraz.at

***Present address:**
Energy Biosciences Institute and Department of Plant and Microbial Biology, University of California, Berkeley, CA, 94720, USA

(Received 29 July 2013, revised 18 October 2013, accepted 21 October 2013)

doi:10.1111/febs.12594

Highly heterogeneous and usually weakly defined substrate morphologies complicate the study of enzymatic cellulose hydrolysis. The cellulose surface has a non-uniform shape in particular, with consequent impacts on cellulase adsorption and activity. We have therefore prepared a cellulosic model substrate which is shown by atomic force microscopy (AFM) to display a completely smooth surface, the residual squared mean roughness being 10 nm or lower, and applied it for kinetic analysis of cellulase action. The substrate consists of an amorphous cellulose matrix into which variably sized crystalline fibers are distributed in apparently irregular fashion. Its conversion into soluble sugars by *Trichoderma* sp. cellulase at 50 °C proceeded without apparent limitation up to 70% completion and was paralleled by a steady increase in cellulase adsorption to the cellulose. Individual cellulase components (CBH I, CBH II, EG) also showed strongly enhanced adsorption with progressing cellulose conversion, irrespective of their preference for degrading the amorphous or crystalline substrate parts as revealed by AFM. The specific activity of the adsorbed cellulases, however, decreased concomitantly. Cellulose surface morphologies evolving as a consequence of cellulase action were visualized by AFM. Three-dimensional surface degradation by the cellulases resulted in a large increase in cellulose surface area for enzyme adsorption. However, the decline in enzyme specific activity during conversion was caused by factors other than surface ablation and disruption. Based on kinetic evidence for enzymatic hydrolyses of the smooth-surface model substrate and microcrystalline cellulose (Avicel), we hypothesize that, due to gradual loss of productive dynamics in their interactions with the cellulose surface, individual cellulases get progressively confined to substrate parts where they are no longer optimally active. This eventually leads to an overall slow-down of hydrolysis.

Introduction

Cellulose is the most abundant carbohydrate-based biomaterial, and it represents a major renewable resource for sustainable production of fuels and bulk commodities [1,2]. Cellulose is built from long unbranched poly-D-glucosyl chains, each containing several hundreds of anhydro-D-glucose molecules

Abbreviations
AFM, atomic force microscopy; BGL, *Aspergillus niger* β-glucosidase; BMIMCl, 1-butyl-3-methylimidazolium chloride; CBH, cellobiohydrolase; DNS, 3,5-dinitrosalicylic acid; EG, endoglucanase; FPU, filter paper unit; MACS, mixed amorphous–crystalline cellulose model substrate; MUF-c, 4-methylumbelliferyl-β-D-cellobioside.

joined by β-1,4-glycosidic linkages and comprising the dimer β-1,4-D-glucosyl anhydro-D-glucose (cellobiosyl; Scheme 1) as the basic repeating unit [3,4]. In plant cell wall cellulose, the individual polysaccharide chains occur densely packed within spatially correlated nanostructures, often referred to as elementary fibrils. These fibrils in turn are further aggregated into higher-order supermolecular assemblies (Scheme 1). A substantial portion (≥ 70%) of the cellulose therefore constitutes a hierarchically organized and highly crystalline material [4] (Scheme 1). Parts of the cellulose that feature positional, directional or orientational disorders of the chains are usually called amorphous. Crystalline cellulose shows pronounced structural resistance to chemical or enzymatic degradation whereas amorphous cellulose is more readily broken down by comparison [5,6].

The cellulosic substrates applied to enzymatic hydrolysis studies are usually processed in multiple steps from natural biomass, typically plant lignocellulose. Mechanical processing causes reduction in the cellulose particle size and therefore increases the externally available surface area. Thermo-chemical pretreatments break up the internal structural organization of cellulose. This creates new internally accessible surface area due to the formation of variably sized fissures, cracks and pores [7–9]. As-processed cellulose therefore shows large and irregularly distributed variation in its morphology, i.e. in the spatial arrangement of its constituent cellulose chains into solid material, across the mesoscopic length scale (≥ 100 nm). There are hints from different investigations that in addition to cellulose crystallinity [10,11] it is the mesoscale substrate morphology that controls reactivity of the cellulose towards hydrolytic degradation by the cellulases [12–15]. Initially, most of the individual chains are not accessible for enzymatic attack because of surrounding cellulosic material. The fraction of β-1,4-glycosidic linkages accessible on the surface for enzymatic hydrolysis may be as low as 0.6% of the total cellulose mass [16]. Additionally it presents a complex geometrical substrate parameter that is determined by both the cellulosic substrate morphology and the molecular size and the shape of the cellulases [17]. However, the cellulose morphology will change substantially over time as hydrolytic conversion proceeds [15], with consequent effects on cellulase activity. It therefore becomes apparent that cellulose saccharification kinetics strongly depend on substrate morphology while at the same time morphology evolution is profoundly affected by enzymatic degradation [13,14,18]. The developing substrate morphology during cellulose hydrolysis might explain a characteristic feature of many experimental conversion studies that the rate of soluble sugar formation from the cellulosic substrate declines rapidly during the enzymatic reaction [10,19]. Because early slow-down of the hydrolysis presents a major limitation on efficient performance of cellulose conversion processes [20,21], mechanistic insights about its occurrence in relation to substrate morphol-

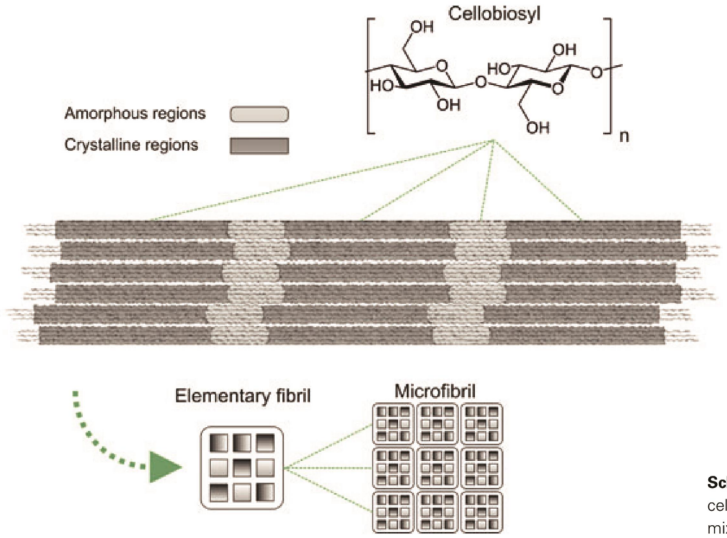

Scheme 1. Structural organization of cellulose chains into solid material that has mixed amorphous–crystalline character.

ogy development might bear important technological implications.

A key requirement for being able to experimentally track cellulose morphology evolution in dependence on enzymatic hydrolysis is effective elimination of topological heterogeneities (e.g. pores, cracks, cavities) from the surface of the cellulose preparation. To this end we have developed a tailor-made cellulosic substrate, which is shown by atomic force microscopy (AFM) to exhibit a very smooth external surface and therefore to be largely devoid of internal enzyme-accessible surface area [9,15]. Also using AFM, we demonstrated that the substrate consists of an amorphous cellulose matrix into which crystalline fibrils of variable width and length are distributed. We refer to this cellulose preparation as mixed amorphous–crystalline cellulosic model substrate (MACS). The particular structural characteristics of the MACS allowed us to monitor dynamic effects on the cellulose surface resulting from individual or combined hydrolytic activities of the main enzyme components of natural cellulase systems, chain-end-cleaving cellobiohydrolases (CBH I, CBH II) and internally chain-cleaving endoglucanase (EG) [3]. Cellulose polymorphism was essential for a comprehensive mechanistic investigation, considering that use of a pure crystalline cellulosic substrate would have biased the analysis largely to CBH I activity and therefore to a surface chain ablation mode of cellulose degradation [22,23], each presenting a strongly restrictive simplification and thus precluding development of a holistic view of the real process. EG requires amorphous cellulose for activity [24], and there is substrate-morphology-dependent synergy between individual cellulases during cellulose conversion [15]. Herein we measured by AFM imaging the substrate morphology evolution during the enzymatic reaction(s) and compared it to key hydrolysis-time-dependent parameters of MACS conversion, namely cellulase adsorption on the insoluble substrate and soluble sugar-releasing activity of the adsorbed enzymes. Observable parameters of substrate morphology were surface topography and surface crystalline character. They were recorded during hydrolysis in a time and laterally resolved manner. Avicel, a commonly used model substrate for highly crystalline cellulose [25–27], was applied as reference in enzyme adsorption and hydrolysis studies. We present evidence in support of the suggestion that hydrolysis slow-down is caused by a loss of productive dynamics in the interactions of cellulases with the cellulose surface undergoing degradation, resulting in individual cellulases getting progressively confined to substrate parts where they are no longer optimally active or even inactive [28,29].

Results and discussion

Cellulosic substrate preparation and characterization

Using the protocol detailed under Experimental procedures, a cellulose model substrate exhibiting purpose-built morphology (i.e. MACS) was obtained. Figure 1 shows the sample's appearance during the different steps of preparation. Representative results of AFM imaging of the MACS are depicted in Fig. 2, where height profiles are shown in (A), material-sensitive phase profiles are shown in (B) and a topographical image overlaid with amplitude information is shown in (C). It must be emphasized that AFM phase analysis enables laterally resolved imaging of material properties, such as cellulose of higher and lower order. The brighter parts in (B) represent more defined crystalline areas, whereas darker parts represent amorphous regions. Therefore, Fig. 2 reveals the MACS to exhibit a large degree of internal structural heterogeneity where crystalline fibrils (width $\leq$ 15 nm; length 100–300 nm) and larger crystallites (100 nm to 10 μm) are distributed in apparently irregular fashion within an amorphous cellulose matrix. The proposed morphology of the MACS was confirmed by the results of AFM imaging of its enzymatic hydrolysis, as shown in Fig. 3A,B. Figure 2C furthermore shows that bright fibril-like structures are present on the surface in different orientations, and some of them are at least partially covered with darker (i.e. amorphous) material. Considering the sheer impossibility of preparing MACS specimens as perfect replicates of one another, and also that AFM imaging usually involves scanning of only a selected surface area of the substrate, we were careful to confirm through analyses of a large number of different samples ($N \geq 20$) and by routinely scanning multiple non-overlapping areas in each sample ($N \geq 5$) that the overall pattern of structural features emphasized in Fig. 2 was highly reproducible both within each sample and across the different MACS preparations used. It has been estimated from AFM image analysis that about 30% of the MACS constitutes crystalline cellulose, which is in good agreement with results of X-ray diffraction (XRD) analysis [9]. The reported XRD data for MACS further indicate that the large crystalline particles are predominantly made of cellulose allomorph I, which is the main allomorph of natural and as-processed celluloses from higher plants, including Avicel. Because cellulose is usually regenerated from ionic liquid solution as allomorph II, not allomorph I [30–32], prevalence of just this allomorph (type I) in the MACS used sup-

ports the notion that crystalline parts of the model substrate originate from undissolved Avicel residue. The internal structural heterogeneity of the MACS provides a useful exemplary representation of structural order and disorder variation in natural as-processed celluloses. Functionality of the MACS for the purpose of visualizing cellulase activity was further determined by its extremely flat surface. After swelling in buffer, the residual mean squared roughness of the substrate's surface was just about 10 nm. Scanning a

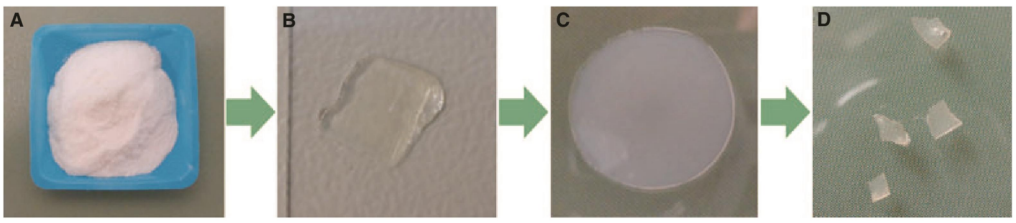

Fig. 1. Appearance of MACS during the different preparation steps used: (A) Avicel; (B) primary gel; (C) secondary gel; (D) MACS in square-like shape.

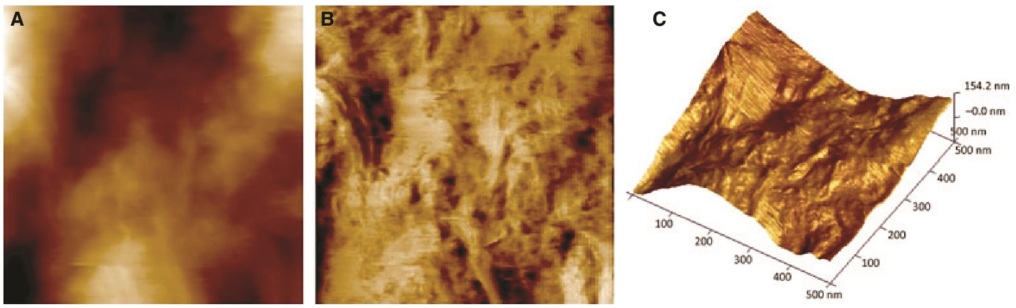

Fig. 2. AFM height (A) and phase (B) images obtained from *in situ* surface measurements of the native MACS, and (C) three-dimensional reconstruction of the surface overlaid with contrast-increasing amplitude information. The overall structural features of the substrate are fully confirmed through analyses of multiple MACS samples and by scanning different areas of the same sample.

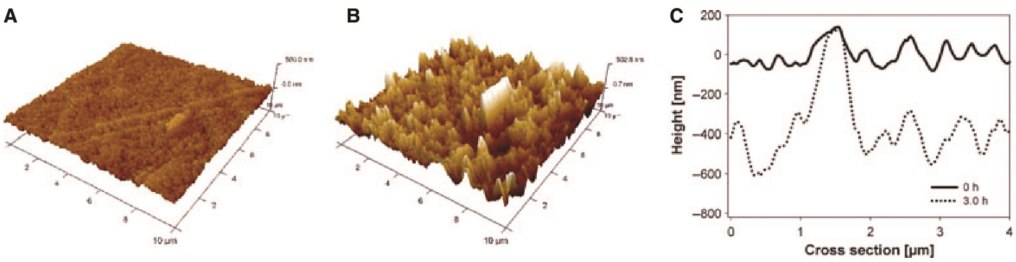

Fig. 3. *In situ* observation of MACS surface disruption caused by action of the complete *Trichoderma* sp. cellulase system. (A) MACS surface prior to and (B) after 3.0 h of incubation with enzyme at 20 °C; (C) cross-section profile before (solid line) and after (dotted line) incubation with enzyme using a highly resistant crystallite as height marker. The enzyme loading was 3.6 $mg_{protein} \cdot g_{substrate}^{-1}$ and the substrate concentration was 0.36 $g \cdot L^{-1}$. Analyses were done on different MACS samples ($N \geq 8$) and the overall trend of the data shown was confirmed.

square surface area of 500 nm side length (Fig. 2C), we observe that with reference to the known molecular dimensions of the cellulases (18–21.5 nm maximum length [17,27]) the surface is smooth and provides unobstructed access to attacking enzymes. Because surface defects such as cavities and pores were completely absent from the MACS, its enzyme-available surface area at reaction start is exclusively external. To summarize, therefore, the key characteristic of MACS morphology exploited in the analysis of cellulase action by AFM was alternating amorphous–crystalline material properties in combination with a highly homogeneous (smooth) surface topography.

In hydrolysis experiments to be reported later, we employed Avicel PH-101 as a second cellulosic substrate next to the MACS. Avicel is a powder and cannot therefore be analyzed by AFM. However, Avicel contrasts the MACS in many structural characteristics, thus making it useful for comparative kinetic analysis. It is highly crystalline with a reported crystallinity index of approximately 60% up to 77% [25]. It has a broad particle size distribution (d_{10} = 10 μm, d_{90} = 140 μm) with a mean particle size of 60 μm and exhibits a highly rugged and irregularly shaped external surface [33]. Finally, Avicel has been widely employed in cellulase studies [27]. Therefore, we aimed at correlating enzyme adsorption and soluble sugar release, which are key time-dependent parameters of the conversion of MACS and Avicel, with specific morphology characteristics of the respective substrate.

Surface structural dynamics of MACS degradation by a complete *Trichoderma* sp. cellulase system

The natural cellulase system expressed by the filamentous fungus *Trichderma reesei* is complete in that it contains all individual enzyme activities (CBH I 60%; CBH II 20%; EG 12%) required for hydrolysis of amorphous and crystalline cellulose [34]. Incubation of the MACS with this complete cellulase system resulted in a rapid and massive three-dimensional degradation of the initially smooth substrate surface. Figure 3 shows AFM images comparing the substrate before (A) and after 3 h exposure to enzyme action (B). The cellulases produced a completely rugged surface, exhibiting a highly irregular shape caused by cavities of extremely variable size and depth. The vertical difference between the highest and lowest point on the degraded surface was as large as 500 nm (Fig. 3). Degradation took place mainly in amorphous regions of the MACS. As a result, the crystalline character of the substrate surface increased noticeably. Moreover, cellulase action produced cracks within the cellulose surface. Figure 3 shows that one large crystallite in the scanned area remained virtually unaffected by the enzymes (B, C). Repetition of the experiment on different MACS samples ($N \geq 10$) confirmed the characteristic pattern of surface degradation by the cellulases shown in Fig. 3 where cavities are produced in amorphous parts, small crystalline fibrils are removed from the surface and large crystallites are attacked very slowly. Soluble sugars released during the enzymatic reaction were also measured directly from the AFM liquid cell, and the degree of substrate conversion at the time of recording the shown image was calculated to be about 4%. Thus established correlation between AFM-visualized and in-solution-measured substrate degradation provides mechanistic insight, demonstrating that MACS surface disruption was a very early event in the overall conversion of this substrate. In addition, full time courses of enzyme adsorption to and soluble sugar release from the MACS are therefore also shown in Fig. 4A,B.

Specific enzyme adsorption (E_ads), i.e. protein mass bound per residual mass of cellulose, increased by almost one order of magnitude as the hydrolysis of MACS progressed over time. Suitable controls ruled out non-specific adsorption of cellulases to plastic tubes. By comparison with the reference reaction using Avicel, E_ads was initially very low on the MACS. Surface degradation by the cellulases and the resulting increase in the external surface area of the substrate are the probable cause for the time- and therefore also conversion-dependent enhancement of E_ads on MACS. On Avicel, by contrast, E_ads was high already very early during the reaction, to increase only slightly in the later phase (Fig. 4B). MACS conversion determined from the soluble sugar concentration proceeded linearly, i.e. apparently unrestricted over time until about 70% of the original substrate was degraded. Avicel was by far more resistant to enzymatic conversion than the MACS under the conditions used.

Time course data for hydrolysis and adsorption were used to calculate specific activities of the adsorbed cellulases (R_ads) in dependence on reaction progress, and Fig. 4C shows the results. Note that enzyme in solution was stable over the time of the experiment, as shown in suitable controls carried out in the absence of substrate. R_ads was similar for both substrates in an early phase of the reaction. With both substrates R_ads decreased with progressing conversion, indicating that the adsorbed enzymes, the cellulosic substrate or both became less reactive during the reaction course. However, whereas on Avicel R_ads dropped

rapidly by almost 10-fold until about 30% substrate had been degraded, there was a rather gradual decrease in R_ads during conversion of the MACS. By comparison with the Avicel data, the R_ads behavior on the MACS was different in particular because it exhibited an initial lag phase between 0% and 20% substrate conversion where R_ads was unaffected by reaction progress (Fig. 4A). Considering evidence from AFM imaging that cellulase activity caused a large amount of MACS surface degradation already at a low degree of overall conversion (~ 4%), these findings suggest that topological changes of the external cellulose surface did not by themselves determine the decrease in R_ads and therefore eliminate a prominent factor of the hydrolysis slow-down, which is widely found in the literature [6,8,13,14,18]. A characteristic commonality of the R_ads dependences on Avicel and MACS was that loss of hydrolytic efficiency of the adsorbed cellulases occurred well ahead of depletion of the amorphous cellulose present in each substrate. This leads to the important suggestion that decrease in R_ads during the reaction was controlled by factors other than the substrate's overall crystallinity. The study of individual cellulases to be described below provided further indication.

Surface structural dynamics of MACS degradation by individual cellulolytic enzymes

The two cellobiohydrolases (CBH I, CBH II) and a major EG of the *Trichoderma* sp. cellulase system were examined for their individual actions on the MACS by using *in situ* AFM imaging. We used a high protein loading exceeding that applied to the study of the complete cellulase by 10-fold (for CBH I and EG) and 361-fold for CBH II, to ensure that enzyme-effected changes in substrate morphology were not missed due to low activity. As with the complete cellulase, soluble sugar release and protein adsorption were determined, and time-dependent parameters for MACS conversion were compared with a corresponding set of parameters for Avicel conversion. Results are summarized in Figs 5–7, separated according to the enzyme used.

In stark contrast to the pronounced surface disruption caused by the complete cellulase system (Fig. 3), the action of CBH I did not result in noticeable three-dimensional degradation of the MACS nano-flat surface. Figure 5A shows that cross-section height profiles of the substrate were almost identical before and after 2.55 h incubation in the presence of CBH I. AFM images depicted in Fig. S1 also show that surface properties of the MACS were hardly affected by treatment with CBH I. Note, however, that CBH I did

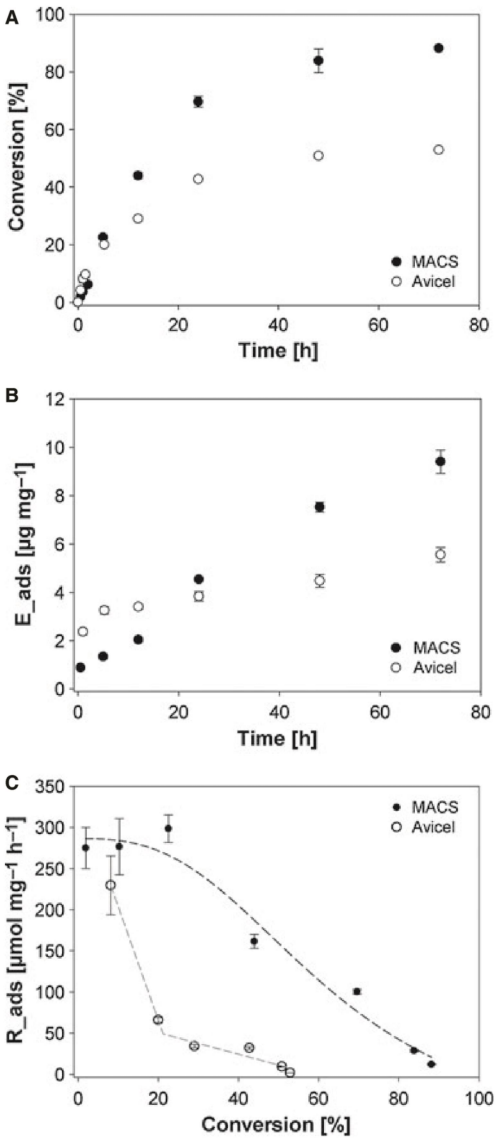

Fig. 4. Enzymatic degradation of Avicel and the MACS by a complete *Trichoderma* sp. cellulase system. The figure shows time courses of hydrolysis (A) and specific protein adsorption (B), and the dependence of R_ads on conversion progress on both substrates (C). Reactions were performed at 50 °C using a cellulose concentration of 7.2 $g \cdot L^{-1}$ and an enzyme loading of 3.6 $mg \cdot g^{-1}$ substrate. Trend of the R_ads dependence is indicated by a dotted line. Error bars are from triplicate experiments.

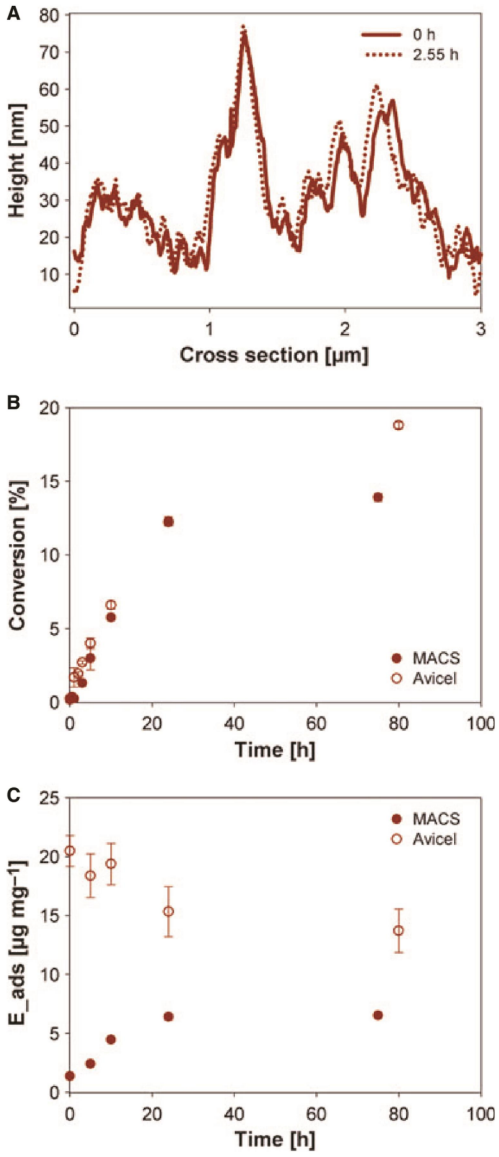

Fig. 5. Activity of CBH I on Avicel and the MACS. (A) Cross-section profile of the MACS before (solid line) and after 2.55 h (dotted line) of incubation with enzyme at 20 °C; (B) release of reducing sugars over time and (C) corresponding E_ads time course at 50 °C. The enzyme loading was 36 $mg_{protein} \cdot g_{substrate}^{-1}$. AFM experiments were repeated on different MACS substrate preparations, and the lack of height degradation by CBH I (A) was fully confirmed. Error bars from triplicate experiments are shown in (B) and (C).

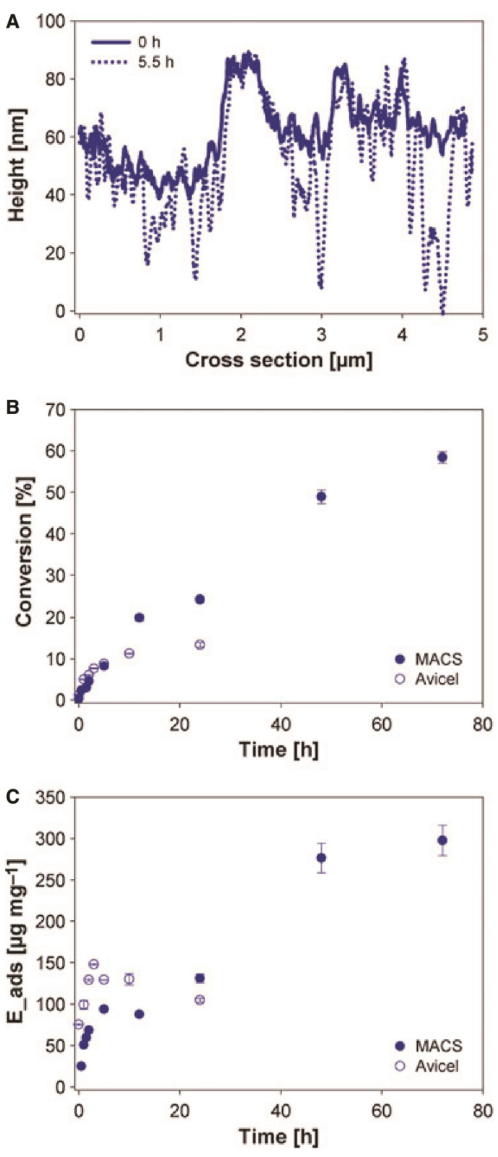

Fig. 6. Activity of CBH II on Avicel and MACS. (A) Cross-section profile of the MACS before (solid line) and after 5.5 h (dotted line) of incubation with enzyme at 20 °C; (B) release of reducing sugars over time and (C) corresponding E_ads time course at 50 °C. The enzyme loading was 36 $mg_{protein} \cdot g_{substrate}^{-1}$. The AFM experiment was repeated on different MACS substrate preparations at room temperature, and vertical substrate degradation by CBH II (A) was fully confirmed. Error bars from triplicate experiments are shown in (B) and (C).

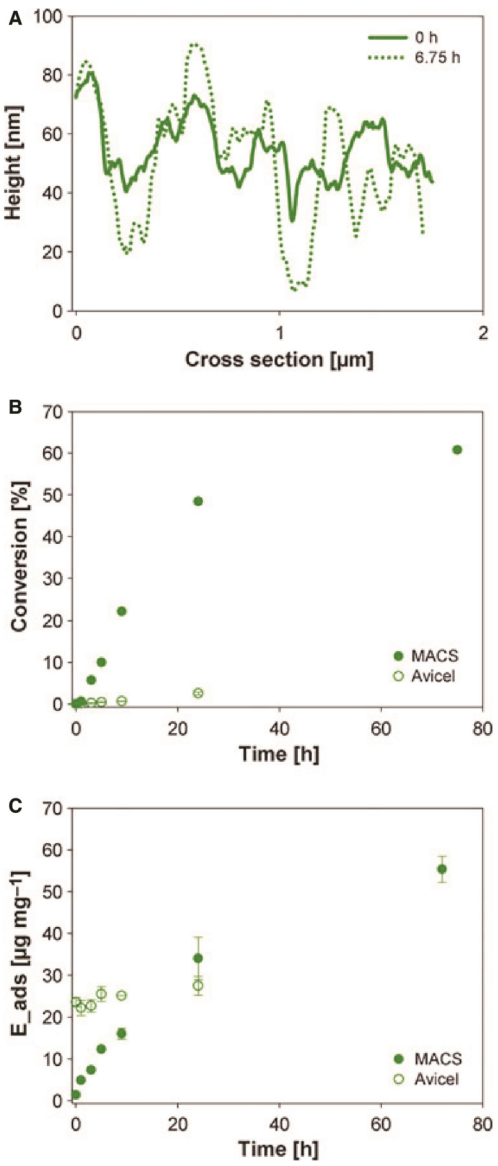

Fig. 7. Activity of EG on Avicel and the MACS. (A) Cross-section profile of the MACS before (solid line) and after 6.75 h (dotted line) of incubation with EG at 20 °C; (B) release of reducing sugars over time and (C) corresponding E_ads time course at 50 °C. The enzyme respective loading was 36 $mg_{protein} \cdot g_{substrate}^{-1}$. The AFM experiment was repeated on different MACS substrate preparations at 20 °C to confirm the characteristic features of surface degradation by EG (A). Error bars from triplicate experiments are shown in (B) and (C).

produce a tiny amount of soluble sugars (substrate conversion ≤ 1%) under the conditions applied to AFM imaging (20 °C), thus ruling out the possibility of a completely inactive enzyme. Using an elevated temperature of 50 °C, hydrolysis of the MACS by CBH I was still quite slow, and maximum conversion of the substrate did not exceed 14% (Fig. 5B). E_ads of CBH I on MACS was low at conversion start (≤ 2 $\mu g \cdot g^{-1}$), and it increased just about 3-fold in the course of the reaction at 50 °C (Fig. 5C). Hydrolysis of the MACS by CBH I stalled after 24 h of incubation, and so did E_ads. The MACS therefore seems to provide only a limited amount of cellulose material that is both accessible for and degradable by CBH I. Knowing from the literature that CBH I is not highly active on short and unordered cellulose chains [35,36], we assume that the amorphous material on the MACS surface (Fig. 3) obstructs CBH I from attacking more crystalline areas lying underneath. On Avicel, interestingly, the adsorption behavior of CBH I was opposite to that on the MACS, with E_ads decreasing by about 2-fold in the course of substrate conversion (Fig. 5B). Adsorption of CBH I was about 10 times higher on Avicel than on the MACS (Fig. 5C). Time-dependent release of soluble sugars was similar for both substrates, whereby maximum conversion of Avicel (20%) surpassed that of the MACS by a significant amount (Fig. 5A).

CBH II differed strongly from CBH I in that its action caused the MACS surface to become rougher and structurally more defined, i.e. crystalline with time of incubation. To clearly elucidate the effect in the course of the AFM experiment, a high CBH II concentration was applied. Figure S2 shows that crystalline features of the substrate were made bare of surrounding amorphous material on the surface as a result of CBH II activity. Overlaying of cross-section height profiles determined before and after incubation with CBH II (Fig. 6A) reveals that the enzyme exclusively promoted vertical degradation of only certain amorphous regions on the MACS surface, thus creating distinctive height differences with time. The suggestion from AFM data that CBH II was preferentially active on amorphous substrate parts was strongly supported by hydrolysis experiments, showing that soluble sugar release proceeded readily up to 60% MACS conversion (Fig. 6B). E_ads increased nearly 10-fold during the enzymatic reaction, implying that a large amount of new surface area for CBH II adsorption was formed as a result of MACS degradation. On Avicel, CBH II was initially about as active as on the MACS (Fig. 6C). However, release of soluble sugars stalled after only 10 h and maximum conversion of

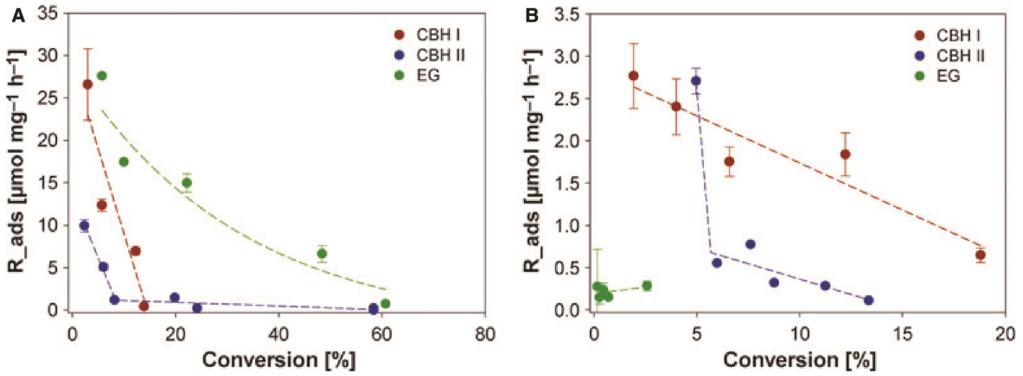

Fig. 8. R_ads of individual cellulases on the MACS (A) and Avicel (B). Trend of the R_ads dependence is indicated by a dotted line. Error bars are from triplicate experiments.

Avicel was just about 13%. E_ads at reaction start was 3-fold higher on Avicel than on MACS. The time course of E_ads on Avicel was also distinct, passing through a maximum early in the reaction only to decrease later on (Fig. 6C).

The action of EG resulted in a major change of the MACS surface structure caused by two different effects. Generally, the surface was roughened and its crystalline character was enhanced due to the efficient removal of amorphous material (Fig. S3). A large amount of three-dimensional degradation was noticed in a comparison of cross-section height profiles before and after incubation with the enzyme (Fig. 7A). Additionally, Fig. 7A shows that the action of EG on the surface of the MACS not only resulted in loss of height in the cross-section profile but there were also parts where the height increased after incubation with the enzyme. This is also recognized qualitatively in the AFM images shown in Fig. S3. A tentative explanation for the observed increase in height (which was never seen in our experiments when using CBH I or CBH II) is that EG activity caused certain areas of the substrate surface to swell. Global swelling of cellulose caused by the action of EG has been reported in previous studies applying thin (spin-cast) cellulose films, supposedly caused by increased hydration of near-surface layers of cellulosic material [37,38].

EG was efficient in hydrolyzing the MACS whereas it was barely active on Avicel (Fig. 7B). The time course of E_ads on MACS started from a very low value, but it increased nearly 50-fold during the reaction (Fig. 7C). E_ads on Avicel was initially much (~ 20-fold) higher than on the MACS; however, it did not change with incubation time.

Specific hydrolytic efficiencies of adsorbed cellulase components and their change during cellulosic substrate degradation

Figure 8 compares R_ads of the three individual cellulases on the MACS (A) and on Avicel (B). It also shows the dependence of R_ads on substrate conversion into soluble sugars. Judged by R_ads at reaction start, each cellulase, in particular EG, was far more active on the MACS than on Avicel. The MACS surface provides amorphous cellulose which can be readily attacked by EG or by CBH II. Furthermore, there are also a large number of small crystalline fibrils for CBH I to act on efficiently (Fig. 2C). By contrast, Avicel appears to restrict its enzymatic degradation rate by both the type and the amount of cellulosic material exposed to the individual cellulases. AFM visualization data (Fig. 3C) revealed that large Avicel crystallites are especially recalcitrant to enzymatic degradation. Time-resolved AFM measurements reported in an earlier publication [15] also showed that single cellulose fibrils in the MACS are broken down considerably faster than the corresponding fibril bundles. We think that the higher R_ads of CBH I on the MACS compared with Avicel is primarily determined by a larger amount of enzyme-accessible cellulose fibrils in the MACS.

However, in an R_ads-based comparison with the complete cellulase system (Fig. 4C), individual enzymes were weakly active both on the MACS and on Avicel. This indicates clearly that their combined (synergistic) action in the cellulase mixture provided a large amount of hydrolytic rate enhancement, especially when Avicel was used (≥ 40-fold). Moreover, use of the complete cellulase system (Fig. 4A) almost

completely eliminated the large reactivity difference observed in experiments with individual cellulolytic enzymes between the MACS and Avicel (Fig. 7) at least in the initial phase of the hydrolysis.

The effect of a substrate-conversion-dependent decrease in R_ads described above for hydrolyses of the MACS and Avicel by the complete cellulase system (Fig. 4A) was even augmented in experiments done with individual cellulolytic enzymes (Fig. 7). On the MACS, R_ads of the two cellobiohydrolases displayed a bi-phasic dependence on reaction progress characterized by a fast and large ($\geq$ 20-fold) drop during the initial reaction phase (conversion $\leq$ 10–15%) that was followed by a longer period of very slow decrease in R_ads until the reaction came to a complete stop. R_ads of EG, by comparison, decreased steadily during the degradation of the MACS. On Avicel, however, low activity of EG precluded precise determination of the change of R_ads with substrate conversion. As observed for EG acting on the MACS, R_ads of CBH I on Avicel showed a steady decline with reaction progress. The slope of the decrease in R_ads of CBH I was 20-fold lower on Avicel than it was in the early phase of reaction on the MACS. For CBH II, the course of R_ads during conversion of Avicel was similarly bi-phasic like the one observed on the MACS.

Interpretation of the conversion-dependent decline in R_ads

Evidence from AFM and kinetic studies of the action of the complete cellulase system on the MACS (Fig. 3) revealed that the increase in overall crystallinity of surface-exposed cellulosic material that resulted from preferential hydrolytic attack of the enzymes on amorphous substrate regions was not responsible for the decline in R_ads. Associated changes in three-dimensional surface topography were likewise not accountable for the lowering effect on R_ads. Moreover, any decrease in R_ads appeared to be completely unrelated to depletion of the total amount of amorphous cellulosic material present in the MACS and Avicel. It therefore seems that change of R_ads with conversion cannot be ascribed solely to the evolution of certain structural characteristics of the substrate surface during enzymatic hydrolysis but that it also involves true loss of hydrolytic efficacy of the adsorbed enzymes. Non-productive adsorption of the cellulases might therefore be responsible for the decrease in R_ads. A recent study by Dale and co-workers also showed that enhanced cellulase adsorption to cellulose does not imply a high reaction rate [39].

In experiments aimed at dissecting the hydrolytic action of the complete cellulase system into individual contributions from its three main cellulolytic activities, we found that a substrate-conversion-dependent decline in R_ads was also a characteristic feature of cellulose degradation by the isolated enzymes. The notion that adsorption of individual cellulases on the cellulose surface can be largely non-productive with regard to hydrolytic activity is strongly supported by evidence on the action of EG on Avicel, where strong adsorption (E_ads, Fig. 7C) is contrasted by extremely low soluble sugar formation (Fig. 7B). Likewise, both cellobiohydrolases became completely inefficient after only a scant period of activity on the MACS surface. A similar trend was seen for CBH II on Avicel.

We hypothesize that the gradient ΔR_ads/Δconversion reveals local limitations in cellulosic material effectively degradable by the individual cellulases, within the substrate surface area accessible to a single adsorbed enzyme through its unobstructed movement on the surface. Cellulosic material not suitable for hydrolysis but also other adsorbed cellulases might present relevant obstacles encountered during movement. It is well documented in the literature that cellulase adsorption does not constitute a readily reversible process, especially within the extended timespan of a typical hydrolysis reaction [23,40]. A probable consequence of quasi-irreversible adsorption combined with restricted enzyme mobility on the cellulose surface is that cellulases get increasingly trapped in areas of the substrate surface where they are no longer highly active [41,42], thus providing a general mechanistic explanation for the drop in R_ads.

The obstacle-free path for processive degradation of cellulose chains within crystalline material by CBH I is expected to be longer in Avicel than in the MACS where only relatively short fibrils are embedded in an amorphous matrix that is not further attacked [38,39]. Amorphous material partly covering crystalline fibrils will obstruct enzyme access to free cellulose chain ends, and it might also lead to interruption of processive chain degradation by CBH I. Consistent with the implication that CBH I becomes progressively confined to largely unreactive amorphous cellulosic material during conversion of the MACS, the relative R_ads gradient was more pronounced on the MACS than on Avicel. Possible reasons for R_ads of CBH I to also decrease on crystalline cellulose (Avicel) are enzyme overcrowding on the surface and 'traffic jams' of simultaneously moving CBH I molecules [23,43]. Note that the high enzyme concentrations used in our experiments might favor the effect of jamming. Cellulose chain-bound CBH I has a low dissociation rate

constant and therefore will be stuck inactivated on the chain once it encounters an obstacle [35]. Patches of inactive CBH I obstacles on the Avicel surface will therefore soon expand, thus shortening the obstacle-free path and eventually stalling the rate, even at low conversion. Jalak and Väljamäe measured catalytic constants for CBH I on Avicel, bacterial microcrystalline cellulose and amorphous cellulose prepared from Avicel. Evidence was obtained that unproductively bound CBH indeed accumulates on the cellulose surface [36].

Unlike Avicel, the MACS fulfills essential requirements for efficient conversion by EG in that it provides a large amount of amorphous cellulosic material both on its enzyme-accessible surface and also in subjacent layers. The R_ads gradient for EG was therefore much shallower than the corresponding R_ads gradient for CBH I, and it arguably resulted from unproductive adsorption of EG to crystalline regions on the evolving surface area of the substrate. Considering that CBH II was also primarily active towards amorphous material on the MACS surface, the much steeper R_ads gradient for CBH II than for EG must be considered. Differences in the chain-cleaving mode of action of the two enzymes, CBH II (exo) and EG (endo), provide a plausible explanation [3,44]. The particular exo-mode of action of CBH II where cellobiose molecules are cleaved off, usually in a processive manner, from the non-reducing end of the cellulose chain necessitates the availability of suitable free chain ends in a cellulosic material to become a usable substrate of the enzyme [21,45]. The average chain length available for unobstructed processive action might also be important. It is therefore clear that the exo-mode of attack of CBH II on amorphous cellulose will be subject to stronger restrictions due to substrate morphology than the corresponding internally chain-cleaving mode of action of EG. R_ads of EG at reaction start was therefore higher than that of CBH II, as expected. On Avicel, finally, the rapid decrease in R_ads of CBH II might reflect crowding of enzymes on crystalline cellulose (in particular due to the high enzyme concentrations used in the experiments) where after depletion of free chain ends the CBH II will no longer be active.

Summarizing, we have applied AFM and kinetic studies to characterize surface dynamic processes involved in enzymatic cellulose hydrolysis. Using a suitable nano-flat and mixed amorphous–crystalline cellulosic substrate allowed us to determine the evolution of distinct substrate morphologies during hydrolytic conversion. Moreover, it enabled us to relate changes in material character and three-dimensional topology of the cellulose surface to key conversion-dependent parameters of the enzymatic reaction, adsorption and hydrolytic efficiency of the cellulases. Three-dimensional degradation of the originally flat substrate surface causes the enzyme-accessible cellulose area to increase and therefore explains the strongly rising enzyme adsorption during the reaction. However, the effect of conversion on lowering the hydrolytic efficiency of the adsorbed cellulases (R_ads) exceeds the potential gain in hydrolysis rate due to enhanced adsorption, and therefore hydrolysis slow-down occurs nonetheless. The decline in R_ads is suggested to result from (a) depletion of hydrolyzable material within the cellulose surface area accessible to a single cellulase through obstacle-free movement on the surface and (b) the apparent inaptitude of the enzyme to escape local restrictions through chain release and surface desorption processes. An efficient way of rescuing stuck enzymes would therefore be through degradation of surrounding cellulosic material by complementary cellulase activities. The effect appears to be particularly pronounced on highly amorphous cellulose such as the MACS, relying on EG as the 'pacemaker activity'. The extreme recalcitrance of large cellulose crystallites present in Avicel will dampen the dynamic interplay between different cellulase activities, with consequent effects on R_ads. Maintenance of cellulase hydrolytic efficiency over the course of substrate conversion requires that productive dynamics in the interaction of individual enzymes with an evolving cellulose surface be sustained.

Experimental procedures

Materials used

Unless stated, the chemicals used were of highest purity available from Carl Roth (Karlsruhe, Germany). Avicel and 1-butyl-3-methylimidazolium chloride (BMIMCl) were from Sigma-Aldrich (St Louis, MO, USA). *Aspergillus niger* β-glucosidase (BGL) was from Megazyme (Dublin, Ireland) and was used without further purification.

Preparation of the MACS

BMIMCl (1 g) was placed in a 50 mL screw-capped glass vial and heated under magnetic stirring (50 r.p.m.) to 100 °C. Avicel PH-101 was added stepwise to a final concentration of 15% (by weight), and stirring at 100 °C was continued for 24 h. Avicel powder was dissolved gradually during that time. The transparent liquid was then poured centrally on a microscope slide and covered with another microscope slide. Microscope cover slips were used as spacers to adjust the average thickness of the liquid phase to 0.435 mm. The liquid was cooled to

room temperature, thus forming a gel-like material that we call primary gel, shown in Fig. 2B. Using inspection in the light microscope, we noticed that the primary gel was not completely transparent but still contained various cellulose particles of different sizes (micron range). This primary gel was dried at room temperature for 7 days and then subjected to a fractional extraction that involved repeated washings of the gel in a glass Petri dish with 50 mL of aqueous ethanol for 30 min. The wash solutions contained increasing concentrations of ethanol, ranging from 30% to 90%. A final washing was performed with absolute ethanol. Extraction with ethanol is essential to remove all BMIMCl from the substrate preparation. We used simultaneous thermal analysis as reported previously to confirm the absence of ionic liquid in the substrate [9]. Prior to further experiments the substrate was cut into squares with an average side length of 2.0 mm as shown in Fig. 2D. In order to conduct AFM experiments a single MACS specimen (Fig. 2D) was embedded in epoxy resin using the SpeciFix-40 kit (Struers, Willich, Germany). Resin and curing agent were blended in a 5 : 2 mass ratio and transferred into free slots of a PELCO® flat embedding mold (Ted Pella, Redding, CA, USA). Subsequently, the specimen was put into the slots and the embedding mold was incubated for at least 4 h at 40 °C to cure the resin. After curing, a single resin-embedded specimen was mounted on a special holder, which fitted in the laboratory-built liquid cell as well as in the ultramicrotome. A first cut was performed with an Ultracut UCT ultramicrotome (Leica Microsystems, Wetzlar, Germany) equipped with an ultra 45° diamond knife (Diatome, Biel, Switzerland). After that, the specimen was subjected to 1 h of swelling in buffer (50 mM sodium citrate, pH 5.0) followed by a promptly performed second cut of the still buffer-soaked specimen with an ultrasonic diamond knife (Diatome), thus resulting in a nano-flat specimen surface. Finally the prepared specimen was stored in buffer at 4 °C for use within the next 24 h. Using the procedures just described, MACS samples were obtained in excellent quality with high reproducibility.

Preparation and characterization of the cellulases used

Fungal cellulases from *Trichoderma* sp. were used. A complete cellulase mixture was obtained from *T. reesei* strain SVG 17 [46]. The organism was grown in a Biostat C4 bioreactor (B. Braun Biotech International, Melsungen, Germany) with a total working volume of 5 L using steam-pretreated wheat straw as the main source of carbon for 7 up to 9 days until no further increase in filter paper units (FPU) was measurable. Other conditions of cultivation and a complete description of the media used are given in the literature [46]. The culture supernatant was recovered by centrifugation (Sorvall RC-5B; 4420 ***g***; 4 °C, 20 min) and filtered through a glass microfiber filter (Whatman, Maidstone, Kent, UK). Using the standardized FPU assay for measurement of cellulase activity, we determined the supernatant to contain about 1 $FPU \cdot mL^{-1}$. Protein content was determined as 0.54 $g \cdot L^{-1}$. The culture supernatant was stored at 4 °C and supplied with 0.05% (w/v) sodium azide. Purified individual cellulases were obtained commercially (CBH I, EG I; each from *Trichoderma longibrachiatum*) or from recombinant single-enzyme production systems (CBH II; from *T. reesei*) [47]. Prior to hydrolysis experiments all enzyme preparations were exchanged to 50 mM sodium citrate buffer pH 5.0 using Vivaspins®500 (Sartorius, Goettingen, Germany).

Adsorption to and hydrolysis of cellulose substrates

All hydrolysis experiments were carried out as duplicates or triplicates in 50 mM sodium citrate buffer, pH 5.0, at 50 °C in Eppendorf tubes using a thermal shaker with no agitation. For both Avicel and the MACS the substrate concentration was 7.2 $g \cdot L^{-1}$ in a total reaction volume of 350 µL. Cellulase loadings were chosen in accordance with the AFM experiments described below: 3.6 $mg_{protein} \cdot g_{substrate}^{-1}$ for the complete cellulase system, 36 $mg_{protein} \cdot g_{substrate}^{-1}$ for CBH I and EG and 1.3 $g_{protein} \cdot g_{substrate}^{-1}$ for CBH II. Additionally, BGL was added to a final concentration of 1 $mg \cdot L^{-1}$ to promote the conversion of cellobiose to glucose and thus avoid cellobiose product inhibition [48]. At suitable times one of the Eppendorf tubes was removed from the thermal shaker and solid material was separated by centrifugation (9 300 ***g***, 1 min). Two hundred microliters of the supernatant was withdrawn to determine the amount of soluble protein. Adsorbed protein was calculated from the difference in initial protein concentration and the protein concentration measured in the sample. The remaining supernatant not used for protein measurement was heated to 95 °C and incubated for 7 min. Precipitated material was removed by centrifugation (9 300 ***g***, 1 min). The cleared supernatant was used for determination of the amount of liberated reducing sugars using a 3,5-dinitrosalicylic acid (DNS) based assay calibrated against glucose [49].

Controls were performed where enzyme was incubated under otherwise identical conditions in the absence of cellulosic substrate. Loss of protein from solution in the absence of noticeable protein precipitation would have indicated non-specific protein adsorption to the walls of the plastic tubes used. Within the limits of experimental error (~ 5%), non-specific adsorption did not occur.

Enzyme and protein assays

The activity of individual cellulases was determined using reported assays on 4-methylumbelliferyl-β-D-cellobioside

(MUF-c) or carboxylmethyl cellulose as substrate. The MUF-c assay was performed at 40 °C in a 96-well half-area plate containing 10 mM MUF-c, 5% dimethylsulfoxide and 50 mM sodium acetate buffer (pH 5.0) in a total reaction volume of 45 μL. The reaction was started by the addition of 5 μL of the respective enzyme stock solution (1.8 $g \cdot L^{-1}$) and monitored continuously through measurement of fluorescence intensity increase (λ_{ex} 365 nm, λ_{em} 445 nm) with time due to the release of 4-methlyumbelliferone. A FLUOstar Omega plate reader (BMG Labtech GmbH, Ortenberg, Germany) was used for fluorescence measurement. Using the MUF-c assay, purified CBH I had a specific activity of 0.3 $\mu mol \cdot mg^{-1} \cdot h^{-1}$. The corresponding activity of EG was 4.1 $\mu mol \cdot mg^{-1} \cdot h^{-1}$. CBH II was 'inactive' in the MUF-c assay, thus sensitively excluding any contamination of the used preparation of CBH II with EG or CBH I. Note that MUF-c is a substrate for hydrolysis by CBH II. However, no 4-methlyumbelliferone is released during the reaction. The carboxylmethyl cellulose assay was performed using a substrate concentration of 10 $g \cdot L^{-1}$ in 50 mM sodium acetate buffer (pH 5.0, 40 °C) in a total reaction volume of 1 mL. The enzyme concentration of individual enzymes was 15 $\mu g \cdot mL^{-1}$ in all experiments. Samples were taken after 0, 1, 3 and 4.5 h and inactivated at 95 °C for 7 min. Afterwards, the amount of liberated sugars was measured using the DNS assay [49]. The specific activity of CBH II and EG was 5.0 $\mu mol \cdot mg^{-1} \cdot h^{-1}$ and 430 $\mu mol \cdot mg^{-1} \cdot h^{-1}$, respectively. CBH I showed no activity on carboxylmethyl cellulose, thus excluding contamination of the CBH I preparation used with CBH II and EG. Specific activities of individual enzymes are in agreement with the literature [50].

Protein determination

The protein concentration for solutions containing the cellulase mixture was measured using Roti-Quant or Roti-Nanoquant assay calibrated using BSA as standard. Absorbances were recorded with a FLUOstar Omega plate reader. The concentration of individual cellulases was determined from UV measurements with a Nanodrop 1000 spectrometer from Thermo Fisher Scientific (Waltham, MA, USA) applying the molar extinction coefficients calculated from the amino acid sequence with PROPARAM [15] ($\varepsilon_{CBH\ I}$ = 88 250 $M^{-1} \cdot cm^{-1}$; $\varepsilon_{CBH\ II}$ = 97 665 $M^{-1} \cdot cm^{-1}$; ε_{EG} = 74 940 $M^{-1} \cdot cm^{-1}$).

Stability of cellulases

Enzymes were dissolved in 50 mM sodium citrate buffer, pH 5.0, at the concentrations used for hydrolysis or AFM experiments. Incubations were done at 20 °C or 50 °C in the absence of agitation. At regular times samples were taken and analyzed for enzyme activity and protein precipitation. The assays described above were used to determine the residual activity of CBH I, CBH II or EG. The standard FPU assay was applied to determine the activity of the *T. reesei* whole cellulase mixture. Protein precipitation was analyzed using visual inspection and determination of protein loss from solution.

Analytical procedures for soluble sugar determination

The DNS assay miniaturized to 96-well plate format was used to determine the liberated reducing sugars. Calibration was performed from 0.1 $g \cdot L^{-1}$ up to 5 $g \cdot L^{-1}$ using glucose as standard. The procedures involved transfer of 20 μL of sample to 40 μL of 50 mM sodium citrate buffer (pH 5.0) in a well of a 96-well PCR plate (Bio-Rad, Hercules, CA, USA). Subsequently, 120 μL DNS reagent was added and the plate was tightly sealed with an aluminum seal (VWR International, Radnor, PA, USA). The reaction mixture was then incubated in a thermo-cycler at 95 °C for 5 min. Finally, a 36 μL aliquot of each incubation mixture was transferred to a new Greiner 96-well plate (Sigma-Aldrich) with 160 μL distilled water. Absorbance at 540 nm was measured in the FLUOstar Omega plate reader.

To prove that soluble sugars had all been converted to glucose due to the presence of BGL, samples of hydrolysis experiments were also examined by high-performance anion exchange chromatography coupled to pulsed-amperometric detection (Dionex BioLC, Thermo Fisher Scientific). The analysis was performed using a CarboPac PA10 column (4 × 250 mm) and an Amino Trap guard column (4 × 50 mm) thermostatted at 30 °C. Glucose, cellobiose and higher cello-oligosaccharides were detected with an ED50A electrochemical detector using a gold working electrode and a silver/silver chloride reference electrode by applying the predefined waveform for carbohydrates. Elution was carried out at a flow rate of 0.5 $mL \cdot min^{-1}$ with an isocratic flow of 100 mM NaOH for 40 min. Samples were diluted with Milli-Q water to an approximate reducing sugar concentration of 1 mM.

Determination of E_ads and R_ads

The amount of enzyme adsorbed to the residual cellulose substrate (E_ads $\mu g \cdot mg^{-1}$) in the course of hydrolysis was determined from protein binding and reducing sugar release data. The concentration of adsorbed protein $[P]_{ads}$ ($mg \cdot mL^{-1}$) was determined as the difference between the initial protein concentration $[P]_0$ ($mg \cdot mL^{-1}$) and the concentration of soluble protein at a certain time of the hydrolysis experiment $[P]_t$ ($mg \cdot mL^{-1}$). The concentration of residual cellulose substrate $[S]_t$ ($mg \cdot mL^{-1}$) was determined as the difference between the initial substrate concentration $[S]_0$ ($mg \cdot mL^{-1}$) and the concentration of hydrolyzed substrate, expressed as anhydro-glucose concentration released into solution ($mg \cdot mL^{-1}$). It was confirmed that measurement of reducing sugars was not compromised by the pres-

ence of soluble sugars other than glucose. E_ads was determined as the ratio of $[P]_{ads}$ and $[S]_t$.

R_ads ($\mu mol \cdot mg^{-1} \cdot h^{-1}$) is the specific activity of the adsorbed cellulase. It is calculated as the ratio of a volumetric glucose release rate R_t ($\mu mol \cdot mL^{-1} \cdot h^{-1}$) and P_ads ($mg \cdot mL^{-1}$) at a certain time of the hydrolysis reaction. Calculation of R_ads assumes that only adsorbed cellulases are actively involved in the release of soluble sugar, consistent with the widely accepted view of the enzyme mode of action. R_t was obtained through linear interpolation between the reducing sugar concentration at the time point of analysis and the next measured time point of the hydrolysis course. R_t was calculated as the ratio of reducing sugar concentration formed and time used. We carefully considered how experimental error and also error propagation affect the determination of E_ads and R_ads. The data shown in the figures are mean values of four independent determinations and error bars show the SD. The relative error on R_ads was typically below 10%.

AFM imaging and image analysis

In situ AFM images were collected using a laboratory-built liquid cell and a commercial Dimension 3100 AFM with a hybrid scan head, a liquid cell tip holder and a Nanoscope IVa controller (Bruker AXS, Santa Barbara, CA, USA). Imaging was performed at 20 °C in sodium citrate buffer (50 mM, pH 5.0) with a TR400PSA cantilever (Olympus Probes, Tokyo, Japan) in TappingMode®. Scan rates, set points and drive amplitude were chosen to maintain a subtle tapping interaction of tip and sample. *In situ* AFM imaging of the structural changes upon enzyme activity was performed with the same enzyme loadings as in the hydrolysis studies described above. The cellulose substrate concentration was $0.36\ g \cdot L^{-1}$. The recorded AFM images were processed and analyzed using GWYDDION (V2.31) and NANOSCOPE ANALYSIS 1.20 (Build R1Sr3.64571, Veeco Instruments Inc., New York, USA) software in order to quantify the features visualized. To represent the degradation evolution between reaction start and certain times of the experiment, two images were used to take profiles on carefully chosen lines. Lines were aligned with respect to at least two static points in the images, which could only be found on crystalline Avicel residues because of their high resistivity to enzymatic degradation. The linewidth of the profiles was chosen with respect to the image resolution in the range 8–16 pixels in order to determine statistically relevant data and prevent false information due to small line errors or thermal drift.

Acknowledgements

We thank Karin Longus and Vera Novy for producing the complete cellulase system; Gregor Trimmel and Timothy Aschl for characterization of the substrate; Anton Glieder for the kind gift of CBH II; and Ferdinand Hofer for discussions. Financial support was from the Austrian Science Fund FWF (grant P 24156-B21 to B.N.). The authors declare no competing financial interest.

References

1 Chundawat SPS, Beckham GT, Himmel ME & Dale BE (2011) Deconstruction of lignocellulosic biomass to fuels and chemicals. *Annu Rev Chem Biomol Eng* **2**, 121–145.
2 Keijsers ERG, Yılmaz G & van Dam JEG (2012) The cellulose resource matrix. *Carbohydr Polym* **93**, 9–21.
3 Lynd L & Weimer P (2002) Microbial cellulose utilization: fundamentals and biotechnology. *Microbiol Mol Biol Rev* **66**, 506–577.
4 Moon RJ, Martini A, Nairn J, Simonsen J & Youngblood J (2011) Cellulose nanomaterials review: structure, properties and nanocomposites. *Chem Soc Rev* **40**, 3941–3994.
5 Ahola S, Turon X, Osterberg M, Laine J & Rojas OJ (2008) Enzymatic hydrolysis of native cellulose nanofibrils and other cellulose model films: effect of surface structure. *Langmuir* **24**, 11592–11599.
6 Desai SG & Converse AO (1997) Substrate reactivity as a function of the extent of reaction in the enzymatic hydrolysis of lignocellulose. *Biotechnol Bioeng* **56**, 650–655.
7 Arantes V & Saddler JN (2010) Access to cellulose limits the efficiency of enzymatic hydrolysis: the role of amorphogenesis. *Biotechnol Biofuels* **3**, 4.
8 Grethlein HE (1985) The effect of pore size distribution on the rate of enzymatic hydrolysis of cellulosic substrates. *Nat Biotechnol* **2**, 155–160.
9 Bubner P, Dohr J, Plank H, Mayrhofer C & Nidetzky B (2012) Cellulases dig deep: *in situ* observation of the mesoscopic structural dynamics of enzymatic cellulose degradation. *J Biol Chem* **287**, 2759–2765.
10 Bansal P, Hall M, Realff MJ, Lee JH & Bommarius AS (2009) Modeling cellulase kinetics on lignocellulosic substrates. *Biotechnol Adv* **27**, 833–848.
11 Hall M, Bansal P, Lee JH, Realff MJ & Bommarius AS (2010) Cellulose crystallinity – a key predictor of the enzymatic hydrolysis rate. *FEBS J* **277**, 1571–1582.
12 Levine SE, Fox JM, Blanch HW & Clark DS (2010) A mechanistic model of the enzymatic hydrolysis of cellulose. *Biotechnol Bioeng* **107**, 37–51.
13 Zhou W, Schüttler H-B, Hao Z & Xu Y (2009) Cellulose hydrolysis in evolving substrate morphologies I: a general modeling formalism. *Biotechnol Bioeng* **104**, 261–274.

14 Zhou W, Xu Y & Schüttler H-B (2010) Cellulose hydrolysis in evolving substrate morphologies III: time-scale analysis. *Biotechnol Bioeng* **107**, 224–234.
15 Ganner T, Bubner P, Eibinger M, Mayrhofer C, Plank H & Nidetzky B (2012) Dissecting and reconstructing synergism – *in situ* visualization of cooperativity among cellulases. *J Biol Chem* **287**, 43215–43222.
16 Zhang YHP & Lynd LR (2004) Toward an aggregated understanding of enzymatic hydrolysis of cellulose: noncomplexed cellulase systems. *Biotechnol Bioeng* **88**, 797–824.
17 Abuja P, Schmuck M, Pilz I, Tomme P, Claeyssens M & Esterbauer H (1988) Structural and functional domains of cellobiohydrolase I from *Trichoderma reesei*. *Eur Biophys J* **9414**, 339–342.
18 Mansfield SD, Mooney C & Saddler J (1999) Substrate and enzyme characteristics that limit cellulose hydrolysis. *Biotechnol Prog* **15**, 804–816.
19 Griggs AJ, Stickel JJ & Lischeske JJ (2012) A mechanistic model for enzymatic saccharification of cellulose using continuous distribution kinetics II: cooperative enzyme action, solution kinetics, and product inhibition. *Biotechnol Bioeng* **109**, 676–685.
20 Monschein M, Reisinger C & Nidetzky B (2012) Enzymatic hydrolysis of microcrystalline cellulose and pretreated wheat straw: a detailed comparison using convenient kinetic analysis. *Bioresour Technol* **128C**, 679–687.
21 Nidetzky B, Zachariae W, Gercken G, Hayn M & Steiner W (1994) Hydrolysis of cellooligosaccharides by *Trichoderma reesei* cellobiohydrolases: experimental data and kinetic modeling. *Enzyme Microb Technol* **16**, 43–52.
22 Liu YS, Baker JO, Zeng Y, Himmel ME, Haas T & Ding SY (2011) Cellobiohydrolase hydrolyzes crystalline cellulose on hydrophobic faces. *J Biol Chem* **286**, 11195–11201.
23 Igarashi K, Uchihashi T, Koivula A, Wada M, Kimura S, Okamoto T, Penttilä M, Ando T & Samejima M (2011) Traffic jams reduce hydrolytic efficiency of cellulase on cellulose surface. *Science* **333**, 1279–1282.
24 Nakazawa H, Okada K, Kobayashi R, Kubota T, Onodera T, Ochiai N, Omata N, Ogasawara W, Okada H & Morikawa Y (2008) Characterization of the catalytic domains of *Trichoderma reesei* endoglucanase I, II, and III, expressed in *Escherichia coli*. *Appl Microbiol Biotechnol* **81**, 681–689.
25 Park S, Baker JO, Himmel ME, Parilla PA & Johnson DK (2010) Cellulose crystallinity index: measurement techniques and their impact on interpreting cellulase performance. *Biotechnol Biofuels* **3**, 10.
26 Zhang Y & Lynd L (2006) A functionally based model for hydrolysis of cellulose by fungal cellulase. *Biotechnol Bioeng* **94**, 888–895.
27 Bubner P, Plank H & Nidetzky B (2013) Visualizing cellulase activity. *Biotechnol Bioeng* **110**, 1529–1549.
28 Moran-Mirabal JM, Bolewski JC & Walker LP (2011) Reversibility and binding kinetics of *Thermobifida fusca* cellulases studied through fluorescence recovery after photobleaching microscopy. *Biphys Chem* **155**, 20–28.
29 Maurer SA, Brady NW, Fajardo NP & Radke CJ (2013) Surface kinetics for cooperative fungal cellulase digestion of cellulose from quartz crystal microgravimetry. *J Colloid Interface Sci* **394**, 498–508.
30 Swatloski RP, Spear SK, Holbrey JD & Rogers RD (2002) Dissolution of cellulose with ionic liquids. *J Am Chem Soc* **124**, 4974–4975.
31 Kim SJ, Dwiatmoko AA, Choi JW, Suh Y-W, Suh DJ & Oh M (2010) Cellulose pretreatment with 1-*n*-butyl-3-methylimidazolium chloride for solid acid-catalyzed hydrolysis. *Bioresour Technol* **101**, 8273–8279.
32 Cheng G, Varanasi P, Li C, Liu H, Melnichenko YB, Simmons BA, Kent MS & Singh S (2011) Transition of cellulose crystalline structure and surface morphology of biomass as a function of ionic liquid pretreatment and its relation to enzymatic hydrolysis. *Biomacromolecules* **12**, 933–941.
33 Benali M, Gerbaud V & Hemati M (2009) Effect of operating conditions and physico-chemical properties on the wet granulation kinetics in high shear mixer. *Powder Technol* **190**, 160–169.
34 Schuster A & Schmoll M (2010) Biology and biotechnology of *Trichoderma*. *Appl Microbiol Biotechnol* **87**, 787–799.
35 Kurasin M & Väljamäe P (2011) Processivity of cellobiohydrolases is limited by the substrate. *J Biol Chem* **286**, 169–177.
36 Jalak J & Väljamäe P (2010) Mechanism of initial rapid rate retardation in cellobiohydrolase catalyzed cellulose hydrolysis. *Biotechnol Bioeng* **106**, 871–883.
37 Cheng G, Datta S, Liu Z, Wang C, Murton JK, Brown PA, Jablin MS, Dubey M, Majewski J, Halbert CE *et al.* (2012) Interactions of endoglucanases with amorphous cellulose films resolved by neutron reflectometry and quartz crystal microbalance with dissipation monitoring. *Langmuir* **28**, 8348–8358.
38 Wang J, Quirk A, Lipkowski J, Dutcher JR, Hill C, Mark A & Clarke AJ (2012) Real-time observation of the swelling and hydrolysis of a single crystalline cellulose fiber catalyzed by cellulase 7B from *Trichoderma reesei*. *Langmuir* **28**, 9664–9672.
39 Gao D, Chundawat SPS, Sethi A, Balan V, Gnanakaran S & Dale BE (2013) Increased enzyme binding to substrate is not necessary for more efficient cellulose hydrolysis. *Proc Natl Acad Sci USA* **110**, 10922–10927.
40 Maurer SA, Bedbrook CN & Radke CJ (2012) Competitive sorption kinetics of inhibited endo- and exoglucanases on a model cellulose substrate. *Langmuir* **28**, 14598–14608.

41 Moran-Mirabal JM, Bolewski JC & Walker LP (2013) *Thermobifida fusca* cellulases exhibit limited surface diffusion on bacterial micro-crystalline cellulose. *Biotechnol Bioeng* **110**, 47–56.
42 Luterbacher JS, Walker LP & Moran-Mirabal JM (2013) Observing and modeling BMCC degradation by commercial cellulase cocktails with fluorescently labeled *Trichoderma reseii* Cel7A through confocal microscopy. *Biotechnol Bioeng* **110**, 108–117.
43 Igarashi K, Wada M, Hori R & Samejima M (2006) Surface density of cellobiohydrolase on crystalline celluloses. A critical parameter to evaluate enzymatic kinetics at a solid–liquid interface. *FEBS J* **273**, 2869–2878.
44 Jalak J, Kurašin M, Teugjas H & Väljamäe P (2012) Endo–exo synergism in cellulose hydrolysis revisited. *J Biol Chem* **287**, 28802–28815.
45 Chanzy H & Henrissat B (1985) Undirectional degradation of valonia cellulose microcrystals subjected to cellulase action. *FEBS Lett* **184**, 285–288.
46 Esterbauer H, Steiner W, Labudova I, Hermann A & Hayna M (1991) Production of *Trichoderma* cellulase in laboratory and pilot scale. *Bioresour Technol* **36**, 51–65.
47 Mellitzer A, Weis R, Glieder A & Flicker K (2012) Expression of lignocellulolytic enzymes in *Pichia pastoris*. *Microb Cell Fact* **11**, 61.
48 Murphy L, Bohlin C, Baumann MJ, Olsen SN, Sørensen TH, Anderson L, Borch K & Westh P (2013) Product inhibition of five *Hypocrea jecorina* cellulases. *Enzyme Microb Technol* **52**, 163–169.
49 Xiao Z, Storms R & Tsang A (2004) Microplate-based filter paper assay to measure total cellulase activity. *Biotechnol Bioeng* **88**, 832–837.
50 Fox JM, Levine SE, Clark DS & Blanch HW (2012) Initial- and processive-cut products reveal cellobiohydrolase rate limitations and the role of companion enzymes. *Biochemistry* **51**, 442–452.

Supporting information

Additional supporting information may be found in the online version of this article at the publisher's web site:

Fig. S1. *In situ* observation of surface structural changes on the MACS resulting from the action of CBH I.

Fig. S2. *In situ* observation of surface structural changes on the MACS resulting from the action of CBH II.

Fig. S3. *In situ* observation of surface structural changes on the MACS resulting from the action of EG.

the FEBS Journal
www.febsjournal.org

Surface structural dynamics of enzymatic cellulose degradation, revealed by combined kinetic and atomic force microscopy studies

Manuel Eibinger, Patricia Bubner, Thomas Ganner, Harald Plank and Bernd Nidetzky

DOI: 10.1111/febs.12594

Supplementary Material

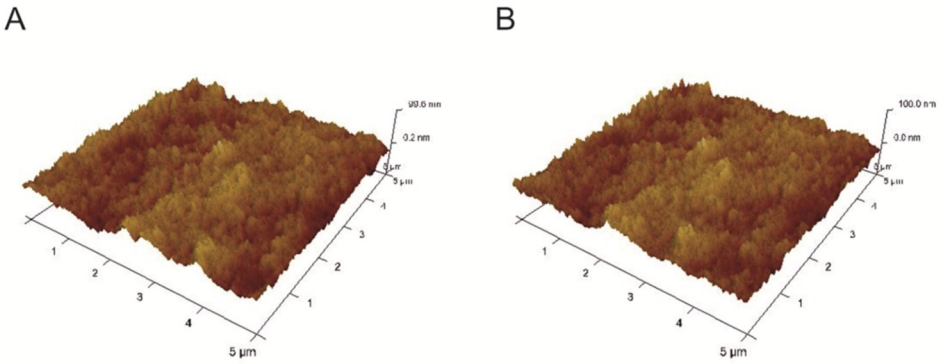

Figure S1: In situ observation of surface structural changes on MACS resulting from action of CBH I. No detectable surface degradation was observed after incubation in the presence of 36 $mg_{protein}/g_{substrate}$ for 2.55 hours at 20 °C (compare panel A and B). However, degradation of small surface-exposed fibrils was observed as previously reported [1].

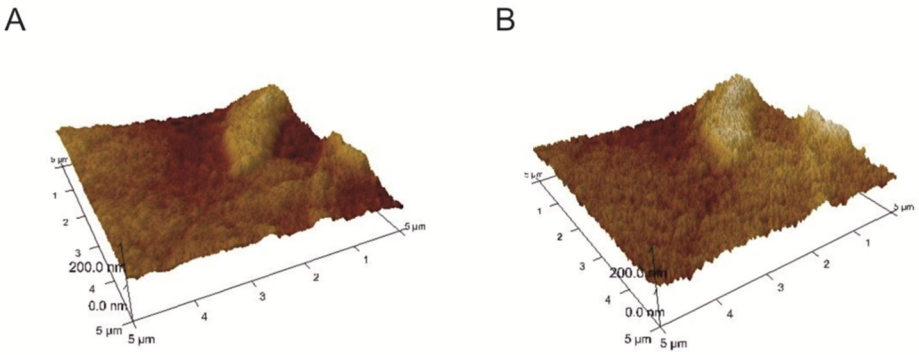

Figure S2: In situ observation of surface structural changes on MACS resulting from action of CBH II. Incubation for 5.5 hours with CBH II at 20 °C leads to an enhancement of the crystalline character of the MACS surface which is indicated by phase information where brighter parts represents more crystalline cellulose (compare panel A and B). Additionally, the formation of cracks was observed in amorphous regions surrounding the crystal. A high enzyme loading of 1.3 $g_{protein}/g_{substrate}$ was used.

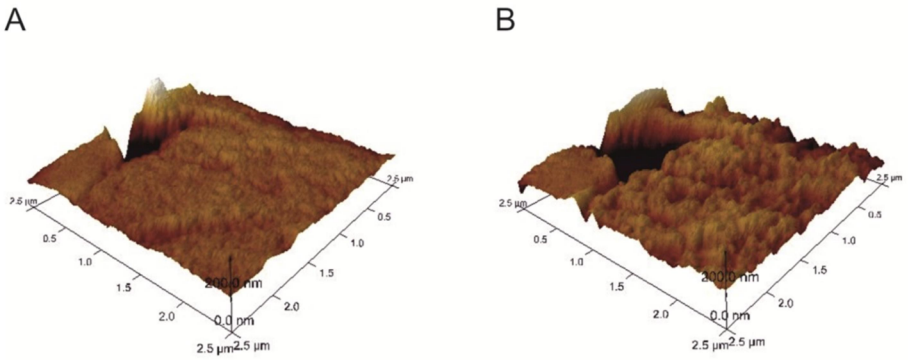

Figure S3: In situ observation of surface structural changes on MACS resulting from action of EG. Three-dimensional surface degradation was observed after incubation with EG for 6.75 h at 20 °C (compare panel A and B). The surface roughness increased noticeable. The enzyme loading was 36 $mg_{protein}/g_{substrate}$.

References

1 Ganner T, Bubner P, Eibinger M, Mayrhofer C, Plank H & Nidetzky B (2012) Dissecting and reconstructing synergism - in situ visualization of cooperativity among cellulases. *J Biol Chem* **287**, 43215–22.

Tunable mixed amorphous–crystalline cellulose substrates (MACS) for dynamic degradation studies by atomic force microscopy in liquid environments

Cellulose (2014) 21:3927–3939
DOI 10.1007/s10570-014-0419-8

ORIGINAL PAPER

Tunable mixed amorphous–crystalline cellulose substrates (MACS) for dynamic degradation studies by atomic force microscopy in liquid environments

Thomas Ganner · Timothy Aschl · Manuel Eibinger · Patricia Bubner · Arno Meingast · Boril Chernev · Claudia Mayrhofer · Bernd Nidetzky · Harald Plank

Received: 10 June 2014 / Accepted: 25 August 2014 / Published online: 4 September 2014

Abstract Atomic force microscopy in liquid environments (L-AFM) became a state of the art technique in the field of enzymatic cellulose degradation due to its capability of in situ investigations on enzymatic relevant scales. Current investigations are however limited to few substrates like valonia cellulose, cotton linters and processed amorphous cellulose as only these show required flatness and purity. Structurally monophasic, these substrates confine conclusions regarding enzymatic degradation of mixed amorphous–crystalline substrates as commonly found in nature. To exploit the full potential of the technique, cellulose substrates with multiphase properties, flat topology and purity are therefore absolutely required. In this study we introduce a special preparation route based on highly crystalline Avicel PH101® cellulose and the ionic liquid 1-butyl-3-methylimmidazolium chloride as dissolution reagent. As comprehensively shown by atomic force microscopy, wide angle X-ray scattering, Raman spectroscopy and electron microscopy, the developed material allows precise control of its polymorphic composition by means of cellulose types I and II embedded in an amorphous matrix. Together with the tunable composition and flat topology over large areas (>10 × 10 μm^2) the material is highly suited for L-AFM studies.

Keywords Cellulose · 1-Butyl-3-methylimmidazolium chloride · Avicel · Atomic force microscope · Enzymatic cellulose degradation · Cellulase

Abbreviations

MACS	Mixed amorphous−crystalline cellulose substrate
$C1_\beta$	Cellulose I_β
C2	Cellulose II
Avicel	Avicel PH101®
BmimCl	1-Butyl-3-methylimmidazolium chloride
UM	Ultramicrotomy
L-AFM	Atomic force microscopy in liquid environments

Thomas Ganner and Timothy Aschl have contributed equally to this work.

T. Ganner · T. Aschl · H. Plank (✉)
Institute for Electron Microscopy and Nanoanalysis, Graz University of Technology, Steyrergasse 17, 8010 Graz, Austria
e-mail: harald.plank@felmi-zfe.at

M. Eibinger · P. Bubner · B. Nidetzky (✉)
Institute of Biotechnology and Biochemical Engineering, Graz University of Technology, Petersgasse 12, 8010 Graz, Austria
e-mail: bernd.nidetzky@tugraz.at

A. Meingast · B. Chernev · C. Mayrhofer · H. Plank
Graz Centre for Electron Microscopy, Steyrergasse 17, 8010 Graz, Austria

B. Nidetzky
Austrian Centre of Industrial Biotechnology, Petersgasse 14, 8010 Graz, Austria

WAXS	Wide angle X-ray scattering
TEM	Transmission electron microscopy
SEM	Scanning electron microscopy
RS	Raman spectroscopy
RMS	Root mean square roughness
FWHM	Full width at half maximum

Introduction

The increasing demand for environmental and sustainable alternatives to crude oil based transportation fuels triggered a renaissance in scientific research of enzymatic cellulose deconstruction over the past decades (Himmel et al. 2007; Rubin 2008; Tilman et al. 2009). Based on the enzymatic decomposition of cellulose by so called cellulases into glucose and the subsequent fermentation to bioethanol, an attractive alternative to fossil based fuels is provided (Lynd et al. 2002). The mechanistic understanding on a molecular scale, although investigated for decades, is still incomplete which may be one of the reasons of yet not economically competitive biofuels from cellulose. Recent research (Wang et al. 2006; Ganner et al. 2012; Eibinger et al. 2014) suggests a close correlation between structural complexity of the substrate and rate limitations of single- or complexed systems of cellulases (Himmel et al. 2007). Diversity in substrate morphology is based on the linear molecular structure of cellulose with hundreds of linked β-1,4-D-glucosyl anhydro-D-glucose (Cellobiosyl, Cellobiose) units promoting the formation of parallel packed cellulose crystals by h-bonding through OH groups (Eibinger et al. 2014). Crystallites are intercepted by unordered amorphous regions forming the elementary fibril (Moon et al. 2011). Complex macromolecular arrangement of fibers, including amorphous and crystalline regions, is reflected in a tendency for microorganisms to require more than one specific cellulase type for efficient cellulose degradation. In more detail, a typical cellulase mixture comprises various cellulase species which act in a cooperative or synergistic way. It is distinctive for such systems that varying substrate specificity but also different modes of action are observed for individual cellulase types (Nidetzky et al. 1994; Bubner et al. 2012; Ganner et al. 2012; Eibinger et al. 2014). The situation of a multiphasic substrate and a complex interplay between individual enzymes is even more aggravated, as ongoing degradation is subjected to changes of substrate morphology (Bubner et al. 2012; Ganner et al. 2012; Eibinger et al. 2014). Thus, knowledge of the substrate structure and mechanistic interplay between systems of cellulases on a real time basis are highly desirable for any attempt to improve the process efficiency. While structural analysis is well established, real time observation of cooperative activity of individual species of cellulase relies on microscopic techniques providing spatial nanometer resolution (Bubner et al. 2013). Since conventional microscopy methods are mainly limited through resolution or inappropriate environmental conditions (e.g. ultra high vacuum), enzymatic kinetics and corresponding process limitations stay elusive. Atomic Force Microscopy in liquid (L-AFM) is a technique which allows dynamic investigations on the nanoscale in natural environments (Korayem and Ebrahimi 2011). However, AFM based techniques mostly require very flat topology and chemical purity to exploit the full potential. This is one reason why many studies have been performed on rather few and often monophasic substrates such as Valonia (Igarashi et al. 2011), cotton linters or processed cellulose (Ahola et al. 2008). In order to expand AFM based studies to the degradation of multiphase substrates (e.g. for direct synergism experiments), a flat cellulose substrate with a tunable content of cellulose allomorphs is highly desired.

In this study we present a simple multi-step approach for the development of tunable, multiphasic and flat cellulose substrates. In more detail, we demonstrate a procedure how crystalline cellulose (Avicel® PH-101; Avicel) can be processed towards substrates with controllable ratios between cellulose allomorph I_β ($C1_\beta$), II (C2) and amorphous cellulose. In order to gain flat substrates for high resolution experiments we present a special preparation routine based on ultramicrotomy (UM). The substrates are characterized by Wide angle X-ray diffraction (WAXS), Raman spectroscopy (RS), L-AFM and transmission electron microscopy (TEM) for a comprehensive chemical and structural insight. According to their characteristics, we call such substrates mixed amorphous−crystalline cellulose substrates or shortly MACS. Such substrates allow simultaneous investigations of enzymatic activities from large crystallites down to elementary

fibrils embedded in an amorphous matrix as already shown in previous studies (Bubner et al. 2012; Ganner et al. 2012; Eibinger et al. 2014).

Materials and methods

Materials

All materials and chemicals used have been purchased in highest available purity unless otherwise stated. Sample vials (4 ml, Rotilabo Ø 15 mm) and microscopy slides were purchased from Carl Roth (Karlsruhe, Germany); Whatman® No. 1 filter paper, Ethanol (Analytical grade, not denatured), Avicel® PH101 (Avicel) and 1-Butyl-3-methylimmidazolium chloride (BmimCl) were purchased from Sigma-Aldrich (St. Louis, MO, USA).

Preparation of MACS

Fabrication of tunable and flat MACS specimens is a multi-step procedure which will be technically described in the following.

Dissolution

1-Butyl-3-immidazolium chloride (BmimCl) was chosen as ionic liquid because of the high dissolution limit for cellulose (Swatloski et al. 2002), a low melting point of 65 °C (Zhang et al. 2005) and high chemical stability. First, BmimCl was placed in 4 ml sample vials, followed by heating to 100 °C in a laboratory build heating container. After liquefaction the corresponding amount of Avicel, as cellulose source, was added. Subsequently, the solution was stirred immediately with a glass stick yielding a milky and homogeneous solution (Fig. 1a; left). Please note, immediate stirring is crucial to gain a homogeneous solution or otherwise agglomeration of Avicel may occur due to rising viscosity during dissolution. Next the temperature was lowered to 95 °C and the mixture was continuously stirred further for 24 h at 30 rpm. Stirring was performed with a laboratory build motorized stirrer with a glass stick attached. Complete dissolution was confirmed by a viscous transparent liquid, further denoted as primary gel (Fig. 1a; right).

Gelation and solvent exchange

As gelation of the primary gel starts by lowering the temperature, further preparation is immediately applied by placing droplets ($\sim$200 µl) of the solution on carefully pre-cleaned microscopy slides (acetone wiping, supersonic assisted isopropyl cleaning and CO_2 spray drying) constantly held at 100 °C. To get uniformly thick gel specimens, a second slide is pressed on top of the bottom slide with two laterally placed glass spacers (objective slides) yielding 300 µm thick specimens (Fig. 1b). The stack was held together by adhesive tape at the outer edges. Primary gel specimens were then dried in parafilm sealed petri dishes for 7 days at room temperature yielding flexible transparent gel specimens, further denoted as secondary gel. A fractional solvent exchange sequence was applied using ethanol/water solutions with varying concentrations of 30, 50 vol%; 2 times 70, 80 vol%; 2 times 90 vol% and 2 times pure ethanol. Samples were placed in each bath for 30 min to remove the ionic liquid. Specimens are now called mixed amorphous–crystalline cellulose substrates (MACS). Different concentrations of used Avicel for fabrication are denoted as e.g. MACS-4 (4 wt% Avicel). MACS specimens were stored in pure ethanol until further used. Visual appearance is semitransparent and depending on the concentration of Avicel. Full transparency is lost at about 12 wt% of used Avicel upon dissolution, indicating significant internal change of morphology (Fig. 1c). Preparation is finished by cutting specimens into 2×2 mm^2 flakes, followed by drying for 12 h between weighted Whatman No. 1 cellulose filter papers to give flat samples. Specimens are now approximately 1×1 mm^2 in size and have a weight of 1.0 ± 0.1 mg. Complete removal of BmimCl was confirmed by mass spectroscopy, STA and EDX analyses as demonstrated in an earlier study (Bubner et al. 2012).

Preparation for instrument measurements

Samples for WAXS require no further preparation. Prior to L-AFM, RS, SEM and TEM studies, samples were embedded in epoxy. Briefly, resin and curing agent of a Specifix-40 epoxy kit (Struers, Willich, Germany) are blended in a mass ratio of 5:2 and filled into free slots of PELCO® flat embedding (Ted Pella, Redding, USA) mold. MACS flakes were positioned

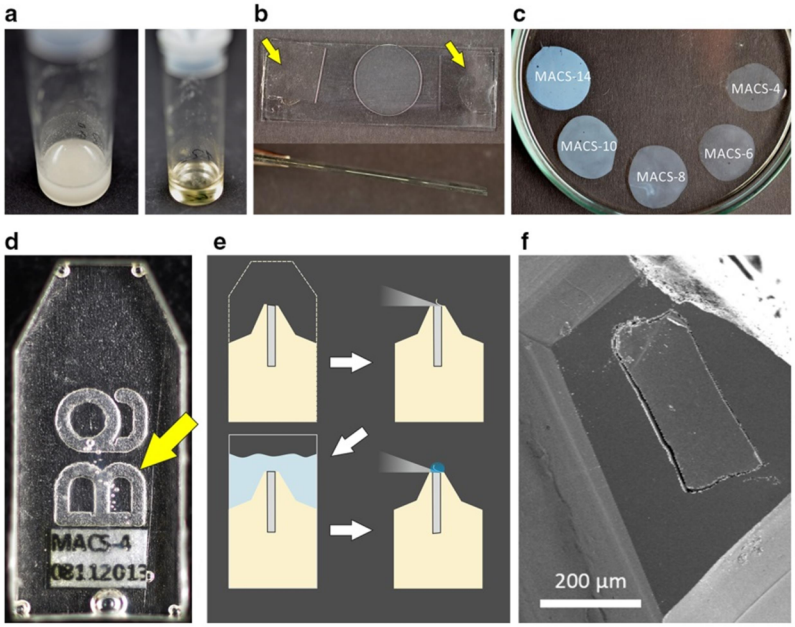

Fig. 1 **a** *Left image* shows a solution of molten BmimCl (*primary gel*) immediately after addition of Acivel and subsequent stirring with a glass stick. Solution is homogenous and milky in appearance. *Right image* shows the same solution after 24 h of constant mixing at 95 °C. Solution is now fully transparent and highly viscous. **b** Gel as prepared immediately after mixing. *Yellow arrows* indicate glass spacers, guaranteeing uniform gel thickness (approx. 300 µm). **c** MACS specimens after solvent exchange stored in pure ethanol. Increasing Avicel concentration upon mixing of the substrates leads to a decreasing transparency of the substrates, indicating concentration dependent change of internal morphology as demonstrated by WAXS, RS, AFM and TEM. **d** MACS-4 sample embedded in epoxy. The position of the specimen is highlighted by the *yellow arrow*. **e** Schematic representation of the UM preparation. See main text for detailed description. **f** Dried MACS-4 sample in the SEM. (Color figure online)

centrally (Fig. 1d) in the slots and cured for 4 h at 40 °C. Specimens were mounted in lab-made sample holders, designed to fit into the UM, RS, SEM and L-AFM to give perpendicular orientation of the substrate surface. UM preparation starts by pre-shaping of specimens by conventional razor blades (Fig. 1e), followed by first rough cuts (Ultra 45° knife, Diatome, Biel, Switzerland) to give flat samples. Subsequently, dry embedded MACS samples were placed into buffer solution (50 mM sodium-citrate buffer, pH 5.0) for at least 2 h to saturate the cellulose with liquid. Still wet specimens were finally cut with an ultrasonic diamond knife (Ultrasonic, Diatome, Biel, Switzerland) to achieve flat surfaces for L-AFM studies (Fig. 1f). Finished specimens were stored in buffer solution up to 24 h at 4 °C until further used for L-AFM measurements. AFM analysis proofed the result of very flat surfaces with root mean square (RMS) roughness below 10 nm over large areas up to $20 \times 20\ \mu m^2$ which are ideal for high-resolution L-AFM studies.

Specimens for RS were carefully dried under ambient conditions and subsequently imaged. SEM specimens were coated by a 10 nm carbon film after RS investigations.

For TEM investigations multiple thin block slices (<100 nm) were produced by UM and transferred to copper/palladium TEM grids (200 mesh, hexagonal). Slices were stained for 2 min with ruthenium-tetroxide by mixing 0.2 g ruthenium trichloride in a 5 % aqueous solution of sodium hypochlorite.

Preparation of cellulose II

Cellulose II (C2) was prepared as described elsewhere (Mittal et al. 2011) by treatment of Avicel ($C1_\beta$) with

16.5 wt% NaOH alkaline solution. Briefly, 10 g of Avicel powder was put into 200 ml of 16.5 wt% NaOH/dH_2O solution and stirred for 2 h at 25 °C. Reaction was stopped by diluting with 600 ml of deionized water, followed by immediate filtration. Filtration cake was washed thoroughly until the wash was neutral and the cake was dried for 24 h at 60 °C to get a dry and clean powder.

Instrument measurements

X-ray diffraction

WAXS analysis was performed on a Siemens D 5005 diffractometer (Siemens, Munich, Germany) using CuK_α (0.154 nm) radiation at 40 kV and 40 mA. MACS specimens were cut into 10 × 10 mm^2 for comparable exposure of all samples and mounted on a zero diffraction silicon crystal holder (Bruker AXS, Santa Barbara, California/USA). Powder specimens (C2, Avicel) were analyzed using the same holder by putting small amounts of powder on it. Source slit was variable (V20 Option) to give constant area illumination (2 × 2 cm^2) throughout the scan. All samples were characterized in locked coupled Θ/2Θ mode from 10° to 60° (2Θ) with an angle increment of 0.05° in 6 s. Selected extended range measurements from 5° to 140° were performed on MACS-4, MACS-8 and MACS-14 with the same scan speeds. Data analysis was performed using Origin 9 (OriginLab cooperation, Northampton, USA). Simulations were performed using Mercury 3.3 (Build RC5) with cellulose structures (.cif files) kindly provided by French (2014). Parameters were carefully chosen to fit experimental data.

Raman spectroscopy

All Raman measurements in this study were performed on a confocal Horiba Jobin–Yvon LabRam 800 HR spectrometer, equipped with a He–Ne laser, emitting at 633 nm, a grating with 300 l/mm and an Olympus BX41 microscope. Samples were prepared accordingly to the AFM samples to give representative results. The objective used was ×100 (NA = 0.9) with a 1,024 × 256 Peltier-cooled CCD. The standard integration function of the LabSpec® software was used to calculate the integrated intensities. Data analysis was performed using Origin 9 (OriginLab cooperation, Northampton, USA).

Raman crystallinity index

Schenzel et al. (2005) reported a method to calculate the crystallinity index of multiphase cellulose substrates by peak de-convolution of the HCH (CH_2) scissors bending vibrations (Wiley and Atalla 1987; Schenzel et al. 2005). Relevant band range between 1,200 and 1,500 cm^{-1} is shown in Fig. 4d. Deconvolution was performed by the Nonlinear Curve Fit tool (Origin 9, OriginLab cooperation, Northampton, USA) via gauss functions. Peak positions where held fixed for the 1,464 cm^{-1} (amorphous) and 1,483 cm^{-1} (crystalline) band to gain the corresponding intensities. Crystallinity index was then calculated by Eq. 1. Error bars were calculated by additional fits by the corresponding instrumental uncertainty of ±2 cm^{-1}.

$$X_c = \frac{I_{1483\ cm^{-1}}}{(I_{1483\ cm^{-1}} + I_{1464\ cm^{-1}})} \times 100 \quad (1)$$

Atomic force microscopy

AFM investigations were carried out on a Dimension 3,100 microscope using a XYZ hybrid scan head (Bruker AXS, Santa Barbara, California/USA) operated by a Nanoscope IVa controller. Specimens were prepared as described below and mounted in a laboratory build liquid cell with a volume of 1.5 ml. All investigations were performed with Olympus RC800PSA silicon nitride cantilevers with spring constants around 0.76 N/m, average tip radii of 20 nm and a tip opening angle of 35°. Specimens, buffer solution and liquid cell were held at 20 °C at least 30 min prior to actual experiments to establish thermal equilibrium. Flat topology of relevant areas was initially confirmed by 10 × 10 μm^2 images on different sample positions to ensure representative results including larger reference crystallites of Avicel. Scan areas were chosen by 10 × 10 μm^2 and 500 × 500 nm^2 to provide comprehensive insight. Operation in liquid was performed in repulsive tapping mode (Korayem and Ebrahimi 2011) while drive amplitudes, set-points and scan rates were adjusted towards lowest energy dissipation onto the specimen and highest possible resolution. Furthermore, all scanned areas where finally investigated at larger scan ranges to exclude tip induced material damage during actual measurements.

Scanning electron microscopy

Scanning electron microscopy (SEM) was performed with a Zeiss Gemini DSM 982 (Zeiss, Oberkochen, Germany), equipped with a Schottky-emitter. In order to reduce e-beam related material damage, low dose conditions were applied with beam currents below 1nA, a primary energy of 5 keV and a working distance of 5 mm.

Transmission electron microscopy

TEM was carried out on a Tecnai F20 (FEI, Hillsboro, Oregon, USA), equipped with a Schottky field emission gun under 200 kV acceleration voltage in TEM mode. Ultrathin slices (<100 nm) of embedded MACS specimens were prepared by UM (Ultracut UCT; Leica microsystems, Wetzlar, Germany). Samples were stained in Ruthenium tetroxide, as described above, in order to visualize crystalline regions in MACS. To ensure significant results, multiple sections were produced ($n > 2$), stained, imaged and analyzed on at least 5 positions to ensure significant results.

Results and discussion

The structural multiphase character of MACS is highly suitable for enzymatic synergism studies in the L-AFM as described in our recent studies (Bubner et al. 2012; Ganner et al. 2012; Eibinger et al. 2014). Although, presence of a multiphase substrate and characteristics were comprehensively analyzed for MACS-15, origin of the observed multiphase character stayed elusive (Ganner et al. 2012; Eibinger et al. 2014). Prior investigations suggested strong dependence on the concentration of Avicel used for fabrication. This study is aimed to give proof for this hypothesis by various methods described in the following. Considering solvability studies of cellulose in BmimCl (Vitz et al. 2009; Mäki-Arvela et al. 2010), we limited our experimental range to concentrations from 4 to 20 wt%, further denoted as MACS-4 to MACS-20. As a starting point, the structural properties of MACS were analyzed using wide angle X-ray diffraction.

Wide angle X-ray diffraction

Figure 2a shows the WAXS diffraction patterns for all MACS specimens investigated. For reference purposes, WAXS patterns of crystalline $C1_\beta$ (Avicel) and C2 (mercerized) cellulose are shown at the top and at the bottom, respectively. Considering the trend from MACS-4 to MACS-20 it is evident that: (1) overall intensities are significantly increasing; and (2) that the central peak around 20° shifts towards higher diffraction angles as summarized in Fig. 2b. Taking identical substrate areas and experimental WAXS conditions for all specimens into account, rising intensities either result from increasing density of cellulose material or from a superposition with an additional cellulose diffraction pattern. As a first step we consider the broad, diffuse peak at around 20° of 2Θ for MACS-4, which coincides with the angle position of amorphous cellulose (Park et al. 2010). Amorphous nature of MACS-4 is confirmed by dedicated AFM and TEM experiments (Figs. 5, 6, 7). In order to investigate the diffraction patterns with respect to additional contributions from other cellulose structures, an amorphous MACS-4 diffraction pattern is subtracted from a MACS-8 and MACS-14 pattern as shown by the (green and red) top graphs in Fig. 3a, b, respectively. Remaining difference diffraction patterns can be interpreted as signal from additional cellulose allomorphs in MACS-8 and MACS-14. Compared to experimental WAXS data for pure C2 and $C1_\beta$ (dark green and dark red) in Fig. 3a, b proof is given that additional allomorphs are present in MACS. To validate experimental data, simulations are given by the black curve (FWHM = 2.0) to show a 100 % crystalline diffraction pattern without other contributions. Simulations in gray (FWHM = 0.1) were used to index peaks by miller indices. Please note that only peaks which were also identified in difference diffraction patterns are indexed. In more detail, for MACS-14, difference pattern show reflections at 15.2°, 16.5°, 22,7° and 34,6° for the $(1\bar{1}0)$, (110), (200) and (004) crystal plane of $C1_\beta$ which is in good correlation with simulation data (French 2014). For MACS-8 not all peaks may be unequivocally identified in the difference diffraction patterns, which results from minor contribution and therefore low signal. However, the correlation between C2 and the difference signal is reflected in numerous resolved peaks, such as those at

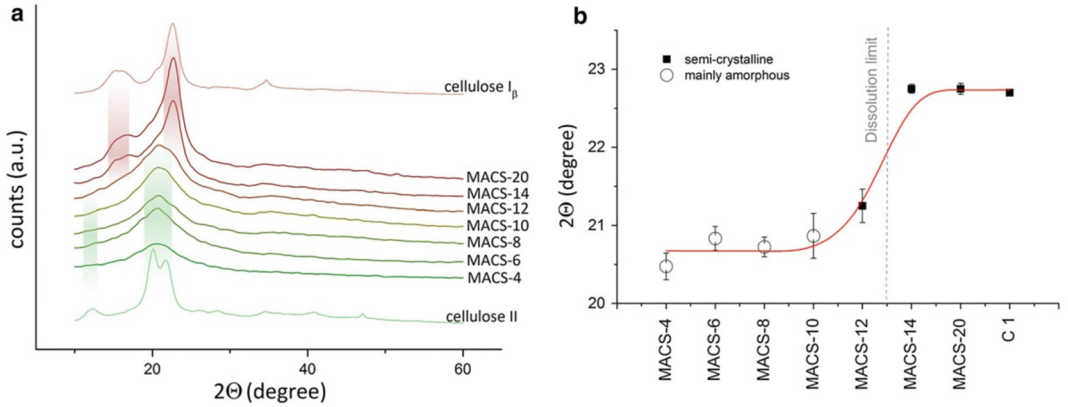

Fig. 2 **a** Stacked WAXS diffraction patterns of MACS specimens form 4 to 20 wt% with the corresponding reference diffraction patterns of cellulose allomorph I_β (Avicel; *red*) and II (mercerized Avicel, *green*). Color transformation from *green* to *red* illustrates the change from amorphous to semi-crystalline cellulose. Specimens below 10 wt% cellulose show mainly amorphous contributions to the pattern with the possibility of small contributions from C2 (see Fig. 3) as illustrated by a *green shading*. For MACS-12 or higher additional peaks appear in the patterns in good correlation with $C1_\beta$ as shown by the *red shading*. **b** Plot of the main peak shift as seen in **a**. Here peak shifts from 20.5 (amorphous) to 22.7 (crystalline (200), $C1_\beta$) degrees of 2Θ. *Circles* and *squares* indicate amorphous and semi-crystalline cellulose. *Error bars* are calculated from multiple diffraction patterns. (Color figure online)

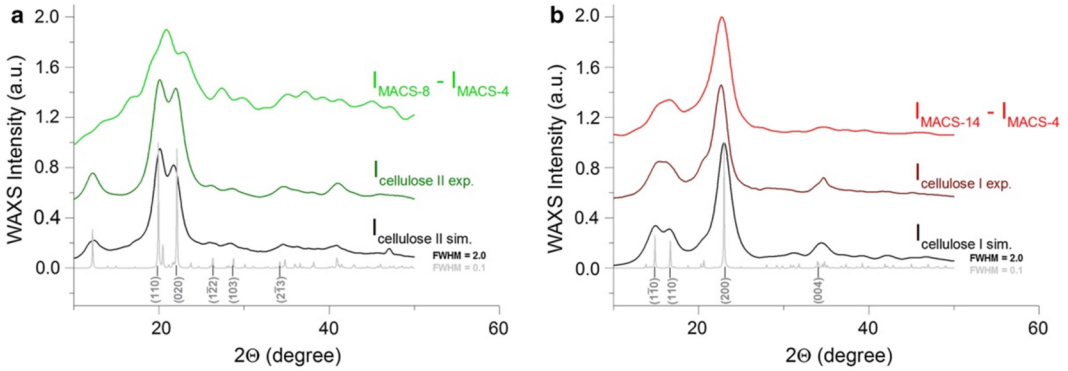

Fig. 3 Difference diffraction patterns of MACS-8 minus MACS-4 (**a**; *green*) and MACS-14 minus MACS-4 (**b**; *red*) shows additional contributions from other cellulose allomorphs. Corresponding experimental data of C2 (*dark green*; mercerized Avicel) and $C1_\beta$ (*dark red*; Avicel) are shown together with simulation data (*black*, FWHM = 2.0; *grey*, FWHM = 0.1). Simulation parameters were carefully chosen accordingly to fit the experimental data. Most relevant peaks resolved in subtracted diffraction patterns and simulation data are indexed with Miller indices. Structures were kindly provided by French (2014). (Color figure online)

20.7°, 22.8°, 27.3°, 29.9° and 35.0° for the (110), (020), $(1\bar{2}2)$, (103) and $(2\bar{1}3)$ reflection which, although slightly shifted to higher diffraction angles for the experiment, correlate well with simulated data. From these comparisons it can be concluded that MACS-8 consists of mainly amorphous cellulose with small amounts of C2. This is not fully unexpected, as cellulose polymers once dissolved recrystallize in allomorph C2. In addition, a rising concentration of cellulose must result in increased tendency to crystallize. This is reflected by an overall rising intensity in the diffraction patterns for MACS-4 to MACS-12 as

seen in Fig. 2a. However, the additional C2 contributions are small compared to the additional contribution found for MACS-14. Here a clear correlation to the $C1_\beta$ allomorph is found (see red and blue graphs in Fig. 3b) stemming from incomplete dissolution of Avicel in MACS. This dissolution limit can be clearly seen in Fig. 2b by the main peak shift from amorphous (and small C2 contributions) towards semi-crystalline cellulose around 12 wt%. This is in good agreement with literature (Vitz et al. 2009). Moreover, the observed changes in the diffraction patterns are in good agreement with the change of transparency on different concentrated MACS specimens as shown in Fig. 1c. However, WAXS basically can only show the transformation to multiphasic substrates, but lacks any spatial information. To gather a more detailed view on MACS as prepared for L-AFM investigations, Raman Spectroscopy was used as described in the following.

Raman spectroscopy

RS has proven to be a versatile tool to distinguish different cellulose allomorphs (Wiley and Atalla 1987; Schenzel and Fischer 2001; Agarwal et al. 2010). To provide comparability to our previous studies (Bubner et al. 2012; Ganner et al. 2012; Eibinger et al. 2014) and complementary techniques applied in this study, all specimens were prepared identical to the L-AFM investigations. Figure 4a shows two typical spectra of a MACS-14 sample recorded on and off a crystallite (Fig. 4b, c). Note, crystallites are found for concentrations higher than MACS-12 due to surpassed dissolution limit, as shown by WAXS. The bands for clear identification are indicated by (+) for $C1_\beta$ (crystalline, red) and (−) for C2/amorphous cellulose (green) (Schenzel and Fischer 2001). Please note, it is well reported (Schenzel and Fischer 2001; Schenzel et al. 2005) that sole amorphous and crystalline cellulose of allomorph II show similar bands and distinction is difficult. However, in accordance with WAXS data the presence of $C1_\beta$ and amorphous cellulose is clear from both spectra. Figure 4b shows a SEM top view image with a representative micrometer sized particle in MACS-14, which can typically be found all over the samples for concentrations above 12 wt%. Figure 4c shows the RS map on the same particle with the color code according to the spectra in Fig. 4a. Substrate in proximity of the crystalline particle shows an amorphous/C2 spectrum. In contrast the central crystallite can be clearly identified as $C1_\beta$ allomorph (red spectra), thus originating from undissolved Avicel residues. Please note that SEM was performed after RS investigations to prevent electron beam induced damage of the specimen. Average spectra of larger areas in MACS-4 to MACS-14 show same significant changes from amorphous to semi crystalline material as shown in Fig. 4d. As reported by Schenzel et al. (2005) analysis of multiphase spectra can be used to calculate the crystallinity index in respect to $C1_\beta$ and amorphous/C2 cellulose as described above. Figure 4d shows the relevant band range between 1,200 and 1,500 cm^{-1}. Bands for calculations are indicated by the red (crystalline) and green arrow (amorphous/C2). Figure 4e shows the calculated crystallinity index plotted against the corresponding substrate. In accordance with WAXS data, the dissolution limit is revealed by a strongly increasing crystallinity around MACS-12. Combined evidence from RS and WAXS derived data clearly suggest that substrates above MACS-12 show a multiphasic spatial organization with increasing allomorph I_β content. To resolve fibrillar structures, as described in recent studies (Ganner et al. 2012; Eibinger et al. 2014) high resolution microscopy methods were applied.

Atomic force microscopy in liquid environments

Multiple L-AFM investigations, probing the enzymatic degradation, uncovered the presence of different allomorphs by a non-uniform speed of deconstruction (Bubner et al. 2012; Ganner et al. 2012; Eibinger et al. 2014). Surface changed from formerly flat to distinctive rough topology. RMS increase was several hundred percent in the first few hours of the experiment. Dedicated additional experiments showed, that beside residual large crystallites, fibers in the nanometer regime are found in the surrounding matrix. Moreover, these fibers were responsible for the pronounced increase of RMS in the AFM experiments. A protocol to resolve different synergistic activity of cellulase revealed a novel mechanism in multiphase substrate degradation (Ganner et al. 2012; Eibinger et al. 2014). While residual large crystallites stayed almost unchanged over the time investigated, nanosized fibers showed significant impact on synergistic deconstruction from the beginning. Here internal structure, in particular the ordered crystalline packing

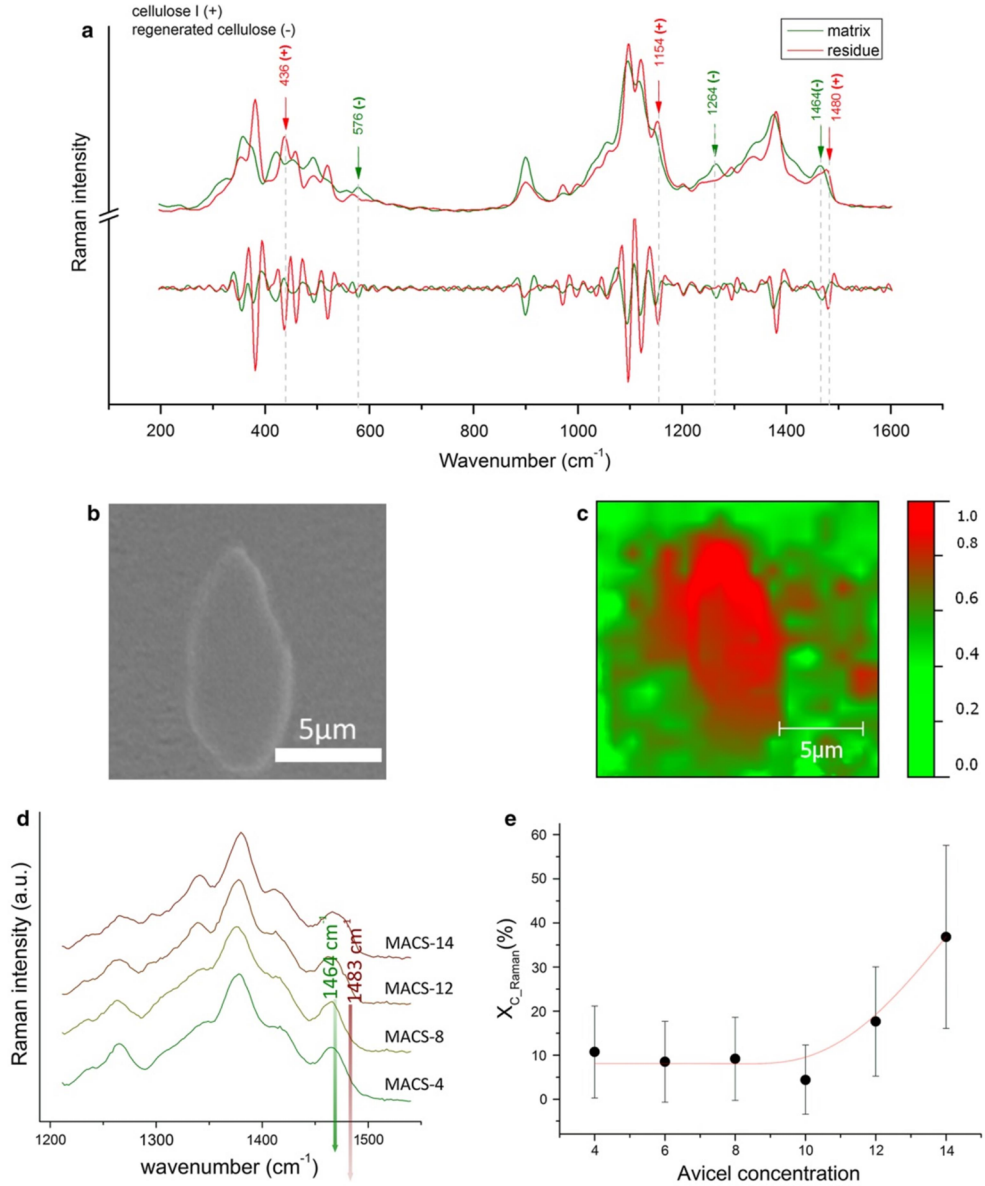

Fig. 4 **a** Raman spectra (*above*) and corresponding second derivatives (*below*) of cellulose allomorphs as found in MACS-14 or higher. Colors of the spectra correlate with the RAMAN color map in **c**. Typical bands are illustrated by (+) for crystalline and (−) for amorphous/C2 cellulose. **b** SEM micrograph of a typical crystalline cellulose particle found in MACS-14, corresponding to the Raman image in (**c**). SEM investigation was performed after RAMAN mapping to prevent electron induced damage of the specimen. **c** Raman map for the same particle as in (**b**) with color scale according to (**a**). **d** MACS Raman spectra in the range of 1,250–1,550 cm^{-1} showing the relevant bands for crystallinity index determination as shown in (**e**). Here the $\delta(CH_2)$ bending vibration of regenerated cellulose at 1,464 cm^{-1} and crystalline cellulose at 1,483 cm^{-1} are used for the calculation as proposed by Schenzel et al. (2005). **e** Calculated crystallinity index for MACS 4 to MACS-14 form the bands as illustrated in (**d**). *Error bars* are calculated from RAMAN spectrometer accuracy of ±2 cm^{-1}

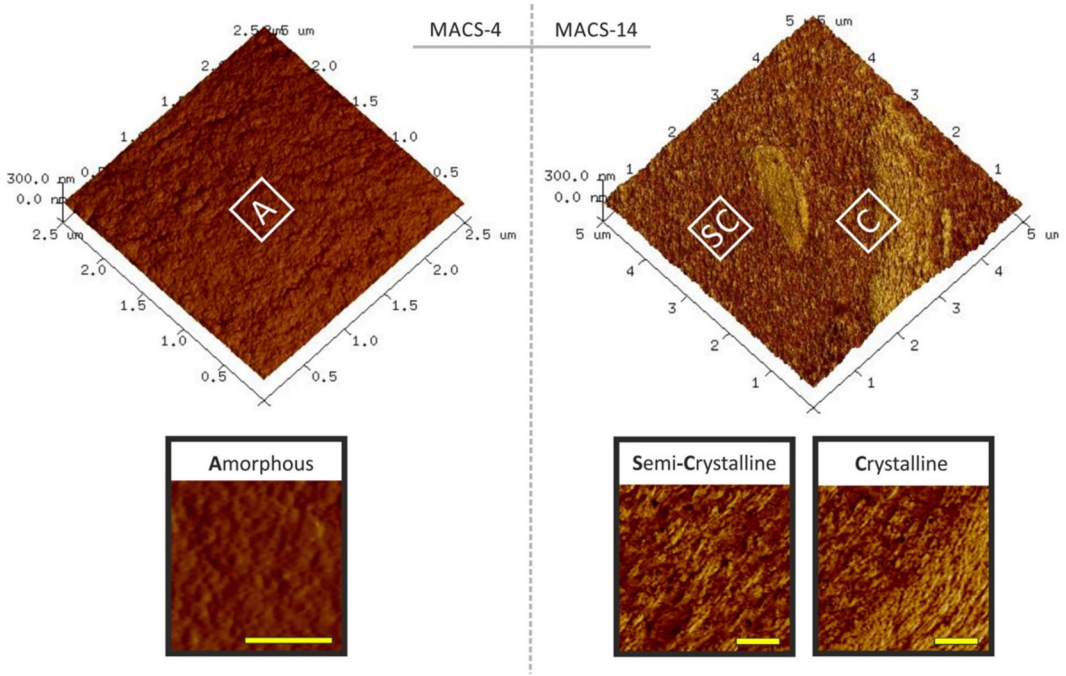

Fig. 5 L-AFM 3D images of an amorphous MACS-4 and semi-crystalline MACS-14 specimen overlaid with phase information (repulsive). For MACS-4 smooth amorphous (*A*) cellulose surfaces are found without any pronounced features. MACS-14 reveals highly heterogeneous surface implementing a semi-crystalline (*SC*) phase and residual micron sized crystallites (*C*). Insets show close up images with featureless amorphous (MACS-4; *A*), semi-crystalline (MACS-14; *SC*) and highly packed crystalline substrate areas (MACS-14; *C*). Fibrillar structures are clearly visible for MACS-14 on crystalline as well semi-crystalline parts of the substrate. *Scale bars* (*yellow*) show 250 nm of the substrate

and the small dimensions, triggered a controversial form of degradation. While amorphous substrate was degraded at uniform speed, areas with fibers embedded featured a slow and a fast phase of substrate removal (Ganner et al. 2012; Eibinger et al. 2014). First, crystalline fibers were excavated and cleaned from the surrounding material, followed by fast degradation from the ends. This fast removal of crystalline material is only possible due to small dimensions of the fibers (approx. 30 nm × 100 nm). Here, the low number of obstacles and high accessibility of fiber ends allows fast and linear processive movement of exo-glucanases. This however, showed that smaller crystalline features of similar dimension found in elementary fibrils are of high importance for synergistic degradation of cellulose. Despite the extensive knowledge from recent studies about the synergistic behavior of such fibers, proof of exact formation during preparation was not given. Therefore, we used the same preparation procedures as described above to investigate surface topography of MACS with varying Avicel concentration. Figure 5 shows representative 3-D AFM images of MACS-4 and MACS-14 with overlaid phase signal. Analysis on MACS-4 supports findings from WAXS with no evidence for fibrillar structures and numerous on MACS-14. In more detail, areas with pure crystalline nature (Fig. 5; MACS-14, C) and pronounced semi crystalline appearance (Fig. 5; MACS-14, SC) can be found in MACS-12 or higher. Fibers in the amorphous matrix as well as on highly crystalline areas correlate in diameter and length indicating similar formation mechanisms. In Fig. 6a a representative image of a fiber rich area on a MACS-14 specimen is shown by an AFM amplitude image revealing well pronounced fibers. Correlated AFM height, phase and amplitude

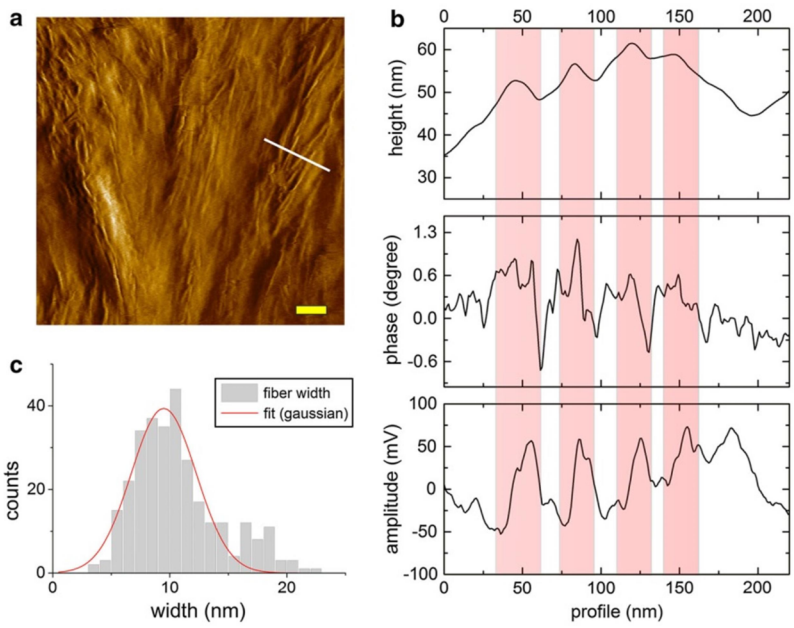

Fig. 6 **a** Amplitude image of MACS-14 surface shows numerous fibrillar structures on a highly crystalline area of the substrate. *Scale bar* (*yellow*) is 100 nm. **b** Cross section profiles as seen in **a** (*white line*) showing height, phase and amplitude data. Areas with high density of fibers feature slightly higher phase signals indicating a higher stiffness of the material in agreement to the phase signal on Avicel residues (see Fig. 5, MACS-14, C). **c** Statistical analysis ($N_f = 300$) of fiber width on numerous MACS-14 specimens ($N_e = 5$) revealing 9.5 ± 2.7 nm of fiber diameter. (Color figure online)

cross sectional analysis is shown in Fig. 6b (see white line in Fig. 6a) revealing mean widths of 10–15 nm. A more detailed analysis reveals that regions with higher fiber density show slightly higher phase signals indicating stiffer regions. This is in good agreement to the observed phase signal on residual Avicel particles (see Fig. 5; MACS-14, C). To gain statistically relevant data, numerous experiments were analyzed with respect to fiber widths as summarized in Fig. 6c. Gaussian peak fitting reveals a fiber width of 9.5 ± 2.7 nm in good agreement with previous literature (Himmel et al. 2007; Kocherbitov et al. 2008; Chinga-Carrasco 2011). Please note that the asymmetric histogram distribution towards broader fibers in Fig. 6c is caused by slightly increasing tip influences for rougher samples. As AFM is limited to surface structures, further TEM investigations have been conducted to access the internal MACS structure for a more comprehensive analysis as discussed in the following.

Transmission electron microscopy

TEM was performed on thin (<100 nm) MACS sections produced by UM. Contrast was enhanced by standard ruthenium tetroxide staining as described above. In Fig. 7 a plot of the density of highly ruthenium stained areas is given against the corresponding specimen. TEM bright field images of MACS-4 and MACS-14 are given as inset. MACS-4 shows less structure compared to MACS-14, where staining shows a fibrous network. As ruthenium tetroxide staining is based on different diffusion velocities in crystalline and amorphous parts of polymers, darker areas are associated with denser and therefore crystalline material. Hence, fibers seen in the L-AFM are not confined to the surface of MACS and multiphasic properties are indeed intrinsic. Interestingly, density of fibers also shows the dissolution limit of MACS by a strong increase of ruthenium dense regions. Most likely, this is the result of increased tendency of the cellulose to recrystallize from an oversaturated solution upon cooling. Determination of exact allomorph of present nanofibrils however, remains elusive due to spatial resolution limitations of suitable techniques (Raman, WAXS). However, considering the missing local evidence for $C1_\beta$ in the amorphous matrix by Raman data and taking recrystallization processes into account (Kroon-Batenburg et al. 1996; Klemm et al. 2005), as indicated by WAXS, nanofibrils might be of allomorph II.

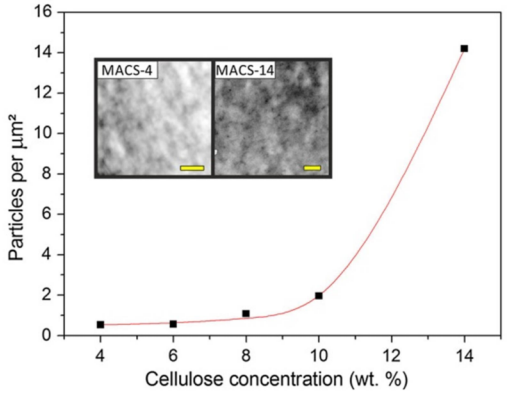

Fig. 7 Areal density of highly ruthenium stained regions in MACS specimens as observed by TEM. Plot shows slightly linear trend below MACS-12 with low densities followed by a sharp increase around MACS-12 correlating with the proposed dissolution limit of 12 wt%. The *insets* show MACS-4 and MACS-14 TEM images which clearly proof the increased number of small stained particles for MACS-14. *Scale bar* is 500 nm. Note, ruthenium is accumulated around crystalline features due to a different diffusion velocity against amorphous parts, indicating highly crystalline regions

Conclusion

In summary, including all data from WAXS, RS, L-AFM and TEM the multiphasic nature of MACS was demonstrated together with the ability to change the intrinsic amount of crystalline cellulose. Already evident from the fabrication process or visual appearance of the corresponding specimen (see Fig. 1c), the dissolution limit of Avicel in BmimCl was shown by WAXS (see Fig. 2b). Here, an increase of $C1_\beta$ associated peaks could be observed after exceeding a mixing ratio of 12 wt%. This is in good agreement with dissolution limits from literature (Vitz et al. 2009; Zavrel et al. 2009; Mäki-Arvela et al. 2010). Closer analysis of amorphous substrates between MACS-4 and MACS-8 showed evidence for a minor contribution of C2 (Fengel et al. 1995). For further clarification RS was used to acquire spatially resolved information. RS revealed that cellulose of allomorph I_β was found in larger crystalline particles (Fig. 4b, c) and amorphous cellulose in the surrounding matrix. L-AFM investigations for high concentrated MACS further showed nano-sized fibers in the amorphous matrix (see Figs. 5, 6) in accordance to recent studies (Ganner et al. 2012; Eibinger et al. 2014). MACS fabricated with concentrations lower than 12 wt% seemed to have no or minor quantity of fibers. These findings are supported by TEM analysis, which showed the increasing density of such fibers going from lower to higher concentrations of Avicel (see Fig. 7). Although fibrous structures were demonstrated by AFM and TEM, the crystalline allomorph of these fibers can only be concluded by WAXS and Raman data. With the missing evidence for $C1_\beta$ in the amorphous part of the substrate by Raman investigations and evidence from WAXS, fibers are therefore most likely of allomorph II. The deliberate incorporation of crystalline features in the amorphous material allows investigations on substrates with a mixed amorphous–crystalline character as shown in recent studies (Ganner et al. 2012; Eibinger et al. 2014). Even though natural sources in their native state are structurally more complicated in respect to additional lignin and hemicelluloses, MACS offers the possibility to emulate the multiphase character of such substrates to a certain extent. With this, valuable information may be gained especially concerning systems of cellulases acting in a synergistic way on structurally diverse substrates. In addition, the applied preparation protocol allows RMS values below 10 nm, which is extremely important for any high resolution investigation to improve our understanding of enzymatic cellulose degradation as a key method in carbohydrate research.

Acknowledgments We thank Stefan Mitsche for helping us with WAXS analysis; Stephanie Rosker for helping us with the experiments; Angelina Orthacker, Robert Winkler and Ferdinand Hofer for discussions. Gratitude goes to the Cambridge Crystallographic Data Centre (CCDC) for the ability to use Mercury 3.3 for simulation purposes. Financial support was provided from the Austrian Science Fund FWF (Grant P 24156-B21 to B.N.).

References

Agarwal U, Reiner R, Ralph S (2010) Cellulose I crystallinity determination using FT-Raman spectroscopy: univariate and multivariate methods. Cellulose 17:721–733. doi:10.1007/s10570-010-9420-z

Ahola S, Turon X, Osterberg M et al (2008) Enzymatic hydrolysis of native cellulose nanofibrils and other cellulose model films: effect of surface structure. Langmuir 24:11592–11599. doi:10.1021/la801550j

Bubner P, Dohr J, Plank H et al (2012) Cellulases dig deep: in situ observation of the mesoscopic structural dynamics of enzymatic cellulose degradation. J Biol Chem 287:2759–2765. doi:10.1074/jbc.M111.257717

Bubner P, Plank H, Nidetzky B (2013) Visualizing cellulase activity. Biotechnol Bioeng 110:1529–1549. doi:10.1002/bit.24884

Chinga-Carrasco G (2011) Cellulose fibres, nanofibrils and microfibrils: the morphological sequence of MFC components from a plant physiology and fibre technology point of view. Nanoscale Res Lett 6:417

Eibinger M, Bubner P, Ganner T et al (2014) Surface structural dynamics of enzymatic cellulose degradation, revealed by combined kinetic and atomic force microscopy studies. FEBS J 281:275–290. doi:10.1111/febs.12594

Fengel D, Jakob H, Strobel C (1995) Influence of the Alkali concentration on the formation of cellulose II. Study by X-ray diffraction and FTIR spectroscopy. Holzforschung 49:505–511. doi:10.1515/hfsg.1995.49.6.505

French AD (2014) Idealized powder diffraction patterns for cellulose polymorphs. Cellulose 21:885–896. doi:10.1007/s10570-013-0030-4

Ganner T, Bubner P, Eibinger M et al (2012) Dissecting and reconstructing synergism: in situ visualization of cooperativity among cellulases. J Biol Chem 287:43215–43222. doi:10.1074/jbc.M112.419952

Himmel ME, Ding S-Y, Johnson DK et al (2007) Biomass recalcitrance: engineering plants and enzymes for biofuels production. Science 315:804–807. doi:10.1126/science.1137016

Igarashi K, Uchihashi T, Koivula A et al (2011) Traffic jams reduce hydrolytic efficiency of cellulase on cellulose surface. Science 333:1279–1282. doi:10.1126/science.1208386

Klemm D, Heublein B, Fink H-P, Bohn A (2005) Cellulose: fascinating biopolymer and sustainable raw material. Angew Chem Int Ed Engl 44:3358–3393. doi:10.1002/anie.200460587

Kocherbitov V, Ulvenlund S, Kober M et al (2008) Hydration of microcrystalline cellulose and milled cellulose studied by sorption calorimetry. J Phys Chem B 112:3728–3734. doi:10.1021/jp711554c

Korayem MH, Ebrahimi N (2011) Nonlinear dynamics of tapping-mode atomic force microscopy in liquid. J Appl Phys 109:084301. doi:10.1063/1.3573390

Kroon-Batenburg LMJ, Bouma B, Kroon J (1996) Stability of cellulose structures studied by MD simulations. Could mercerized cellulose II be parallel ? Biomacromolecules 9297:5695–5699

Lynd LR, Weimer PJ, van Zyl WH, Pretorius IS (2002) Microbial cellulose utilization: fundamentals and biotechnology. Microbiol Mol Biol Rev 66:506–577. doi:10.1128/MMBR.66.3.506-577.2002

Mäki-Arvela P, Anugwom I, Virtanen P et al (2010) Dissolution of lignocellulosic materials and its constituents using ionic liquids—a review. Ind Crops Prod 32:175–201. doi:10.1016/j.indcrop.2010.04.005

Mittal A, Katahira R, Himmel M, Johnson D (2011) Effects of alkaline or liquid-ammonia treatment on crystalline cellulose: changes in crystalline structure and effects on enzymatic digestibility. Biotechnol Biofuels 4:41

Moon RJ, Martini A, Nairn J et al (2011) Cellulose nanomaterials review: structure, properties and nanocomposites. Chem Soc Rev 40:3941–3994. doi:10.1039/c0cs00108b

Nidetzky B, Steiner W, Hayn M, Claeyssens M (1994) Cellulose hydrolysis by the cellulases from *Trichoderma reesei*: a new model for synergistic interaction. Biochem J 298 :705–710

Park S, Baker J, Himmel M et al (2010) Cellulose crystallinity index: measurement techniques and their impact on interpreting cellulase performance. Biotechnol Biofuels 3:10

Rubin EM (2008) Genomics of cellulosic biofuels. Nature 454:841–845. doi:10.1038/nature07190

Schenzel K, Fischer S (2001) NIR FT Raman spectroscopy—a rapid analytical tool for detecting the transformation of cellulose polymorphs. Cellulose 8:49–57. doi:10.1023/A:1016616920539

Schenzel K, Fischer S, Brendler E (2005) New method for determining the degree of cellulose i crystallinity by means of FT Raman spectroscopy. Cellulose 12:223–231. doi:10.1007/s10570-004-3885-6

Swatloski RP, Spear SK, Holbrey JD, Rogers RD (2002) Dissolution of cellose with ionic liquids. J Am Chem Soc 124:4974–4975. doi:10.1021/ja025790m

Tilman D, Socolow R, Foley JA et al (2009) Beneficial biofuels—the food, energy, and environment trilemma. Science 325:270–271. doi:10.1126/science.1177970

Vitz J, Erdmenger T, Haensch C, Schubert US (2009) Extended dissolution studies of cellulose in imidazolium based ionic liquids. Green Chem 11:417–424. doi:10.1039/B818061J

Wang L, Zhang Y, Gao P et al (2006) Changes in the structural properties and rate of hydrolysis of cotton fibers during extended enzymatic hydrolysis. Biotechnol Bioeng 93:443–456. doi:10.1002/bit.20730

Wiley H, Atalla RH (1987) Band Assignments in the Raman spectra of celluloses. Carbohydr Res 160:113–129

Zavrel M, Bross D, Funke M et al (2009) High-throughput screening for ionic liquids dissolving (ligno-)cellulose. Bioresour Technol 100:2580–2587. doi:10.1016/j.biortech.2008.11.052

Zhang H, Wu J, Zhang J, He J (2005) 1-Allyl-3-methylimidazolium chloride room temperature ionic liquid: a new and powerful nonderivatizing solvent for cellulose. Macromolecules 38:8272–8277. doi:10.1021/ma0505676

Cellulose Surface Degradation by a Lytic Polysaccharide Monooxygenase and Its Effect on Cellulase Hydrolytic Efficiency

⌘ *Author's Choice*

THE JOURNAL OF BIOLOGICAL CHEMISTRY VOL. 289, NO. 52, pp. 35929–35938, December 26, 2014

Cellulose Surface Degradation by a Lytic Polysaccharide Monooxygenase and Its Effect on Cellulase Hydrolytic Efficiency*

Received for publication, August 1, 2014, and in revised form, October 17, 2014 Published, JBC Papers in Press, October 31, 2014, DOI 10.1074/jbc.M114.602227

Manuel Eibinger[‡1], Thomas Ganner[§1], Patricia Bubner[‡1], Stephanie Rošker[§], Daniel Kracher[¶], Dietmar Haltrich[¶], Roland Ludwig[¶], Harald Plank[§2], and Bernd Nidetzky[‡‖3]**

*From the [‡]Institute of Biotechnology and Biochemical Engineering, Graz University of Technology, Petersgasse 12, A-8010 Graz, Austria, [§]Institute of Electron Microscopy and Nanoanalysis and **Graz Centre for Electron Microscopy, Steyrergasse 17, A-8010 Graz, Austria, [¶]Department of Food Science and Technology, BOKU-University of Natural Resources and Life Sciences, Muthgasse 18, A-1190 Vienna, Austria, and [‖]Austrian Centre of Industrial Biotechnology, Petersgasse 14, A-8010 Graz, Austria*

Background: Lytic polysaccharide monooxygenase (LPMO) has recently been discovered to depolymerize cellulose.
Results: Dynamic imaging was applied to reveal the effects of LPMO and cellulase activity on solid cellulose surface.
Conclusion: Critical features of surface morphology for LPMO synergy with cellulases are recognized.
Significance: Direct insights into cellulose deconstruction by LPMO alone and in synergy with cellulases are obtained.

Lytic polysaccharide monooxygenase (LPMO) represents a unique principle of oxidative degradation of recalcitrant insoluble polysaccharides. Used in combination with hydrolytic enzymes, LPMO appears to constitute a significant factor of the efficiency of enzymatic biomass depolymerization. LPMO activity on different cellulose substrates has been shown from the slow release of oxidized oligosaccharides into solution, but an immediate and direct demonstration of the enzyme action on the cellulose surface is lacking. Specificity of LPMO for degrading ordered crystalline and unordered amorphous cellulose material of the substrate surface is also unknown. We show by fluorescence dye adsorption analyzed with confocal laser scanning microscopy that a LPMO (from *Neurospora crassa*) introduces carboxyl groups primarily in surface-exposed crystalline areas of the cellulosic substrate. Using time-resolved *in situ* atomic force microscopy we further demonstrate that cellulose nano-fibrils exposed on the surface are degraded into shorter and thinner insoluble fragments. Also using atomic force microscopy, we show that prior action of LPMO enables cellulases to attack otherwise highly resistant crystalline substrate areas and that it promotes an overall faster and more complete surface degradation. Overall, this study reveals key characteristics of LPMO action on the cellulose surface and suggests the effects of substrate morphology on the synergy between LPMO and hydrolytic enzymes in cellulose depolymerization.

Plant cell wall cellulose is the most abundant carbohydrate material in nature. It is built from linear polysaccharide chains of several hundreds of β-1,4-linked D-glucosyl units. Multiple chains are organized spatially into a densely packed crystalline material (1, 2). More disordered parts of the cellulose, which are also present in natural or technologically processed substrates, are usually called amorphous. In contrast to amorphous regions, crystalline cellulose is highly resistant to degradation. The low efficiency of its conversion threatens the commercial viability of biofuels or base chemicals produced from cellulosic biomass (3, 4).

Cellulases represent the current paradigm for enzymatic cellulose degradation through hydrolytic depolymerization (1, 4). Cellulases comprise internally chain-cleaving endoglucanases (EG)[4] and processively chain end-cleaving cellobiohydrolases (CBHs) as their main activities (1). Different cellulolytic activities operate synergistically; that is, combinations of enzymes are hydrolytically more efficient than expected from the sum of their individual activities (5–7). Cellulase synergism originates from the dynamic interplay between endo- and exo-modes of cellulose chain cleavage as well as from complementary enzyme specificities for degrading crystalline and amorphous cellulose material (Fig. 1*a*) (6–9). Cellulases adsorb strongly to cellulose (7, 10), and their combined action on the solid surface is reflected by strong three-dimensional degradation where amorphous material is degraded at higher rates than crystalline structures (8, 11).

Originally discovered for its activity on chitin (12, 13), lytic polysaccharide monooxygenase (LPMO) employs a unique principle of cellulose degradation utilizing C-H activation followed by O_2-dependent chain cleavage (12, 14–16). LPMO is a mononuclear type II copper enzyme (14, 17) that requires an

* This work was supported by Austrian Science Fund FWF Grant P 24156-B21 (to B. N.) and Doctoral program BioToP-Molecular Technology of Proteins Grant W1224 (to D. K.).
⌘ *Author's Choice*—Final version full access.
[1] These authors should be considered equal first authors.
[2] To whom correspondence may be addressed. Tel.: 43-316-873-8821; Fax: 43-316-873-811596; E-mail: harald.plank@felmi-zfe.at.
[3] To whom correspondence may be addressed: Institute of Biotechnology and Biochemical Engineering, Graz University of Technology, Petersgasse 12, A-8010 Graz, Austria. Tel.: 43-316-873-8400; Fax: 43-316-873 8434; E-mail: bernd.nidetzky@tugraz.at.

[4] The abbreviations used are: EG, endoglucanase; LPMO, lytic polysaccharide monooxygenase; CBH, cellobiohydrolase; AFM, atomic force microscopy; CLSM, confocal laser scanning microscopy; MACS, mixed amorphous-crystalline cellulosic substrate; HPAEC-PAD, high performance anion exchange chromatography coupled to pulsed-amperometric detection.

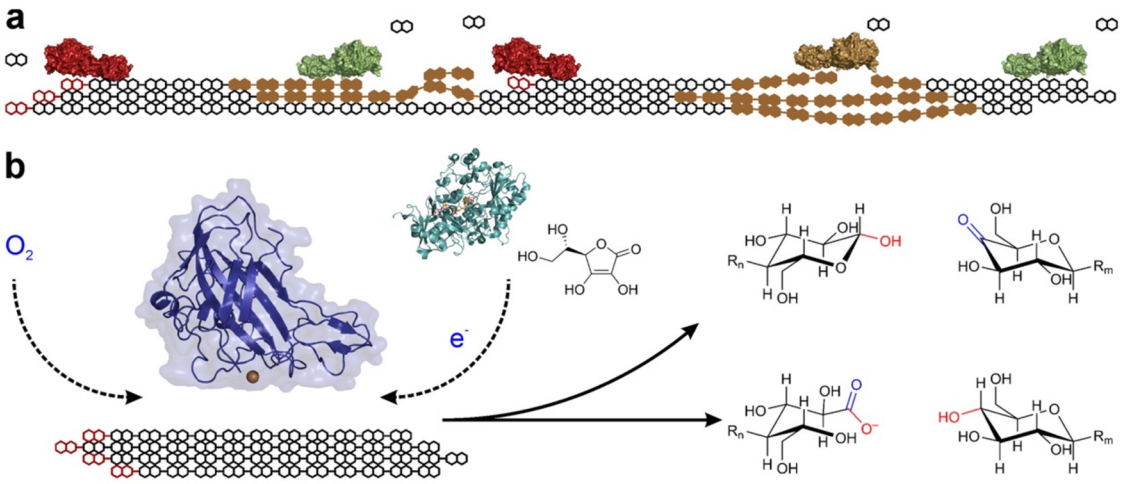

FIGURE 1. *a*, hydrolysis of crystalline-ordered and amorphous-unordered (*brown*) cellulose is catalyzed by a typical set of fungal cellulases, including chain end-cleaving cellobiohydrolases (CBH I, *red*; CBH II, *green*) and internally chain-cleaving endoglucanase (*brown*). Linear cellulose chains are represented by their cellobiosyl-dimer units, with the reducing end shown in *red*. Cellobiose is the main soluble sugar produced by the cellulases. *b*, oxidative O_2-dependent attack of LPMO on the cellulose surface, resulting in internal chain cleavages and release of C1′ or C4 oxidized oligosaccharides harboring one oxygen atom from the O_2 oxidant (indicated in *blue*) (18–20). C1′ oxidation produces a 1,5-lactone product that hydrolyzes rapidly to give a D-gluconic acid moiety, which is shown. LPMO contains surface-exposed catalytic copper (*brown sphere*) that is required for activity (12, 14, 16). The structure of GH61D (PDB code 4B5Q) from *Phanerochaete chrysosporium* is used for depiction (21). Electrons required in the LPMO reaction *in vitro* can be delivered from the flavo-heme protein cellobiose dehydrogenase or from a small-molecule reductant such as L-ascorbic acid (12, 14).

external electron donor, a small molecule, or a partner redox-protein for activity (12, 14, 18). Glycosidic bond cleavage in cellulose involves oxidation of C1′ or C4 of an intrachain cellobiosyl moiety (Fig. 1*b*) depending on the type of LPMO used (19, 20). A common feature of LPMO structures is a flat protein face with the active site located near its center and the catalytic metal exposed outward (14, 20–23). Interaction of LPMO with cellulose surfaces is, therefore, thought to occur via the flat protein face (12). Oxidative chain cleavages in crystalline areas of the substrate are expected to cause local disruptions of the ordered cellulose structure (12, 24, 25). Substrate decrystallization effects might, therefore, facilitate hydrolytic cellulose depolymerization. LPMO is, therefore, believed to have significant potential of enhancing the efficiency of cellulosic biomass conversion (17, 25–27), and a number of studies have shown that LPMO does act in synergy with cellulase activities (5, 26, 28).

Current understanding of cellulose degradation by LPMO is limited by the absence of immediate and direct evidence on the enzyme action on the solid surface of the substrate. LPMO activity has been demonstrated from the slow release of oxidized soluble cello-oligosaccharides (19, 20, 27), but the proposed chemical and structural disruption of the cellulose surface has not been demonstrated so far. Thinking of how LPMO might act alone and in synergy with cellulases in insoluble cellulose degradation is, therefore, mostly hypothetical and has so far been inferred only indirectly from protein structures and biochemical data on soluble product formation from cellulosic substrates. The present study provides relevant insight based on so far elusive direct evidence. LPMO caused changes in the surface morphology of a mixed amorphous-crystalline cellulosic substrate at spatial and temporal resolution were measured, and their effects on subsequent surface degradation by cellulases were uncovered. A refined view of the action of LPMO on the cellulose surface shows the possibility for synergy but also for competition with cellulases in crystalline cellulose degradation. Morphological targets for synergy between LPMO and cellulases were thus identified on the cellulose surface.

EXPERIMENTAL PROCEDURES

Materials—Unless stated, standard chemicals were of the highest purity available from Carl Roth (Karlsruhe, Germany).

Enzymes—Purified LPMO from *Neurospora crassa* (LPMO-03328 gene product (NCBI accession number XP_955892)) was prepared by a reported protocol (29). Complete *Trichoderma reesei* cellulase was from fungal culture (strain SVG17) on wheat straw (30, 31). CBH I was purified from the complete *T. reesei* cellulase via a modified ion exchange protocol as described elsewhere (32). Purified *T. reesei* CBH II was recombinant enzyme preparation from *Pichia pastoris* (33). EG (from *Trichoderma longibrachiatum*) was from Megazyme (Dublin, Ireland) and used without further purification. β-Glucosidase from *Aspergillus niger* was from Megazyme.

Protein Determination—Molar extinction coefficients for individual enzymes in solution were determined from the protein sequence from UniProt using ProtParam or were taken from literature (ϵ_CBH I (P62694) = 86,760 $M^{-1}cm^{-1}$; ϵ_CBH II (P07987) = 97,665 $M^{-1}cm^{-1}$; ϵ_EG (Q12714) = 74,940 $M^{-1}cm^{-1}$; ϵ_LPMO-03328 = 51,130 $M^{-1}cm^{-1}$).

Cellulosic Substrates—Avicel PH-101 was from Carl Roth. A mixed amorphous-crystalline cellulosic substrate (MACS) was prepared from Avicel PH-101 using partial dissolution in and regeneration from the ionic liquid 1-butyl-3-methylimidazolium chloride as described elsewhere (30, 34, 35). The absence

of ionic liquid in the final substrate preparation was confirmed by mass spectroscopy and simultaneous thermal analysis, as described in an earlier study (34). The MACS substrate presents an amorphous cellulose matrix in which cellulose crystallites of different size are distributed in an irregular fashion (8, 30, 34). Nanocrystalline cellulose was prepared from Whatman® (Sigma) qualitative filter paper according to a protocol from literature (36).

Enzymatic Reactions—Experiments were done at 1.0 mg cellulose ml^{-1} in 50 mM sodium phosphate buffer, pH 6.0, using a total volume of 500 μl in static Eppendorf tubes sealed with oxygen-permeable Parafilm. Each experiment was done in independent triplicates using an individual Eppendorf tube for each sampling point. L-Ascorbic acid was present at 7.5 μM. Enzyme loadings (μg of protein mg^{-1} cellulosic substrate) were as follows: LPMO (9), complete cellulase (25), CBH I (100), CBH II (100), and EG (100). β-Glucosidase was added to each reaction at a loading of 5 μg mg^{-1} cellulosic substrate.

Synergy between LPMO and cellulases was examined in two different assays that are referred to as "sequential" or "simultaneous." In the sequential assay, which involved pretreatment of substrate with LPMO before the action of cellulases, the used cellulosic substrate was incubated at 25 °C with LPMO. The negative control did not contain LPMO or contained LPMO lacking L-ascorbic acid. The total liquid volume was 450 μl. Incubation was for 5 h in all reactions except for 12 h for the reaction where complete cellulase was added in the second step. Reaction tubes were heated to 50 °C, and 50 μl of hydrolytic enzyme solution (complete cellulase, CBH I, CBH II, or EG) were added. Samples were withdrawn every 15 min up to 1 h. For sampling, one of the reaction tubes was removed, and enzyme was inactivated at 95 °C for 10 min. Solid material was removed by centrifugation at 9300 × *g* for 1 min at 4 °C. The cleared supernatant was used for soluble product analyses.

In the simultaneous assay, which did not involve substrate pretreatment by LPMO, cellulosic substrate was incubated at 50 °C with LPMO and CBH I, both added at the same time. β-Glucosidase was also present. The total reaction volume was 500 μl. The negative control did not contain LPMO or contained LPMO lacking L-ascorbic acid. Samples were withdrawn after 5 and 96 h and were processed as described above for the sequential assay.

Fluorescence Dye Adsorption Analyzed with Confocal Laser Scanning Microscopy (CLSM)—MACS substrate was incubated with LPMO for 12 h as described above. Enzyme was removed by washing with absolute ethanol followed by repeated washing with Milli-Q water. Sample was equilibrated for 2 h in staining buffer (2.5 mM $MgCl_2 \cdot 6H_2O$, 16 mM $(NH_4)_2SO_4$, 67 mM Tris-HCl, pH 8.4) and then transferred into an aluminum foil-covered reaction tube with 10 ml of freshly prepared staining buffer that contained 5 μM SYTO-62 (Invitrogen). Staining was done for 12 h at 4 °C followed by dye removal through extensive washing with staining buffer. Sample was stored in staining buffer under exclusion of light until CLSM analysis within maximally 4 h. Negative controls were prepared in exactly the same manner except that no SYTO-62 staining was used, no LPMO was applied, or LPMO without L-ascorbic acid was applied.

Sample analysis was performed with a Leica TCS SPE confocal laser microscope (Leica Microsystems, Wetzlar, Germany). Samples were excited with a 635-nm laser beam, and emitted light was detected in the range 645–709 nm. At the same time, transmission images of the transparent samples were obtained at 488 nm. Photomultiplier gain, offset, and Z-step size were carefully optimized for each channel to provide the best signal/noise ratio possible. Confocal stacks were acquired with a Leica ACS APO × 63 OIL CS objective (NA: 1.30). Image analysis and background subtraction was performed using ImageJ 1.47v (rsbweb.nih.gov).

Atomic Force Microscopy (AFM) Imaging—A commercial Dimension 3100 Hybrid AFM operated by a Nanoscope 4a Controller (Bruker Nano Surface Offices, Santa Barbara, CA) was used in Tapping Mode (liquid). The instrument was equipped with a liquid probe holder and OMCL-RC800PSA cantilevers (Olympus Probes, Tokyo, Japan). Experiments were performed at ~20 °C using a laboratory-built liquid cell (8, 30). Scan rates, set points, and drive amplitudes were observed continuously to ensure stable measurement conditions and to prevent image convolution by tip-related artifacts along with lowest possible energy dissipation on the sample. Areas of interest on the specimens were carefully chosen based on light microscopy images, and a series of reference images ($N \geq 5$) was recorded to ensure the homogeneity of the substrate surface. For time-resolved AFM imaging with quantitative evaluation of surface volume degradation, it was important to select an area of the substrate surface that contained a large cellulose crystallite, which because of its very slow enzymatic degradation served as a height marker to follow degradation of the surrounding material.

Before the AFM experiments, the MACS was treated as described previously (8, 30) to prepare a nano-flat surface and mounted in the liquid cell, and reference images were taken before the injection of the enzyme solution. The cellulose substrate concentration was 0.50 mg ml^{-1}, and enzyme loadings were as described above. Enzymatic reactions were followed at 20 °C in a continuous manner for typically 5 h.

AFM image processing and analysis was performed using Gwyddion 2.31 (released 02/21/2013) and Nanoscope (Build R3Sr4.94136, Bruker Nano Surface Offices). Data analysis was performed using Origin 8.5 (OriginLab Corp., Northampton, MA).

Analytics—D-Glucose was determined colorimetrically with glucose oxidase and peroxidase (37). Cellobiose and higher oligosaccharides were analyzed with high performance anion exchange chromatography coupled to pulsed-amperometric detection (HPAEC-PAD) (Dionex BioLC, Thermo Fisher Scientific, Waltham, MA) as described elsewhere (30). Soluble products of LPMO were also analyzed by HPAEC-PAD. Briefly, a CarboPac® PA200 column (3 × 250 mm) and a CarboPac® PA200 guard column (3 × 50 mm), both from Thermo Fisher Scientific, were used. Temperature was 30 °C, and the flow rate was 0.4 ml min^{-1}. The column was equilibrated with 120 mM sodium hydroxide for 5 min. Samples were analyzed with a linearly ascending gradient in sodium acetate (up to 250 mM). The identity of D-gluconic acid was assigned using authentic standard. Identification of other products was not pursued.

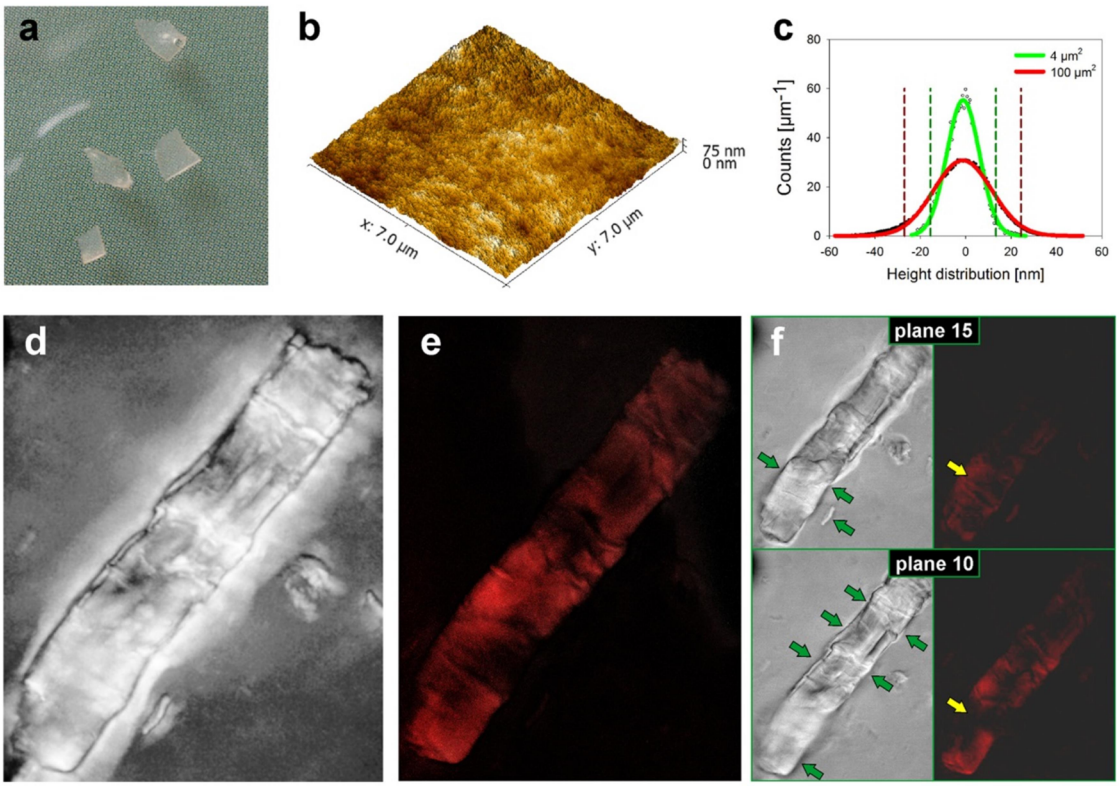

FIGURE 2. **LPMO is specific for oxidizing crystalline cellulose surfaces and does so by introducing carboxylic acid groups.** *a*, visual appearance of the mixed amorphous-crystalline cellulose substrate prepared from Avicel PH-101 using partial dissolution in and regeneration from ionic liquid. *b*, AFM height image of the substrate surface in a ultramicrotome-cut cellulose sample. *c*, height distribution analysis reveals the nano-flat character of the substrate surface. *d*, maximum intensity projection of the recorded transmission microscopic images of a substrate area where a large cellulose crystallite is embedded in an amorphous matrix. The crystallite is a remnant from the original Avicel PH-101 not dissolved during ionic liquid treatment. It is composed of cellulose allomorph I, as shown by XRD (33). *e*, maximum intensity projection of the recorded fluorescence signal from the same substrate area after incubation with LPMO (9 mg g^{-1}; supplemented with 7.5 μM L-ascorbic acid; 25 °C; 12 h) and subsequent staining for 12 h with 5 μM SYTO-62, a small molecule fluorescent probe for carboxyl groups (38). The figure shows that crystalline surfaces are preferentially labeled with the fluorescent dye after substrate incubation in the presence of LPMO. This suggests preferred attack of LPMO on these surfaces. *f*, transmission microscope images (*left panel*) with the corresponding fluorescence images (*right panel*) from two focal planes separated by a vertical distance of 4 μm. Focused specimen parts, which are recognized clearly by detailed structures in the transmission images (indicated with *green arrows*), correspond to the surface of the cellulose crystallite. CLSM images reveal that the SYTO-62 fluorescence signal is confined exclusively to crystalline parts in focus over different planes (*yellow arrow* in image in *plane 15*) and that the fluorescence signal is not present at interior parts of the crystallite (*yellow arrow* in image in *plane 10*). Therefore, these images show that LPMO action is restricted to the surface of the cellulose crystallite. Suitable controls showed that untreated cellulose crystals or cellulose crystals treated with LPMO in the absence of L-ascorbic acid did not become fluorescent when stained with SYTO-62. Fluorescence images in (*e* and *f*) are background-subtracted and contrast-enriched. *Scale bars*, 10 μm.

RESULTS AND DISCUSSION

The LPMO used in this study was the LPMO-03328 gene product from the fungus *N. crassa*. In the sequence-based classification of LPMOs among the carbohydrate-active enzymes (14), the enzyme belongs to Auxiliary Activity family 9 (AA9, formerly GH-61). Also based on sequence similarity (18, 19) and shown biochemically (19), the LPMO used was further categorized into the group of C1-oxidizing LPMOs. Highly purified recombinant enzyme was obtained from *P. pastoris* expression culture as described previously (29). A specially designed model substrate, providing amorphous and crystalline regions alternating on a nano-flat cellulose surface (Fig. 2, *a*–*c*) (8, 30, 34) was key in the characterization of the enzymatic degradation process catalyzed by the LPMO. Effects of LPMO action on cellulose surface chemistry and structure were, therefore, measured for the first time. A fundamentally new LPMO assay based on adsorption of the fluorescent dye SYTO-62, originally developed for measurement of carboxyl groups on polymer bead surfaces (38), was adapted here to identify and localize LPMO-catalyzed formation of carboxyl groups on the cellulose surface. Analysis by CLSM provided spatial resolution of the fluorescence intensities, thus allowing for characterization of the specificity of the LPMO for attacking cellulose surface material. Lateral and vertical degradation activities of the LPMO could also be measured. Time-resolved *in situ* AFM in liquid environments was used to measure changes in surface topology and material character caused by LPMO action.

LPMO-catalyzed Cellulose Surface Oxidation Revealed by Using Fluorescence Dye Adsorption—Cellulose model substrate was incubated with LPMO, and the fluorescence dye adsorp-

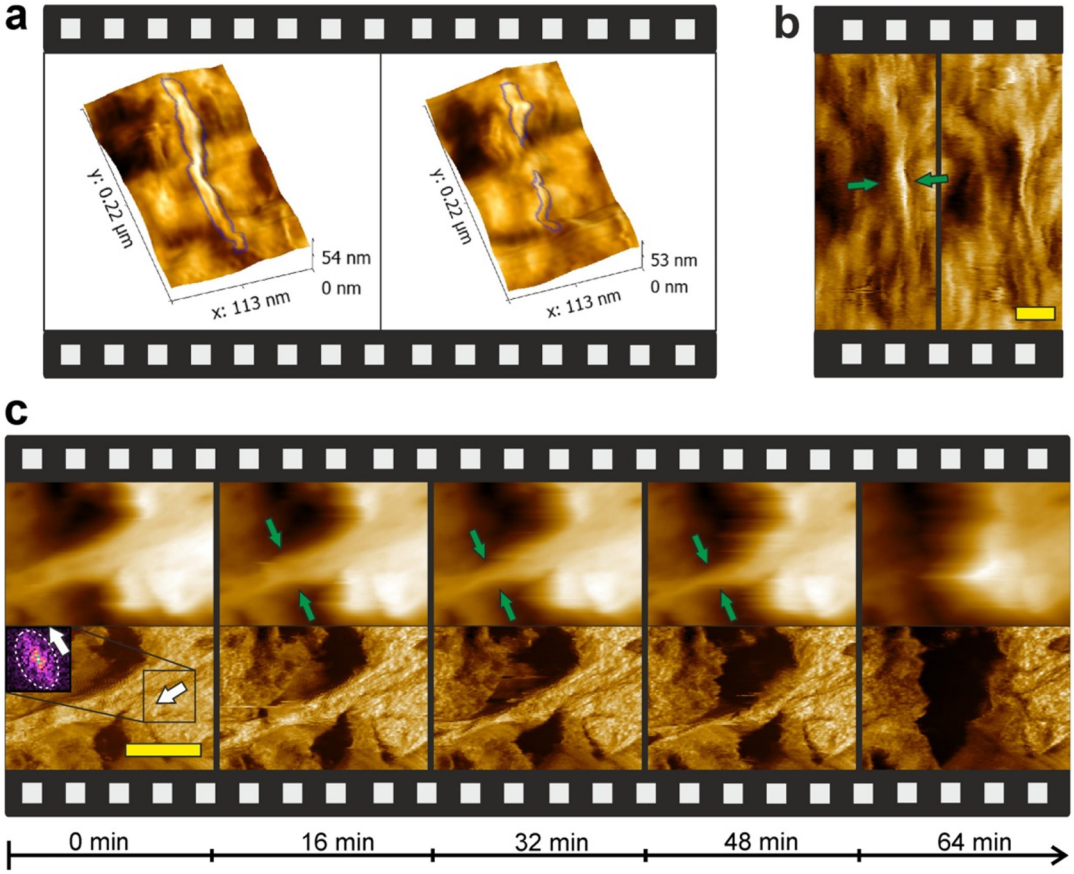

FIGURE 3. **AFM imaging of LPMO action on the cellulose surface and its effect on CBH I activity.** *a*, three-dimensional surface representation overlaid with phase information to show the attack of LPMO (9 mg g^{-1} substrate; 20 °C; 12 h) on a cellulose fibril (*blue outline*) in the *middle* and from the *top*, thus causing a large amount of internal degradation. *b*, phase images showing fibril degradation by LPMO through major thinning from the sides, as indicated by *green arrows*. AFM images show substrate before and after 12 h of incubation with LPMO supplemented with 7.5 μM L-ascorbic acid as reductant. Amorphous material is visualized by a dark color in phase or phase-overlaid images. It was resistant against degradation by LPMO. *Scale bar*, 30 nm. *c*, time-resolved AFM sequences (height images on *top*, phase images on *bottom*) showing surface degradation by CBH I on a substrate preincubated with LPMO. Gradual degradation of a crystalline surface feature is observed as a result of thinning from the top and from the sides, as indicated by *green arrows*, eventually leading to complete dissolution of a large set of fibril bundles. Fiber orientation on the crystalline surface is demonstrated by 2D Fast Fourier Transformation analysis (embedded in Gwyddion 2.31) of the *highlighted rectangle*. Deviation from a circular symmetric to an ellipsoid spectrum (*white dotted envelope*) shows the fiber orientation by a 90° rotation (*white bold arrows*). *Scale bar*, 300 nm.

tion assay was applied for subsequent surface characterization. Fig. 2, *d–f*, shows transmission/fluorescence microscopic images of LPMO-treated and then SYTO-62-stained substrate. A strong increase in SYTO-62 fluorescence from the cellulose surface after incubation with enzyme under turnover conditions in the presence of L-ascorbic acid provided a clear indication for carboxyl group formation by the LPMO (Fig. 2*e*). Suitable controls (see "Experimental Procedures") did not show increased surface fluorescence after treatment with SYTO-62 (data not shown). Interestingly, fluorescence signals were detected almost exclusively from crystalline surface areas of the cellulose, as shown in Fig. 2, *e–f*, demonstrating high selectivity of the LPMO for oxidizing just the ordered substrate structures. Using CLSM, we showed that SYTO-62 fluorescence was emitted from the outermost surface of the crystalline material, whereas subjacent layers of the crystalline cellulose were clearly non-fluorescent (Fig. 2*f*). Therefore, the LPMO activity appeared to have caused only minimal oxidative substrate degradation in the vertical direction. Fig. 2*e* also reveals that the crystalline cellulose surface was oxidized in large patches of up to 1500 μm^2, consistent with surface degradation through multiple site attacks by the LPMO.

Cellulose Surface Degradation by LPMO Monitored with AFM—Time-resolved AFM data were obtained from LPMO-catalyzed surface degradation of the nanoflat cellulosic substrate. Results showed that LPMO promoted cellulose surface structure degradation to only a small degree. The overall volume degradation of surface material was minimal. However, enzyme activity was detected clearly on crystalline regions of the substrate, which were removed at a slow rate (Fig. 3, *a* and

b). Regions of surrounding amorphous material were not affected. Interestingly, small crystalline nano-fibrils, present in large number on the cellulose surface where they were irregularly distributed within otherwise predominantly amorphous material, were degraded effectively by the LPMO, as also shown in Fig. 3, *a* and *b*. Fibril degradation proceeded primarily by thinning, starting from the side walls, but also by cleavage in the middle to create smaller and shorter fragments. Discrete crystalline surface structures were thus dissolved as a result of the action of the LPMO. Even though formation of oxidized oligosaccharides was detectable in solution (*e.g.* D-gluconic acid), the released amount was too small for exact quantification. It seems, therefore, that activity of the LPMO used was captured not only more directly but also more sensitively through analysis of the oxidative surface degradation that it produced.

Synergy between LPMO and Hydrolytically Cellulose-degrading Enzymes—We proceeded by examining the synergy effects between LPMO and hydrolytic enzymes. Cellulose pretreated with LPMO (sequential assay) was used as the substrate for cellulases, and the resulting surface degradation was analyzed with *in situ* AFM. Comparison of time-resolved AFM sequences for conversion of LPMO treated and untreated substrate revealed a basis for cooperativity between oxidative and hydrolytic enzymes depending on the morphology of the cellulose surface. Because no cellulose specimen is the exact replica of another, comparative analysis is possible to the extent that highly characteristic features of the surface degradation are worked out. AFM observations reported recur within different areas of a single sample and are fully reproducible across different substrate specimen.

In a recent AFM study we characterized the specificities of the major fungal cellulases (EG, CBH I, CBH II) for surface material degradation in the same cellulose substrate that was now used to investigate the action of LPMO (8, 30). EG and CBH II degrade amorphous material (8, 30), and we found here that neither enzyme takes advantage of substrate pretreatment with LPMO in terms of enhanced rate or completeness of the overall surface degradation. Crystalline material not attacked in untreated substrate (small fibrils, large crystallites) remained completely resistant to EG or CBH II activity after the incubation with LPMO. The initial rate of soluble sugar release by each of the two cellulases was also unaffected within error limit by substrate treatment with the LPMO. Considering studies that state up to 2-fold LPMO-caused stimulation in cellulose conversion by different EG enzymes or by CBH II (17, 28), it is important to emphasize key differences in the ways LPMO-cellulase synergy was assayed herein and in several other studies.

Our sequential assay involves defined preincubation of cellulosic substrate with the LPMO under established conditions for lytic oxidation (29) and defines synergy with the cellulase in question as the ratio of initial rates of reducing sugar release from LPMO-treated and untreated substrate in the second step of the overall oxidative-hydrolytic cellulose depolymerization. The simultaneous assay used in several earlier studies (5, 26, 28, 39) and also herein (see later) measures the enhancement of soluble sugar release (typically after a long incubation time of several days) caused by supplementation of the cellulase with LPMO. The reason to prefer the sequential assay here as our main analytical tool was that it rigorously evaluates the immediate effect of substrate transformation by the LPMO (see Fig. 2, *e* and *f*, and Fig. 3, *a* and *b*) on the cellulase activity, whereas it excludes potential ambiguity of the simultaneous assay where LPMO and cellulase can influence each other in various ways in their activity and also stability. Finally, sequential actions of LPMO and cellulases might be just as relevant biologically as is their simultaneous action.

Being mainly active on crystalline cellulose (1, 40), CBH I complements EG and CBH II in their substrate specificity. However, in the mixed amorphous-crystalline cellulosic substrate used herein, surface degradation by CBH I is measurable only on exposed small fibrils, whereas larger crystalline parts are not degraded within limits of detection, just as the amorphous material (8, 30). Interestingly, therefore, prior action of the LPMO made some of the larger crystalline areas of the substrate clearly accessible for the degradation by CBH I. The time-resolved AFM sequences in Fig. 3*c* reveal gradual degradation of a prominent large-sized and elongated crystalline feature of the substrate, where the enzymatic attack took place primarily through thinning from the sides, and complete dissolution occurred within ~1 h of incubation. Nearby crystalline material also showed clear indications of progressing degradation with incubation time. In untreated substrate incubated with CBH I, degradation of similarly sized crystalline cellulose structures has never been observed, as already reported in previous papers (8, 30) and also confirmed in this study by investigating multiple substrate samples ($N \geq 5$).

The herein discovered synergy between LPMO and CBH I in the degradation of highly recalcitrant cellulosic material (*i.e.* large crystallites) is, however, not reflected by a boost in the rate of reducing sugar formation from substrate pretreated with LPMO. On the contrary, as shown in Fig. 4*a*, hydrolytic activity of CBH I was lowered significantly (~3-fold) on LPMO-treated as compared with untreated cellulose, suggesting inhibition effects rather than synergy between LPMO and CBH I during degradation of the particular cellulosic substrate used. The apparent conflict in these findings (Figs. 3*c* and 4*a*) is resolved considering that LPMO-catalyzed oxidative degradation of nano-fibrils on the cellulose surface (Fig. 3, *a* and *b*) could have removed or rendered inaccessible the major substrate material for hydrolysis by CBH I. Larger crystalline features, identified from AFM data as major sites of synergy between CBH I and LPMO (Fig. 3*c*), accounted for only a small part (≤5%) of the total available surface area in the substrate used so that in the overall hydrolysis measured as the release of soluble sugars, competition between the two enzymes appears to have outweighed their locally observed synergistic interaction.

We also found, again based on measurement of soluble sugar formation, that LPMO did not exhibit synergy with CBH I in the degradation of isolated crystalline nano-fibrils (Fig. 4*a*). On Avicel PH-101, which despite its poorly defined morphology is a widely used model substrate for highly crystalline cellulosic material (10, 41, 42), a small but significant stimulation (1.1-fold) of the soluble sugar release rate by CBH I was observed when the substrate had been preincubated with LPMO (Fig. 4*a*). Therefore, these results suggest that crystalline cellulosic

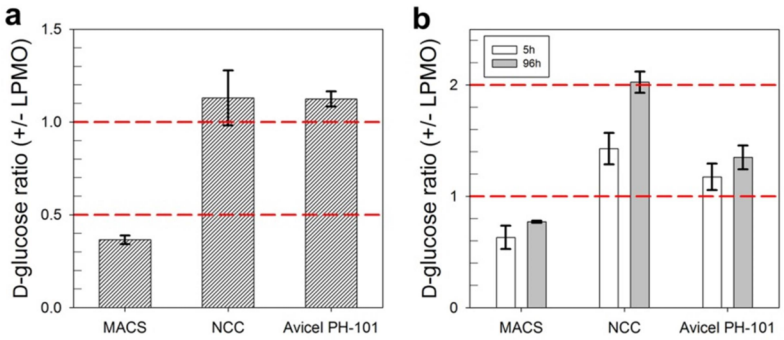

FIGURE 4. **Synergy between LPMO and CBH I during degradation of different cellulosic substrates determined in sequential (*a*) and simultaneous (*b*) assays.** The substrates used were MACS, nanocrystalline cellulose (*NCC*), and Avicel PH-101. For the sequential assay (*panel a*), LPMO (9 μg ml^{-1}) was incubated with either cellulose preparation (1 mg ml^{-1}) in 50 mM sodium phosphate buffer, pH 6.0, for 5 h at 25 °C. L-Ascorbic acid (7.5 μM) was present as the reductant. The total volume was 500 μl, and incubations were done in static Eppendorf tubes. CBH I (100 μg ml^{-1}) supplemented with β-glucosidase (5 μg ml^{-1}) was added to the reaction mixture, and incubation was continued at 50 °C for 1 h. The simultaneous assay (*panel b*) used identical conditions except that all reactants were already present at reaction start. Temperature was 50 °C, and reaction time was 96 h. The D-glucose concentration was measured with an enzymatic assay. It was confirmed using analysis with high performance anion exchange chromatography with pulsed amperometric detection that D-glucose accounted for ≥99% of the total soluble products present in the supernatant under these conditions. The measured data are plotted as ratio of sugar formed in reactions containing or lacking LPMO. A value exceeding unity, therefore, indicates a synergistic effect. A value below unity indicates that preincubation with LPMO (*panel a*) or the presence of LPMO (*panel b*) results in apparent inhibition of the D-glucose release by CBH I. Results are shown in *bars* with S.D. from the three independent experiments indicated.

material presents mesoscopic (that is, above the nano-fibril size) morphological targets for cooperativity between LPMO and CBH I. Local disruption of larger crystalline cellulose surfaces due to oxidation events (Fig. 2, *e* and *f*) might be important to allow for a facilitated attack of CBH I (Fig. 3*c*).

Considering previous work done on the synergy between oxidative-lytic and hydrolytic cellulose-degrading enzymes (5, 26), we also performed simultaneous assays of the combined cellulolytic action of LPMO and CBH I in order to be able to put our results into useful context with literature. Moreover, use of the two enzymes together was also meant to ensure that potential substrate limitation to CBH I caused by prior action of the LPMO was excluded. Using the three cellulosic substrates applied before, release of D-glucose was determined after 5 and 96 h under conditions where CBH I was used in combination with the LPMO or alone. The degree of synergy is expressed as the ratio of the two D-glucose measurements at each time, and the results are summarized in Fig. 4*b*.

Clear lack of synergy between LPMO and CBH I acting on the mixed amorphous-crystalline cellulosic substrate was confirmed from results of the simultaneous assay: CBH I acting alone was ~1.6-fold more efficient in producing D-glucose at 5 h than the two-enzyme mixture containing LPMO. To the best of our knowledge, turnover frequency of LPMO on crystalline cellulose has not been determined. However, there is good evidence of a relatively slow action of the enzyme (26, 28, 43), one that appears to be minimally an order of magnitude slower than the known action of CBH I on crystalline cellulose (44–46). Therefore, the result in Fig. 4*b* might imply that LPMO and CBH I compete for the same binding (adsorption) sites in the cellulosic substrate used or that only a small amount of cellulose surface degradation by the LPMO is sufficient to achieve significant inhibition of the CBH I. There was a large excess of CBH I (1.54 μM) over LPMO (0.38 μM) present in the reaction, making it somewhat unlikely that LPMO could have outcompeted CBH I from binding to its reaction sites on the cellulose surface. Interestingly, the negative effect of LPMO on D-glucose release was mitigated significantly at longer incubation times, perhaps indicating that substrate material initially less accessible to CBH I when LPMO was present was degraded by CBH I in a later phase of the hydrolysis.

Using nanocrystalline cellulose and Avicel PH-101 as substrates, we observed that, somewhat contrary to results obtained with the sequential assay where synergy between LPMO and CBH I was detectable only to a very small degree (Fig. 4*a*), simultaneous action of the two enzymes gave a substantial stimulation of D-glucose release compared with CBH I acting alone. The synergistic effect was particularly strong when using nanocrystalline cellulose, as seen in Fig. 4*b*. Generally, synergy was increased at long incubation time. With Avicel PH-101 at 5 h, the degree of synergy measured in simultaneous and sequential assays was, however, similar. We are careful in trying to relate cause to effect in respect to enzyme synergy on the nanocrystalline material. Although it is tempting to speculate that LPMO-catalyzed oxidative surface degradation has facilitated the hydrolysis of this highly recalcitrant cellulosic substrate by CBH I, through generation of new free chain ends, for example, one must also consider the possibility of secondary (indirect) effects of the LPMO action. One such effect potentially relevant for hydrolytic degradation of the nanocrystalline cellulose used herein is that the relatively high tendency of the cellulose nanofibrils to form aggregates from colloidal suspension is reduced significantly upon the introduction of additional surface carboxylate groups by LPMO activity. Charged surface groups are known from literature to strongly stabilize colloidal suspensions of nanocrystalline cellulosic material (36, 47, 48).

In summary, synergy between LPMO and CBH I on predominantly crystalline cellulose substrates was demonstrated, in agreement with previous findings in literature (17, 28). Apparent inhibition of CBH I activity on mixed amorphous-crystal-

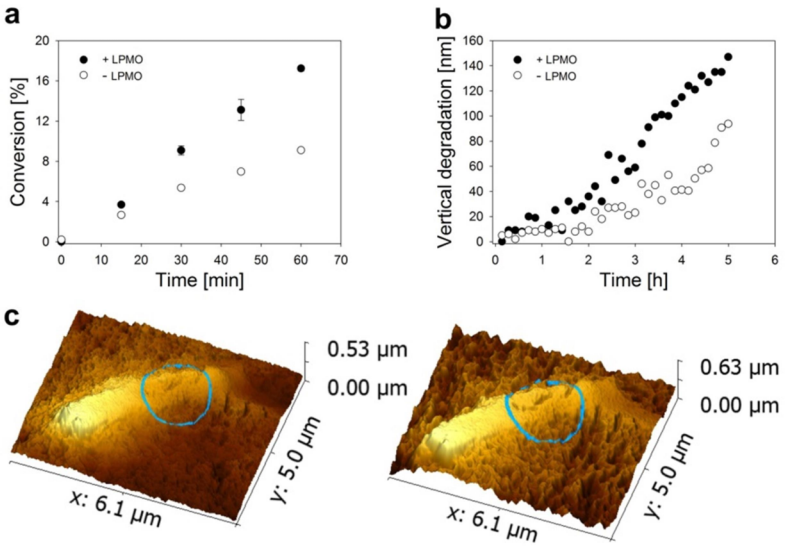

FIGURE 5. **Effect of substrate pretreatment with LPMO on activity of the complete *T. reesei* cellulase for degrading mixed amorphous-crystalline cellulose analyzed in supernatant (*a*) and directly on the cellulose surface (*b* and *c*).** *a*, LPMO (9 mg g^{-1}) was incubated with either cellulose preparation (1 mg ml^{-1}) in 50 mM sodium phosphate buffer, pH 6.0, for 12 h at 25 °C. L-Ascorbic acid (7.5 µM) was present as the reductant. Cellulase (25 mg g^{-1}) supplemented with β-glucosidase (5 mg g^{-1}) was added to the reaction mixture, and incubation was continued at 50 °C for 1 h. The D-glucose concentration was measured enzymatically. It was confirmed using analysis with HPAEC-PAD that D-glucose accounted for ≥99% of the total soluble products present in the supernatant under these conditions. Percent conversion is calculated from the anhydroglucose release. Symbols show measured data, and *error bars* show S.D. from three independent experiments. Pretreatment of substrate by LPMO boost the cellulase activity by a factor of ~2. *b* and *c*, experiments in the AFM liquid cell were performed in exactly the same way as described above, except that the temperature of the hydrolysis reaction was 20 °C. *Panel c* shows AFM height images that depict a representative surface area of the substrate after LPMO treatment immediately before the addition of cellulase (*left image*) and after 5 h of hydrolysis reaction (*right image*). A large cellulose crystallite (*bright color*) is seen embedded in amorphous material (*darker color*). A *blue circle* is used to indicate part of the cellulose surface where structural disruptions occur within highly crystalline material. Comparison of the *left* and *right* image reveals that cellulase activity results in strong volume degradation in regions of amorphous cellulose, causing the overall surface to become completely rugged with time. Additionally, there is clear activity in the highlighted crystalline region of the substrate where fissures become larger and generally more distinct with time. It is important to emphasize that activity in the highly crystalline areas has only been observed when substrate was pretreated with LPMO. *Panel b* shows a quantitative analysis of time-resolved AFM sequences that were used to measure vertical surface degradation by the cellulases. Slowly degraded crystallites such as the one seen in *panel c* were used as reference points. Pretreatment of substrate with LPMO enhanced surface degradation by the cellulases by a factor of ~2. Despite different reaction temperatures used in hydrolysis reactions shown in *panel a* and *panel b*, it is worth noting that synergy factors determined from the measurement of soluble product release and measurement of surface degradation were identical within error limit.

line cellulose by prior action of LPMO (sequential assay; Fig. 4*a*) or by the presence of LPMO (simultaneous assay; Fig. 4*b*) is ascribed to the particular nature and composition of the surface of this cellulosic substrate (Fig. 3), and plausible interpretation of the findings was obtained using real-time AFM imaging combined with kinetic analysis of soluble sugar release.

Synergy between LPMO and the Complete T. reesei Cellulase System—Contrary to the individual hydrolytic enzymes examined, a complete EG- and CBH-containing cellulase system clearly benefited from pretreatment of the substrate with LPMO through substantial (~2-fold) acceleration of surface volume degradation and soluble sugar release, as shown in Fig. 5 *a* and *b*. AFM data reveal furthermore that prior action of the LPMO enabled the cellulases to degrade crystalline surface structures otherwise extremely resistant to enzymatic conversion. Large crystallites like the one shown in Fig. 3*c* remained completely unchanged during prolonged exposure (≥4 h) to cellulase activity alone. After preincubation with LPMO, however, attack of the cellulases promoted strong crystallite surface erosion. This was reflected by material removal and consequent cavity formation predominantly at the sides but also on the top surface of the cellulose crystallite where small cracks grew larger and became clearly more distinct with time (Fig. 5*c*). LPMO synergy with a dynamically interacting system of EG and CBH enzymes could have multiple causes. Interplay between LPMO and CBH I activity was most probably responsible for a unique surface disruption in large crystallite structures (Fig. 3*c*), as already discussed above. Enhancement of cellulose surface degradation in the vertical direction (Fig. 5*b*) was, however, due to the faster loss of amorphous material (and the small fibrils contained in it) from the substrate after pretreatment with LPMO as compared with the untreated substrate. How LPMO becomes involved in the cooperativity among cellulases to degrade mainly amorphous cellulose is an interesting problem. A suggestion supported by the combined evidence from this study and a previous paper of the authors (8) is that LPMO contributes to the degradation of small crystalline fibrils, which are constantly being uncovered on the cellulose surface due to removal of amorphous material (by EG and CBH II) and which in the absence of LPMO are left to degradation by CBH I alone.

In summary, key characteristics of cellulose surface degradation by an Auxiliary Activity family 9-type C1′-oxidizing LPMO from *N. crassa* are revealed, and critical features of surface morphology for LPMO synergy with individual cellulases are rec-

ognized. Dynamic interplay between LPMO and CBH I activity appears to be beneficial for degradation of large, hence highly resistant crystalline substrate structures. The effect of LPMO on cellulose saccharification efficiency by a complete mixture of *T. reesei* cellulases involves substrate morphology as a key parameter. A proposed role of "substrate factors" in determining LPMO-cellulase synergy (4, 5, 12) is strongly substantiated through direct observations from the cellulose surface being degraded.

REFERENCES

1. Chundawat, S. P., Beckham, G. T., Himmel, M. E., and Dale, B. E. (2011) Deconstruction of lignocellulosic biomass to fuels and chemicals. *Annu. Rev. Chem. Biomol. Eng.* **2,** 121–145
2. Kim, I. J., Lee, H. J., Choi, I.-G., and Kim, K. H. (2014) Synergistic proteins for the enhanced enzymatic hydrolysis of cellulose by cellulase. *Appl. Microbiol. Biotechnol.* **98,** 8469–8480
3. Himmel, M. E., Ding, S.-Y., Johnson, D. K., Adney, W. S., Nimlos, M. R., Brady, J. W., and Foust, T. D. (2007) Biomass recalcitrance: engineering plants and enzymes for biofuels production. *Science* **315,** 804–807
4. Harris, P. V., Xu, F., Kreel, N. E., Kang, C., and Fukuyama, S. (2014) New enzyme insights drive advances in commercial ethanol production. *Curr. Opin. Chem. Biol.* **19,** 162–170
5. Hu, J., Arantes, V., Pribowo, A., Gourlay, K., and Saddler, J. N. (2014) Substrate factors that influence the synergistic interaction of AA9 and cellulases during the enzymatic hydrolysis of biomass. *Energy Environ. Sci.* **7,** 2308–2315
6. Fox, J. M., Jess, P., Jambusaria, R. B., Moo, G. M., Liphardt, J., Clark, D. S., and Blanch, H. W. (2013) A single-molecule analysis reveals morphological targets for cellulase synergy. *Nat. Chem. Biol.* **9,** 356–361
7. Levine, S. E., Fox, J. M., Blanch, H. W., and Clark, D. S. (2010) A mechanistic model of the enzymatic hydrolysis of cellulose. *Biotechnol. Bioeng.* **107,** 37–51
8. Ganner, T., Bubner, P., Eibinger, M., Mayrhofer, C., Plank, H., and Nidetzky, B. (2012) Dissecting and reconstructing synergism: *in situ* visualization of cooperativity among cellulases. *J. Biol. Chem.* **287,** 43215–43222
9. Wang, J., Quirk, A., Lipkowski, J., Dutcher, J. R., and Clarke, A. J. (2013) Direct *in situ* observation of synergism between cellulolytic enzymes during the biodegradation of crystalline cellulose fibers. *Langmuir* **29,** 14997–15005
10. Alasepp, K., Borch, K., Cruys-Bagger, N., Badino, S., Jensen, K., Sørensen, T. H., Windahl, M. S., and Westh, P. (2014) *In situ* stability of substrate associated cellulases studied by scanning calorimetry. *Langmuir* **30,** 7134–7142
11. Ahola, S., Turon, X., Osterberg, M., Laine, J., and Rojas, O. J. (2008) Enzymatic hydrolysis of native cellulose nanofibrils and other cellulose model films: effect of surface structure. *Langmuir* **24,** 11592–11599
12. Horn, S. J., Vaaje-Kolstad, G., Westereng, B., and Eijsink, V. G. (2012) Novel enzymes for the degradation of cellulose. *Biotechnol. Biofuels* **5,** 45
13. Vaaje-Kolstad, G., Westereng, B., Horn, S. J., Liu, Z., Zhai, H., Sørlie, M., and Eijsink, V. G. (2010) An oxidative enzyme boosting the enzymatic conversion of recalcitrant polysaccharides. *Science* **330,** 219–222
14. Hemsworth, G. R., Davies, G. J., and Walton, P. H. (2013) Recent insights into copper-containing lytic polysaccharide mono-oxygenases. *Curr. Opin. Struct. Biol.* **23,** 660–668
15. Kim, S., Ståhlberg, J., Sandgren, M., Paton, R. S., and Beckham, G. T. (2014) Quantum mechanical calculations suggest that lytic polysaccharide monooxygenases use a copper-oxyl, oxygen-rebound mechanism. *Proc. Natl. Acad. Sci. U.S.A.* **111,** 149–154
16. Kjaergaard, C. H., Qayyum, M. F., Wong, S. D., Xu, F., Hemsworth, G. R., Walton, D. J., Young, N. A., Davies, G. J., Walton, P. H., Johansen, K. S., Hodgson, K. O., Hedman, B., and Solomon, E. I. (2014) Spectroscopic and computational insight into the activation of O_2 by the mononuclear Cu center in polysaccharide monooxygenases. *Proc. Natl. Acad. Sci. U.S.A.* **111,** 8797–8802
17. Quinlan, R. J., Sweeney, M. D., Lo Leggio, L., Otten, H., Poulsen, J.-C., Johansen, K. S., Krogh, K. B., Jørgensen, C. I., Tovborg, M., Anthonsen, A., Tryfona, T., Walter, C. P., Dupree, P., Xu, F., Davies, G. J., and Walton, P. H. (2011) Insights into the oxidative degradation of cellulose by a copper metalloenzyme that exploits biomass components. *Proc. Natl. Acad. Sci. U.S.A.* **108,** 15079–15084
18. Phillips, C. M., Beeson, W. T., Cate, J. H., and Marletta, M. A. (2011) Cellobiose dehydrogenase and a copper-dependent polysaccharide monooxygenase potentiate cellulose degradation by *Neurospora crassa*. *ACS Chem. Biol.* **6,** 1399–1406
19. Vu, V. V., Beeson, W. T., Phillips, C. M., Cate, J. H., and Marletta, M. A. (2014) Determinants of regioselective hydroxylation in the fungal polysaccharide monooxygenases. *J. Am. Chem. Soc.* **136,** 562–565
20. Forsberg, Z., Mackenzie, A. K., Sørlie, M., Røhr, Å. K., Helland, R., Arvai, A. S., Vaaje-Kolstad, G., and Eijsink, V. G. (2014) Structural and functional characterization of a conserved pair of bacterial cellulose-oxidizing lytic polysaccharide monooxygenases. *Proc. Natl. Acad. Sci.* **111,** 8446–8451
21. Wu, M., Beckham, G. T., Larsson, A. M., Ishida, T., Kim, S., Payne, C. M., Himmel, M. E., Crowley, M. F., Horn, S. J., Westereng, B., Igarashi, K., Samejima, M., Ståhlberg, J., Eijsink, V. G., and Sandgren, M. (2013) Crystal structure and computational characterization of the lytic polysaccharide monooxygenase GH61D from the Basidiomycota fungus *Phanerochaete chrysosporium*. *J. Biol. Chem.* **288,** 12828–12839
22. Hemsworth, G. R., Henrissat, B., Davies, G. J., and Walton, P. H. (2014) Discovery and characterization of a new family of lytic polysaccharide monooxygenases. *Nat. Chem. Biol.* **10,** 122–126
23. Li, X., Beeson, W. T., 4th, Phillips, C. M., Marletta, M. A., and Cate, J. H. (2012) Structural basis for substrate targeting and catalysis by fungal polysaccharide monooxygenases. *Structure* **20,** 1051–1061
24. Dimarogona, M., Topakas, E., and Christakopoulos, P. (2013) Recalcitrant polysaccharide degradation by novel oxidative biocatalysts. *Appl. Microbiol. Biotechnol.* **97,** 8455–8465
25. Agger, J. W., Isaksen, T., Várnai, A., Vidal-Melgosa, S., Willats, W. G., Ludwig, R., Horn, S. J., Eijsink, V. G., and Westereng, B. (2014) Discovery of LPMO activity on hemicelluloses shows the importance of oxidative processes in plant cell wall degradation. *Proc. Natl. Acad. Sci. U.S.A.* **111,** 6287–6292
26. Harris, P. V., Welner, D., McFarland, K. C., Re, E., Navarro Poulsen, J.-C., Brown, K., Salbo, R., Ding, H., Vlasenko, E., Merino, S., Xu, F., Cherry, J., Larsen, S., and Lo Leggio, L. (2010) Stimulation of lignocellulosic biomass hydrolysis by proteins of glycoside hydrolase family 61: structure and function of a large, enigmatic family. *Biochemistry* **49,** 3305–3316
27. Westereng, B., Ishida, T., Vaaje-Kolstad, G., Wu, M., Eijsink, V. G., Igarashi, K., Samejima, M., Ståhlberg, J., Horn, S. J., and Sandgren, M. (2011) The putative endoglucanase PcGH61D from *Phanerochaete chrysosporium* is a metal-dependent oxidative enzyme that cleaves cellulose. *PLoS ONE* **6,** e27807
28. Langston, J. A., Shaghasi, T., Abbate, E., Xu, F., Vlasenko, E., and Sweeney, M. D. (2011) Oxidoreductive cellulose depolymerization by the enzymes cellobiose dehydrogenase and glycoside hydrolase 61. *Appl. Environ. Microbiol.* **77,** 7007–7015
29. Kittl, R., Kracher, D., Burgstaller, D., Haltrich, D., and Ludwig, R. (2012) Production of four *Neurospora crassa* lytic polysaccharide monooxygenases in *Pichia pastoris* monitored by a fluorimetric assay. *Biotechnol. Biofuels* **5,** 79
30. Eibinger, M., Bubner, P., Ganner, T., Plank, H., and Nidetzky, B. (2014) Surface structural dynamics of enzymatic cellulose degradation, revealed by combined kinetic and atomic force microscopy studies. *FEBS J.* **281,** 275–290
31. Novy, V., Krahulec, S., Wegleiter, M., Müller, G., Longus, K., Klimacek, M., and Nidetzky, B. (2014) Process intensification through microbial strain evolution: mixed glucose-xylose fermentation in wheat straw hydrolyzates by three generations of recombinant *Saccharomyces cerevisiae*. *Biotechnol. Biofuels* **7,** 49
32. Medve, J., Lee, D., and Tjerneld, F. (1998) Ion-exchange chromatographic purification and quantitative analysis of *Trichoderma reesei* cellulases cellobiohydrolase I, II and endoglucanase II by fast protein liquid chromatography. *J. Chromatogr. A* **808,** 153–165
33. Mellitzer, A., Weis, R., Glieder, A., and Flicker, K. (2012) Expression of

lignocellulolytic enzymes in *Pichia pastoris*. *Microb. Cell Fact.* **11,** 61
34. Bubner, P., Dohr, J., Plank, H., Mayrhofer, C., and Nidetzky, B. (2012) Cellulases dig deep: *in situ* observation of the mesoscopic structural dynamics of enzymatic cellulose degradation. *J. Biol. Chem.* **287,** 2759–2765
35. Ganner, T., Aschl, T., Eibinger, M., Bubner, P., Meingast, A., Chernev, B., Mayrhofer, C., Nidetzky, B., and Plank, H. (2014) Tunable mixed amorphous: crystalline cellulose substrates (MACS) for dynamic degradation studies by atomic force microscopy in liquid environments. *Cellulose* **21,** 3927–3939
36. Lu, P., and Hsieh, Y.-L. (2010) Preparation and properties of cellulose nanocrystals: rods, spheres, and network. *Carbohydr. Polym.* **82,** 329–336
37. Wildberger, P., Luley-Goedl, C., and Nidetzky, B. (2011) Aromatic interactions at the catalytic subsite of sucrose phosphorylase: their roles in enzymatic glucosyl transfer probed with Phe-52 → Ala and Phe-52 → Asn mutants. *FEBS Lett.* **585,** 499–504
38. Rödiger, S., Ruhland, M., Schmidt, C., Schröder, C., Grossmann, K., Böhm, A., Nitschke, J., Berger, I., Schimke, I., and Schierack, P. (2011) Fluorescence dye adsorption assay to quantify carboxyl groups on the surface of poly (methyl methacrylate) microbeads. *Anal. Chem.* **83,** 3379–3385
39. Cannella, D., Hsieh, C.-W., Felby, C., and Jørgensen, H. (2012) Production and effect of aldonic acids during enzymatic hydrolysis of lignocellulose at high dry matter content. *Biotechnol. Biofuels* **5,** 26
40. Fox, J. M., Levine, S. E., Clark, D. S., and Blanch, H. W. (2012) Initial- and processive-cut products reveal cellobiohydrolase rate limitations and the role of companion enzymes. *Biochemistry* **51,** 442–452
41. Bubner, P., Plank, H., and Nidetzky, B. (2013) Visualizing cellulase activity. *Biotechnol. Bioeng.* **110,** 1529–1549
42. Hall, M., Bansal, P., Lee, J. H., Realff, M. J., and Bommarius, A. S. (2010) Cellulose crystallinity: a key predictor of the enzymatic hydrolysis rate. *FEBS J.* **277,** 1571–1582
43. Loose, J. S., Forsberg, Z., Fraaije, M. W., Eijsink, V. G., and Vaaje-Kolstad, G. (2014) A rapid quantitative activity assay shows that the *Vibrio cholerae* colonization factor GbpA is an active lytic polysaccharide monooxygenase. *FEBS Lett.* **588,** 3435–3440
44. Cruys-Bagger, N., Tatsumi, H., Ren, G. R., Borch, K., and Westh, P. (2013) Transient kinetics and rate-limiting steps for the processive cellobiohydrolase Cel7A: effects of substrate structure and carbohydrate binding domain. *Biochemistry* **52,** 8938–8948
45. Jalak, J., and Väljamäe, P. (2010) Mechanism of initial rapid rate retardation in cellobiohydrolase catalyzed cellulose hydrolysis. *Biotechnol. Bioeng.* **106,** 871–883
46. Igarashi, K., Uchihashi, T., Koivula, A., Wada, M., Kimura, S., Okamoto, T., Penttilä, M., Ando, T., and Samejima, M. (2011) Traffic jams reduce hydrolytic efficiency of cellulase on cellulose surface. *Science* **333,** 1279–1282
47. Beck-Candanedo, S., Roman, M., and Gray, D. G. (2005) Effect of reaction conditions on the properties and behavior of wood cellulose nanocrystal suspensions. *Biomacromolecules* **6,** 1048–1054
48. Araki, J., Wada, M., Kuga, S., and Okano, T. (1998) Flow properties of microcrystalline cellulose suspension prepared by acid treatment of native cellulose. *Colloids Surf. A Physicochem. Eng. Asp.* **142,** 75–82

Cellular automata modeling depicts degradation of cellulosic material by a cellulase system with single-molecule resolution

Eibinger *et al. Biotechnol Biofuels (2016) 9:56*
DOI 10.1186/s13068-016-0463-8

Biotechnology for Biofuels

RESEARCH

Open Access

Cellular automata modeling depicts degradation of cellulosic material by a cellulase system with single-molecule resolution

Manuel Eibinger[1†], Thomas Zahel[1†], Thomas Ganner[2], Harald Plank[2,3] and Bernd Nidetzky[1,4*]

Abstract

Background: Enzymatic hydrolysis of cellulose involves the spatiotemporally correlated action of distinct polysaccharide chain cleaving activities confined to the surface of an insoluble substrate. Because cellulases differ in preference for attacking crystalline compared to amorphous cellulose, the spatial distribution of structural order across the cellulose surface imposes additional constraints on the dynamic interplay between the enzymes. Reconstruction of total system behavior from single-molecule activity parameters is a longstanding key goal in the field.

Results: We have developed a stochastic, cellular automata-based modeling approach to describe degradation of cellulosic material by a cellulase system at single-molecule resolution. Substrate morphology was modeled to represent the amorphous and crystalline phases as well as the different spatial orientations of the polysaccharide chains. The enzyme system model consisted of an internally chain-cleaving endoglucanase (EG) as well as two processively acting, reducing and non-reducing chain end-cleaving cellobiohydrolases (CBHs). Substrate preference (amorphous: EG, CBH II; crystalline: CBH I) and characteristic frequencies for chain cleavage, processive movement, and dissociation were assigned from biochemical data. Once adsorbed, enzymes were allowed to reach surface-exposed substrate sites through "random-walk" lateral diffusion or processive motion. Simulations revealed that slow dissociation of processive enzymes at obstacles obstructing further movement resulted in local jamming of the cellulases, with consequent delay in the degradation of the surface area affected. Exploiting validation against evidence from atomic force microscopy imaging as a unique opportunity opened up by the modeling approach, we show that spatiotemporal characteristics of cellulose surface degradation by the system of synergizing cellulases were reproduced quantitatively at the nanometer resolution of the experimental data. This in turn gave useful prediction of the soluble sugar release rate.

Conclusions: Salient dynamic features of cellulose surface degradation by different cellulases acting in synergy were reproduced in simulations in good agreement with evidence from high-resolution visualization experiments. Due to the single-molecule resolution of the modeling approach, the utility of the presented model lies not only in predicting system behavior but also in elucidating inherently complex (e.g., stochastic) phenomena involved in enzymatic cellulose degradation. Thus, it creates synergy with experiment to advance the mechanistic understanding for improved application.

Keywords: Cellulose, Cellulase, System-level modeling, Cellular automata, AFM imaging, Hydrolysis, Surface degradation

*Correspondence: bernd.nidetzky@tugraz.at
†Manuel Eibinger and Thomas Zahel contributed equally to this work
[1] Institute of Biotechnology and Biochemical Engineering, Graz University of Technology, NAWI Graz, Petersgasse 12, 8010 Graz, Austria
Full list of author information is available at the end of the article

Background

Cellulose is a water-insoluble linear polysaccharide composed of several hundred or more β-1,4-linked D-glucosyl units. Its depolymerization by hydrolytic enzymes occurs through repeated endo- and exo-type cleavages inside of and from the ends of the cellulose chain, respectively [1, 2]. Regarding only a single chain, therefore, the enzymatic hydrolysis might appear as a fairly simple transformation. However, from a system-level viewpoint, degradation of cellulosic material represents an extremely complicated process [1–7]. Its kinetics involves an array of heavily entangled, enzyme- and substrate-related complexities appearing at different length scales in dependence of time and conversion [5, 8–14]. Despite much progress made in delineating function of individual elements [1–3, 15–22], coherent description of the degradation process as a whole proved elusive. Bottom-up reconstruction of total cellulose/cellulase system behavior therefore constitutes an increasingly important research aim of high fundamental but also practical significance.

Core problem of enzymatic cellulose degradation in the way analyzed herein is to depict the spatiotemporally correlated action of distinct polysaccharide chain-cleaving cellulase activities confined to the dynamically evolving surface of the insoluble substrate. Progress in this effort is restrained severely by difficulties in unraveling interfacial enzyme catalysis experimentally. The problem in general is exacerbated in the case of the cellulose–cellulase system due to the fact that the actual substrate is a solid material of typically high morphological irregularity [1, 3, 9]. Depending on cellulose source and isolation procedure, there is variation and uneven distribution in the spatial arrangement of the polysaccharide chains [1, 5, 9]. Parts of the cellulose that feature disorder in position, direction, or orientation of the chains therefore alternate with highly organized, crystalline material. Most of the cellulose chains are initially not accessible to the enzymes due to the surrounding material [5]. Individual cellulases differ in preference for degrading crystalline compared to amorphous cellulose [1, 2, 7, 14]. Crystalline cellulose is degraded primarily through chain ablation promoted by exo-cellulases acting in a processive manner (Scheme 1) [16, 19]. Degradation of amorphous material additionally involves internal disruptions of cellulose chains by endo-cellulases (Scheme 1) [13, 14]. The spatial distribution of structural order across the cellulose surface therefore imposes constraints on the attack by different cellulases and also on the dynamic interplay between the enzymes. What results therefore is a highly uneven distribution in the local rates of removal of surface material by lateral and vertical degradation [14]. Morphology and also shape of the cellulose surface thus undergo large spatiotemporal changes as the conversion makes progress [14, 15, 23], with consequent reciprocal action on the chain fragmentation activity by the adsorbed enzymes. While providing a convenient measure of the overall cellulose degradation efficiency, release of soluble sugars is a frequently used but highly convoluted parameter that does not support direct inference to cellulase action on the evolving cellulose surface. Owing to limitations in resolving interfacial processes by experiment, mathematical modeling has traditionally played a leading role in developing the mechanistic thinking of cellulose degradation [5, 8–12, 24–35].

Paradigmatic approach of modeling enzymatic cellulose degradation involves development of a set of differential equations describing the relevant physical and chemical steps of the reaction (e.g., cellulase adsorption, chain fragmentation) under the constraints of mass balance [5, 11]. Despite notable recent progress [11, 12, 25, 26], mathematical representation of the substrate's morphology and the change thereof with time and conversion in mutual dependency on the chain fragmentation activity of the locally adsorbed cellulases is at the very limit of what current mass balance-based models are capable of delivering. Spatial heterogeneities in cellulose morphology can only be implemented in the form of distribution functions [12, 25, 26], but not explicitly for individual substrate samples. Model validation including determination of unknown parameters is therefore limited to comparison with lumped experimental data that lack spatial resolution.

Cellular automata (CA) models present an interesting alternative by virtue of their ability to literally depict the spatiotemporal behavior of complex systems across length scales [36]. CA models constitute mathematical systems constructed from many small entities, each simple and obeying preassigned rules, but together capable of complex performance. Evidence from CA modeling is suitable for visual inspection, and what is

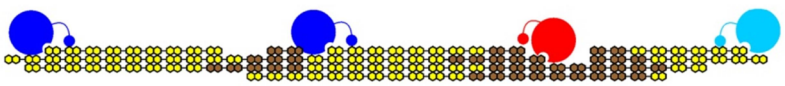

Scheme 1 A typical set of fungal cellulases acting on mixed amorphous–crystalline cellulose. Chain end-cleaving cellobiohydrolases (CBH I *blue*; CBH II *cyan*) and internally chain-cleaving endoglucanases (*red*) catalyze the hydrolysis of crystalline (*yellow*) and amorphous (*brown*) cellulosic material

most important, it offers the unique opportunity to be validated against time and laterally resolved data from advanced imaging analysis. Visualization by real-time AFM [13, 14, 16, 19] and high-resolution fluorescence spectroscopy [6, 7, 17, 18] has recently provided unprecedented insight into the dynamics of cellulose degradation at different length scales down to single-enzyme resolution. Therefore, this emphasizes the need but also the potential of a modeling approach optimally aligned to the capabilities of the emerging visualization techniques. CA modeling has already been applied to the study of enzymatic hydrolysis of cellulose in a few earlier papers [30, 31, 36–39], but the important link to experimental visualization as a validation tool has not been established.

Using CA-based formalism, comprehensive system-level modeling of cellulose degradation by cellulases is reported. The herein developed substrate model allowed for realistic representation of amorphous–crystalline cellulosic material previously applied by this group of authors in AFM imaging experiments [14]. The enzyme model incorporated the three main activities of non-complexed fungal cellulase systems: two processively chain-end cleaving cellobiohydrolases (CBHs) acting from the reducing (CBH I) and non-reducing (CBH II) end of the cellulose chain, respectively; and an internally chain cleaving endoglucanase (EG). CBH I was known from experiment to attack crystalline material, whereas CBH II and EG degraded amorphous substrate parts [14]. We show in simulations, here for the first time, that observable characteristics of cellulose surface degradation by the synergizing set of cellulases (e.g., local surface height degradation rates; surface morphology evolution) were reproduced in useful quantitative agreement with the experiment [14]. Interestingly, the simulations also reproduced a counterintuitive experimental finding: once uncovered from obstructing amorphous material, crystalline nanofibrils were degraded significantly faster than supposedly less resistant amorphous cellulose in their surrounding [14]. Simulations also revealed that slow release of cellulose chains by CBH II resulted in pronounced jamming of processively acting enzymes at the interface of the amorphous and crystalline phases. In addition to the intrinsically slow kinetics of CBH I action [20, 35, 40], this was clear additional factor of rate limitation in the degradation of crystalline cellulose as simulated. The model might aid in the elucidation of inherently complex phenomena of cellulose degradation and thus create synergy with experiment to advance the mechanistic understanding as well as the application.

Results and discussion

A CA model of mixed amorphous–crystalline cellulose

Figure 1 shows a two-dimensional representation of the three-dimensional matrix model of the cellulosic substrate. Cellulose chains were coarse-grained with the dimer cellobiose as their smallest unit (assumed length: 1 nm). Similar approaches of modeling of cellulose chains have been described before [30, 31, 36, 37]. In the matrix system used, the crystalline and amorphous phases were identified through tokens 1 and 2, respectively, assigned to each cellobiose molecule comprised in the cellulose. Token 0 was used to indicate the liquid bulk phase. A secondary matrix assigned the cellulose chain orientation in space, as illustrated in Fig. 1. Other structural characteristics of the cellulose were assigned using additional matrices, as follows. Crystalline nanofibrils were modeled as cuboids (length: 100 nm; width/height: 8–16 nm) assembled from orientationally and directionally ordered cellulose chains (Fig. 2a). Their size corresponded approximately to nanofibrils of the real

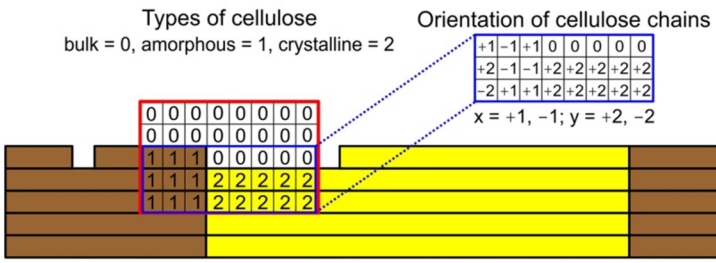

Fig. 1 CA model of mixed amorphous–crystalline cellulose. Cellulose material is modeled as a large 3D matrix (depicted here in a schematic 2D *y–z* view) composed of *substrate automata* that represent cellobiose units. Tokens '1' and '2' are used to indicate *cellobiose units* in amorphous and crystalline material environment. Token '0' is used to indicate *bulk molecules*. The corresponding matrix is framed *red*. Further properties of the cellulose chains such as the orientation in space and the location of the hydrophobic faces are assigned through additional matrices of identical size, as shown in the matrices framed in *blue*. Each cellobiose unit in the cellulose model is identified unambiguously through the positions in all substrate matrices

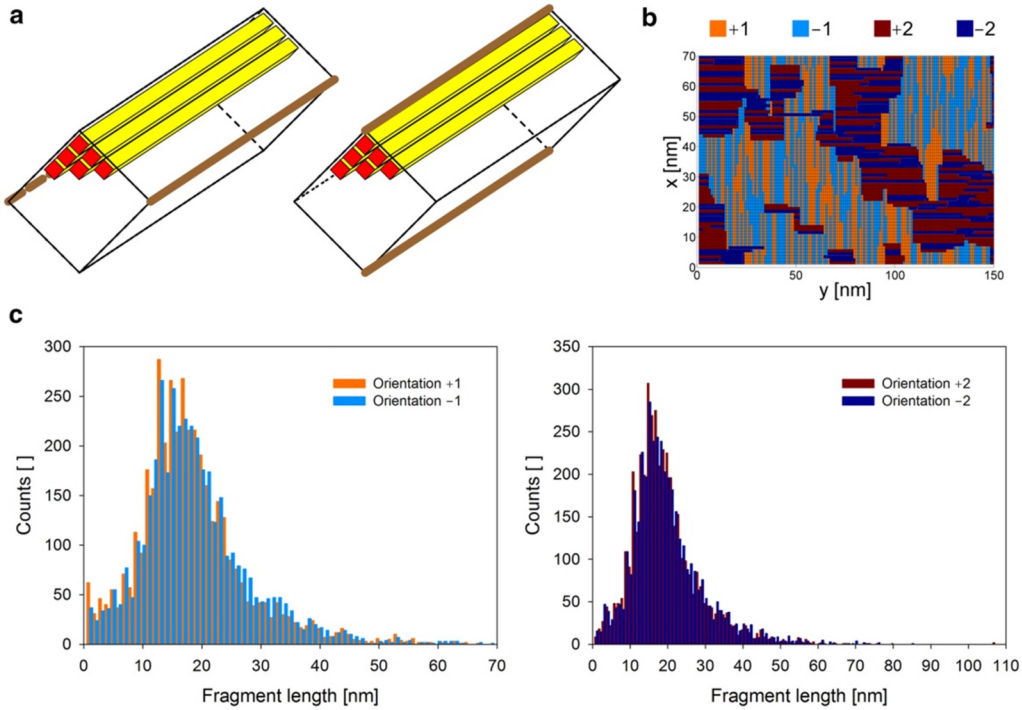

Fig. 2 Structure of crystalline (**a**) and amorphous (**b**) cellulose as implemented in the CA model. **a** Cellulose nanocrystals were modeled in analogy to the natural elementary fibril of cellulose allomorph I and were composed of up to 144 cellulose chains (16 nm crystals). Their length was constant at 100 nm equaling 100 cellobiose units per chain, and the width/height varied between 8 and 16 nm. *Yellow bars* show the cellulose chains with their reducing end indicated in *orange*. Shown in *brown* are the so-called hydrophobic faces of the cellulose nanocrystal which is where attack by CBH I takes place. Two orientations of the nanocrystal within amorphous material are considered whereby the crystal's hydrophobic faces are aligned horizontally (*left*) or vertically (*right*). **b** A random positioning algorithm (Additional file 1) was used to create amorphous cellulose layers with a final mean fragment length of 18 cellobiose units. The figure shows an exemplary amorphous plane. It also shows how amorphous chains with varying orientation are combined in one plane. Amorphous chains can be oriented in *x* or *y* direction in one *z*-plane. Tokens '±1' and '±2' are used within the amorphous chain orientation matrix to distinguish *x* and *y* direction, respectively. The internal direction of an amorphous chain is indicated by an algebraic sign ('+' or '−') and relative to the origin of the *z*-plane (0, 0). A chain oriented from the reducing to the non-reducing end with respect to the origin has a positive sign ('+') and a vice versa oriented chain is indicated by a negative sign ('−'). Amorphous cellulose material was obtained by stacking multiple layers of amorphous cellulose on top of each other. **c** The distribution pattern for the cellulose chain lengths in 30 independent planes making up the amorphous material is shown for *x*- (*left panel*) and *y*-oriented (*right panel*) cellulose chains demonstrating the essentially random distribution of the chains in all orientations

cellulose substrate used in experiments [41]. The internal chain organization was that of cellulose allomorph I that was known to account chiefly for the crystalline phases in the experimental substrate [41]. Figure 2a additionally shows the so-called hydrophobic faces of the nanofibril, indicating the crystalline surfaces where enzymatic attack takes place [19, 42]. A similar modeling concept was used recently to describe the orientation and accessibility of the hydrophobic faces in cellulose nanofibrils [30, 43]. Note: the possibility that individual cellulose chains of the hydrophobic face differ in "decrystallization energy" and therefore in accessibility to enzymatic attack, as has been suggested in in-depth modeling studies of the crystalline cellulose structure [32, 44], was not considered in our model. This is not an intrinsic limitation of the coarse-grained modeling approach used here. Individual crystalline cellulose chains on the hydrophobic face could be assigned distinct enzyme accessibility properties. However, in view of the focus of current study description of the crystalline phase down to the level of the individual chains' "energy" was considered to be not necessary.

Amorphous cellulose has no unique structure by definition [45], and little is known from experiment about its structural organization. Any model of amorphous cellulose is therefore hypothetical. The idea pursued in this study was to represent the amorphous substrate as a material consisting of completely randomly organized cellulose chains. We have no way of knowing, however, how well this model represents the real amorphous cellulose used in the experiment. Algorithm was developed to create randomized orientation of fragments of cellulose chains in space (Fig. 2b). Fragments with varying length, mimicking a Gaussian distribution, were generated and placed in a 2D plane with random orientation in x or y direction. The internal direction of cellulose chains, from the reducing to the non-reducing end or from the non-reducing to the reducing end, was also considered and implemented in the model (Fig. 2b). A mean fragment length of 18 cellobiose units was obtained, corresponding well to the mean free path length reported from amorphous cellulose [46]. An example of how an amorphous cellulose plane was generated is shown in Additional file 1. The modeled cellulose chain length was 150 cellobioses, representing the estimated degree of polymerization of the experimental substrate derived from microcrystalline cellulose (Avicel) [37, 47, 48]. Figure 2c shows that chain fragment orientations were normally distributed across different planes analyzed, confirming a completely random structural organization of the modeled amorphous material. Each field of amorphous cellulose therefore has a probability of 2/150 to be a free chain end. The free chain ends comprise equal portions of reducing and non-reducing chain-end types. We are well aware of the fact that our cellulose model presents a strong simplification. Note, therefore, that a more detailed distinction and further diversification of cellulosic material would be possible in the model. One way of achieving this would be through a more sophisticated representation of the substrate structure and by introducing multiple complexation rate constants [11, 30, 49], which are dependent on the organization of the cellulosic substrate and the type of attacking enzyme. However, comparing the physical dimensions of our CA model (see the "Methods" section) and the estimated degree of polymerization of cellulose (as stated above), it is not likely that we have multiple cellulosic phases present at the same time. Thus, we decided to reduce the complexity of the substrate to a two-phase substrate model (crystalline and amorphous).

Basic CA model of the cellulases and their action on the cellulose surface

All cellulases were modeled as cubes (while interacting with cellulose) and as spheres (while interacting with other enzymes), as shown in Fig. 3. The edge length or diameter was 5 nm so that the modeled enzyme size was approximately that of the catalytic modules of cellulases from the fungus *Hypocrea jecorina* (formerly *Trichoderma reesei*) [2, 50]. In reality, each catalytic module is flexibly linked to a cellulose-binding module of considerably smaller size (~2 nm), as depicted in Scheme 1. By consolidating the two-module structure–function principle of cellulases into a single cellular automaton, the enzyme model was computationally efficient. We emphasize that the aim of the work was to describe the behavior of several hundreds of cellulases acting together, not that of a single enzyme. Model refinement to account for a two-module cellulase was therefore considered unnecessary. Based on the assumed footprint of a bound cellulase, requirements for accommodating the enzymes on the cellulose surface are depicted in Fig. 3a. The light green enzyme's center is set within a distance of three water or cellobiose units to a randomly chosen point on the cellulosic surface (indicated in dark green). For enzyme placement to be allowed the adsorption footprint on the surface must be completely flat, that is, it must not contain any protruding cellobiose units. Furthermore, distance rules apply concerning the presence of other enzymes. A sphere with a diameter of 5.75 nm around the enzyme's center point is calculated and must be available to the enzyme to be placed successfully. Thus, the attack of an enzyme on a cellobiose unit covered by another enzyme is avoided. For the initial adsorption, enzymes are positioned on the surface one after the other, starting with the set of EG molecules followed by the CBH I set and then the CBH II set. Note that enzyme placement of the cellulose is random not only regarding surface position but also surface material (amorphous, crystalline) and chain orientation.

In the current model focusing on *surface-bound* characteristics of cellulase action, enzyme adsorption was simplified to a quasi-irreversible process. It comprised a completely random positioning on the cellulose surface of a defined number of enzymes of each cellulase type, as will be described under *Programming, Simulation, and Data Processing* in more detail. Once positioned, enzymes ultimately remained surface bound over the entire time course of the simulation. This was effectuated by an immediate and again random re-positioning on the surface of any cellulase "released" from the surface.

This was modeled as a new round of random positioning on the cellulose surface of all enzymes except the ones being in "complexed" state, that is, the CBH acting processively on polysaccharide chains [22, 51]. Surface diffusion of the cellulases could be assumed from experimental evidence [18, 52, 53] to be at least 100 times faster than the overall process of chain cleavage (k_{cat}). For each

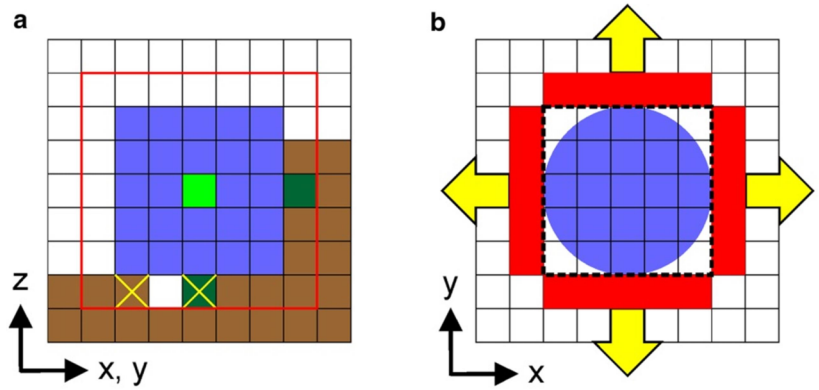

Fig. 3 The CA model of the cellulases interacting with and degrading the cellulose surface. **a** The footprint of the enzyme is shown in *blue* and the center of the enzyme is shown in *light green*. The center of an enzyme is set within a distance of three water or cellobiose units to a randomly chosen point on the cellulosic surface (one of two *dark green squares*). Enzymes screen for substrate sites in their immediate surrounding (*red box*). For EG, any cellobiose (*brown*) of amorphous cellulose is a substrate, whereas for the cellobiohydrolases, only cellobioses lacking a neighbor cellobiose (indicated with a *yellow cross*) are substrates. **b** Top view of a CBH molecule in processive motion is shown. The wall in front of the enzyme in moving direction (*red rectangle*) is checked for structural obstacles (cellobiose molecules). The enzyme is represented against other enzymes as a sphere (*blue circle*) to calculate collision events. If neither substrate nor enzyme obstacles are present, the cellobiohydrolase moves along the chain, cleaving one cellobiose per $1/k_{cat}$ time interval

time span equal to 0.07 s ($0.25/k_{cat}$ CBH I), therefore, the non-complexed enzymes were made to undergo randomization of their distribution on the surface. We considered that cellulase adsorption might directly target distinct substrate morphologies [54–56]. However, due to the relatively small surface areas (~1×10^4 nm^2) analyzed in our simulations, diffusional randomization superseded completely possible effects of enzyme specificity during cellulase adsorption to the cellulose surface. Computational rules for enzyme release were different for EG and the processively acting CBHs.

Based on their individual substrate requirements, the bound cellulases began searching for accessible cellulose chain types in immediate adjacency to them, as shown in Fig. 3a. For EG, any cellobiose of amorphous cellulose is a substrate, whereas for the CBH only cellobioses lacking a neighbor cellobiose are substrates (Fig. 3a). Cellobiohydrolase furthermore evaluates the free cellobioses for material property (crystalline, amorphous) and chain end type (non-reducing, reducing) to distinguish substrate sites for CBH I and CBH II. The enzymes thus became active in chain cleavage (modeled as replacement of a cellobiose by a water unit). The EG is then "released," enabling it to become randomly re-positioned on the cellulose surface. The CBH screens the possibility to enter into the processive mode of action and, if possible, they remain "complexed" (attached to a cellulose chain) which prevents them from being redistributed on the surface. Once complexed, the CBH performed multiple cleavages on a single cellulose chain. Cellobiose was substituted by water on each cleavage, which occurred with time constant of $1/k_{cat}$. Processive action continued until an obstacle or chain end was encountered or the characteristic time of decomplexation ($1/k_{off}$) had elapsed. Note that each CBH has an internal "stopwatch" to monitor if $1/k_{off}$ has already expired. The "stopwatch" is started once processive action is initialized and only reset if the enzyme is released from the surface. Structural obstacles are perceived in moving direction in a wall located in front of the enzyme (Fig. 3b). Cellobiohydrolases obstructed in their processive action due to obstacles encountered are required to wait a time corresponding to $1/k_{off}$ to switch back to the non-complexed (redistribution-able) state. Alternatively, blocked enzymes are allowed to continue processive action if the obstacle is removed. To account for a certain flexibility of both the enzymes [57, 58] and the threaded cellulose chain [59], the minimum size of a substrate obstacle obstructing processive motion of the CBH is defined as three cellobiose units.

Table 1 summarizes the k_{cat} and k_{off} values used in the final CA model of the cellulases. For CBH I, the k_{cat} [16] and the k_{off} [46] were taken from literature. The k_{cat} for CBH II and EG as well as the k_{off} for CBH II were not known and therefore used as adjustable parameters in a comparison of simulation results with experimental data (see "Results and discussion" section).

Table 1 Enzyme kinetic parameters used in the CA model of cellulase action

CA model parameter				
Enzyme	**Type of cellulose material attacked**	**Type of chain cleavage**	k^{a}_{cat} [s^{-1}]	k^{b}_{off} [s^{-1}]
CBH I	Crystalline	Exo	3.6[c]	0.7×10^{-3}[d]
CBH II	Amorphous	Exo	0.7[e]	0.7×10^{-2}[e]
		Endo	0.03	–
EG	Amorphous	Endo	1.2[e]	–

[a] The k_{cat} is the rate constant for polysaccharide cleavage in exo-mode, endo-mode, or both

[b] The k_{off} is the rate constant of chain dissociation for a cellobiohydrolase acting in processive chain cleavage mode; its reciprocal ($1/k_{off}$) is the time the cellobiohydrolase remains bound to the cellulose chain in such a mode of action event; an enzyme having $k_{off} = 0$ is perfectly processive, that is, it does not release the chain until it has reached its end. Therefore, in the case an obstacle is encountered during processive chain cleavage, this enzyme remains trapped until the obstacle is removed. Note that a cellobiohydrolase having $k_{off} > 0$ is not an endoglucanase. It is an exo-acting enzyme that shows reduced processivity and is less likely to become trapped by obstacles to processive action

[c] Reference [16]

[d] Reference [46]

[e] Estimated on comparing results of CA modeling to experimental data of AFM imaging

Each chain cleavage by EG had to be modeled so that it produced both a reducing and a non-reducing chain end. Under framework conditions of the coarse-grained CA model of the cellulose chain (Fig. 1), it was convenient and also computationally efficient to have EG release one cellobiose for each cleavage performed, thereby creating the two types of chain end as required. In reality, according to the widely held view of EG action [1, 11, 60], this may not occur as the attack of EG on longer cellulose chains is thought to take place primarily by chain fission. However, we note that EG releases cellobiose in the experiment already at very early stages of the reaction which is difficult to explain by chain fission only. Moreover, EG might even exhibit a small degree of processivity as shown by Väljamäe and coworkers [46]. We therefore decided not to consider modeling of the EG as a pure chain-fission enzyme for mainly two reasons. First of all, it is not clear how such an enzyme can produce soluble sugars unless additional assumptions about the release of oligosaccharides from the solid material into solution are made. Furthermore, the additional algorithms needed to evaluate the length and the solubility of every surface-exposed cellulose chain in the system in each computational step are highly time-consuming. Secondly, the EG will not produce vertical degradation of the cellulose surface in the absence of further model assumptions and computational steps. In addition, we considered that random chain fragmentation by the EG ultimately results in the formation of cellobiose anyway. A possible error regarding the formation of soluble cellobiose was therefore small and the model of EG action was still considered suitable. The time course of cellobiose release was determined by calculating after each 7.0 s (i.e., a time span corresponding to 25 k_{cat} events of CBH I) the residual amount of all cellobiose units in the CA model and subtracting it from the initial amount of cellobiose units. We show that the time resolution of the simulated data was adequate and a more frequent readout of the residual amount of cellobiose units was therefore considered unnecessary.

Degradation of amorphous cellulose by EG and CBH II

On incubation of the cellulose substrate with native *H. jecorina* cellulase or cellulase reconstituted from purified enzymes, amorphous material was removed from the surface with an average vertical degradation rate (V_z) of 0.7 (±0.1) nm/min, as shown by AFM measurements [14]. According to our CA model supported from experiment [13, 14], attack on the amorphous cellulose is performed solely by EG and CBH II, whereas CBH I is not active on this material. We are sensible to the fact that strict categorization of the cellulases according to activity on amorphous or crystalline cellulose not only presents a strong simplification of what may be their true interaction with the insoluble substrate but is also at variance with some earlier observations made with these enzymes. CBH I was reported to be active on amorphous cellulose [21, 46] and CBH II showed degradation of crystalline cellulose [2, 61]. It should be noted therefore that first of all we refer to our own findings made with a special cellulosic substrate preparation [13, 14, 41]. Other celluloses used in earlier studies of cellulase specificity were different. Secondly, however, speaking of a purely amorphous or crystalline cellulose is difficult which leads to the problem of interpreting the measurements of soluble sugar release in terms of amorphous or crystalline material in the substrate having become degraded by the cellulase examined. The substrate used here was well characterized [13, 14,

41] and its degradation by the individual cellulases was measured not only by saccharification but also directly on the solid surface [13, 14]. Thirdly, for the purpose of modeling a clear-cut distinction between the different enzyme activities was considered useful. Finally, we believe that in the less strict sense, considering the effort in the modeling to represent the *main characteristic* properties of the individual cellulases, the CA models of CBH I, CBH II, and EG used here will not be controversial.

We started our modeling approach, therefore, by examining the actions of EG and CBH II, alone or in combination, on amorphous cellulose. Task of the modeling in particular was to determine the unknown k_{cat} values of the two enzymes. The cellulose substrate was modeled with a nanocrystal (16 × 100 × 16 nm) completely buried in amorphous material.

Simulations of individual enzyme reactions revealed that the V_z of EG was solely limited by the enzyme's k_{cat}. The V_z was independent of the number of chain ends accessible on the surface. We also noted and describe later that V_z of EG was unaffected by obstacles on the surface such as stuck CBH II molecules. CBH II alone, by contrast, showed low efficiency of surface material degradation. Its modeled V_z was hardly significant. This was explicable from the modeled action of the enzyme as a perfect exo-cellulase and, consequently, the absolute dependence of its activity on the availability of accessible non-reducing chain ends in the substrate. Limitation by accessible substrate sites is recognized in Fig. 4a where the modeled reactions of CBH II are shown to cease quickly with time. Progress curves of cellobiose release leveled out at a maximum of about 1.5×10^{-5} µmol cellobiose per 25 mm^2 surface. Variation in the simulated k_{cat} of CBH II impacted on the reaction rate but not on the conversion of the substrate, as expected (Fig. 4a). We noted that the simulation results did not agree with experimental evidence, showing that CBH II was able to generate a significant V_z of up to 0.13 nm/min and to degrade up to 60 % of the cellulosic substrate used [13, 14]. Therefore, this was strong indication that the real action of CBH II was not that of a perfect exo-cellulase but also involved "EG-like" behavior to a certain degree. Literature also shows that CBH II might possess endocellulase activity [43, 46, 62, 63]. The CA model of CBH II was therefore expanded, assigning to the uncomplexed enzyme a certain probability of endo-type chain cleavage, expressed in the first-order rate constant k_{endo}, while performing the diffusion-like "motion" on the cellulose surface. However, estimation of k_{endo} required knowledge of the k_{cat}.

Estimation of the k_{cat} of EG and CBH II

AFM experiments showed that EG activity alone was sufficient to cause substantial height degradation in amorphous material ($V_z \geq 0.4$ nm/min). However, action of the EG also produced a "surface swelling" effect, which precluded determination of a well-defined V_z and thus assessment of the enzyme's k_{cat} directly from surface

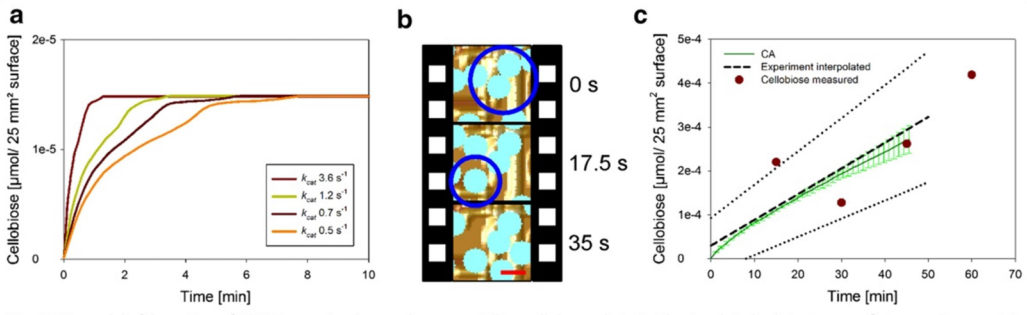

Fig. 4 CA model of the action of CBH II on a mixed amorphous–crystalline cellulose substrate. The simulated substrate was a flat amorphous matrix in which a nanocrystal of 16 nm width/height and 100 nm length was embedded in plane. CBH II was placed in saturating amount on the cellulose surface (24 nmol/m^2). **a** Effect of the enzyme's k_{cat} on the time course of cellobiose released from 25 mm^2 of cellulose surface. The same amorphous material was used on all simulations. Note that the rate of cellobiose release depends on the k_{cat}, whereas the maximum amount of cellobiose does not. **b** When degradation of amorphous cellulose by CBH II (*light blue*) was simulated whereby CBH II was modeled as a perfectly processive exo-cellulase ($k_{off} = 0$), it was noted that CBH II became gradually trapped at amorphous material (*blue circle*). Collision between a complexed CBH II molecule and a structural obstacle (nanocrystal or amorphous material) was the origin of the jam, and a thus stuck CBH II presented an obstacle for other CBH molecules acting processively on amorphous cellulose chains nearby (*blue circle*). The *red scale bar* shows 5 nm. **c** Modeled time courses of cellobiose release by CBH II were not consistent with experiment unless the CA model of the enzyme was expanded to include endo-type chain cleavage in amorphous cellulose. *Modeled results* are shown for a k_{endo} of 0.03 s^{-1} and are compared with experimental data. The k_{off} of CBH II was set to $0.7 \times 10^{-2} \cdot s^{-1}$ in the simulation (Table 1)

imaging data of [13, 14]. The experimental V_z of 0.7 nm/min for the combined action of CBH II and EG restricted the k_{cat} of EG to an upper limit of 1.5 s^{-1}, where the individual activity of the EG was already sufficient to produce the experimental V_z. Note that the release of soluble sugars by EG under the relevant reaction conditions was not considered at this point, for it might strongly underestimate the actual turnover of the enzyme on the solid surface. EG, CBH II, and CBH I were therefore placed in a 3:1:1 ratio (see "Programming, simulation, and data processing" section) on the substrate to mimic the experimental conditions used [14] and CBH I was set inactive. Simulations were performed starting from a k_{cat} of 3.6 s^{-1} for CBH II, the same as that of CBH I [16], and a k_{cat} of 1.2 s^{-1} for EG. The endo-activity of CBH II was turned off ($k_{endo} = 0$) because, as long as EG was present in the system, the k_{endo} of CBH II was not a relevant factor of V_z. The k_{cat} of EG was decreased in various steps until the simulated V_z dropped significantly below the experimental value. This sensitivity analysis suggested a k_{cat} of about ~1 s^{-1} for the EG. Tracking of the individual CBH II automata revealed that in the case of a perfectly processive CBH action ($k_{off} = 0$), the CBH II molecules became gradually trapped at places where other CBH II molecules or crystalline material presented obstacles for their further movement (Fig. 4b). We will show later that maintenance of surface dynamics in the action of CBH II via imperfect enzyme processivity (k_{off} >0) was essential for the CA model to reproduce characteristic spatiotemporal features of the substrate degradation by the complete cellulase system. Note that a CBH having k_{off} >0 is not an EG. It is an exo-acting enzyme that shows reduced processivity. This in turn enabled experimental validation of the k_{off}. However, to obtain k_{cat} estimates for EG and CBH II, the plausible assumption was made first that the k_{off} for CBH II lies anywhere within two magnitude orders above or below the k_{off} for CBH I. Note that the final estimate of k_{off} clearly falls into this range.

Figure 5a shows that different combinations of k_{cat} for CBH II and EG were consistent with a V_z of about 0.7 nm/min, provided that the k_{off} for CBH II was very high. The different k_{cat} conditions tested in the simulations are summarized in Table 2. Interestingly, therefore, when the k_{off} was decreased, enzyme combinations having k_{cat} (CBH II) > k_{cat} (EG) showed a significant decline in the degradation rate whereby the effect was especially pronounced for the pair of relatively fastest CBH II and slowest EG (Fig. 5a). Lateral rather than vertical surface degradation became the predominant mode of substrate conversion in these cases, for the activity of CBH II progressively outweighed that of EG. The effect is understandable because under conditions in which the generation of new chain ends by the action of EG is limiting, the activity by CBH II becomes increasingly confined to the processive degradation of the cellulose chains already available on the surface. The overall rate of cellulose degradation also slows down as a result. The enzyme combination of relatively fast EG and slow CBH II exhibited a V_z approximately at target value that was however independent of k_{off} in the set range (Fig. 5a). Generally, under conditions in which the k_{cat} (EG) exceeds the k_{cat} (CBH II), the effect of the EG activity on reducing the free path length for the processive action of CBH II has the consequence that a more local and hence vertical degradation of surface material is favored. Suggestion from these simulations that k_{cat} (EG) should exceed k_{cat} (CBH II) was reinforced by evidence from statistical analysis of the functional state, processively chain-cleaving or inactively awaiting chain dissociation, the CBH II molecules were in during the simulated reaction. Figure 5b shows that for an assumed k_{off} for CBH II of only 0.7 × 10^{-3}·s^{-1}, the system featuring a high-k_{cat} CBH II rapidly went into a state where all of the CBH molecules simulated were just "resting." Under conditions of a low-k_{cat} CBH II, by contrast, the CBH II molecules in the system remained in the actively chain-cleaving state for a substantially longer period of time Fig. 5b). Intuitively, therefore, one would favor the system with a comparably low k_{cat} for CBH II while refuting others that resulted in largely inactive CBH II populations. The k_{cat} of EG was thus estimated at about 1.2 s^{-1} and that of CBH II at about 0.7 s^{-1}. Compared to literature [46, 64], the k_{cat} of EG is relatively small, being lowered by a factor between 2.9 and 6.8. The differences in k_{cat} probably arise from the different cellulosic substrates used. In addition, this study used room temperature (~20 °C) to perform the enzymatic reactions, whereas in literature 30 °C or higher was used.

We proceeded by introducing k_{endo} into the CA model of CBH II and analyzed the V_z of the enzyme degrading a purely amorphous cellulosic substrate. The cellulose surface was saturated with CBH II. Using a k_{cat} of 0.7 s^{-1}, the value of k_{endo} was iteratively varied until a V_z of 0.13 ± 0.02 nm/min was obtained. The k_{endo} was thus estimated as 0.03 s^{-1}. We show in Fig. 4c that the exo–endo model of CBH II gave a prediction of the time-dependent cellobiose release by the enzyme that agreed with the experimental data within a twofold range. The CBH II model was also able to describe conversion of the substrate in substantial amounts (>40 %), which the pure exo-model could not. The overall V_z applying all modeled cellulases was not significantly influenced by the assignment of k_{endo} to CBH II (Table 2).

A small piece of experimental evidence whose possible significance was not previously recognized [13, 14], namely that the presence of active CBH I weakly boosts

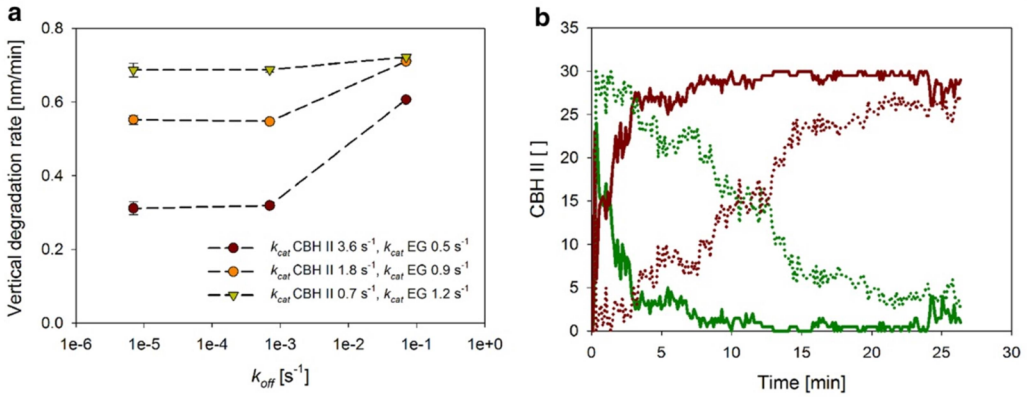

Fig. 5 Degradation of amorphous cellulose by EG and CBH II. Different combinations of k_{cat} for EG and CBH II satisfy the criterion of the experimental V_z in amorphous cellulose, but only the combination k_{cat} (EG) > k_{cat} (CBH II) results in a plausible system behavior. **a** The value of k_{off} affects V_z strongly when k_{cat} (EG) < k_{cat} (CBH II), whereas it does not affect V_z when k_{cat} (EG) > k_{cat} (CBH II). **b** Apparent inactivation of CBH II occurs as result of switch of the enzyme into a resting state on collision with structural obstacles or other enzymes. *Green lines* indicate the fraction of active CBH II enzymes, while *red lines* indicate the fraction of resting CBH II enzymes. *Solid lines* met the criteria k_{cat} (EG) < k_{cat} (CBH II) and *dotted lines* met the criteria k_{cat} (EG) > k_{cat} (CBH II). The k_{off} for CBH II was fixed at $0.7 \times 10^{-3} \cdot s^{-1}$. A relatively low k_{off} was chosen because the shown effect is particularly pronounced under these conditions (panel **a**)

Table 2 Summarization of the tested k_{cat} values for EG and CBH II and the resulting V_z

k_{cat} [s^{-1}]		V_z (nm/min) *without active CBH I molecules present*			V_z (nm/min) *with active CBH I molecules present*			
EG	CBH II	CBH II k_{off} [s^{-1}]			CBH II k_{off} [s^{-1}]			
		0.7 ×			0.7 ×			
		10^{-1}	10^{-3}	10^{-5}	10^{-1}	10^{-3}	10^{-5}	10^{-2a}
0.9	1.8	0.71	0.55	0.55	–	–	–	–
0.9	1.2	0.64	0.55	0.54	–	–	–	–
0.6	3.6	0.65	0.37	0.37	–	–	–	–
0.5	3.6	0.61	0.32	0.31	–	–	–	–
1.2	1.2	0.77	0.70	0.71	0.83	0.73	0.75	–
1.2	0.9	0.75	0.70	0.69	0.81	0.74	0.73	–
1.2	*0.7*	0.72	0.69	0.69	0.77	0.73	0.73	*0.75*[b]
1.2	0.6	0.71	0.69	0.68	0.75	0.73	0.73	–

Simulations were performed in the absence or presence of active CBH I molecules and the k_{off} of CBH II was varied at the values indicated. The values are shown as mean V_z (nm/min). The relative SD is below 5 % in all cases and therefore not shown. Simulations were performed in triplicates and over a time of 1575 s. Simulations matching the condition k_{cat} (EG) < k_{cat} (CBH II) were not tested with active CBH I molecules (see *Estimation of the k_{cat} of EG and CBH II*). The finally chosen k_{cat} pair and the results obtained with an optimized k_{off} of CBH II are highlighted

[a] Optimized k_{off} of CBH II

[b] Mean value of V_z is not affected by the implementation of k_{endo} for CBH II

the V_z of EG and CBH II, now turns out to be useful in the validation of the modeling results. Enhancement of V_z by about 3–10 % due to CBH I was reproduced by the model in good quantitative agreement (Table 2) with experiment. Despite its complete lack of activity on amorphous cellulose, the modeled CBH I affects the performance of EG and CBH II. It does so by virtue of removing crystalline substrate parts that restrict the unhindered access of the two other cellulases to the amorphous material.

Degradation of crystalline fibrils within an amorphous cellulose matrix

Figure 6 shows time courses of Δh_max determined from experimental AFM sequences in which concurrent

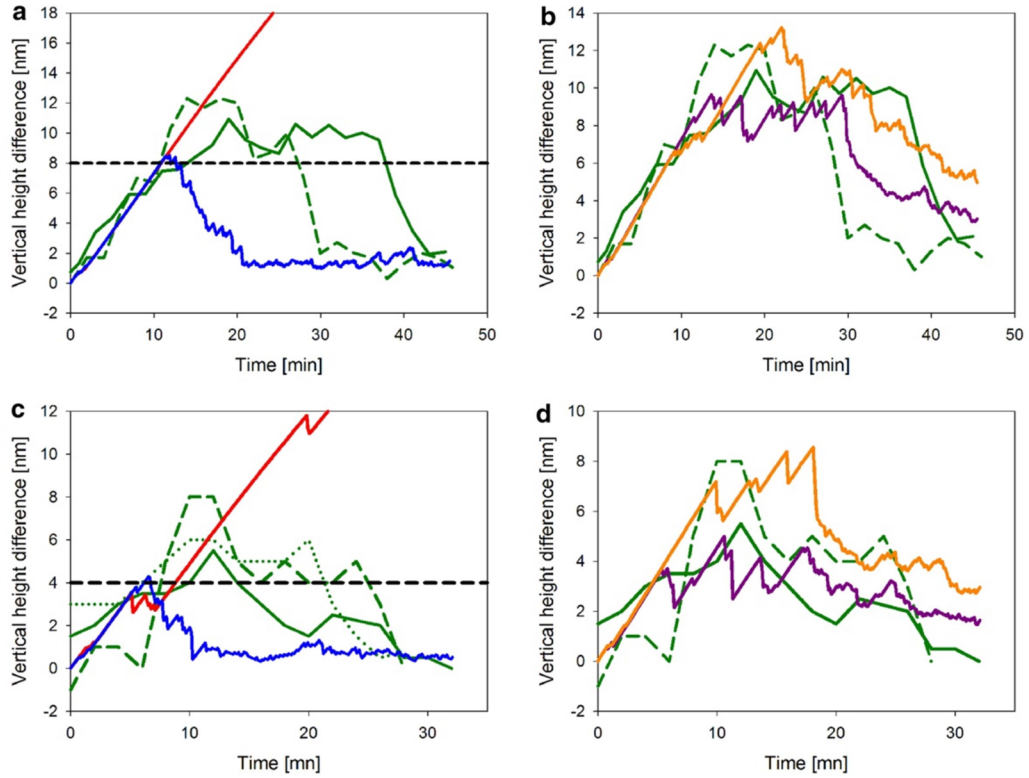

Fig. 6 Dynamics of crystalline cellulose degradation depends on the k_{off} of CBH II. The k_{off} of CBH II is key to explain the dynamics of crystalline cellulose degradation by cellulases as modeled. Shown are time courses of Δh_max (vertical height difference between the highest point on a cellulose crystallite and the amorphous material surrounding the crystallite) during enzymatic degradation of large (~16 nm height; panels **a**, **b**) and small (~8 nm height; panels **c**, **d**) nanocrystals analyzed by experiment and simulation. Nanocrystals were modeled with their hydrophobic faces aligned horizontally and with their top face touching the enzyme-accessible surface. The Δh_max required to expose the crystal's hydrophobic faces was therefore half the height, which is indicated by the *dashed black line*. Experimental time courses are shown in *green*. Simulated time courses of Δh_max using low and high boundary values of k_{off} are shown in *red* ($0.7 \times 10^{-3} \cdot s^{-1}$) and *blue* ($0.7 \times 10^{-1} \cdot s^{-1}$), respectively. Shown in *orange* and *magenta* are two simulations using the iteratively "optimized" value of $0.7 \times 10^{-2} \cdot s^{-1}$ for k_{off}

degradation of cellulose nanofibrils and the amorphous cellulose matrix surrounding them was revealed. We note substantial variability in the results obtained from individual crystals, and trends of the Δh_max values were certainly overlapped with considerable scatter. However, we think that some discontinuity in the Δh_max curves is also intrinsic, as will be discussed later. Shared feature of degradation of relatively large (Fig. 6a, b; diameter 14–18 nm) and small (Fig. 6c, d; diameter 8–10 nm) nanocrystals was a triphasic time course in which Δh_max increased gradually to a maximum value in the first phase, then stayed approximately constant for some time, only to drop off afterwards and vanish at the end of the process (Δh_max ~0). Degradation of large nanocrystals took longer overall and involved a higher Δh_max change than degradation of the comparably small crystals (Fig. 6a, c). The rate of Δh_max evolution in the first degradation phase was similar irrespective of the cellulose nanocrystal selected for analysis. Its average value of about 0.7 nm/min was consistent with the suggestion that it reflected primarily the removal of amorphous material surrounding the crystals. Figure 6a and c also shows that only after having been uncovered from the amorphous matrix at about half of their diameter, the nanocrystals started to become degraded. Interestingly, therefore, the clear evidence that Δh_max decreased again in the final

phase of the reaction (Fig. 6a, c) implies that the crystalline material was degraded faster than the amorphous cellulose.

Vertical degradation rates were estimated to differ by a factor of around five. The V_z of about 3.5 nm/min for degradation of crystalline cellulose was consistent with the results of Ganner et al. [14]. Applying the parameter values from Table 1, the CA model was capable of reproducing the dynamics of Δh_max in useful qualitative and even (semi)-quantitative agreement with the experiment. First insight from the simulations however was that a time dependence of Δh_max was observed only in the case that the nanocrystal was embedded in amorphous cellulose with its hydrophobic face buried. If in contrast the crystal's hydrophobic face was exposed on the surface, as shown for the crystal in vertical orientation in Fig. 1a, degradation of the crystal was limited by removal of the surrounding amorphous cellulose, hence Δh_max was zero throughout. The model prediction was consistent with AFM measurements [14], showing that at various places on the flat surface of the cellulose the material degradation did in fact involve removal of nanocrystalline phases without generating a significant height difference to the immediately surrounding amorphous matrix.

Modeling the degradation of nanocrystals in horizontal orientation where both hydrophobic faces were buried in amorphous cellulose revealed a pronounced dependence of the dynamics of Δh_max on the k_{off} of CBH II, as shown in Fig. 6. Simulations performed at varied k_{off} for degradation of a large nanocrystal showed that change in k_{off} affected primarily the rate of Δh_max decrease after the first phase of reaction (Fig. 6a, c). When the k_{off} was set too high ($\geq 0.7 \times 10^{-1} \cdot s^{-1}$), due to fast degradation of the crystal the emergence of Δh_max was much smaller than observed experimentally. When by contrast the k_{off} was set too low ($\leq 0.7 \times 10^{-3} \cdot s^{-1}$), the nanocrystal was hardly degraded in the relevant time span of the simulation experiment. Of note, therefore, this finding implies CBH II to have a substantially higher k_{off} than CBH I. At the single-molecule level, the immediate consequence of lowering the k_{off} of CBH II was an increased tendency of enzyme jamming at the interface of crystalline and amorphous cellulose.

Because the analysis is performed at the single-nanocrystal level, and it has to be done in that way to capture local characteristics of the substrate degradation, the stochastic effects introduce large variability in the time courses of Δh_max, both when degradation of the *same* nanocrystal is examined in multiple simulations or when degradation of *different* but similarly sized nanocrystals is studied experimentally. Figure 6 shows that both experiment and simulation yielded a relatively broad ensemble of Δh_max time courses, and it was clear that averaging would not have eliminated the stochastic effects. However, despite this it was still possible to perform an iterative search for a k_{off} of CBH II that allowed the model to reproduce the overall trend of the data. Using the time courses for degradation of two large nanocrystals, as shown in panel b of Fig. 6, the k_{off} of CBH II was estimated to be about 0.70 (± 0.10) $\times 10^{-2} \cdot s^{-1}$. Thus, simulated time courses of Δh_max were well consistent with the experimental results, except for the systematic difference that the Δh_max at the end of the nanocrystal degradation cycle did not drop to zero (Fig. 6b). In the simulation, due to the constant V_z in amorphous material surrounding the nanocrystal, a height difference develops inevitably between this material and the amorphous material underneath the crystal. The height difference is eliminated only gradually in the simulation as result of a slightly elevated V_z in the protruding material, which offers a larger enzyme-accessible area than the flat surfaces adjacent to it. Effects involved in the experiment but not accounted for in the CA model are not clear at this time. However, not necessarily it is implied that the CA model of cellulase action presents an oversimplification. It is also possible that the small surface structures in amorphous material arising in the simulation after the nanocrystal has become degraded are not stable in the experiment, e.g., because they are only loosely attached to the surrounding material which might even result in their removal by the AFM tip.

In a final step, the dataset for small nanocrystal degradation was used for model validation. Results are shown in Fig. 6d. The high and low boundary values for k_{off} were completely inconsistent with the experimental evidence, as indicated in panel C of Fig. 6. Using the "optimized" k_{off}, however, useful trend agreement between simulated and experimental time courses was obtained (Fig. 6d). Moreover, for both small and large nanocrystals, the V_z of crystalline material degradation of about 3.1 ± 0.1 nm/min was predicted in almost perfect accordance with the experimental observations.

CA modeling reveals single-molecule dynamics of degradation of amorphous–crystalline cellulose

A full video of a simulated degradation of a large nanocrystal embedded in amorphous material is provided (Additional file 2). The video illustrates the main dynamic features of enzymatic cellulose surface degradation revealed in this study. At the mesoscopic level, time-dependent evolution and decay of a height difference between crystalline and amorphous material is shown (Fig. 7a–c). At the level of the single enzymes, the repeated occurrence of cycles of formation and dissipation of enzyme jams on crystalline cellulose is demonstrated. Snapshots from the video are shown in Fig. 7

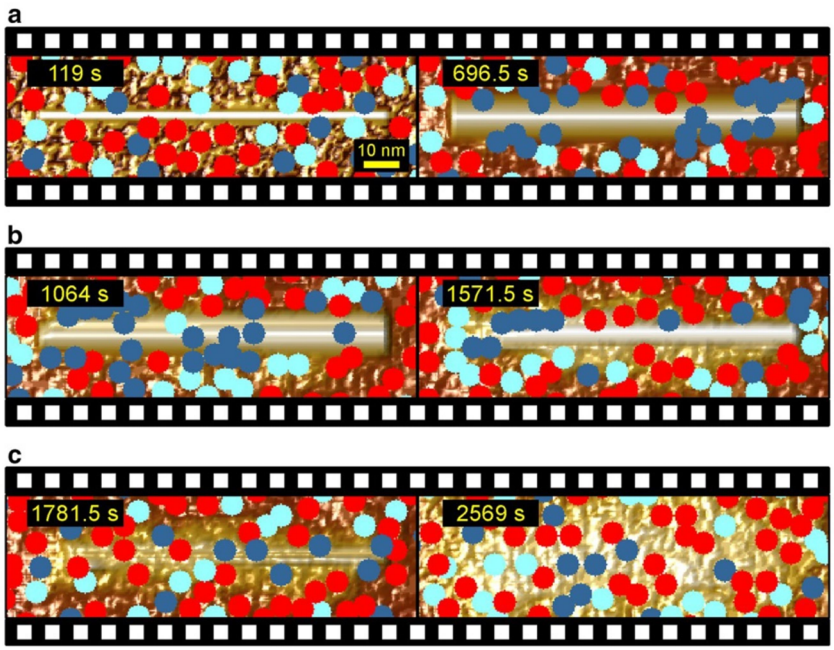

Fig. 7 Time-resolved sequences from a simulated degradation of mixed amorphous–crystalline cellulose by the cellulase system. Cellulases are identified by *color* EG (*red*), CBH II (*light blue*), and CBH I (*dark blue*). **a** A crystallite is gradually uncovered over time until the horizontally oriented hydrophobic face is revealed. **b** Upon revealing of the hydrophobic face, the crystallite is attacked in an asymmetric manner. **c** Finally, the crystallite becomes completely degraded over time. A video of the shown degradation sequence is available (Additional file 2). Please note that occasional visual overlapping of enzymes is caused by their position in different *z*-planes of the substrate

to demonstrate the effect, revealing that stochastic processes determine when and where the jams occur. Jams of CBH I molecules moving along the surface of crystalline cellulose in repeated stop-and-go cycles have been observed in experiments before [16]. These jams were however intrinsic to the action of CBH I. What is unexpected and new here, as emphasized in Fig. 7 and in more detail in Fig. 8, is the suggestion that jams of CBH I caused by trapped CBH II molecules might play a decisive role in determining the dynamics of degradation of amorphous–crystalline cellulose material.

The dynamics of formation and dissipation of enzyme jams caused by stuck CBH II molecules is clearly recognized in Fig. 8 and Additional files 2 and 3. CBH II molecules awaiting chain dissociation represent obstacles for processively acting CBH I molecules, and this results in an intermittent stopping of cellulose degradation in the crystalline surface areas affected by the jam (Fig. 8a–c) and an accumulation of trapped CBH I molecules (Fig. 8b–e). Because surrounding amorphous material is degraded rather continuously, degradation of the crystal in discrete stop-and-go phases results in a discontinuous up-and-down trend of Δh_max within the time domain of $1/k_{off}$. This was observed experimentally and also reproduced by the model (see Fig. 6). Jamming events caused by CBH II are intrinsically stochastic in consequence of both the random structure of the amorphous material and the random diffusion of uncomplexed CBH molecules on the surface.

Also due to stochastic effects in the simulation, it was possible that traffic jams occurred predominantly on one side of the cellulose crystal or in temporally delayed fashion (compare Fig. 8b, f), thus resulting in a pronouncedly asymmetric degradation of the crystal from the side opposite to the jam. This result was interesting because similar patterns of asymmetric degradation of cellulose crystals were noted in AFM imaging experiments [14].

CA modeling suggests "hidden" morphological targets for cellulase synergy in the degradation of crystalline cellulose

It was earlier suggested from experiment [22, 46] that efficiency of CBH I for degradation of different celluloses is

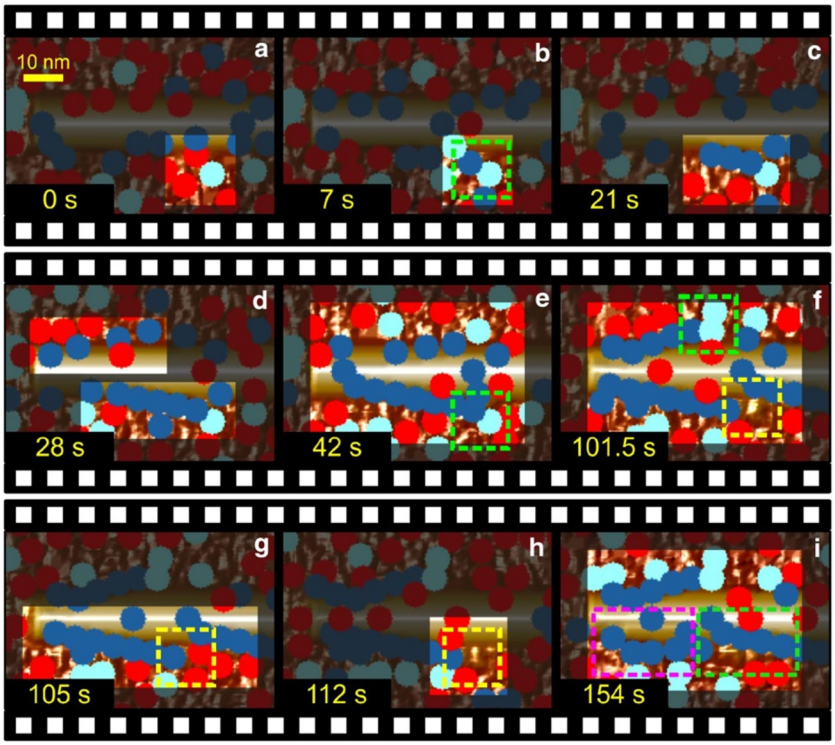

Fig. 8 Dynamic formation and dissipation of enzyme traffic jams at the amorphous–crystalline interface. Cellulases are identified by *color* EG (*red*), CBH II (*light blue*), and CBH I (*dark blue*). For an easier viewing, the background is darkened through all panels. **a**, **b** An already-trapped CBH II molecule at the interface of crystalline and amorphous cellulose (*green rectangle*) causes a traffic jam of CBH I molecules. **c** CBH I molecules move processively from left to right on the upper edge of the crystal and an accumulation of CBH I can be observed (21 s). **d**, **e** Degradation starts on the other site of the crystallite too but is soon stopped by another collision with a CBH II molecule (*green rectangle*, panel **f**). **f** After $1/k_{off}$ is passed, CBH II dissociates but the amorphous material below the dissociated CBH II is clearly elevated in comparison to the surrounding amorphous material (*yellow rectangle*). Note: the elevated height is recognized by *bright color* in the *yellow framed area*. The lower lying surrounding material is indicated by (*dark*) *brown color*. **g**, **h** EG molecules attack the (elevated) amorphous part (*yellow rectangle*) and clearly alter it by reducing its height. **i** Eventually, CBH I molecules resume hydrolysis (*green square*, 154 s). However, the next group CBH I enzymes trying to slide along the crystal on a lower plane are trapped again (*pink square*). Note that, the crystallite shows already degradation (*pink square*) caused by the first group of enzyme sliding along. A video is available (Additional file 3)

limited by the mean free path length of the enzyme's processive chain cleavage. Simulations made herein revealed that obstacles from surrounding amorphous cellulose restricted the processivity of CBH I on crystalline substrate. Removal of the obstructing material by the partner cellulases, in particular EG, restored the processive action of CBH I and thus enhanced the free path length of chain cleavage for the enzyme. Figure 8e, f shows an example where a CBH II molecule that had become temporarily stuck right next to the cellulose crystal prevented degradation of amorphous material lying underneath or in immediate proximity to it. Therefore, this resulted in a local increase in amorphous height in the surface region affected. After the release of the trapped CBH II, the protruding amorphous surface constituted a structural obstacle for attack of CBH I on the cellulose crystallite. As a consequence, additional CBH I traffic jams were created and complete crystalline chain degradation toward the non-reducing end was prevented (Fig. 8f–h). Only after removal of the obstacle, here through attack by EG molecules (Fig. 8g, h) did the degradation of the crystal resume, as shown in Fig. 8i. It is worthy of note that similar structural obstacles could arise anytime during the simulated reaction also in the absence of a stuck CBH II

molecule, for they represent an intrinsic feature of the spatiotemporal dynamics of surface degradation by the CA model based on random principles. These obstacles are identified as clear morphological targets for synergy between amorphous material-degrading cellulases and CBH I. Moreover, a new potential role of CBH II and EG in facilitating degradation of crystalline cellulose by CBH I is suggested. Besides uncovering cellulose crystals from amorphous material to make attack by CBH I possible in the first place, the two cellulases are also required to remove dynamically appearing local obstacles of amorphous cellulose that obstruct the processive action of CBH I. Overall, therefore, CBH II and EG contribute to enhancement of the mean free path length of processive chain cleavage by CBH I, and this is expected to be beneficial for efficient substrate degradation as a whole.

CA modeling the release of soluble sugars

Knowing that prominent features of cellulose surface degradation were represented realistically in the simulations, it was interesting to examine the CA model's capability of predicting the soluble product release. Figure 9 compares time courses of cellobiose formation in experiment and simulation, showing that the model only slightly (by about 30 %) underestimated the experimental cellobiose release. Given the model's complexity plus the fact that parameters of enzyme action were both realistic and not excessively fine-tuned to match the experiment, the CA modeling can be considered to have provided a very close prediction of the actual hydrolysis rate. From the sugar release rate and the amount of total protein adsorbed, a specific activity of the bound "cellulase" of 1.77 ± 0.05 μmol/(min mg_protein) was calculated.

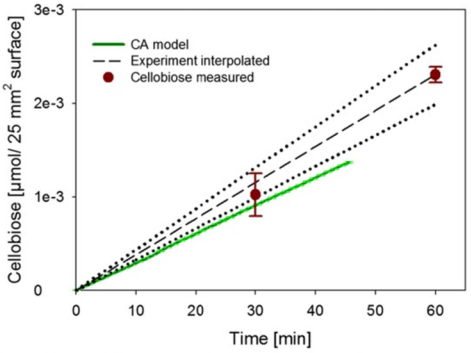

Fig. 9 Modeled time course of cellobiose formation is compared to experiment performed under exactly comparable conditions. The experimentally measured initial production of glucose is expressed as cellobiose released (glucose release/2). The absolute amount of calculated cellobiose is plotted as a function of released cellobiose from 25 mm^2 cellulose surface with *black dashed line* and the range of error is shown as *dotted line*. Experimentally measured points are indicated in *red*. All experiments and simulations were conducted at least in triplicates

Advances made in CA modeling of the enzymatic cellulose degradation

The current CA model of enzymatic cellulose degradation is unique in having been designed for effective use in combination with time and laterally resolved experimental data from high-resolution imaging analysis. An important novel feature was the CA model of a mixed amorphous–crystalline substrate whereby the amorphous material was built from surface layers of completely randomly organized cellulose chains. Previous CA models have focused mostly on crystalline cellulose and represented its ordered structure at different levels of detail [31, 36, 43]. Coarse-grained models of crystalline cellulose were applied to simulate pretreatment effects on the substrate structure [65, 66] or to construct potential free energy surfaces for an atomistically represented cellulose-binding module [67]. Kumar and Murthy [37] included regions of amorphous material in their 3D matrix model of a microfibrillar cellulose structure. However, in their model the amorphous regions were created from single cellulose chains that alternated between being embedded in the crystalline fibril structure or being released from it. Disorder in direction and orientation of the cellulose chains was therefore not modeled. However, the evidence from the current modeling work supports the suggestion that the interface between crystalline and (randomly organized) amorphous material constitutes an important region of high local dynamics in substrate morphology and in the correlated synergistic interplay of the cellulases.

With only one (EG) or two (CBH I, CBH II) main adjustable parameters (k_{cat}, k_{off}), the herein used CA model of enzyme action confined to the cellulose surface was simple and focused. CA models in the literature usually included enzyme adsorption and desorption additionally [31, 36, 43]. Surface diffusion was implemented in some [30, 36, 43] but not all models [31, 37]. A few studies tried to correlate the results of their modeling with experimental data of soluble sugar release [36, 37]. However, the experimental substrate was usually very different from the substrate modeled (e.g., Avicel compared to a cellulose fibril [37]), thus making a direct comparison challenging.

Conclusions

CA modeling is shown to depict realistically the degradation of mixed amorphous–crystalline cellulose by a three-enzyme-type cellulase system. Total system

behavior is successfully reconstructed by combining kinetic data sets from high-resolution single-molecule studies. Most noticeable, salient dynamic features of cellulose surface degradation by different cellulases acting in synergy are reproduced and close prediction of the actual hydrolysis rate is thus achieved. Results of the modeling can be analyzed visually and are therefore ideal for comparison with the evidence from high-resolution visualization experiments. Moreover, the modeling approach employed in this work illustrates the importance of spatial resolution at single-molecule level in both in situ and in silico studies. Besides aiding in the mechanistic interpretation of intrinsically complex effects from the experiment, the modeling also provides deepened insight into the possible interplays, some of them of a stochastic nature, of individual cellulases during cellulose degradation. The model thus helps making explicit what is usually only implicit in experimental observations of enzymatic cellulose hydrolysis. In particular, the k_{off} of CBH II is suggested here for the first time to have a key role in maintaining the dynamics of action of the processively cleaving CBHs at the interface of amorphous and crystalline cellulosic material. The current model is expandable. More complex substrate structures can be defined, to incorporate non-productive binding to the cellulose or a finite enzyme lifetime due to inactivation for example. Enzyme adsorption dynamics at subsaturating enzyme loading can also be included. It would also be of interest to implement surface diffusion over distances greater than simulated here. Using simulation, the impact of change at the single-molecule level on total system behavior can thus be studied. Insights obtained from CA modeling are of fundamental significance but also relevant for practical application in enzymatic cellulose hydrolysis.

Methods

Programming, simulation, and data processing

All programming was done in MATLAB [Version 7.11.1.866 (R2010b) service pack 1]. The complete program code is available on request. A Monte Carlo approach was used and individual steps are discussed in detail in "Results and discussion" section. Simulations were performed in a cuboid box with dimensions of 70 × 150 × 100 nm for the *x*, *y*, and *z* (height) coordinates, respectively. The cellulose substrate was modeled as an initially completely flat surface that was continuous (i.e., did not contain walls) in the *x* and *y* direction. Cellulosic planes were assembled on top of each other in the *z* direction, making up a material layer of up to 90 nm.

Crystalline phases were included as cellulose nanofibrils. For clarity reason, the nanofibrils were oriented always in plane parallel to the cellulose surface. Their hydrophobic faces were aligned horizontally or vertically, as shown in Fig. 2a. Any orientation of the nanofibril is however possible in the model. A water phase (Fig. 1) was included to indicate the accessible cellulose surface.

To mimic the experimental conditions of AFM imaging in which completely saturating cellulase loadings (4×10^4 mg protein/m^2 cellulosic surface) were applied in solution, all simulations were performed at an assumed maximum surface coverage with enzyme of 24 nmol/m^2. Lying in between the maximum cellulase adsorption capacity estimated from a "two-dimensional liquid crystal" approximation of the adsorbed cellulase (16 nmol/m^2; [68]) and the one determined experimentally by Maurer et al. [68, 69], the assumed surface loading appeared to be realistic. The composition of the adsorbed cellulase was set approximately according to the substrate sites available in the cellulose as 60 % EG and 20 % of each CBH. The total number and the composition of the cellulases were invariant during the simulation. The enzyme kinetic parameters from Table 1 were used. Considering the involvement of multiple random steps in the CA model of cellulase action, simulations were performed in at least 10-fold replicates to obtain statistic validation. Parameters obtained from simulation data are therefore provided as mean values with standard deviation.

Reaction time courses were recorded as movies of cellulose surface degradation. These movies were used for qualitative comparison with time-resolved evidence from AFM imaging. The rate of height removal in amorphous material and also the rates of emergence and degradation of crystalline nanofibrils could be compared quantitatively between experiment and simulation. Cellobiose released from the surface was also calculated and compared with experiment. Parameter used to express enzymatic action of the crystalline material was the time-dependent height difference between the highest point on the crystal and the mean height of surrounding amorphous material (Δh_max). Because the rate of degradation of crystalline was highly dependent on the nanofibril's aspect ratio, we modeled crystals of large (14–18 nm) and small (8–10 nm) diameters.

AFM imaging and data analysis

Experimental data were from our recent studies where in situ AFM imaging was used to monitor surface degradation in a nanoflat mixed amorphous–crystalline substrate [41]. In that way, the time-dependent change in Δh_max could be determined. More specifically, section profiles were taken from an individual nanofibril at each time to determine the highest point in relation to surrounding amorphous level (Fig. 10). The values of Δh_max are color-coded to match the color code used for the height measured in the AFM imaging experiments.

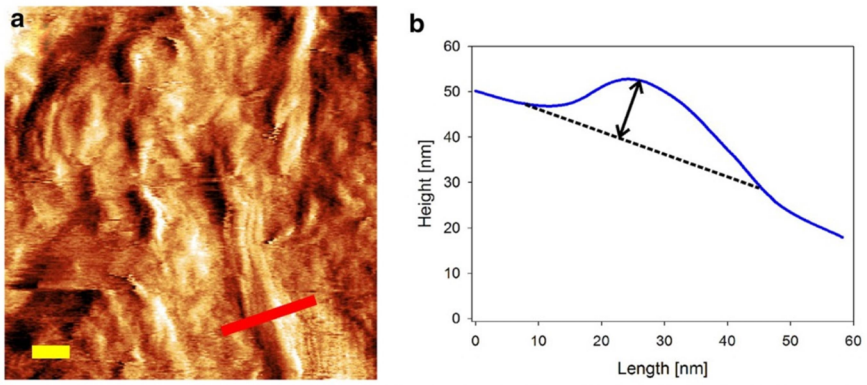

Fig. 10 Exemplary processing of AFM images of enzymatic degradation to determine Δh_max. Crystalline fibrils embedded in amorphous cellulose matrix provide time-resolved quantitative data for comparison of simulation results with the experiment. **a** Height profiles (*red line*) of crystals were taken from AFM sequences recorded from enzymatic reactions carried out as described by Ganner et al. [14]. For easier viewing, the amplitude image of the corresponding position is shown. The *yellow scale bar* shows 10 nm. **b** The highest point on a cellulose crystallite was found by moving the section profile along the crystallite, and the vertical height difference between the highest point and the amorphous material (indicated by the *arrow*) surrounding the crystallite was calculated (Δh_max)

Additionally, the AFM data were used to calculate at different points of the surface the vertical degradation of amorphous cellulosic material. A large micron-sized crystallite that was completely resistant to enzymatic degradation in the time span of the experiment was used as a height marker [14, 70]. AFM image processing and analysis was performed using Gwyddion 2.31 (released 02/21/2013) and Nanoscope (Build R3Sr4.94136, Bruker Nano Surface Offices). However, to improve the manual processing of multiple images, an automated routine in MATLAB was developed with which the images from an AFM sequence could be matched one on another in an exactly comparable fashion.

Enzymatic hydrolysis

Experiments were performed in triplicates at 20 °C in sodium acetate buffer (pH 5.0). The mixed amorphous–crystalline cellulose applied to AFM studies was used. The substrate concentration was 2.0 mg/mL and the total reaction volume was 500 µL. Substrate was cut into pieces with dimensions of approximately 5 × 5 × 0.2 mm. Based on this geometry, an initially available surface area of 54 mm^2 was calculated.

Reactions using the complete *H. jecorina* cellulase system contained 25 µg protein/mg cellulose. β-Glucosidase (Megazyme, Wicklow, Ireland) was added at 5 µg protein/mg cellulose. Reactions using purified CBH II alone also contained 25 µg protein/mg cellulose and β-glucosidase (2 µg/mg protein). Samples were taken at suitable times and analyzed for D-glucose using glucose oxidase and peroxidase [70]. D-Glucose concentrations below detection limit of the enzymatic assay were analyzed by high-performance anion-exchange chromatography with pulsed amperometric detection [13]. To compare experimental hydrolysis data with the modeling results of soluble sugar release, the amount of cellobiose formed in the experiment was assumed to be half that of the D-glucose measured. The µmol amounts of cellobiose released per 25 mm^2 surface were compared.

Additional files

Additional file 1. Exemplary construction of the chain orientation matrix of one amorphous cellulose plane. Cellobiose units not yet oriented in plane are shown in green. Otherwise the colour coding of Fig. 2b is used. The orientation (*x*, *y*) and internal direction ('+','−') of each chain with respect to the origin of the *z*-plane are indicated by colour: orange (*x*; +1), light blue (−*x*; −1), red (*y*, +2) and dark blue (−*y*, −2). A time-efficient multistep algorithm was designed to saturate an amorphous cellulose plane with fragments mimicking a Gaussian distribution. Chains are positioned by the following procedure: at first, cellulose chains with random length according to a normal distribution (μ 15 nm, σ 3 nm) are generated and randomly positioned and oriented in the layer. Note: one cellobiose automaton is 1 nm. The possibility for chain positioning at first try decreases significantly with progressing surface coverage until a limiting surface coverage of about 80 % is reached (Additional file 1, 0–19 s). The remaining 20 % of the surface are filled as follows: existing cellulose chains are elongated in a random process by attaching terminal cellobiose units without orientation (green) to the chain (Additional file 1, 20–30 s). Thus, the elongation process can be applied until a surface coverage of above 95 % is reached. In the case that cellobiose units without an orientation are encapsulated and no chain end terminates in direction of the not yet oriented cellobioses (green), shorter chain fragments with a random orientation are used to fill the area (Additional file 1, 31–34 s). Note, that changing the orientation of already oriented cellobiose units is

widely prohibited during all steps. However, to achieve a 100 % surface coverage in a reasonable time (<30 s per plane) exceptions to this rule are implemented in the algorithm. These exceptions cause a negligible deviation from the normal distribution (see Fig. 2c). A mean free path length of 18 nm is reached eventually.

Additional file 2. Time-resolved sequences from simulations of mixed amorphous-crystalline cellulose degradation by the cellulase system. Cellulases are identified by color: EG (red), CBH II (light blue), CBH I (dark blue). A crystallite is gradually uncovered over time until the horizontally orientated hydrophobic faces are exposed (Additional file 2, 0–60 s). Upon revealing of the hydrophobic faces CBH I molecules are moving processive along the crystallite (Additional file 2, 60–65 s) thereby exposing new hydrophobic sites (see Fig. 2a). A typical sequence of events hindering CBH I molecules in their possessive motion is initiated after 68 s in Additional file 2. This sequence includes CBH I molecules jamming with a CBH II molecule (Additional file 3, 68–76 s) and later with amorphous material (Additional file 2, 78–84 s). This sequence is shown in more detail in Fig. 8 and Additional file 3. Similar events of CBH I molecules blocked by CBH II molecules or amorphous obstacles can be observed until the crystallite is completely degraded (Additional file 2, 170 s). The video is speeded up by a factor of 10.5.

Additional file 3. Details of dynamic formation and dissipation of enzyme traffic jams in a simulated degradation of mixed amorphous-crystalline cellulose by the cellulase system. Cellulases are identified by color: EG (red), CBH II (light blue), CBH I (dark blue). Initially, an already trapped CBH II molecule at the interface of crystalline and amorphous cellulose causes a traffic jam of CBH I molecules and an accumulation of CBH I molecules (Additional file 3, 0–10 s). After $1/k_{off}$ is passed, CBH II dissociates but the amorphous material below the dissociated CBH II is clearly elevated in comparison to the surrounding amorphous material (see Additional file 3, 14 s). Thus, not all CBH I enzymes are allowed to proceed with their processive motion (Additional file 3, 10–15 s). Multiple EG molecules attack the (elevated) amorphous part and alter it by reducing its height and thinning it (Additional file 3, 15–21 s). Eventually, CBH I molecules resume hydrolysis (Additional file 3, 21–23 s). However, the next group CBH I enzymes trying to slide along the crystal on a lower plane are trapped again (Additional file 3, 24–27 s). The highlights of this process are depicted in Fig. 8. The video is speeded up by a factor of 7.

Abbreviations
CA: cellular automata; AFM: atomic force microscopy; CBH: cellobiohydrolase; EG: endoglucanase; V_z: vertical degradation rate.

Authors' contributions
TZ and BN designed the research. ME and TZ developed the model, did the programming, performed simulations, and analyzed data. TG and HP provided AFM data. ME and BN wrote the paper. All authors read and approved the final manuscript.

Author details
[1] Institute of Biotechnology and Biochemical Engineering, Graz University of Technology, NAWI Graz, Petersgasse 12, 8010 Graz, Austria. [2] Institute for Electron Microscopy and Nanoanalysis, Graz University of Technology, Steyrergasse 17, 8010 Graz, Austria. [3] Graz Centre for Electron Microscopy, Steyrergasse 17, 8010 Graz, Austria. [4] Austrian Centre of Industrial Biotechnology, Petersgasse 14, 8010 Graz, Austria.

Acknowledgements
We thank Dr. Zdenek Petrasek (Institute of Biotechnology and Biochemical Engineering, Graz University of Technology, Austria) for his support.

Competing interests
The authors declare that they have no competing interests.

Funding
Financial support from the Austrian Science Funds (FWF Project P- 24156-B21 to B.N.) is gratefully acknowledged.

Received: 18 December 2015 Accepted: 19 February 2016
Published online: 08 March 2016

References

1. Chundawat SPS, Beckham GT, Himmel ME, Dale BE. Deconstruction of lignocellulosic biomass to fuels and chemicals. Annu Rev Chem Biomol Eng. 2011;2:121–45.
2. Payne CM, Knott BC, Mayes HB, Hansson H, Himmel ME, Sandgren M, Ståhlberg J, Beckham GT. Fungal cellulases. Chem Rev. 2015;115:1308–448.
3. Resch MG, Donohoe BS, Baker JO, Decker SR, Bayer EA, Beckham GT, Himmel ME. Fungal cellulases and complexed cellulosomal enzymes exhibit synergistic mechanisms in cellulose deconstruction. Energy Environ Sci. 2013;6:1858.
4. Bubner P, Plank H, Nidetzky B. Visualizing cellulase activity. Biotechnol Bioeng. 2013;110:1529–49.
5. Zhang YHP, Lynd LR. Toward an aggregated understanding of enzymatic hydrolysis of cellulose: noncomplexed cellulase systems. Biotechnol Bioeng. 2004;88:797–824.
6. Luterbacher JS, Moran-Mirabal JM, Burkholder EW, Walker LP. Modeling enzymatic hydrolysis of lignocellulosic substrates using fluorescent confocal microscopy II: pretreated biomass. Biotechnol Bioeng. 2015;112:32–42.
7. Fox JM, Jess P, Jambusaria RB, Moo GM, Liphardt J, Clark DS, Blanch HW. A single-molecule analysis reveals morphological targets for cellulase synergy. Nat Chem Biol. 2013;9:356–61.
8. Bansal P, Hall M, Realff MJ, Lee JH, Bommarius AS. Modeling cellulase kinetics on lignocellulosic substrates. Biotechnol Adv. 2009;27:833–48.
9. Mosier NS, Hall P, Ladisch CM, Ladisch MR. Reaction kinetics, molecular action, and mechanisms of cellulolytic proteins. Adv Biochem Eng Biotechnol. 1999;65:23–40.
10. Zhang Y, Lynd L. A functionally based model for hydrolysis of cellulose by fungal cellulase. Biotechnol Bioeng. 2006;94:888–98.
11. Levine SE, Fox JM, Blanch HW, Clark DS. A mechanistic model of the enzymatic hydrolysis of cellulose. Biotechnol Bioeng. 2010;107:37–51.
12. Zhou W, Schüttler H-B, Hao Z, Xu Y. Cellulose hydrolysis in evolving substrate morphologies I: a general modeling formalism. Biotechnol Bioeng. 2009;104:261–74.
13. Eibinger M, Bubner P, Ganner T, Plank H, Nidetzky B. Surface structural dynamics of enzymatic cellulose degradation, revealed by combined kinetic and atomic force microscopy studies. FEBS J. 2014;281:275–90.
14. Ganner T, Bubner P, Eibinger M, Mayrhofer C, Plank H, Nidetzky B. Dissecting and reconstructing synergism—in situ visualization of cooperativity among cellulases. J Biol Chem. 2012;287:43215–22.
15. Bubner P, Dohr J, Plank H, Mayrhofer C, Nidetzky B. Cellulases dig deep: in situ observation of the mesoscopic structural dynamics of enzymatic cellulose degradation. J Biol Chem. 2012;287:2759–65.
16. Igarashi K, Uchihashi T, Koivula A, Wada M, Kimura S, Okamoto T, Penttilä M, Ando T, Samejima M. Traffic jams reduce hydrolytic efficiency of cellulase on cellulose surface. Science. 2011;333:1279–82.
17. Shibafuji Y, Nakamura A, Uchihashi T, Sugimoto N, Fukuda S, Watanabe H, Samejima M, Ando T, Noji H, Koivula A, Igarashi K, Iino R. Single-molecule imaging analysis of elementary reaction steps of *Trichoderma reesei* cellobiohydrolase I (Cel7A) hydrolyzing crystalline cellulose Iα and Iβ. J Biol Chem. 2014;289:14056–65.
18. Jung J, Sethi A, Gaiotto T, Han JJ, Jeoh T, Gnanakaran S, Goodwin PM. Binding and movement of individual Cel7A cellobiohydrolases on crystalline cellulose surfaces revealed by single-molecule fluorescence imaging. J Biol Chem. 2013;288:24164–72.
19. Liu YS, Baker JO, Zeng Y, Himmel ME, Haas T, Ding SY. Cellobiohydrolase hydrolyzes crystalline cellulose on hydrophobic faces. J Biol Chem. 2011;286:11195–201.

20. Praestgaard E, Elmerdahl J, Murphy L, Nymand S, McFarland KC, Borch K, Westh P. A kinetic model for the burst phase of processive cellulases. FEBS J. 2011;278:1547–60.
21. Jalak J, Väljamäe P. Mechanism of initial rapid rate retardation in cellobiohydrolase catalyzed cellulose hydrolysis. Biotechnol Bioeng. 2010;106:871–83.
22. Jalak J, Kurašin M, Teugjas H, Väljamäe P. Endo-exo synergism in cellulose hydrolysis revisited. J Biol Chem. 2012;287:28802–15.
23. Wang J, Quirk A, Lipkowski J, Dutcher JR, Clarke AJ. Direct in situ observation of synergism between cellulolytic enzymes during the biodegradation of crystalline cellulose fibers. Langmuir. 2013;29:14997–5005.
24. Fox JM, Levine SE, Clark DS, Blanch HW. Initial- and processive-cut products reveal cellobiohydrolase rate limitations and the role of companion enzymes. Biochemistry. 2012;51:442–52.
25. Zhou W, Xu Y, Schüttler HB. Cellulose hydrolysis in evolving substrate morphologies III: time-scale analysis. Biotechnol Bioeng. 2010;107:224–34.
26. Zhou W, Hao Z, Xu Y, Schüttler H-B. Cellulose hydrolysis in evolving substrate morphologies II: numerical results and analysis. Biotechnol Bioeng. 2009;104:275–89.
27. Griggs AJ, Stickel JJ, Lischeske JJ. A mechanistic model for enzymatic saccharification of cellulose using continuous distribution kinetics II: cooperative enzyme action, solution kinetics, and product inhibition. Biotechnol Bioeng. 2012;109:676–85.
28. Converse AO, Ooshima H, Burns DS. Kinetics of enzymatic-hydrolysis of lignocellulosic materials based on surface-area of cellulose accessible to enzyme and enzyme adsorption on lignin and cellulose. Appl Biochem Biotechnol. 1990;24–5:67–73.
29. Converse AO, Optekar JD. A synergistic kinetics model for enzymatic cellulose hydrolysis compared to degree-of-synergism experimental results. Biotechnol Bioeng. 1993;42:145–8.
30. Shang BZ, Chang R, Chu JW. Systems-level modeling with molecular resolution elucidates the rate-limiting mechanisms of cellulose decomposition by cellobiohydrolases. J Biol Chem. 2013;288:29081–9.
31. Asztalos A, Daniels M, Sethi A, Shen T, Langan P, Redondo A, Gnanakaran S. A coarse-grained model for synergistic action of multiple enzymes on cellulose. Biotechnol Biofuels. 2012;5:55.
32. Beckham GT, Bomble YJ, Bayer EA, Himmel ME, Crowley MF. Applications of computational science for understanding enzymatic deconstruction of cellulose. Curr Opin Biotechnol. 2011;22:231–8.
33. Luterbacher JS, Parlange JY, Walker LP. A pore-hindered diffusion and reaction model can help explain the importance of pore size distribution in enzymatic hydrolysis of biomass. Biotechnol Bioeng. 2013;110:127–36.
34. Chauve M, Huron M, Hudebine D, Decottignies D, Perez S, Ferreira NL. Kinetic modeling of β-glucosidases and cellobiohydrolases involved in enzymatic hydrolysis of cellulose. Ind Biotechnol. 2013;9:345–51.
35. Cruys-Bagger N, Elmerdahl J, Praestgaard E, Tatsumi H, Spodsberg N, Borch K, Westh P. Pre-steady-state kinetics for hydrolysis of insoluble cellulose by cellobiohydrolase Cel7A. J Biol Chem. 2012;287:18451–8.
36. Warden AC, Little BA, Haritos VS. A cellular automaton model of crystalline cellulose hydrolysis by cellulases. Biotechnol Biofuels. 2011;4:39.
37. Kumar D, Murthy GS. Stochastic molecular model of enzymatic hydrolysis of cellulose for ethanol production. Biotechnol Biofuels. 2013;6:63.
38. Väljamäe P, Sild V, Pettersson G, Johansson G. The initial kinetics of hydrolysis by cellobiohydrolases I and II is consistent with a cellulose surface-erosion model. Eur J Biochem. 1998;253:469–75.
39. Fenske JJ, Penner MH, Bolte JP. A simple individual-based model of insoluble polysaccharide hydrolysis: the potential for autosynergism with dual-activity glycosidases. J Theor Biol. 1999;199:113–8.
40. Sørensen TH, Cruys-Bagger N, Borch K, Westh P. Free energy diagram for the heterogeneous enzymatic hydrolysis of glycosidic bonds in cellulose. J Biol Chem. 2015;290:22203–11.
41. Ganner T, Aschl T, Eibinger M, Bubner P, Meingast A, Chernev B, Mayrhofer C, Nidetzky B, Plank H. Tunable mixed amorphous–crystalline cellulose substrates (MACS) for dynamic degradation studies by atomic force microscopy in liquid environments. Cellulose. 2014;21:3927–39.
42. Lehtiö J, Sugiyama J, Gustavsson M, Fransson L, Linder M, Teeri TT. The binding specificity and affinity determinants of family 1 and family 3 cellulose binding modules. Proc Natl Acad Sci USA. 2003;100:484–9.
43. Shang BZ, Chu J-W. Kinetic modeling at single-molecule resolution elucidates the mechanisms of cellulase synergy. ACS Catal. 2014;4:2216–25.
44. Beckham GT, Matthews JF, Peters B, Bomble YJ, Himmel ME, Crowley MF. Molecular-level origins of biomass recalcitrance: decrystallization free energies for four common cellulose polymorphs. J Phys Chem B. 2011;115:4118–27.
45. Kondo T, Sawatari C. A fourier transform infra-red spectroscopic analysis of the character of hydrogen bonds in amorphous cellulose. Polymer. 1996;37:393–9.
46. Kurasin M, Väljamäe P. Processivity of cellobiohydrolases is limited by the substrate. J Biol Chem. 2011;286:169–77.
47. Ogeda TL, Silva IB, Fidale LC, El Seoud OA, Petri DFS. Effect of cellulose physical characteristics, especially the water sorption value, on the efficiency of its hydrolysis catalyzed by free or immobilized cellulase. J Biotechnol. 2012;157:246–52.
48. Gupta R, Lee YY. Mechanism of cellulase reaction on pure cellulosic substrates. Biotechnol Bioeng. 2009;102:1570–81.
49. Lin Y, Silvestre-Ryan J, Himmel ME, Crowley MF, Beckham GT, Chu J-W. Protein allostery at the solid-liquid interface: endoglucanase attachment to cellulose affects glucan clenching in the binding cleft. J Am Chem Soc. 2011;133:16617–24.
50. Ståhlberg J, Johansson G, Pettersson G. A New model for enzymatic hydrolysis of cellulose based on the two-domain structure of cellobiohydrolase I. Nat Biotechnol. 1991;9:286–90.
51. Kostylev M, Moran-Mirabal JM, Walker LP, Wilson DB. Determination of the molecular states of the processive endocellulase *Thermobifida fusca* Cel9A during crystalline cellulose depolymerization. Biotechnol Bioeng. 2012;109:295–9.
52. Jervis EJ, Haynes CA, Kilburn DG. Surface diffusion of cellulases and their isolated binding domains on cellulose. J Biol Chem. 1997;272:24016–23.
53. Moran-Mirabal JM, Bolewski JC, Walker LP. *Thermobifida fusca* cellulases exhibit limited surface diffusion on bacterial micro-crystalline cellulose. Biotechnol Bioeng. 2013;110:47–56.
54. Guo J, Catchmark JMJ. Binding specificity and thermodynamics of cellulose-binding modules from *Trichoderma reesei* Cel7A and Cel6A. Biomacromolecules. 2013;14:1268–77.
55. Beckham GT, Matthews JF, Bomble YJ, Bu L, Adney WS, Himmel ME, Nimlos MR, Crowley MF. Identification of amino acids responsible for processivity in a family 1 carbohydrate-binding module from a fungal cellulase. J Phys Chem B. 2010;114:1447–53.
56. Cheng G, Datta S, Liu Z, Wang C, Murton JK, Brown PA, Jablin MS, Dubey M, Majewski J, Halbert CE, Browning JF, Esker AR, Watson BJ, Zhang H, Hutcheson SW, Huber DL, Sale KL, Simmons BA, Kent MS. Interactions of endoglucanases with amorphous cellulose films resolved by neutron reflectometry and quartz crystal microbalance with dissipation monitoring. Langmuir. 2012;28:8348–58.
57. Abuja P, Schmuck M, Pilz I, Tomme P, Claeyssens M, Esterbauer H. Structural and functional domains of cellobiohydrolase I from *Trichoderma reesei*. Eur Biophys J. 1988;9414:339–42.
58. Receveur V, Czjzek M, Schulein M, Panine P, Henrissat B. Dimension, shape, and conformational flexibility of a two domain fungal cellulase in solution probed by small angle x-ray scattering. J Biol Chem. 2002;277:40887–92.
59. Parkkinen T, Koivula A, Vehmaanperä J, Rouvinen J. Crystal structures of *Melanocarpus albomyces* cellobiohydrolase Cel7B in complex with cello-oligomers show high flexibility in the substrate binding. Protein Sci. 2008;17:1383–94.
60. Lynd LR, Weimer PJ, van Zyl WH, Pretorius IS. Microbial cellulose utilization: fundamentals and biotechnology. Microbiol Mol Biol Rev. 2002;66:506–77.
61. Koivula A, Kinnari T, Harjunpää V, Ruohonen L, Teleman A, Drakenberg T, Rouvinen J, Jones TA, Teeri TT. Tryptophan 272: an essential determinant of crystalline cellulose degradation by *Trichoderma reesei* cellobiohydrolase Cel6A. FEBS Lett. 1998;429:341–6.
62. Varrot A, Hastrup S, Schülein M, Davies GJ. Crystal structure of the catalytic core domain of the family 6 cellobiohydrolase II, Cel6A, from *Humicola insolens*, at 1.92 A resolution. Biochem J. 1999;337:297–304.
63. Armand S, Drouillard S, Schulein M, Henrissat B, Driguez H. A bifunctionalized fluorogenic tetrasaccharide as a substrate to study cellulases. J Biol Chem. 1997;272:2709–13.
64. Claeyssens M, Van Tilbeurgh H, Tomme P, Wood TM, McRae SI. Fungal cellulase systems. Comparison of the specificities of the cellobiohydrolases isolated from *Penicillium pinophilum* and *Trichoderma reesei*. Biochem J. 1989;261:819–25.
65. Bellesia G, Chundawat SPS, Langan P, Redondo A, Dale BE, Gnanakaran S. Coarse-grained model for the interconversion between native and liquid ammonia-treated crystalline cellulose. J Phys Chem B. 2012;116:8031–7.

66. López CA, Bellesia G, Redondo A, Langan P, Chundawat SPS, Dale BE, Marrink SJ, Gnanakaran S. MARTINI coarse-grained model for crystalline cellulose microfibers. J Phys Chem B. 2015;119:465–73.
67. Bu L, Beckham GT, Crowley MF, Chang CH, Matthews JF, Bomble YJ, Adney WS, Himmel ME, Nimlos MR. The energy landscape for the interaction of the family 1 carbohydrate-binding module and the cellulose surface is altered by hydrolyzed glycosidic bonds. J Phys Chem B. 2009;113:10994–1002.
68. Maurer SA, Bedbrook CN, Radke CJ. Cellulase adsorption and reactivity on a cellulose surface from flow ellipsometry. Ind Eng Chem Res. 2012;51:11389–400.
69. Maurer SA, Bedbrook CN, Radke CJ. Competitive sorption kinetics of inhibited endo- and exoglucanases on a model cellulose substrate. Langmuir. 2012;28:14598–608.
70. Eibinger M, Ganner T, Bubner P, Rošker S, Kracher D, Haltrich D, Ludwig R, Plank H, Nidetzky B. Cellulose surface degradation by a lytic polysaccharide monooxygenase and its effect on cellulase hydrolytic efficiency. J Biol Chem. 2014;289:35929–38.

Functional characterization of the native swollenin from *Trichoderma reesei*: study of its possible role as C1 factor of enzymatic lignocellulose conversion

Eibinger *et al. Biotechnol Biofuels (2016) 9:178*
DOI 10.1186/s13068-016-0590-2

Biotechnology for Biofuels

RESEARCH Open Access

Functional characterization of the native swollenin from *Trichoderma reesei*: study of its possible role as C_1 factor of enzymatic lignocellulose conversion

Manuel Eibinger[1†], Karin Sigl[1†], Jürgen Sattelkow[2], Thomas Ganner[2], Jonas Ramoni[3], Bernhard Seiboth[3], Harald Plank[2,4*] and Bernd Nidetzky[1,5*]

Abstract

Background: Through binding to cellulose, expansin-like proteins are thought to loosen the structural order of crystalline surface material, thus making it more accessible for degradation by hydrolytic enzymes. Swollenin SWO1 is the major expansin-like protein from the fungus *Trichoderma reesei*. Here, we have performed a detailed characterization of a recombinant native form of SWO1 with respect to its possible auxiliary role in the enzymatic saccharification of lignocellulosic substrates.

Results: The *swo1* gene was overexpressed in *T. reesei* QM9414 Δ*xyr1* mutant, featuring downregulated cellulase production, and the protein was purified from culture supernatant. SWO1 was *N*-glycosylated and its circular dichroism spectrum suggested a folded protein. Adsorption isotherms (25 °C, pH 5.0, 1.0 mg substrate/mL) revealed SWO1 to be 120- and 20-fold more specific for binding to birchwood xylan and kraft lignin, respectively, than for binding to Avicel PH-101. The SWO1 binding capacity on lignin (25 µmol/g) exceeded 12-fold that on Avicel PH-101 (2.1 µmol/g). On xylan, not only the binding capacity (22 µmol/g) but also the affinity of SWO1 ($K_d = 0.08$ µM) was enhanced compared to Avicel PH-101 ($K_d = 0.89$ µM). SWO1 caused rapid release of a tiny amount of reducing sugars (<1 % of total) from different substrates (Avicel PH-101, nanocrystalline cellulose, steam-pretreated wheat straw, barley β-glucan, cellotetraose) but did not promote continued saccharification. Atomic force microscopy revealed that amorphous cellulose films were not affected by SWO1. Also with AFM, binding of SWO1 to cellulose nanocrystallites was demonstrated at the single-molecule level, but adsorption did not affect this cellulose. SWO1 exhibited no synergy with *T. reesei* cellulases in the hydrolysis of the different celluloses. However, SWO1 boosted slightly (1.5-fold) the reducing sugar release from a native grass substrate.

Conclusions: SWO1 is a strongly glycosylated protein, which has implications for producing it in heterologous hosts. Although SWO1 binds to crystalline cellulose, its adsorption to xylan is much stronger. SWO1 is not an auxiliary factor of the enzymatic degradation of a variety of cellulosic substrates. Effect of SWO1 on sugar release from intact plant cell walls might be exploitable with certain (e.g., mildly pretreated) lignocellulosic feedstocks.

Keywords: SWO1, Swollenin, Expansin, *Trichoderma reesei*, Glycoprotein, Cellulose degradation, Synergism, Amorphogenesis, Atomic force microscopy

*Correspondence: harald.plank@felmi-zfe.at; bernd.nidetzky@tugraz.at
†Manuel Eibinger and Karin Sigl should be considered equal first authors
[1] Institute of Biotechnology and Biochemical Engineering, Graz University of Technology, Petersgasse 12/1, 8010 Graz, Austria
[2] Institute for Electron Microscopy and Nanoanalysis, Graz University of Technology, Steyrergasse 17, 8010 Graz, Austria
Full list of author information is available at the end of the article

Background

Through integrated developments in pretreatment technologies and cellulase engineering, much progress has been made in enhancing the efficiency of soluble sugar release from lignocellulosic feedstocks [1, 2]. However, the enzyme costs incurred in the saccharification step are still significant [2, 3]. There is high interest, therefore, in further decreasing the enzyme loading required in the process. Besides making the cellulases more effective *per se*, through improving their intrinsic activity [4–6] and facilitating their production [5, 7, 8], the reinforcement of existing cellulase preparations by auxiliary proteins and enzymes has attracted considerable attention [5, 9–13]. Lytic polysaccharide monooxygenase is a prominent example of an auxiliary enzyme, which is already in use to supplement cellulase preparations [10, 11, 14, 15]. Proteins lacking enzyme activity could also, in different ways, exert an auxiliary function in cellulose bioconversion. Inspired by Elwyn Reese's early C_1–C_x postulate (or updated variants thereof), invoking a non-hydrolytic, cellulose structure-disrupting C_1 factor that acts in synergy with hydrolytic enzymes (the C_x factor), the discovery of a possible C_1 factor of cellulose degradation has been a clear focus of interest in the research on auxiliary proteins [5, 10, 16].

Originally discovered from plants as cell wall-loosening proteins, expansins and expansin-like proteins constitute a widely distributed superfamily of proteins [17–19]. Besides plants, phylogenetically diverse microorganisms including bacteria and fungi, most of which grow in association with plants, were also found to contain expansins [20, 21]. Biologically, expansins are described to function as physical catalysts of cell wall enlargement and stress relaxation in plants. They appear to do so by promoting a rearrangement in the network of non-covalent interactions between the cell wall polysaccharides, in particular, those matrix glycans that interconnect individual cellulose microfibrils [19, 22]. By partly disrupting the bonding these glycans have to the microfibril surface and to each other, expansin action is supposed to enable the displacement of the cell wall polymers and, thus, to promote slippage in the points of their adhesion [19, 22, 23]. In microorganisms, expansins appear to be important factors of the colonization of plant tissues [24–27]. Although expansins do not weaken the cell wall or cause a lasting change in the wall structure [19] (except altering its size and shape [28]), they might, however, cause processes, sometimes referred to collectively as "amorphogenesis", in which cellulose or lignocellulose structures become disaggregated and loosened up. This amorphogenesis, and the beneficial effect it might have on the action of hydrolytic enzymes could make expansins broadly useful in cellulosic biomass conversion [21, 29–31].

Originally discovered by Saloheimo and colleagues [25] who showed it to cause swelling of cotton fibers, swollenin is a special expansin-like protein from fungi. It differs from the canonical expansins in size (~493 compared to ~225 amino acids) and also in the arrangement of structural modules within the protein structure. Expansins are modular proteins built of two discrete domains connected by a short linker [5, 26, 32]. The N-terminal domain shows weak resemblance to the catalytic module of family GH-45 glycoside hydrolases, lacking their full catalytic machinery, however [5, 25]. We refer to this aspect later under "Results" section, but expansins are generally described to lack polysaccharide hydrolase activity. The C-terminal domain resembles certain carbohydrate-binding modules (e.g., CBM family 3 or 63) [25, 33]. Both domains are required for the full cell wall-loosening activity of the expansins [32, 33].

Swollenin deviates from the basic expansin conformation by having an additional CBM from family 1 located N-terminally [5, 18, 25]. The expansin-like domain and the family 1 CBM are connected by a putative linker and/or fibronectin-III (Fn-III)-like domain [18, 34]. Linkers, in general, serve as flexible elements in protein structures [18, 35, 36]; however, little is currently known about the actual role of the linker region in swollenin. It is noted though that multiple Ser/Thr residues for *O*-glycosylation are present in the linker/Fn-III-like domain of swollenin [5, 37].

Expansin/swollenin "activity" has been assayed in different ways but it is generally difficult to evaluate. A biomechanical assay measures directly the effect of the protein on the fiber strength of the cellulosic material [19, 32]. Light microscopy was used often to track fiber disaggregation and other morphological changes in cellulosic material on incubation with swollenin [18, 34, 37–39]. Cellulose crystallinity was also determined to monitor the amorphogenesis [37, 38, 40]. To identify and characterize swollenin-caused changes in the surface properties of cellulose, biological methods (e.g., adsorption of CBM [41, 42]) and high-resolution microscopy (SEM and AFM) were used [18, 37, 41]. Synergy with cellulases in releasing soluble sugars from lignocellulosic substrates presents a highly indirect but use-inspired way of expressing swollenin activity [34, 37, 40, 43–45]. Table 1 summarizes the results from different papers analyzing the possible involvement of swollenin in the degradation of lignocellulosic substrates. The studies were selected because besides synergy with cellulases, which has been the topic of numerous papers, they also examined the effect of swollenin on the morphology of the cellulosic substrate used. As it becomes clear from Table 1, the current literature does not offer a conclusive picture, thus motivating the present study to obtain clarification.

Table 1 Summary of reported structural changes in lignocellulosic substrates caused by swollenin preparations obtained through different strategies of protein expression and production

Native source/produced in/purification/aMm	Substrates	Experimental setup; employed methods	Effects	Ref.
T. reesei/*S. cerevisiae*/CS/~75 kDa	Mercerized cotton fibers	0.25 $\mu g_{Swo}/g_{substrate}$, 25 °C, 4 h; light microscopy	Local disruption of cotton fibers, no release of sugars	[18]
T. reesei/*S. cerevisiae*/CS/~75 kDa	Whatman No. 3 filter paper	5 mL CS/filter paper strip, room temperature, 15 min; paper strength test	Reduction of tensile strength and average peak load (15–20 %)	[18]
T. reesei/*A. niger*/AC/~80–95 kDa	*Valonia* sp. cell wall fragments	10 $\mu g_{Swo}/g_{substrate}$, 45 °C, 48 h; AFM, light microscopy	Partial disintegration to isolated fibers, no release of sugars	[18]
A. fumigatus/*A. oryzae*/AC/~85 kDa	Avicel PH-101, filter paper (603 cellulose thimbles)	0.8 $\mu g_{Swo}/mg_{Avicel}$, 8 $\mu g_{Swo}/mg_{filter\ paper}$, 40 °C, 72 h; light microscopy, visual examination	Avicel PH-101 particle size reduction (~50 %), effect is pH- and temperature-dependent; complete disruption of filter paper, no release of sugars	[34]
T. reesei/*K. lactis*/IMAC/~100 kDa	Whatman No. 1 filter paper, α-cellulose, Avicel PH-101, sigmacell 101	20 $\mu g_{Swo}/mg_{substrate}$, 45 °C, 48 h; XRD, laser diffraction	Reduction of CrI (~10 up to 22 %) and particle size (up to ~30 %) was observed for all substrates except Sigmacell	[37]
T. reesei/*K. lactis*/IMAC/~100 kDa	Whatman No. 1 filter paper	20 $\mu g_{Swo}/mg_{substrate}$, 45 °C, 48 h; SEM, photography	Deagglomeration of filter paper (reduction of particle size and count); SEM showed an increased surface roughness; no swelling was observed	[37]
T. asperellum/*E. coli*/refolding, AC/~35–50 kDa	Avicel PH-101	5 $\mu g_{Swo}/mg_{substrate}$, 50 °C, 91 h; light microscopy	Partial disruption of Avicel PH-101 particles	[38]
T. pseudokoningii/*A. niger*/HIC/~75 kDa	Avicel PH-101, filter paper	5–20 $\mu g_{Swo}/mg_{Avicel}$, 0.5–2 $\mu g_{Swo}/mg_{filter\ paper}$, 40 °C, 48–72 h; light microscopy, XRD	No effects were observed by applying light microscopy; CrI was increased (88–90 %)	[40]
T. reesei/*T. reesei*/IMAC, IE/n.a.	Mercerized cotton fibers	10 $\mu g_{Swo}/mg_{substrate}$, 50 °C, overnight; CBM adsorption assay, SEM	Available surface for CBMs was increased (~38 %); SEM showed a smoothed surface upon *Tr*Swo1 treatment	[41]
T. reesei/*E. coli* and *N. tabacum*/CS/n.a.	Mercerized cotton fibers	0.2–2 $\mu g_{Swo}/mg_{substrate}$, 37 °C or 50 °C, 8 h; phase contrast microscopy	Fiber expansion, inner fiber structure was altered independent of the *Tr*Swo1 source	[28]
P. oxalicum/*T. reesei*/precipitation, IMAC/~90 kDa	Avicel PH-101	4 $\mu g_{Swo}/mg_{substrate}$, 50 °C, 48 h; light microscopy, protein binding assay	Partial disruption of Avicel PH-101 particles; B_{max} for cellulases was increased (~20 %)	[39]
T. reesei/*T. reesei*/IMAC, IE/n.a.	Dissolving pulp, various lignocellulosic pulps	50 $\mu g_{Swo}/mg_{substrate}$, 50 °C, overnight; high-resolution fiber quality analyzer	Fragmentation was observed to a low extent for dissolving pulp fibers but not for lignocellulosic pulps	[42]
Orpinomyces sp. strain C1A/*E. coli*/refolding, IMAC/~67 kDa	Cotton fibers	0.25–5 $\mu g_{Swo}/mg_{substrate}$, 39 °C, 12 h; ESEM, Congo red cotton assay	Average cotton fiber width was increased (~56 %); dye adsorption was increased (CAE ~0.4 for 5 $\mu g_{Swo}/mg_{substrate}$)	[78]

aMm apparent molecular mass, *CS* enriched culture supernatant, *AC* affinity chromatography, *IMAC* immobilized metal adsorption chromatography (via His-tag), *HIC* hydrophobic interaction chromatography, *IE* ion exchange chromatography, *n.a.* not available

In the absence of a clear parameter able to capture the functionality of swollenin in an alleged amorphogenesis process, it is crucially important in the search of cause-and-effect relationships that the protein preparation used is well defined in its main structural characteristics. In addition, for the purpose of rigorously establishing an intrinsic biological reference, the swollenin should be as native-like as possible. Previous studies have obtained the recombinant swollenin through heterologous expression of the coding gene in foreign hosts (e.g., *Escherichia coli*, *Pichia pastoris*, *Saccharomyces cerevisiae*, *Aspergillus* sp.) [18, 28, 37–40, 43, 45], bearing in each case the risk that non-native post-translational processing, especially glycosylation, could affect the protein function [46, 47]. Fusion tags were also used to facilitate protein purification [42, 44, 48], but whether these modifications of the native structure are functionally silent or interfere with the original function of the swollenin is not known. The yield of recombinant swollenin from heterologous production was usually in the low (≤20–100) mg/L culture range [21], and to our knowledge, proper folding of the recombinant protein was never assessed.

In this study of SWO1, the major swollenin of *Trichoderma reesei* (anamorph *Hypocrea jecorina*), we addressed the urgent concern about the nativeness of recombinant swollenin by producing the protein via homologous overexpression in the native host. To largely eliminate the otherwise huge cellulase and hemicellulase background in the secretome of *T. reesei*, a mutant QM9414 strain was used in which, as shown in earlier work, the hydrolytic enzyme production was strongly downregulated due to *xyr1* transcriptional regulator gene knockout [49]. Using the target protein thus produced and purified from culture supernatant, a detailed functional characterization of SWO1 was performed. Besides adsorption studies, this included direct measurements of a possible cellulose structure-disrupting activity of SWO1. Synergy with *T. reesei* cellulases was evaluated during degradation of different cellulose substrates.

Results

Recombinant production and purification of the native SWO1

The genetic background of *T. reesei* QM9414 Δ*xyr1* was previously shown to present a useful vehicle for the overexpression of individual secreted proteins in an overall cellulase- and hemicellulase-free environment [49]. The coding region of the *swo1* gene was, therefore, integrated genomically under control of the *cdna1* promoter. In positive recipient strains, the presence of the *swo1* expression cassette was verified by PCR, and secretion of the target protein into the culture supernatant was also clearly indicated in SDS-PAGE. The recombinant SWO1 was produced in a 2-L bioreactor cultivation of the *T. reesei* integrant strain, using glucose as the carbon source. The fungal secretome comprised SWO1 as a major protein component, as shown in Fig. 1a. Prominent protein band at about 75 kDa mass which was absent from the supernatant of the control strain indicated secretion of recombinant protein. Using batch chromatography on Avicel PH-101 as an affinity adsorbent, SWO1 was isolated from the supernatant in just a single step of downstream processing, as shown in Fig. 1b. The protein yield was about 4 mg/L of culture. The apparent molecular mass of SWO1 in SDS-PAGE (~75 kDa) differed substantially from the mass of 49 kDa expected from protein's amino acid sequence, consistent with the observations of Saloheimo et al. [18] who used Western blotting for detection of SWO1 in *T. reesei* culture supernatants. This unusually high molecular mass plus the fact that the purified protein migrated as a single but relatively diffuse band in SDS-PAGE suggested that the recombinant SWO1 was strongly glycosylated. There are four *N*-glycosylation sites in the sequence of SWO1, three of which are identified as strong candidates to become glycosylated [48]. The linker/Fn-III-like domain might be additionally *O*-glycosylated [18, 37, 48]. Figure 1c shows that on incubation with Endo H for removal of protein *N*-glycans, the apparent molecular mass of the native SWO1 was only slightly reduced (~5 kDa). This suggests that the difference between the calculated and observed molecular mass cannot be explained only as a result of *N*-glycosylation, and that *O*-glycosylation might contribute to the difference. Direct glycostaining in the gel confirmed the presence of glycans on both the native and the Endo H-treated SWO1 (Fig. 1d). We, therefore, concluded that the recombinant SWO1 was *N*-glycosylated but also strongly *O*-glycosylated.

Structural analysis of SWO1 using circular dichroism spectroscopy and protein modeling

The far-UV CD spectrum of purified SWO1 is shown in Fig. 2a. This suggested a folded protein with a high content of β-strand relative to α-helical secondary structure. It also indicated a large portion of the protein structure to lack a discrete organization into secondary structural elements. Analysis of the spectrum with DichroWeb suggested SWO1 to be composed of just 7 % α-helices, 34 % β-strands, 18 % turns and 34 % unordered structure. Structural modeling of SWO1 (UniProt ID: Q9P8D0) was done with Phyre2 [50], analyzing the entire protein except for the amino acids 1–18, which are predicted to be cleaved off after secretion. Figure 2b shows a hypothetical structure of SWO1 rendered from the models of the two modules. Due to the amount of proteins with known three-dimensional structure ($N \geq 10$) resembling

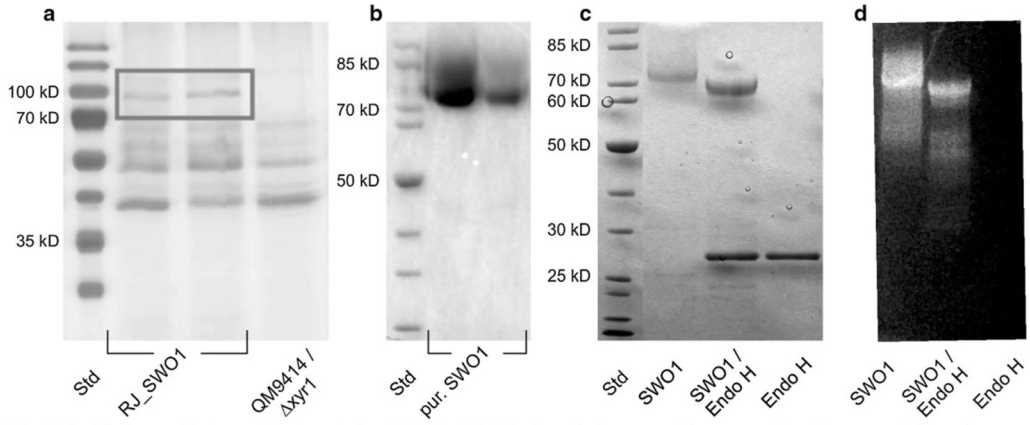

Fig. 1 Identification, purification and deglycosylation of SWO1. **a** SWO1 (indicated with a *rectangle*) was recombinantly expressed in *T. reesei* QM9414 Δxyr1 (designated as RJ_SWO1) and secreted into the culture media (two independent fermentations are shown). A prominent band at about 75 kDa, which was absent in an untransformed control strain, was identified as SWO1. **b** Single-step batch chromatography on Avicel PH-101 as adsorbent was used to purify SWO1 (two independent purifications are shown). The purified protein migrated as a single but relatively diffuse protein band, suggesting that the recombinant SWO1 was strongly glycosylated. **c** Deglycosylation of SWO1 with Endo H resulted in a decrease of the apparent molecular mass by roughly 5 kDa and a more sharply focused protein band was obtained in the SDS-polyacrylamide gel. **d** Direct glycostaining of the same gel shown in **c** confirmed the presence of glycans on both the native and the Endo H-treated SWO1

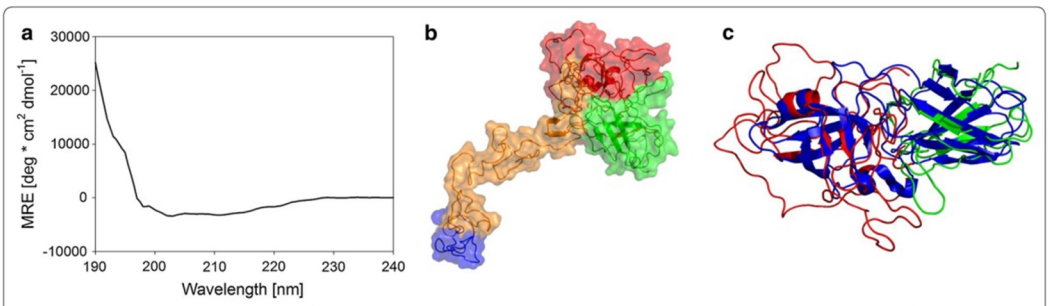

Fig. 2 CD spectra and homology model of native SWO1. **a** Smoothed CD spectrum of native SWO1 in 50 mM sodium acetate buffer, pH 5.0, at room temperature. For further details of the measurement, see the "Methods" section. **b** The automated protein structure homology-modeling server Phyre2 was used to predict the protein structure of SWO1 (UniProt ID: Q9P8D0). The distinct domains are colored as follows: family 1 CBM (*blue*); linker/Fn-III-like domain (*orange*); GH45 domain (*red*); expansin-like CBM (*green*). **c** A structural overlay of the modeled expansin-like domain from SWO1 with EXLX1 from *B. subtilis* (PDB ID: 4FG2) was made to allow visual comparison. The distinct domains are colored as follows: EXLX1 (*blue*); GH45 domain (*red*); expansin-like CBM (*green*). Overall, 87 % of the input sequence was modeled at >90 % confidence, and 61 residues were modeled ab initio. The depicted model was used to calculate the percentage of secondary structure elements

either expansins or CBMs and sufficient sequence similarity, the structural models of the family 1 CBM (CBD form EG I, sequence identity: 50 %) and the expansin-like domain (e.g. β-expansin from maize, sequence identity: 28 %) appear to be plausible. In addition, a structural overlay of the modeled expansin-like domain with a crystallized bacterial expansin (EXLX1 from *B. subtilis*, PDB ID: 4FG2) is provided in Fig. 2c to allow a visual comparison of the related domains. Overall, 87 % of the input sequence was modeled at >90 % confidence, and 61 residues were modeled ab initio. Moreover, the relative content of secondary structure elements calculated from the structure model was reasonably similar to that determined from the CD spectrum. It was 3 % α-helices, 23 % β-strands, 41 % turns and 33 % unordered structure. Finally, the sequence-based prediction tool (JPred4)

[51] suggested a similar content of α-helices (3 %) and β-strands (20 %). In summary, these results provided good evidence suggesting that the SWO1 as isolated was most likely properly folded.

Adsorption of SWO1 to insoluble polysaccharides

Isotherms for the adsorption of SWO1 to Avicel PH-101, birchwood xylan and kraft lignin were determined at 25 °C and pH 5.0 employing the insoluble substrate in a concentration of 1.0 mg/mL. Using Avicel PH-101 under comparable conditions, preliminary experiments showed that most of the SWO1 was bound rapidly within 30 min and that apparent adsorption equilibrium was reached after 60 min. In accordance with an earlier study from Jäger et al. [37], isotherms were, therefore, obtained from incubations for 120 min, and the results are shown in Fig. 3. With each substrate, the binding of SWO1 appeared to correspond to a simple Langmuir adsorption isotherm. Note that Avicel PH-101 contains minor fractions of xylan (<2 %) and lignin (<1 %) [52, 53]. However, nothing is known about their localization and structural organization. For this reason and also supported by the seemingly appropriate fit ($R^2 \geq 0.98$), we do not consider the use of an alternative multiple binding site isotherm for Avicel PH-101. The corresponding fit of the data gave the binding constants summarized in Table 2. Remarkably, the binding capacity (B_{max}) of SWO1 was much higher (≥12-fold) on xylan and lignin than it was on Avicel PH-101. The binding affinity in terms of the reciprocal dissociation constant (K_d) was also higher (11-fold) on xylan than on Avicel PH-101. In terms of B_{max}/K_d, therefore, the specificity of SWO1 for binding to xylan exceeded that for binding to Avicel PH-101 almost 120-fold. The specificity for binding to lignin lay in between the two (Table 2). Based on K_d values reported, recombinant SWO1 obtained by heterologous expression in *Kluyveromyces lactis* bound to Avicel PH-101 with similar affinity as the natively produced SWO1 does. This result could be interpreted to mean that the binding affinity of SWO1 on Avicel PH-101 is not majorly affected by the degree of nativeness its glycosylation has. Interestingly, expansin-like proteins of bacterial origin bound to Avicel PH-101 with K_d values similar to that of SWO1, suggesting perhaps that the glycosylation is not a crucial element of binding as far as the K_d is concerned. Only to note, cellulases harboring a family 1 carbohydrate-binding module showed K_d values of Avicel PH-101 binding agreeing with the K_d of SWO1 within the same order of magnitude [37, 54, 55].

Table 2 Summarized adsorption parameters of SWO1 on Avicel PH-101, birchwood xylan and lignin

Substrate	Avicel PH-101	Lignin	Xylan
B_{max} (μmol/g)	2.11 ± 0.39	25.1 ± 1.48	22.3 ± 3.13
K_d (μM)	0.89 ± 0.30	0.53 ± 0.11	0.08 ± 0.04
Absolute specificity (L/g)[a]	2.4	47.4	279
Relative specificity[b]	1.00	20.0	118

SWO1 showed the highest affinity and specificity for xylan followed by lignin and pure cellulose. B_{max} maximum binding capacity, K_d dissociation constant

[a] B_{max}/K_d

[b] Absolute specificities normalized on Avicel PH-101

Is the native SWO1 active on its own in the depolymerization of glycan substrates?

Andberg et al. [48] reported a His-tagged preparation of SWO1 to promote the release of reducing sugars from different substrates, in particular, barley β-glucan, whose conversion involved a remarkably high specific activity of SWO1 of 7 U/mg. The SWO1 produced and purified from *Aspergillus niger* var. *awamori* showed a similar specific activity on β-glucan substrate. As these findings

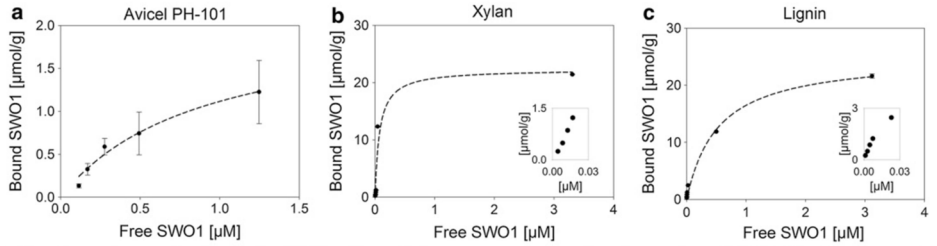

Fig. 3 Adsorption isotherms of purified native SWO1 on lignocellulose components. Experiments were done at 25 °C in 50 mM sodium acetate, pH 5.0, over 2 h with shaking (500 rpm). Substrate concentration was 1 mg/mL in a total reaction volume of 200 μL. *Symbols* show the measured data and *error bars* show the SD from three independent experiments. *Insets* present a zoomed view on the initial data points for SWO1 adsorption on xylan and kraft lignin. The fitted Langmuir isotherms are shown as *dashed lines* and the corresponding parameters, maximum binding capacity related to the unit mass of substrate (B_{max}) and the dissociation constant K_d, are summarized in Table 2

implied SWO1 to be active enzymatically, with certain substrates at least, we also examined the native SWO1 for its ability to degrade different insoluble glycans via soluble sugar release. Figure 4a shows the results. Compared to incubations in which BSA was used as an inactive control, incubations with SWO1 caused a slightly enhanced sugar formation. However, only a tiny amount of soluble sugars was produced in comparison to the total sugar available from the substrates in polymeric form. Sugars released from cellulose were detected as glucose, because β-glucosidase was added to the reaction samples later. The product released from the β-glucan was shown to be mainly cellobiose (≥90 %). We calculated that the sugar release from the β-glucan (Fig. 4a) would correspond to a specific activity of only around 0.1 mU/mg, equivalent to just six turnovers of SWO1 within 24 h. Andberg et al. [48] observed a comparable conversion (≤1.2 mg/g) when studying the conversion of β-glucan. However, their reported specific activity of SWO1 was increased by orders of magnitude (7 U/mg). The apparent conflict in these findings is resolved by considering that the kinetics of sugar formation by SWO1 was completely unlike a "normal" enzymatic reaction. They reported a rapid accumulation of sugar in the supernatant initially (≤10 min) but no further release on prolonged incubation up to 24 h.

In our view, therefore, these effects of SWO1 appear inconsistent with its action as a true cellulase, however, weakly active. An alternative explanation is that the observable SWO1 "activity" on Avicel PH-101 and CNC resulted from the release into solution of sugars (e.g., short oligosaccharides) that were initially tightly associated with the solid material but became detached on binding of the SWO1. Note: even BSA, which we assume to interact completely unspecifically with the cellulose preparations used, caused release of trace amounts of soluble sugars as reported previously [44] (Fig. 4a).

The sugar release from barley β-glucan (Fig. 4a) might, however, reflect a tiny intrinsic hydrolase activity of SWO1. BSA does not produce detectable sugars from this substrate. Following Andberg et al., we, therefore, also examined cellotetraose as a substrate of SWO1 and show the results in Fig. 4b. While being absent from the controls, cellobiose was clearly formed in the incubation with SWO1. The amount of cellobiose released (200 µM) was explained by the cellotetraose converted (100 µM). Since no glucose was formed, the cleavage of cellotetraose appeared to have been quite specific. Utilization of the oligosaccharide substrate was also specific because cellotriose, which was present in the reaction from the beginning due to the composition of the commercial cellotetraose preparation, was not attacked at all by the SWO1. The turnover of the cellotetraose substrate by SWO1 was extremely low (0.14 min^{-1}). It is called in remembrance that the C-terminal domain of SWO1 resembles structurally the catalytic modules of family GH-45 glycoside hydrolases but lacks their full active-site machinery due to the absence of a catalytic base. Therefore, considering the low level of activity that family GH-45 enzymes retain on substitution of their catalytic

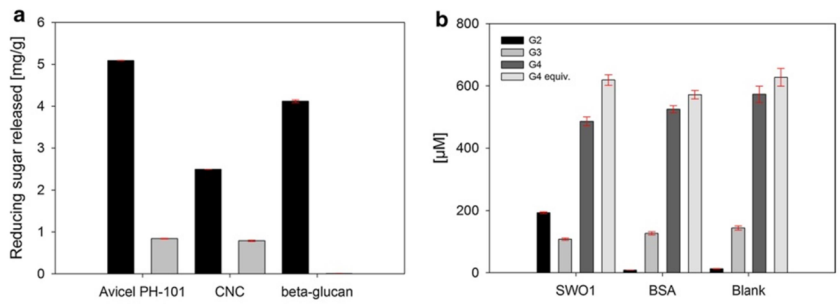

Fig. 4 Activity of SWO1 on various glycan substrates. **a** The substrates used were Avicel PH-101, CNC and β-glucan (1 mg/mL each) in 50 mM sodium acetate buffer, pH 5.0. Incubation was for 24 h at 40 °C with shaking (500 rpm). Avicel PH-101 and CNC were incubated with 0.4 µM SWO1 (*black bars*) or an equimolar amount of BSA (*grey bars*). Reactions were stopped by heating and incubated with β-glucosidase. The glucose released was measured with an enzymatic assay. *Error bars* show SD from four independent experiments. Barley β-glucan was incubated with either 0.2 µM SWO1 or BSA. The liberated sugars were assayed with HPAEC-PAD, and cellobiose was identified as the main product of SWO1 activity. *Error bars* are from two independent experiments. **b** Cellotetraose (0.5 mg/mL) was incubated with either 0.5 µM SWO1 or BSA in 50 mM sodium acetate buffer, pH 5.0, for 24 h at 40 °C with shaking (500 rpm). The product distribution (*G2* cellobiose, *G3* cellotriose, *G4* cellotetraose) was determined with HPAEC-PAD. *Error bars* were estimated from two independent experiments

base by a non-functional residue [5, 26], one would not expect SWO1 to be a proficient catalyst of the hydrolysis of glycosides.

We also assayed the hydrolysis of 4-methylumbelliferyl-β-D-cellobioside, a suitable substrate for various cellulases [5, 56], but did not observe activity of the purified SWO1 in any of the possible cleavage modes, releasing 4-methylumbelliferone or 4-methylumbelliferyl-β-D-glucoside.

Effect of SWO1 on cellulose crystallinity measured by wide-angle x-ray scattering

Avicel PH-101 was incubated for 72 h in the presence of an SWO1 concentration, which according to the adsorption isotherm (Fig. 3; Table 2) was "catalytic" (0.05 mol %) relative to the available binding sites on this substrate. We considered that a possible amorphogenesis, caused by the dynamic action of SWO1, might be detectable as a decrease in the overall crystallinity of Avicel PH-101 which we measured by wide-angle x-ray scattering (WAXS) [57–59]. The results are shown in Fig. 5. A lowering of the crystallinity index would show in the WAXS profile as an intensity decrease in the major scattering peak at about 22.7°. Changes in the peak's shape and position would also indicate transformations of the original crystalline cellulose (allomorph I_β) into another allomorph or into amorphous material [58, 60]. Figure 5 is clear in showing that SWO1 had no effect on Avicel PH-101 structure to the extent detectable with the WAXS method used. This result contrasts, to some extent, with the findings of Jäger et al. [37] who reported changes in Avicel PH-101 crystallinity index on incubation with a *Tr*SWO1 produced recombinantly in *K. lactis*.

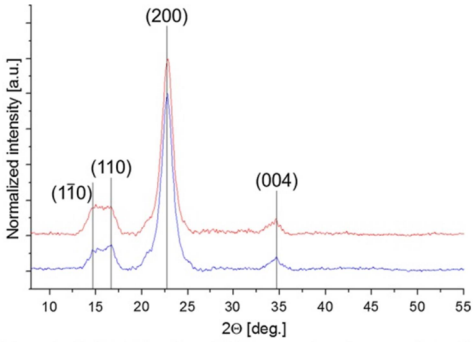

Fig. 5 Stacked WAXS profiles of SWO1-treated and untreated Avicel PH-101. Avicel PH-101 (10 mg/mL) was incubated in 50 mM sodium acetate buffer, pH 5.0, with 0.01 μM SWO1 (*red*) or without enzyme (*blue*), for 72 h at 40 °C with agitation (150 rpm). Relevant peaks for cellulose I_β were resolved and indexed with Miller indices. No changes in intensity or peak's shape and position were observed

Effect of SWO1 on fully amorphous and highly crystalline cellulose preparations measured by atomic force microscopy in a liquid environment

We considered that while global parameters of cellulose structural organization such as the crystallinity index (see Fig. 5) might not be suitable to capture the relevant components of an SWO1-caused amorphogenesis, a method able to reveal even subtle changes in cellulose surface morphology, and to do so in a time and laterally resolved manner, could be very useful for the identification and characterization of hidden SWO1 functions. Like in our previous studies of cellulases [57, 61, 62] and LPMO [12], atomic force microscopy (AFM) in a liquid environment was used, because the protein function could, thus, be analyzed in a setting modeled on the natural process. To contrast the effect of two completely different types of cellulose, we examined a fully amorphous cellulose film (ATFC) and cellulose nanocrystals (CNC), both spin-cast on silicon wafers [57].

Figure 6 shows the analysis of the amorphous cellulose treated with SWO1. The cellulose film provides a homogeneous and nanoflat surface for SWO1 to act upon (Fig. 6a, b). The overall surface roughness was below 5 nm. Height profiles were recorded from the surface at two representative regions of 1 μm^2 area before and after treatment with SWO1. The results did not reveal changes in the surface topography as result of SWO1 action. Local effects of SWO1 on swelling or disruption of the cellulose surface, both of which would change the height, would have been clearly detectable with the method used (Fig. 6c, d). It appears, therefore, that on the amorphous cellulose used, SWO1 was inactive as a structure-loosening factor.

CNCs present a highly recalcitrant form of cellulose. From the herein applied method of their preparation [57, 63], the CNCs appeared as needle-like structures of about 100–200 nm length and about 3–70 nm width, as shown in Fig. 8. The CNCs were incubated with SWO1 and also with BSA as a control, and a representative area of each specimen (>1 μm^2) was analyzed with AFM. In spite of extensive data analysis that involved the characterization of numerous CNCs in each image ($N \geq 20$) at different levels of their structure, significant changes in the substrate were recognized neither in the SWO1 incubation nor in the BSA control. To examine the samples in more detail, they were washed after 24 h of incubation, dried and again analyzed with AFM. Results in Fig. 7A, B served to localize single BSA molecules, showing that they were attached mostly to the surface of the silicon wafer, apparently in a random fashion, and only occasionally to the CNCs. The situation was notably different when SWO1 was used, as shown in panels C and D of Fig. 7. Despite unspecific binding to the wafer surface

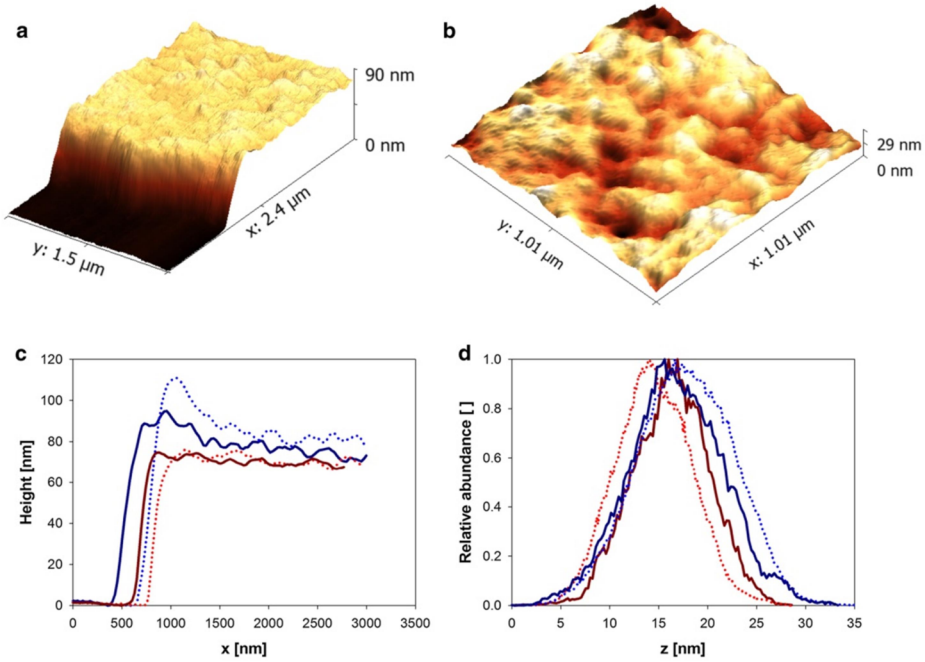

Fig. 6 AFM imaging of SWO1 action on ATFC. **a** A three-dimensional representation of the experimental setup. ATFC of defined height is placed on a silicon wafer, which can be used as reference. **b** The ATFC surface is homogenous and nanoflat with a mean surface roughness below 5 nm. **c** ATFC substrates on a single silicon wafer (~1 cm^2) were incubated in 50 mM sodium acetate buffer, pH 5.0, at 40 °C with mild agitation in a total reaction volume of 2 mL. Two exemplary height profiles from ATFC substrates after incubation with (*blue*) or without 0.4 µM SWO1 (*red*) after 24 h are shown. No significant changes induced by SWO1 incubation were found. Note that the edges of amorphous cellulose films were slightly deformed due to a cutting process prior to the addition of SWO1. Thus, only the surface with a certain distance (~1.0 µm) to the edge was analyzed. **d** Height distribution profiles of spots on the ATFC surface after incubation with (*blue*) or without SWO1 (*red*) using the same experimental conditions as stated above. A broadening of the peak, which would indicate degradation or swelling, is not visible. Analyzed areas were at least 1 μm^2

to some degree, SWO1 showed the clear trend to become enriched around the CNCs (panel C). Imaging of single CNCs at a resolution down to single protein particles revealed multiple sphere-like SWO1 molecules bound at both sides of the cellulose rod (panel D). Specific adsorption of SWO1 to CNCs is, therefore, suggested to surpass a mere adhesion of the protein to the hydrophobic surface of the wafer. Analysis of the distribution of height and width in multiple CNCs after the incubation and comparison of the result with the corresponding distribution of the untreated sample reveal that BSA really had no effect whatsoever on the size properties of the cellulosic substrate (Fig. 7E). SWO1, by contrast, caused the width distribution to shift by about 3 nm to an elevated mean value (Fig. 7E). Adsorption of SWO1 along the sides of the nanocrystals is likely to have caused this effect.

Interesting observation from these AFM analyses was that despite having a similar apparent mass like BSA (~66 kDa), SWO1 particles appeared distinctly larger (10–30 nm diameter) in the images than BSA particles, as recognized clearly when comparing panels B and D in Fig. 7. We think that the high glycosylation of SWO1 and the consequently pronounced hydration of the protein could explain the effect. Features of the cellulose nanocrystals recorded from the SWO1 experiment appear strongly blurred in comparison to the BSA experiment, which is most likely related to hydration. Figure 8 illustrates the effect in more detail, comparing height (panel A) and phase (panel B) images from the experiment with SWO1. Phase imaging depicts the dissipative interaction energy density and allows a clear distinction between materials with different characteristics (e.g., CNCs and enzymes). By comparison with the height

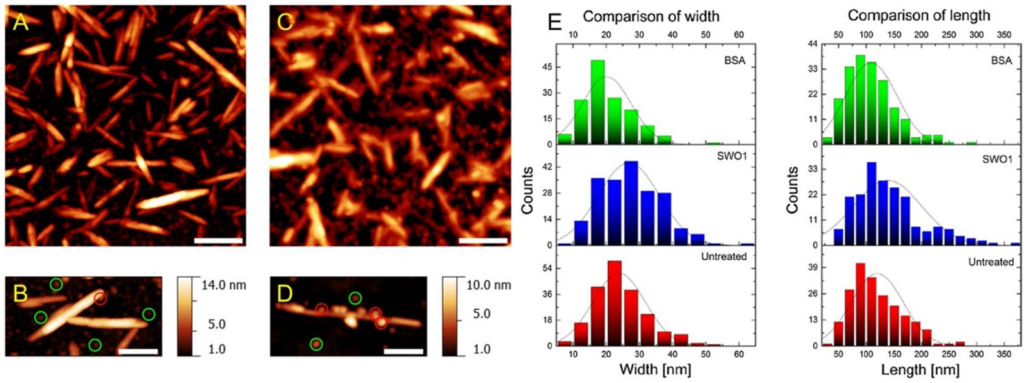

Fig. 7 AFM imaging of SWO1 action on CNCs. CNCs on a single silicon wafer (~1 cm^2) were incubated with either 0.4 μM BSA (**A**, **B**) or SWO1 (**C**, **D**) in 50 mM sodium acetate buffer, pH 5.0, at 40 °C with mild agitation. Incubation was done over 24 h in a total reaction volume of 2 mL. AFM imaging was done on dried silicon wafers at room temperature. No evidence for BSA- or SWO1-induced structural changes were found by visual examination. However, the presence of molecules attached to either CNCs or the silicon wafer can be observed (**A**–**D**). Most of the BSA molecules are positioned randomly on the silicon wafer (**A**). An exemplary amplified section is shown in **B**. Multiple BSA molecules are visible (*green circles*), and only one BSA molecule seems to be associated with a crystallite (*red circle*). Contrary, SWO1 showed a clear trend to become attached to CNCs (**C**). An exemplary amplified CNC confirmed that the ratio of molecules attached to crystals (*red circles*) and particles on the surface (*green circles*) has significantly increased (**D**). Note that for an easier viewing, not all BSA/SWO1 molecules are highlighted (**D**). **E** Statistical analysis of the size distribution showed an apparent increase in the width of CNCs upon incubation with SWO1. However, this effect is attributed to the size of the adsorbed protein and the presence of a hydration shell (see Fig. 8). *Scale bars* 100 nm

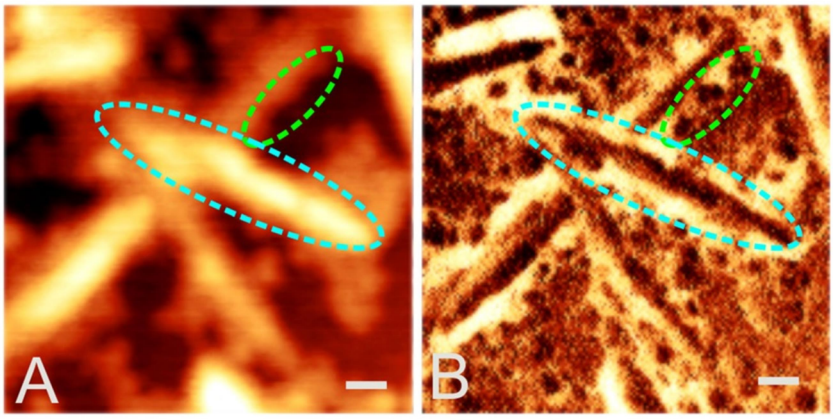

Fig. 8 Details of SWO1 binding to CNCs revealed by AFM phase imaging. CNCs on a single silicon wafer (~1 cm^2) were incubated with 0.4 μM SWO1 in 50 mM sodium acetate buffer, pH 5.0, at 40 °C with agitation. Incubation was done over 24 h in a total reaction volume of 2 mL. AFM imaging was done on dried silicon wafers at room temperature. **A** Recorded height images of CNCs are blurred, and structural features or proteins are not readily visible. **B** Phase imaging allowed the visualization of features like CNC-attached proteins (*green dashed ellipse*) covered by a hydration shell (bright layer enveloping CNCs). By comparison with the height image (*cyan dashed ellipse*), it is clear that the hydration shell is also, at least, partly responsible for the apparent broadening of the CNCs (Fig. 7E). The hydration shell is not present or significantly reduced upon incubation with BSA. *Scale bars* 30 nm

data, the phase image reveals the presence of multiple structural features, which are convoluted and blurred in the height image. First, CNCs appear to be thinner in phase imaging, and second, CNCs are surrounded by a bright layer with a unique phase signal, which represents most likely a hydration shell. In addition, SWO1

molecules, either free or attached to CNCs, embedded in the hydration shell can be observed, which are not readily visible in the height image (Fig. 8). The hydration shell is contributing to the apparent broadening of the CNCs and is not present or significantly reduced upon incubation with BSA.

Synergy between SWO1 and *T. reesei* cellulases in releasing soluble sugars from different lignocellulosic substrates

Ability of SWO1 to boost the hydrolysis of different lignocellulosic substrates by the complete *T. reesei* cellulase system was analyzed. Figure 9 shows time courses of reducing sugar release from Avicel PH-101 and CNCs under conditions in which the celluloses were pre-incubated with SWO1 or BSA for 24 h and cellulases were then added to initiate the hydrolysis. The results are clear in showing that SWO1 did not enhance the substrate conversion. We also examined the effect of SWO1 on the hydrolysis of filter paper but found none. Note: using light microscopy, we further analyzed if incubation with SWO1 alone caused disintegration of the fibrous filter paper material. This did not occur. Wheat straw, that had been pretreated by steam explosion, and birchwood xylan were also tested as substrates of enzymatic hydrolysis in the absence and presence of SWO1. Again, there was no boosting effect by SWO1 within the limits of experimental error, and the SWO1 lacked sugar-releasing activity on its own.

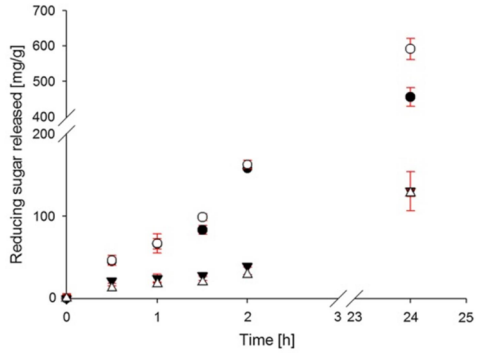

Fig. 9 Effect of SWO1 pretreatment on the enzymatic hydrolysis of cellulosic substrates. The substrates used were Avicel PH-101 (○/●) and CNCs (△/▼). The substrate concentration was 1 mg/mL. All reactions were done in 50 mM sodium acetate buffer, pH 5.0, at 40 °C with shaking (500 rpm) in a total reaction volume of 1.5 mL. Prior to the addition of cellulase, the substrate preparation was incubated with 0.4 μM SWO1 (●/▼) or BSA (○/△) for 24 h. *T. reesei* cellulase and β-glucosidase were then added in a small volume (60 μL) to a final enzyme loading of 20 μg/mg substrate and 4 μg/mg substrate, respectively. The mixture was incubated for another 24 h using the same conditions as stated above. The liberated glucose was measured with an enzymatic assay. *Error bars* show SD from four independent experiments

Finally, we examined a lignocellulose substrate, which, except for drying, had not been pretreated at all. A sample of cock's-foot grass (*Dactylis glomerata*) was used. Figure 10 compares the sugar release and also the visual appearance of the substrate after incubation with cellulases in the presence and absence of SWO1. Compared to the BSA control, the reaction containing the SWO1 showed a 1.5-fold improved sugar formation and appeared more completely degraded. The untreated material is shown for reference.

Discussion

Preparation of recombinant native-like SWO1 via homologous expression in *T. reesei*

Despite different approaches tried, as shown in Table 1, preparation of the *T. reesei* SWO1 in a recombinant form is currently not well established. Most studies seem to agree, at least implicitly, that recombinant production of SWO1 is highly problematical due to the very low protein titers formed in different host organisms. There is, however, good evidence already from the seminal discovery of Saloheimo et al. [18] that the native SWO1 is strongly post-translationally modified. The protein is glycosylated [37, 43, 48] and its carbohydrate-binding module likely involves multiple disulfide bonds [39]. Since it is not known in which way the post-translational modifications affect the function of SWO1, we considered it crucial to prepare the protein in its native host and additionally avoided the use of purification tags, which also bear the risk of affecting the function in an unpredictable fashion. The native-like SWO1 so obtained was purified to apparent homogeneity from *T. reesei* culture supernatant. The isolated protein was shown to be heavily glycosylated. From analysis of the apparent molecular mass before and after treatment with endo-*N*-glycosylase, we concluded that *N*-glycans constituted only a small portion of the total protein-linked glycans present. SWO1, thus, appeared to be *O*-glycosylated in substantial amount. From its CD spectrum, the protein seemed to be properly folded. Its functional characterization was considered to be of a general interest as it could provide basic evidence to advance the current debate about a possible role of SWO1 as C_1 factor of enzymatic lignocellulose degradation. Interpretation of any C_1-like activity that a certain recombinant form of SWO1 may show, as such or relative to another form produced differently, hinges essentially on an assessment of the nativeness of the protein used. This, in turn, requires knowledge about the behavior of the canonical (native) form of SWO1.

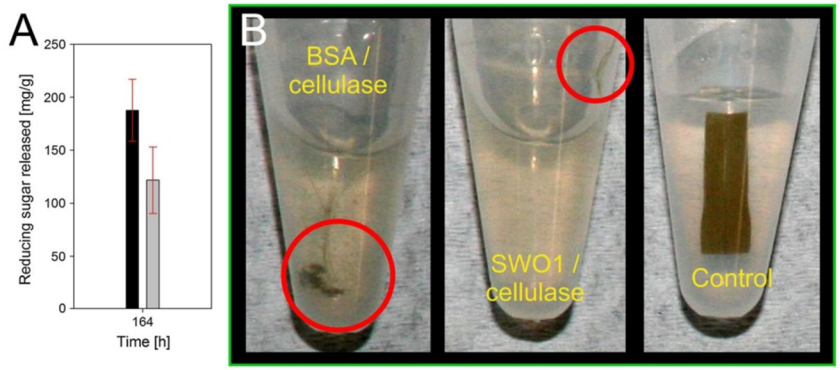

Fig. 10 Effect of SWO1 supplementation on the enzymatic hydrolysis of cock's-foot grass. **A** Reactions were done in 50 mM sodium acetate buffer, pH 5.0, at 40 °C with shaking (500 rpm) in a total reaction volume of 1 mL over 164 h. Substrate concentration was 5.0 mg/mL, and cellulase was added to a final protein loading of 2 µg/mg substrate. SWO1 was present at 0.02 µM (*black bar*), and the reference experiment used an equimolar amount of BSA (*grey bar*) instead of SWO1. The amount of reducing sugars released was measured colorimetrically with the 3,5-DNS assay calibrated against glucose. *Error bars* were estimated from two independent experiments. **B** By comparison with the BSA-containing control reaction (*left panel*), cock's-foot grass appeared to be more completely degraded in the presence of SWO1 (*central panel*) after 164 h. The remaining substrate parts are highlighted for an easier viewing. The untreated material is shown as reference (*right panel*)

Characteristics of function of the native-like SWO1

Although SWO1 binds to crystalline cellulose, as we have shown here in equilibrium adsorption studies and for the first time at single-molecule resolution by AFM, it has a much higher specificity for binding to xylan as compared to cellulose. Differences in binding specificity are not only a consequence of a different binding affinity, which is higher for xylan, but also reflect a substantially larger binding capacity of SWO1 on xylan than cellulose (Avicel PH-101). Adsorption experiments with lignin demonstrate the ability of SWO1 to bind also to the non-carbohydrate residue of lignocellulose with relatively high specificity. Interestingly, a recombinant swollenin from *A. fumigatus* produced in *A. oryzae* was reported not to bind to xylan [34]. Contrarily, most bacterial expansins are reported to bind on xylan [21, 26, 54, 64, 65].

By employing assays and analytical techniques able to capture even subtle effects of an SWO1-caused structural disintegration of amorphous and crystalline cellulose, we gathered a considerable body of evidence coherent in the overall suggestion that the native-like SWO1 was essentially inactive as an "amorphogenesis" factor on pure celluloses. Neither did SWO1 loosen or roughen up the cellulose surface [18, 34, 37] nor did it cause swelling of the cellulose material [18, 28, 37]. But also the opposite effect, that SWO1 smoothens an otherwise rough cellulose surface [41], was not observed. However, a noticeable effect from the incubation of CNCs with SWO1 was that after drying, there remained an apparent hydration shell, which surrounded the absorbed SWO1 molecules and the CNCs. It is known from molecular dynamics simulations [66] and low-field nuclear magnetic resonance studies [67, 68] that the surface hydration is a key parameter in enzymatic cellulose hydrolysis, affecting both the enzyme adsorption and the conversion. In general, a higher degree of hydration is beneficial; however, the availability of "free" water [67, 68] and the water activity [69] seem to be particularly important. A protein retaining its hydration shell even after drying is quite unlikely to increase the amount of readily available water at the cellulose surface, for activity of the hydrolytic enzymes or structural changes in the substrate requiring penetration of water. Thus, the evidence from the AFM imaging also suggests that SWO1 is probably not an "amorphogenesis" factor on pure cellulose. However, the use of a protein with a substantial hydration layer could be of interest when using high solid loadings. In recent studies, it was hypothesized that constrained low-entropy water significantly contributes to the biomass recalcitrance in polymer suspensions (≥10 % dry solid, *w/w*) [68]. A proposed mechanism includes the release of energetically unfavorable water, so revealing hydrophobic spots on the substrate surface and, thus, facilitating unproductive binding of the cellulases. In addition, the formation of steric hindrances due to polymer–polymer junction zones might be possible as a result [68]. It is conceivable that SWO1 with its substantial hydration layer could cover these energetically unfavorable hydrophobic spots and thereby affect the conversion yield positively. However, it is worth noticing that even BSA

is reported to exert a similar function in lignocellulose pretreatment by reducing the unproductive adsorption of cellulases to lignin [70]. However, we have to emphasize strongly that those images were recorded under non-physiological conditions. These findings are clearly at variance, and appear difficult to reconcile, with a number of recent papers and also the original work of Saloheimo et al. [18], reporting a cellulose structure-altering activity of the respective SWO1 preparation used. The question of how much of the difference in the findings can be attributed to the varying SWO1 preparations used is difficult to answer. Significant variations in the experimental conditions used are noted. However, even experiments with a comparable setup gave widely differing results. For instance, using Avicel PH-101, which is a commonly applied and well-characterized model substrate for crystalline cellulose [58, 71, 72], a number of studies reported a reduction in particle size after incubation with SWO1 [34, 37, 38, 40]. Furthermore, three studies using Avicel PH-101 from the same manufacturer, comparable enzyme loadings, incubation time and temperature also tried to quantify the particle size reduction [34, 37, 40] (see Table 1). Despite high similarity of the experimental setup used, the size reduction varied between ~50 % [34], ~25 % [37] and even nil in one study [40]. Thus, we think that SWO1 is probably a prime source of variability in the different studies.

Georgelis et al. [20] examined several expansin-like proteins from different microorganisms, including *Aspergillus niger*. They found all proteins to be active in a cell wall extension assay, whereas none of them showed synergy with individual *T. reesei* cellulases or the complete enzyme complex hydrolyzing filter paper. The picture emerging from several studies of expansin synergy with cellulases is that expansin exhibits highest effectiveness when lignocellulosic feedstocks, not pure celluloses, are used as the substrates [44, 54, 73]. This notion is in agreement with our finding that SWO1 prefers to bind to xylan and that synergy with cellulases was detectable on an untreated lignocellulosic substrate. Gourlay et al. [44] reported large factors of synergy between individual xylanases and SWO1 in the release of xylose from steam-pretreated corn stover. Summing up, these findings fit quite well together and already suggest a potential structural target for synergistic interplay of SWO1 with cellulases and hemicellulases, respectively. Moreover, in earlier studies, xylan and xylooligomers [68, 74, 75] were recognized as potent inhibitors for cellulases. Thus, understanding and overcoming inhibition caused by xylans and xylooligomers eventually would be highly interesting from a scientific and applied point of view. However, we did not observe synergy between SWO1 and *T. viride* β-xylanase M1 (data not shown) in the conversion of xylan into reducing sugars. Overall, the effectiveness of SWO1 in acting in synergy with cellulases and hemicellulases deserves further systematic investigation. Ultimately, our results suggest that SWO1 is not a C_1 factor of degradation of pure cellulose. Still, there is a possibility that unknown proteins or co-factors (e.g., metals) are necessary to fully unlock the potential of SWO1 in that function. Although, according to our knowledge, there is no evidence in the literature for additional proteins or factors required to promote the activity of SWO1 or expansins in general, this possibility might inspire promising future investigations.

Conclusions

In summary, some basic biochemical characteristics of the native SWO1 were presented. The protein is strongly glycosylated. O-glycosylation appeared to predominate over N-glycosylation. Results of CD spectroscopic characterization agree with evidence from molecular modeling, suggesting a folded protein with a high relative content of β-strands. Although SWO1 binds to crystalline cellulose, its adsorption to xylan is much stronger. A role of isolated SWO1 as a factor of amorphogenesis of pure cellulose was not supported. According to the classical C_1–C_x postulate, SWO1 is not a C_1 factor of degradation of the pure cellulosic substrates examined herein, neither in regard to affecting their morphology on adsorption, nor to acting in synergy with the cellulases in their hydrolysis. However, the release of sugar from barley β-glucan and cellotetraose might reflect a weak intrinsic hydrolase activity of SWO1. Synergy with *T. reesei* cellulases strongly depended on the substrate used. While absent with pure celluloses, a slight beneficial effect of SWO1 on soluble sugar release from untreated biomass sample with intact plant cell walls was observed. This might be relevant, with certain (e.g., mildly pretreated) lignocellulosic substrates, and even exploitable if the effect is preserved at increased substrate loadings.

Methods

Enzymes and substrates

Complete *T. reesei* cellulase was from fungal culture (strain SVG17) on wheat straw. *Tr*CBH I was purified from the cellulase mixture using a reported ion exchange protocol [76]. Serum albumin fraction V (BSA) was bought from Roth (Karlsruhe, Germany), β-glucosidase from *Aspergillus niger* and β-xylanase M1 from *T. viride* were obtained from Megazyme International (Wicklow, Ireland). Avicel PH-101 and lignin (alkali, low sulfonate content) were obtained from Sigma-Aldrich (St. Louis, MO, USA), barley β-glucan (high viscosity > 100 cST) from Megazyme International (Wicklow, Ireland), birch xylan from Roth (Karlsruhe, Germany), cellotetraose and

4-methylumbelliferyl-β-D-cellobioside from Carbosynth (Compton, UK). CNC was prepared from Whatman® qualitative filter paper (Sigma-Aldrich, St. Louis, MO, USA) using H_2SO_4 according to Lu et al. [63]. Amorphous thin film cellulose (ATFC) was prepared from trimethylsilyl cellulose by a reported procedure [57].

Construction of a *T. reesei* expression strain for SWO1 production, and culture conditions used

T. reesei Δ*xyr1* was used as the recipient strain for the *swo1* expression plasmid and maintained on potato dextrose agar at 28 °C. The strain is deleted in the major cellulase and xylanase regulator *xyr1* and derived from strain QM9414 (ATCC 26921). Fermentations were carried out in Biostat® A Plus bioreactors (Sartorius, Göttingen, Germany) in a 2-L working volume. One liter of fermenter medium comprised 4.6 g $(NH_4)_2SO_4$, 3 g KH_2PO_4, 0.3 g $MgSO_4{\cdot}7H_2O$, 0.4 g $CaCl_2$, 20 mL of 50× trace elements solution (250 mg/L $FeSO_4{\cdot}7H_2O$, 80 mg/L $MnSO_4{\cdot}H_2O$, 70 mg/L $ZnSO_4{\cdot}7H_2O$, 100 mg/L $CoCl_2{\cdot}2H_2O$), 0.5 mL Tween 80 and 50 g D-glucose. The fermenter was inoculated with a preculture. Therefore, about 10^6 spores/mL were added to 250 mL minimal medium [49] in a 1-L Erlenmeyer flask and grown for about 24 h at 28 °C in a rotary shaker at 250 rpm. Fermentation conditions were 28 °C, 500 rpm, an air flow rate of 2–3 L/min and pH 5.0 adjusted with 1 M NH_4OH or 1 M HCl. Supernatants were separated from fungal biomass by centrifugation for 20 min at 4 °C and 4200 rpm followed by filtration of the supernatants through a Miracloth sheet (Calbiochem, San Diego, CA, USA). Samples were stored at −20 °C prior to purification.

Construction of *swo1*-expressing *T. reesei* strains

The *swo1* coding region (XP_006969225.1) including 575 bp of its terminator region was PCR-amplified with primers infuse_swo1_fw (5′-caacttctctcatcgatgaactgttagacgggatggc-3′) and infuse_swo1_rv (5′-tgcaggtcgacatcgatgcgtgcctgtgtatcaattg-3′) from genomic DNA of *T. reesei* QM6a (ATCC13631) and cloned into the ClaI-digested pLH_hph_Pcdna1 expression plasmid using the InFusion® HD Cloning Kit (Clontech Laboratories, Inc., Mountain View, CA, USA). This *swo1* expression plasmid (p_swo1oe) contains the hygromycin B phosphotransferase (*hph*) expression cassette as fungal selection marker and 930 bp of the *T. reesei cdna1* promoter region [49] to drive *swo1* expression. DNA fragments were purified using the QIAquick gel extraction kit (QIAGEN GmbH, Hilden, Germany). The circular p_swo1oe was used to transform *T. reesei* QM9414Δ*xyr1* via electroporation. Conidia of a fully sporulated PDA Petri dish (Difco, Detroit, MI, USA) were harvested, filtered through glass wool and inoculated in 100 mL of YPD (10 g/L yeast extract, 20 g/L peptone) +2 % D-glucose followed by incubation in a rotary shaker for 4 h at 30 °C and 300 rpm. Then, the conidia were pelleted, washed three times with cold 1.1 M D-sorbitol (Alfa Aesar GmbH & Co KG, Karlsruhe, Germany), and resuspended in 300 µL of cold 1.1 M D-sorbitol. Seventy-five-microliter aliquots were mixed with 10–15 µL (10–30 µg) of p_swo1oe and electroporated at 1.8 kV using 0.1-cm cuvettes in a MicroPulser (Biorad, Hercules, CA, USA). Thereafter, cells were recovered in a premixed solution of 400 µLöö 1.1 M D-sorbitol + 125 µL YPD and incubated in a Thermomixer (Eppendorf, Hamburg, Germany) for 1 h at 28 °C and 800 rpm before plated on selection medium (PDA + 100 mg/L hygromycin B (Carl Roth + Co KG, Karlsruhe, Germany). Transformants were purified by single spore isolations on selection medium containing 0.1 % *v/v* Triton X-100. From the transformants, genomic DNA was extracted, and the presence of the *swo1* expression cassette was verified by diagnostic PCR using the primer swo1_conf_for (5′-GCCGGCTTCAAAACACACAG-3′) and swo1_conf_rev (5′-GTTGTGTGGAATTGTGAGCGG-3′) resulting in a 2.2-kb fragment in positive transformants. Expression of SWO1 in positive strains was examined using SDS-PAGE. The culture supernatant was analyzed, and the strain designated as RJ_SWO1 was used for further studies.

Purification of SWO1 from *T. reesei* culture supernatant

The supernatant was thawed and centrifuged (5 min, 5000 rpm, 4 °C). About 50 mL of supernatant (~2 mg total protein) was mixed with 50 mL of sodium acetate buffer (50 mM; pH 5.0), and Avicel PH-101 (2 g) was added. The suspension was stirred for 2 h at room temperature. Avicel PH-101 was first separated from the supernatant by sedimentation and then washed three times with 50 mL of the same sodium acetate buffer. The Avicel PH-101 was recovered by centrifugation (5 min, 5000 rpm, 4 °C) and then packed under gravity into a disposable 10-mL polypropylene gravity flow column (Thermo Fisher Scientific, Waltham, MA, USA). The column was washed twice in each case with adsorption buffer and doubly distilled H_2O to remove non-specifically adsorbed protein. SWO1 was eluted with 1 % triethylamine (TEA) in doubly distilled H_2O and collected in an excess of gently mixed adsorption buffer. The eluted fraction was concentrated using ultrafiltration concentrator tubes (Vivaspin®6, MWCO 10 kD) from Sartorius (Goettingen, Germany). SDS-PAGE with Coomassie Brilliant Blue staining showed a single, slightly diffusive protein band with the expected apparent molecular mass.

Note that a minor fraction (≤20 %) of partly purified SWO1 was already eluted during the washing step with water. We conducted preliminary adsorption

experiments using Avicel PH-101 as adsorbent with both SWO1 fractions. The SWO1 eluted with 1 % TEA showed a slightly higher affinity to Avicel PH-101, however, within the range of experimental error (data not shown). To avoid ambiguities, we only used the SWO1 fraction eluted with TEA in all experiments reported from this study.

The protein concentration of solutions of purified SWO1 was determined by intrinsic UV-absorption on a DeNovix DS-11 spectrophotometer (DeNovix Inc., Wilmington, DE, USA). The molar extinction coefficient of SWO1 was determined from the protein sequence from UniProt using ProtParam (ε_SWO1 (Q9P8D0) = 88,655 M^{-1} cm^{-1}). The purified and concentrated SWO1 was stored at 4 °C.

Deglycosylation of SWO1

Deglycosylation of SWO1 was performed according to a standard Endo H protocol (New England Biolabs, Frankfurt, Germany). The purified protein (10 µg) was mixed with 10× denaturation buffer (5 % SDS, 400 mM DTT) up to 40 µL of total volume and incubated at 95 °C for 10 min. Subsequently, one-tenth volume of 10× G7 reaction buffer (500 mM sodium phosphate buffer, pH 7.5) was added. The mixture was incubated with 300 U Endo H at 37 °C for 90 min. Reaction was stopped by heating for 10 min to 95 °C. Deglycosylated samples and untreated controls were analyzed by SDS-PAGE (NuPAGE® Bis–Tris 4–12 %) with glycostaining and subsequent Coomassie Brilliant Blue staining (Thermo Fisher Scientific, Waltham, MA, USA). Glycostaining was done with the Pro-Q Emerald 300 glycostain kit (Invitrogen, Carlsbad, CA) according the manufacturer's protocol.

Circular dichroism and modeling of reference data

Circular dichroism spectra were acquired on a Jasco J-175 spectropolarimeter (Jasco Analytical Instruments, Groß-Umstadt, Germany) using a 10-mm cylindrical quartz cell. SWO1 was used at a concentration of 0.1 mg/mL in 50 mM sodium acetate buffer, pH 5.0, at room temperature. The baseline of the spectra was obtained from pure buffer. The standard parameters for protein evaluation were chosen with a sensitivity of 100 mdeg, a start wavelength of 250–320 nm, an end wavelength of 190–250 nm and a data pitch of 1 nm. For good data quality, a slow scanning mode with a continuous scanning speed of 10 nm/min was chosen. The combined spectra were evaluated online with DichroWeb, which calculated the secondary structure elements of SWO1.

To obtain reference date for SWO1, the automated protein structure homology-modeling server Phyre2 was used to predict the protein structure of SWO1 [50]. The sequence of SWO1 from UniProt (ID: Q9P8D0) was used except for the amino acids 1–18, which are predicted to be cleaved off after secretion. The obtained protein model was used to calculate the percentage of secondary structure elements. A second set of reference data was obtained using the sequence-based JNet algorithm (JPred4) (http://www.compbio.dundee.ac.uk/jpred4/index.html) to calculate the percentage of secondary structure elements as described elsewhere [51].

Characterization of SWO1 binding affinity

All adsorption isotherm measurements were carried out in 1.5-mL Eppendorf tubes containing serial dilutions of SWO1 (0.2–25 µM) mixed with an equal volume of an aqueous suspension of substrate (Avicel PH-101, birchwood xylan and lignin) to a final concentration of 1 mg/mL in 50 mM sodium acetate buffer (pH 5.0) in a total reaction volume of 200 µL. All adsorption experiments were conducted in triplicates at 25 °C with orbital shaking (500 rpm) over 2 h using an Eppendorf Thermomixer comfort (Eppendorf AG, Hamburg, Germany). An incubation time of 2 h was sufficient to reach adsorption equilibrium according to previously published articles [37] and preliminary experiments on Avicel PH-101 (data not shown). The samples were then centrifuged (5 min, 13,000 rpm, 25 °C) to remove solids. The clear supernatant was collected, and protein concentration was determined by BCA (Thermo Fisher Scientific, Waltham, MA, USA) (Avicel PH-101) and Roti-Nanoquant assay (Carl Roth + Co KG, Karlsruhe, Germany) (xylan and lignin). *Tr*CBH I was used as standard. The equilibrium association constants (K_d) were determined by nonlinear regression of bound versus free protein concentrations to Langmuir model as described previously. A control showed that unspecific binding of SWO1 to the reaction tubes was negligible.

Activity of SWO1 on crystalline cellulose substrates

SWO1 was incubated with Avicel PH-101 or CNC in 50 mM sodium acetate buffer, pH 5.0, in a total reaction volume of 500 µL at 40 °C and 500 rpm using an Eppendorf Thermomixer comfort (Eppendorf AG, Hamburg, Germany). Experiments were done in four replicates, and the substrate concentration was 1.0 mg/mL (Avicel PH-101 or CNC). Samples were incubated with either 0.4 µM SWO1 or an equimolar amount BSA. Samples were taken after 12 and 24 h, respectively. About 100 µL of the supernatant was withdrawn and heated to 95 °C for 10 min to stop the reaction. Subsequently, the samples were centrifuged (13,000 rpm, 1 min, 25 °C), and β-glucosidase was added to a final concentration of 2 µg/mL to the cleared supernatant. The reaction mixture was incubated for 1 h at 37 °C to convert of released

cello-oligosaccharides to glucose. Finally, the amount of released glucose in the supernatant was assayed colorimetrically with glucose oxidase and peroxidase as described in earlier works [12].

Hydrolysis of β-glucan and cellotetraose by SWO1

Hydrolysis of soluble glucans was studied at 1 mg/mL (β-glucan) or 0.5 mg/mL (cellotetraose), respectively. All experiments were carried out as duplicates in 50 mM sodium acetate buffer, pH 5.0, in a total reaction volume of 400 µL at 40 °C and 500 rpm. The reaction was started with the addition of SWO1 or an equimolar amount of BSA. The final enzyme concentration was 0.2 (β-glucan) or 0.5 µM (cellotetraose), respectively. The reaction was stopped after 24 h by adding an equal volume of 100 mM NaOH. Precipitated material was removed by centrifugation (3 min, 13,000 rpm, 25 °C). The cleared supernatant was analyzed with high-performance anion-exchange chromatography coupled to pulsed-amperometric detection (HPAEC-PAD) (Dionex BioLC, Thermo Fisher Scientific, Waltham, MA) as described elsewhere [57]. Identity and amount of released sugars were assayed using authentic standards.

Enzymatic hydrolysis of crystalline cellulose pretreated with SWO1

The impact of SWO1 supplementation on the hydrolysis of a typical fungal cellulase set was assayed in 50 mM sodium acetate buffer, pH 5.0 at 40 °C and 500 rpm in an Eppendorf Thermomixer comfort (Eppendorf AG, Hamburg, Germany). Substrate concentration was 1.0 mg/mL of cellulose (Avicel PH-101 or CNC) in a total reaction volume of 1.5 mL. Reactions were repeated four times. Pretreatment was done over 24 h with 0.4 µM SWO1 or BSA as reference. Afterward, *T. reesei* cellulase and β-glucosidase were added in a small volume (60 µL) to a final enzyme loading of 20 µg and 4 µg/mg substrate, respectively.

Sampling was performed at suitable time points. In brief, 150 µL of the well-mixed supernatant was withdrawn and heated to 95 °C for 10 min to stop the reaction. Subsequently, the samples were centrifuged (13,000 rpm, 1 min, 25 °C), and the amount of released glucose in the supernatant was assayed colorimetrically with glucose oxidase and peroxidase as described above.

Enzymatic hydrolysis of lingocellulosic material with supplementation of SWO1

Hydrolysis experiments with *Dactylis glomerata* grass were conducted in duplicates in a parallel assay. Fifty mM sodium acetate buffer, pH 5.0, was used in a total volume of 1 mL at 40 °C. The samples were shaken at 500 rpm in an Eppendorf Thermomixer comfort (Eppendorf AG, Hamburg, Germany). Prior to hydrolysis experiments, *Dactylis glomerata* grass was dried at 80 °C overnight. Substrate concentration was 5.0 mg/mL, and cellulase was added to a final protein loading of 2 µg/mg substrate. SWO1 was present at 0.02 µM, and the reference experiment used an equimolar amount of BSA instead of SWO1. Sampling was performed at suitable times. About 100 µL of the well-mixed supernatant was withdrawn and mixed with 100 µL of 100 mM NaOH to stop the reaction. Subsequently, the samples were centrifuged (13,000 rpm, 1 min, 25 °C), and the amount of released sugars in the cleared supernatant was assayed colorimetrically with the 3,5-dinitrosalicylic acid-based assay calibrated against glucose [77].

Atomic force microscopy (AFM) imaging of SWO1 activity

Investigations of the incubated samples were carried out on a FastScan Bio AFM (Bruker AXS, CA, USA), operated by a NanoScope V controller and FastScan A cantilevers (Bruker AXS, CA, USA) at room temperature. Setpoints, scan rates and controlling parameters were chosen carefully to ensure lowest possible energy dissipation to the sample and to exclude tip-driven artifacts.

Prior to AFM investigation, fully amorphous (ATFC) and highly crystalline cellulose (CNC) preparations were spin-casted on silicon wafers as described previously. Experiments were conducted as duplicates at 40 °C in a water bath with mild agitation. A single silicon wafer covered with cellulosic material was used as the substrate in a total reaction volume of 2 mL of 50 mM sodium acetate buffer (pH 5.0). Cellulosic material was equilibrated in buffer for 30 min prior to the addition of enzyme. The respective enzyme, SWO1 or BSA (only CNC) as negative control, was added to a final concentration of 0.4 µM. The reaction was conducted over 24 h and stopped by removing the silica wafers from the reaction mixture and rinsing them with 15 mL doubly distilled H_2O to remove salt crystals.

Afterward, CNC-coated silica wafers were dried for 24 h up to 48 h at room temperature prior to AFM investigations. Silica wafers coated with ATFC were stored at 4 °C in doubly distilled H_2O and examined in a laboratory-built liquid cell. The storage time did not exceed 6 h.

AFM image processing and analysis was performed using NanoScope Analysis 1.50 (Build R2.103555, Bruker AXS, CA, USA) and Gwyddion 2.31 (Released 2013-02-01, http://gwyddion.net/).

Wide-angle x-ray scattering (WAXS)

Wide-angle x-ray scattering analysis (WAXS) was carried out on a Siemens D 5005 diffractometer (Siemens, Berlin, Germany) using CuKα (0.154 nm) radiation at 40 kV and 40 mA. 10 mg/mL Avicel PH-101 was incubated with

0.01 μM SWO1 for 72 h in a shaking water bath (GFL 1083) at 50 rpm. As a reference, Avicel PH-101 without SWO1 incubation was used. The probes were dried at 60 °C overnight, and were put on a zero-diffraction silicon crystal holder (Bruker AXS, CA, USA). All samples were characterized in locked coupled Θ/2Θ mode from 10° to 60° (Θ/2Θ) with an angle increment of 0.05° in 6 s. Data analysis was performed using Origin 9.0 (OriginLab Corp., Northampton, MA, USA).

Abbreviations

WAXS: wide-angle x-ray scattering analysis; CNC: cellulose nanocrystals; ATFC: amorphous thin film cellulose; BSA: bovine serum albumin; HPAEC-PAD: high performance anion exchange chromatography coupled to pulsed-amperometric detection; SD: standard deviation; CBH: cellobiohydrolase; EG: endoglucanase; CBM: carbohydrate-binding module; Fn-III: fibronectin-III; SEM: scanning electron microscope; ESEM: environmental scanning electron microscope; CAE: congo red adsorption enhancement; TEA: triethylamine.

Authors' contributions

ME, KS and BN designed the research. JR and BS constructed the *T. reesei* strain and produced the culture supernatant containing SWO1. KS and ME planned and performed the biochemical experiments and analyzed the data. JS, TG and ME carried out the AFM and WAXS measurements and analyzed the data under the guidance of HP. All authors contributed to drafting of the manuscript. ME and BN wrote the paper with assistance from KS. All authors read and approved the final manuscript.

Author details

[1] Institute of Biotechnology and Biochemical Engineering, Graz University of Technology, Petersgasse 12/1, 8010 Graz, Austria. [2] Institute for Electron Microscopy and Nanoanalysis, Graz University of Technology, Steyrergasse 17, 8010 Graz, Austria. [3] Research Division Biochemical Technology, Institute of Chemical Engineering, TU Wien, Gumpendorferstrasse 1A/166, 1060 Vienna, Austria. [4] Graz Centre for Electron Microscopy, Steyrergasse 17, 8010 Graz, Austria. [5] Austrian Centre of Industrial Biotechnology, Petersgasse 14, 8010 Graz, Austria.

Acknowledgements

Dr. Christian Berg (Institute of Plant Sciences, University of Graz) provided the sample of cock's foot grass. Christian Fercher (Institute of Molecular Biosciences, University of Graz) supported the CD measurements. Natascha Loppitsch (Institute of Biotechnology and Biochemical Engineering, Graz University of Technology) assisted in SWO1 purification.

Competing interests

The authors declare that they have no competing interests.

Funding

Financial support was from the Austrian Science Fund, projects P24156-B21 (to BN) and P24219 (to BS). BS further acknowledges support from the European Regional Development Fund: Regio 13—Impulse für Oberösterreich.

Received: 30 May 2016 Accepted: 15 August 2016
Published online: 26 August 2016

References

1. Chundawat SPS, Beckham GT, Himmel ME, Dale BE. Deconstruction of lignocellulosic biomass to fuels and chemicals. Annu Rev Chem Biomol Eng. 2011;2:121–45.
2. Himmel ME, Ding SY, Johnson DK, Adney WS, Nimlos MR, Brady JW, Foust TD. Biomass recalcitrance: engineering plants and enzymes for biofuels production. Science. 2007;315:804–7.
3. Sims REH, Mabee W, Saddler JN, Taylor M. An overview of second generation biofuel technologies. Bioresour Technol. 2010;101:1570–80.
4. Kari J, Olsen J, Borch K, Cruys-Bagger N, Jensen K, Westh P. Kinetics of cellobiohydrolase (Cel7A) variants with lowered substrate affinity. J Biol Chem. 2014;289:32459–68.
5. Payne CM, Knott BC, Mayes HB, Hansson H, Himmel ME, Sandgren M, Ståhlberg J, Beckham GT. Fungal cellulases. Chem Rev. 2015;115:1308–448.
6. Wu I, Arnold FH. Engineered thermostable fungal Cel6A and Cel7A cellobiohydrolases hydrolyze cellulose efficiently at elevated temperatures. Biotechnol Bioeng. 2013;110:1874–83.
7. Wilson DB. Cellulases and biofuels. Curr Opin Biotechnol. 2009;20:295–9.
8. Peterson R, Nevalainen H. *Trichoderma reesei* RUT-C30—thirty years of strain improvement. Microbiology. 2012;158:58–68.
9. Horn SJ, Vaaje-Kolstad G, Westereng B, Eijsink VG. Novel enzymes for the degradation of cellulose. Biotechnol Biofuels. 2012;5:45.
10. Hu J, Chandra R, Arantes V, Gourlay K, van Dyk JS, Saddler JN. The addition of accessory enzymes enhances the hydrolytic performance of cellulase enzymes at high solid loadings. Bioresour Technol. 2015;186:149–53.
11. Müller G, Várnai A, Johansen KS, Eijsink VGH, Horn SJ. Harnessing the potential of LPMO-containing cellulase cocktails poses new demands on processing conditions. Biotechnol Biofuels. 2015;8:187.
12. Eibinger M, Ganner T, Bubner P, Rošker S, Kracher D, Haltrich D, Ludwig R, Plank H, Nidetzky B. Cellulose surface degradation by a lytic polysaccharide monooxygenase and its effect on cellulase hydrolytic efficiency. J Biol Chem. 2014;289:35929–38.
13. Harris PV, Xu F, Kreel NE, Kang C, Fukuyama S. New enzyme insights drive advances in commercial ethanol production. Curr Opin Chem Biol. 2014;19:162–70.
14. Cannella D, Jørgensen H. Do new cellulolytic enzyme preparations affect the industrial strategies for high solids lignocellulosic ethanol production? Biotechnol Bioeng. 2014;111:59–68.
15. Cannella D, Hsieh C-WC, Felby C, Jørgensen H. Production and effect of aldonic acids during enzymatic hydrolysis of lignocellulose at high dry matter content. Biotechnol Biofuels. 2012;5:26.
16. Hu J, Arantes V, Pribowo A, Saddler JN, Gourlay K, Saddler JN. Substrate factors that influence the synergistic interaction of AA9 and cellulases during the enzymatic hydrolysis of biomass. Energy Environ Sci. 2014;7:2308–15.
17. Sampedro J, Cosgrove DJ. The expansin superfamily. Genome Biol. 2005;6:242.
18. Saloheimo M, Paloheimo M, Hakola S, Pere J, Swanson B, Nyyssönen E, Bhatia A, Ward M, Penttilä M. Swollenin, a *Trichoderma reesei* protein with sequence similarity to the plant expansins, exhibits disruption activity on cellulosic materials. Eur J Biochem. 2002;269:4202–11.
19. Cosgrove DJ. Loosening of plant cell walls by expansins. Nature. 2000;407:321–6.
20. Georgelis N, Nikolaidis N, Cosgrove DDJ. Biochemical analysis of expansin-like proteins from microbes. Carbohydr Polym. 2014;100:17–23.
21. Liu X, Ma Y, Zhang M. Research advances in expansins and expansion-like proteins involved in lignocellulose degradation. Biotechnol Lett. 2015;37:1541–51.
22. Cosgrove DJ. New genes and new biological roles for expansins. Curr Opin Plant Biol. 2000;3:73–8.
23. McQueen-Mason S, Cosgrove DJ. Disruption of hydrogen bonding between plant cell wall polymers by proteins that induce wall extension. Proc Natl Acad Sci USA. 1994;91:6574–8.
24. Brotman Y, Briff E, Viterbo A, Chet I. Role of swollenin, an expansin-like protein from *Trichoderma*, in plant root colonization. Plant Physiol. 2008;147:779–89.
25. Georgelis N, Nikolaidis N, Cosgrove DJ. Bacterial expansins and related proteins from the world of microbes. Appl Microbiol Biotechnol. 2015;99:3807–23.
26. Yennawar NH, Li L-C, Dudzinski DM, Tabuchi A, Cosgrove DJ. Crystal structure and activities of EXPB1 (Zea m 1), a beta-expansin and group-1 pollen allergen from maize. Proc Natl Acad Sci USA. 2006;103:14664–71.
27. Kerff F, Amoroso A, Herman R, Sauvage E, Petrella S, Filée P, Charlier P, Joris B, Tabuchi A, Nikolaidis N, Cosgrove DJ. Crystal structure and activity of *Bacillus subtilis* YoaJ (EXLX1), a bacterial expansin that promotes root colonization. Proc Natl Acad Sci USA. 2008;105:16876–81.

28. Verma D, Jin S, Kanagaraj A, Singh ND, Daniel J, Kolattukudy PE, Miller M, Daniell H. Expression of fungal cutinase and swollenin in tobacco chloroplasts reveals novel enzyme functions and/or substrates. PLoS One. 2013;8:e57187.
29. Arantes V, Saddler JN. Access to cellulose limits the efficiency of enzymatic hydrolysis: the role of amorphogenesis. Biotechnol Biofuels. 2010;3:4.
30. Seki Y, Kikuchi Y, Yoshimoto R, Aburai K, Kanai Y, Ruike T, Iwabata K, Goitsuka R, Sugawara F, Abe M, Sakaguchi K. Promotion of crystalline cellulose degradation by expansins from *Oryza sativa*. Planta. 2014;241:83–93.
31. Kim ES, Lee HJ, Bang W-G, Choi I-G, Kim KH. Functional characterization of a bacterial expansin from *Bacillus subtilis* for enhanced enzymatic hydrolysis of cellulose. Biotechnol Bioeng. 2009;102:1342–53.
32. Georgelis N, Tabuchi A, Nikolaidis N, Cosgrove DJ. Structure-function analysis of the bacterial expansin EXLX1. J Biol Chem. 2011;286:16814–23.
33. Georgelis N, Yennawar NH, Cosgrove DJ. Structural basis for entropy-driven cellulose binding by a type-A cellulose-binding module (CBM) and bacterial expansin. Proc Natl Acad Sci USA. 2012;109:14830–5.
34. Chen X, Ishida N, Todaka N, Nakamura R, Maruyama J, Takahashi H, Kitamoto K. Promotion of efficient Saccharification of crystalline cellulose by *Aspergillus fumigatus* Swo1. Appl Environ Microbiol. 2010;76:2556–61.
35. Beckham GT, Bomble YJ, Bayer EA, Himmel ME, Crowley MF. Applications of computational science for understanding enzymatic deconstruction of cellulose. Curr Opin Biotechnol. 2011;22:231–8.
36. Kostylev M, Wilson D. A distinct model of synergism between a processive endocellulase (TfCel9A) and an exocellulase (TfCel48A) from *Thermobifida fusca*. Appl Environ Microbiol. 2014;80:339–44.
37. Jäger G, Girfoglio M, Dollo F, Rinaldi R, Bongard H, Commandeur U, Fischer R, Spiess ACC, Büchs J. How recombinant swollenin from *Kluyveromyces lactis* affects cellulosic substrates and accelerates their hydrolysis. Biotechnol Biofuels. 2011;4:33.
38. Wang Y, Tang R, Tao J, Gao G, Wang X, Mu Y, Feng Y. Quantitative investigation of non-hydrolytic disruptive activity on crystalline cellulose and application to recombinant swollenin. Appl Microbiol Biotechnol. 2011;91:1353–63.
39. Kang K, Wang S, Lai G, Liu G, Xing M. Characterization of a novel swollenin from *Penicillium oxalicum* in facilitating enzymatic saccharification of cellulose. BMC Biotechnol. 2013;13:42.
40. Zhou Q, Lv X, Zhang X, Meng X, Chen G, Liu W. Evaluation of swollenin from *Trichoderma pseudokoningii* as a potential synergistic factor in the enzymatic hydrolysis of cellulose with low cellulase loadings. World J Microbiol Biotechnol. 2011;27:1905–10.
41. Gourlay K, Arantes V, Saddler JN. Use of substructure-specific carbohydrate binding modules to track changes in cellulose accessibility and surface morphology during the amorphogenesis step of enzymatic hydrolysis. Biotechnol Biofuels. 2012;5:51.
42. Gourlay K, Hu J, Arantes V, Penttilä M, Saddler JN. The use of carbohydrate binding modules (CBMs) to monitor changes in fragmentation and cellulose fiber surface morphology during cellulase- and swollenin-induced deconstruction of lignocellulosic substrates. J Biol Chem. 2015;290:2938–45.
43. Wang M, Cai J, Huang L, Lv Z, Zhang Y, Xu Z. High-level expression and efficient purification of bioactive swollenin in *Aspergillus oryzae*. Appl Biochem Biotechnol. 2010;162:2027–36.
44. Gourlay K, Hu J, Arantes V, Andberg M, Saloheimo M, Penttilä M, Saddler J. Swollenin aids in the amorphogenesis step during the enzymatic hydrolysis of pretreated biomass. Bioresour Technol. 2013;142C:498–503.
45. Wang W, Liu C, Ma Y, Liu X, Zhang K, Zhang M. Improved production of two expansin-like proteins in *Pichia pastoris* and investigation of their functional properties. Biochem Eng J. 2014;84:16–27.
46. Payne CM, Resch MG, Chen L, Crowley MF, Himmel ME, Taylor LE, Sandgren M, Ståhlberg J, Stals I, Tan Z, Beckham GT. Glycosylated linkers in multimodular lignocellulose-degrading enzymes dynamically bind to cellulose. Proc Natl Acad Sci USA. 2013;110:14646–51.
47. Jeoh T, Michener W, Himmel ME, Decker SR, Adney WS. Implications of cellobiohydrolase glycosylation for use in biomass conversion. Biotechnol Biofuels. 2008;1:10.
48. Andberg M, Penttilä M, Saloheimo M. Swollenin from *Trichoderma reesei* exhibits hydrolytic activity against cellulosic substrates with features of both endoglucanases and cellobiohydrolases. Bioresour Technol. 2015;181:105–13.
49. Uzbas F, Sezerman U, Hartl L, Kubicek CP, Seiboth B. A homologous production system for *Trichoderma reesei* secreted proteins in a cellulase-free background. Appl Microbiol Biotechnol. 2012;93:1601–8.
50. Kelley LA, Sternberg MJE. Protein structure prediction on the web: a case study using the Phyre server. Nat Protoc. 2009;4:363–71.
51. Drozdetskiy A, Cole C, Procter J, Barton GJ. JPred4: a protein secondary structure prediction server. Nucleic Acids Res. 2015;43:389–94.
52. Várnai A, Siika-aho M, Viikari L. Restriction of the enzymatic hydrolysis of steam-pretreated spruce by lignin and hemicellulose. Enzym Microb Technol. 2010;46:185–93.
53. Rowe RC, McKillop AG, Bray D. The effect of batch and source variation on the crystallinity of microcrystalline cellulose. Int J Pharm. 1994;101:169–72.
54. Bunterngsook B, Eurwilaichitr L, Thamchaipenet A, Champreda V. Binding characteristics and synergistic effects of bacterial expansins on cellulosic and hemicellulosic substrates. Bioresour Technol. 2015;176:129–35.
55. Kim IJ, Ko HJ, Kim TW, Nam KH, Choi IG, Kim KH. Binding characteristics of a bacterial expansin (BsEXLX1) for various types of pretreated lignocellulose. Appl Microbiol Biotechnol. 2013;97:5381–8.
56. Sharrock KR. Cellulase assay methods: a review. J Biochem Biophys Methods. 1988;17:81–105.
57. Ganner T, Rošker S, Eibinger M, Kraxner J, Sattelkow J, Rattenberger J, Fitzek H, Chernev B, Grogger W, Nidetzky B, Plank H. Tunable semicrystalline thin film cellulose substrate for high-resolution, in-situ AFM characterization of enzymatic cellulose degradation. ACS Appl Mater Interfaces. 2015;7:27900–9.
58. Park S, Baker JO, Himmel ME, Parilla PA, Johnson DK. Cellulose crystallinity index: measurement techniques and their impact on interpreting cellulase performance. Biotechnol Biofuels. 2010;3:10.
59. Goacher RE, Selig MJ, Master ER. Advancing lignocellulose bioconversion through direct assessment of enzyme action on insoluble substrates. Curr Opin Biotechnol. 2014;27:123–33.
60. Ganner T, Aschl T, Eibinger M, Bubner P, Meingast A, Chernev B, Mayrhofer C, Nidetzky B, Plank H. Tunable mixed amorphous—crystalline cellulose substrates (MACS) for dynamic degradation studies by atomic force microscopy in liquid environments. Cellulose. 2014;21:3927–39.
61. Ganner T, Bubner P, Eibinger M, Mayrhofer C, Plank H, Nidetzky B. Dissecting and reconstructing synergism—in situ visualization of cooperativity among cellulases. J Biol Chem. 2012;287:43215–22.
62. Eibinger M, Bubner P, Ganner T, Plank H, Nidetzky B. Surface structural dynamics of enzymatic cellulose degradation, revealed by combined kinetic and atomic force microscopy studies. FEBS J. 2014;281:275–90.
63. Lu P, Hsieh Y-L. Preparation and properties of cellulose nanocrystals: rods, spheres, and network. Carbohydr Polym. 2010;82:329–36.
64. Kim IJ, Ko HJ, Kim TW, Choi IG, Kim KH. Characteristics of the binding of a bacterial expansin (BsEXLX1) to microcrystalline cellulose. Biotechnol Bioeng. 2013;110:401–7.
65. Lee HJ, Kim IJ, Kim JF, Choi I-G, Kim KH. An expansin from the marine bacterium *Hahella chejuensis* acts synergistically with xylanase and enhances xylan hydrolysis. Bioresour Technol. 2013;149:516–9.
66. Chundawat SPS, Bellesia G, Uppugundla N, da Costa Sousa L, Gao D, Cheh AM, Agarwal UP, Bianchetti CM, Phillips GN, Langan P, Balan V, Gnanakaran S, Dale BE. Restructuring the crystalline cellulose hydrogen bond network enhances its depolymerization rate. J Am Chem Soc. 2011;133:11163–74.
67. Selig MJ, Thygesen LG, Johnson DK, Himmel ME, Felby C, Mittal A. Hydration and saccharification of cellulose Iβ, II and IIII at increasing dry solids loadings. Biotechnol Lett. 2013;35:1599–607.
68. Selig MJ, Thygesen LG, Felby C. Correlating the ability of lignocellulosic polymers to constrain water with the potential to inhibit cellulose saccharification. Biotechnol Biofuels. 2014;7:159.
69. Selig MJ, Hsieh CWC, Thygesen LG, Himmel ME, Felby C, Decker SR. Considering water availability and the effect of solute concentration on high solids saccharification of lignocellulosic biomass. Biotechnol Prog. 2012;28:1478–90.
70. Yang B, Wyman CE. BSA treatment to enhance enzymatic hydrolysis of cellulose in lignin containing substrates. Biotechnol Bioeng. 2006;94:611–7.
71. Zhang Y, Lynd L. A functionally based model for hydrolysis of cellulose by fungal cellulase. Biotechnol Bioeng. 2006;94:888–98.

72. Bubner P, Plank H, Nidetzky B. Visualizing cellulase activity. Biotechnol Bioeng. 2013;110:1529–49.
73. Bunterngsook B, Mhuantong W, Champreda V, Thamchaiphenet A, Eurwilaichitr L. Identification of novel bacterial expansins and their synergistic actions on cellulose degradation. Bioresour Technol. 2014;159:64–71.
74. Qing Q, Yang B, Wyman CE. Xylooligomers are strong inhibitors of cellulose hydrolysis by enzymes. Bioresour Technol. 2010;101:9624–30.
75. Qing Q, Wyman CE. Supplementation with xylanase and β-xylosidase to reduce xylo-oligomer and xylan inhibition of enzymatic hydrolysis of cellulose and pretreated corn stover. Biotechnol Biofuels. 2011;4:18.
76. Medve J, Lee D, Tjerneld F. Ion-exchange chromatographic purification and quantitative analysis of *Trichoderma reesei* cellulases cellobiohydrolase I, II and endoglucanase II by fast protein liquid chromatography. J Chromatogr A. 1998;808:153–65.
77. Xiao Z, Storms R, Tsang A. Microplate-based filter paper assay to measure total cellulase activity. Biotechnol Bioeng. 2004;88:832–7.
78. Morrison JM, Elshahed MS, Youssef NH. Defined enzyme cocktail from the anaerobic fungus *Orpinomyces* sp. strain C1A effectively releases sugars from pretreated corn stover and switchgrass. Sci Rep. 2016;6:29217.

Single molecule study of oxidative enzymatic deconstruction of cellulose

Single molecule study of oxidative enzymatic deconstruction of cellulose

Manuel Eibinger[1], Jürgen Sattelkow[2], Thomas Ganner[2], Harald Plank[2,3]*, Bernd Nidetzky[1,4]*

[1]Institute of Biotechnology and Biochemical Engineering, Graz University of Technology, Petersgasse 10-12/1, 8010 Graz, Austria.
[2]Institute for Electron Microscopy and Nanoanalysis, Graz University of Technology, Steyrergasse 17, 8010 Graz, Austria.
[3]Graz Centre for Electron Microscopy, Steyrergasse 17, A-8010 Graz, Austria.
[4]Austrian Centre of Industrial Biotechnology, Petersgasse 14, 8010 Graz, Austria.

*Correspondence to: bernd.nidetzky@tugraz.at (B.N.); harald.plank@felmi-zfe.at (H.P.)

Abstract

LPMO (lytic polysaccharide monooxygenase) represents a new paradigm of cellulosic biomass degradation by an oxidative mechanism. Understanding the role of LPMO in deconstructing crystalline cellulose is fundamental to the enzyme's biological function and will help to specify the use of LPMO in biorefinery applications. We show here with real-time atomic force microscopy that LPMOs from *Neurospora crassa* bind to nanocrystalline cellulose with high preference for the very same substrate surfaces that are also used by a processive cellulase (*Trichoderma reesei* CBH I) to move along during hydrolytic cellulose degradation. The bound LPMOs, however, are immobile during their adsorbed residence time (~0.6 min) on cellulose. Treatment with LPMO resulted in fibrillation of crystalline cellulose and strongly (≥ 2-fold) enhanced the cellulase adsorption. It also increased enzyme turnover on the cellulose surface, thus boosting the hydrolytic conversion.

Sustainable production of fuels, chemicals and materials from plant biomass represents a major effort of global importance.[1] The potential advantages, whether for diversifying the energy portfolios, decreasing emissions or supporting rural developments, are important for society in the long run.[2] The capability of biotechnology-based biorefineries to play a significant role depends on finding sustainable and cost effective ways of deconstructing the complex lignocellulosic composites in abundant biomass feedstocks, like agricultural residues and forestry wastes.[3,4] Most of the current biorefinery designs involve advanced biofuels, predominantly ethanol, produced from sugars released from the feedstock by enzymatic saccharification.[5] The high resistance of biomass polysaccharides, most notably that of cellulose, constitutes a main hurdle any viable process design must overcome.[3,4] Besides effective pretreatment, enzyme efficiency in breaking down the cellulose is key. Enzyme systems for cellulose degradation all are mixtures of a core set of individual activities, typically hydrolases that use chain-end cleavage (cellobiohydrolases) or internal chain cleavage (endoglucanases) for cellulose depolymerization.[6] Because these activities work in synergy, the mixture's overall efficiency is determined by its composition. Huge research efforts were already targeted at engineering of cellulase systems.[6,7] A new mechanism of cellulose degradation via O_2-dependent oxidative chain cleavage was discovered recently.[8–11] This fueled expectations of a truly disruptive improvement of enzymatic deconstruction efficiency resulting from a suitable combination of hydrolytically and oxidatively chain-cleaving activities. The relevant oxidative enzyme, LPMO, is included in the currently most advanced enzyme cocktails for cellulose saccharification.[12] However, deepened understanding of the effect of LPMO on deconstructing cellulosic material is urgently required to define the oxidative enzyme's most appropriate use in biomass processing. Despite significant progress in characterizing LPMO structurally and mechanistically[9–13], evidence on the behavior of LPMO on the actual site of its catalytic action - the solid cellulose surface - is limited. To advance this evidence is not only fundamental to the enzyme's biological function in cellulose degradation but it will also help specifying the exploitation of LPMO in emergent biorefinery applications.

LPMO is a metalloenzyme with a homonuclear Cu^{2+} center in the active site.[9–11,13] Catalysis depends on external supply of electrons for O_2 reduction, sources of which can be small-molecule redox mediators or partner redox-proteins.[14,15] Polysaccharide chain cleavage occurs with insertion of a single oxygen atom from O_2 at C'1 or C4 of an intrachain cellobiosyl moiety[10,13], depending on the type of LPMO used. LPMO structures suggest a likely binding mode of the enzyme to cellulose surfaces via the protein face that exposes the catalytic metal

outward.[9] Oxidative chain cleavages in crystalline areas of the substrate are expected to cause local disruptions of the ordered cellulose structure.[16] This "decrystallization" of the substrate might facilitate the hydrolytic chain depolymerization by cellulases. We previously used atomic force microscopy to visualize the effect of LPMO on cellulose surface degradation.[17] We demonstrated that in amorphous-crystalline cellulose films LPMO attacked preferably the crystalline substrate areas and effectively degraded small fibrils exposed on the surface. Treatment of the substrate with LPMO enabled cellulases to break down crystalline cellulose nanostructures otherwise highly resistant to degradation.

In the present study, we succeeded in analyzing the dynamic interaction of LPMO with crystalline cellulose in detail, applying real-time AFM with lateral and temporal resolutions suitable for tracking single enzyme molecules on the cellulose surface. Besides visualizing the LPMO, we were also able to study effects on substrate degradation and showed surface fibrillation to occur as result of the LPMO action. We furthermore demonstrated increased overall adsorption to cellulose and enhanced surface mobility of a well-characterized cellulase, the cellobiohydrolase I from *Trichoderma reesei*, in the presence of LPMO. We studied two LPMOs from the fungus *Neurospora crassa*, one (*Nc*LPMO9F) representing the C1' and the other (*Nc*LPMO9C) the C4 oxidizing type of reactivity.[18] Both LPMOs are classified in the carbohydrate-active enzymes (CAZy) database into auxiliary activities (AA) family AA9.[19] Besides different chain cleavage mode, the two LPMOs also differed in that *Nc*LPMO9C contains a carbohydrate-binding module (CBM)[20] whereas *Nc*LPMO9F is lacking one. The presence of a family 1 CBM, which is also present in many cellulases (e.g. CBH I)[6], was of interest for it might affect how the enzyme binds to and processes further on the cellulose surface.[21]

Results

We initially analyzed the *T. reesei* CBH I for two reasons. First, Igarashi and colleagues[22] previously showed the same CBH I to slide undirectionally along crystalline cellulose surfaces. The enzyme's movement likely arose from its well-characterized processive mode of cellulose chain degradation, involving successive cleavages of terminal cellobiose units from the same chain without intermediate chain release from enzyme.[6] Being able to track the movement of CBH I in our studies served to validate the general experimental set-up as well as the temporal resolution of the AFM method used (Fig. 1). Second, in natural cellulase systems of which the one from *T. reesei* is prototypical, the CBH I is mainly responsible for the degradation of crystalline cellulose.[6] Action of LPMO on the same cellulose material is

therefore expected to influence the CBH I strongest among the different enzymes present in the cellulase mixture. Evidence on the individual action of the CBH I was therefore required as a reference.

Single molecule analysis of LPMO and CBH I

An exemplary sliding motion of a CBH I molecule on the cellulose surface is shown in Fig. 1a. The enzyme moved from right to left along an upward path on the side wall of the cellulose nanocrystal, as clearly seen in time-resolved height images and the corresponding quantitative height profiles. Analyzing 50 enzymes on 5 cellulose nanocrystals, we determined that roughly 10 - 20% of the adsorbed CBH I molecules were moving on the surface, and they did so mostly on the side walls of the cellulose nanocrystals, generally similar as in Figure 1 (A), although the exact path of enzyme motion - upward, downward or horizontal - varied depending on the crystal. The average velocity of continuous CBH I movement was measured as 3.1 ± 0.9 nm/s, consistent with the literature[23,24], however, unresolved into discrete stop and go phases, observed using higher time resolution.[22,25] Although LPMO is only about half the size of CBH I (~24 kDa), we were able to visualize the enzymes clearly on the crystalline cellulose, as shown in Fig. 1b. In stark contrast to CBH I, LPMO stayed at the place of its adsorption to the cellulose over several min. Of ≥400 enzyme molecules (C1'-oxidzing LPMO) analyzed on 20 nanocrystals, none moved on the surface until it became eventually desorbed again. The C4-oxidizing LPMO additionally equipped with CBM was also completely immobile on the cellulose surface (Supplementary Fig. 1). Clearly, therefore, LPMO is not a processively moving enzyme like CBH I is.

Localization of LPMO and CBH I

CBH I and LPMO both showed pronounced (≥ 5-fold) preference for binding to the side walls of the cellulose nanocrystals, as compared to binding to the nanocrystals' top surface. Figure 1c illustrate the effect, and counting single enzymes (80 molecules, 12 individual nanocrystals) provided quantitative results. Comparing positions of the adsorbed enzymes based on their average footprint area on the cellulose surfaces, we find that LMPO bound to surface regions of the cellulose crystals ("sites") also used by CBH I for binding. Crowding of LPMO and CBH I on the top surface of a cellulose crystal is furthermore shown in Fig. 1d. Overlapping specificity for adsorption to crystalline cellulose surfaces is therefore suggested for the two enzymes. The cellulose nanocrystals used represent cellulose polymorph I_β, the main crystalline form of cellulose in the plant cell wall. Evidence from experimental and computational studies (reviewed by Payne et al.[6]) suggests that CBH I binds preferentially to

the hydrophobic faces of cellulose I. The cellulose nanocrystals used have an aspect ratio of ~2.5. Orientation of the nanocrystals on the grid such that their broader surface is in contact with the graphite surface would expose the presumably relevant hydrophobic faces on the side walls.

Adsorption kinetics of LPMO

We then monitored adsorption-desorption of single LPMO molecules in a time-resolved fashion, as illustrated in Fig. 2a. An average residence time of around 0.6 min was determined for LPMO bound to the cellulose surface, as shown in Fig. 2b. Comparison of top and side wall-associated LPMO molecules based on normalized residence time distributions showed a comparable average residence time for both LPMO populations, as shown in Fig. 2b. The on- and off-rate of LPMO binding to the crystalline cellulose was determined from the AFM data (~450 events, 8 microfibrils), as indicated in Fig. 2c. Both the on- and the off-rate were found to be about 4.5-fold higher on the side faces of the cellulose nanocrystals than on the crystals' top face (Fig. 2c). The locally observed differences in protein adsorption dynamics are consistent with a preference of LPMO for binding to, hence attacking, the side surfaces of the nanocrystals. From the reported turnover number of LPMO (k_{cat} = 0.3 - 6 min^{-1})[18,26,27], we calculate that the average time of adsorption is sufficient to allow the bound enzyme to undergo between 0.2 and 3.6 catalytic events.

LPMO-catalyzed oxidative deconstruction of cellulose nanocrystals

Oxidative chain cleavages are expected to destabilize the spatial order of cellulose chains in crystalline material. Computational studies support the intuition[16], but experimental evidence of the presumed "deconstruction effect" of LPMO action is lacking. We were able to visualize local fibrillation events at the side surfaces of the cellulose nanocrystals in consequence of treatment with LPMO. The partial detachment of cellulose chain bundles (fibrils) in enzymatically attacked nanocrystals is demonstrated in Fig. 3a. Additional data are shown in supplementary Fig. 2a-c. Using careful comparison of the forward and backward direction of AFM line scans, we showed that the loosened parts of the fibrils were moveable in both directions by the AFM tip. Their anchoring points in the cellulose crystal, however, were completely unchanged in trace-retrace sequences of analysis. Therefore, this rigorously eliminated the possibility that the observed fibrils were not cellulose. Fibrillation occurred in about 15-20% of the 150 nanocrystals analyzed. Fibrillation was detectable only after extended incubation times in the presence of LPMO, suggesting it to represent a late stage in the overall substrate degradation by the enzyme.

Synergy between LPMO and CBH I

A number of studies show that LPMO synergizes with CBH I in terms of enhanced saccharification of cellulose.[5,12,17,28–30] Based on single molecule visualization results we succeeded in establishing a mechanistic basis of the synergistic effect. CBH I binding to the cellulose nanocrystals was strongly enhanced (≥ 2.0-fold) in the presence of LPMO, as shown in Fig. 3c-e. The increase in CBH I adsorption involved enhanced binding at the side surfaces of the cellulose crystal. The largest part of it, however, was due to binding of CBH I at the top surface of the cellulose crystals. LPMO action appears to create adsorption sites for CBH I in crystalline cellulose surface otherwise not accessible to the cellulase. Tracking individual enzyme molecules in time resolved AFM sequences, we were able to show increased dynamics on the cellulose surface when LPMO and CBH I both were present. The frequency of adsorption-desorption events was apparently enhanced as compared to CBH I acting alone and enzyme processive mobility on the cellulose surface was also increased significantly (Supplementary Movie 5). The effect was difficult to quantify precisely due to crowding of the individual enzyme molecules on the surface. However, the portion of adsorbed CBH I molecules detected in motion was enhanced, reflected also by an increase in the maximum speed of unidirectionally moving CBH I molecules, as shown in supplementary Fig. 3. LPMO stimulated the CBH I adsorption independent of its addition before, after or at the same time CBH I was added. Eventually this resulted in a 2-fold enhancement of the soluble sugar release by CBH I, as shown in Fig. 3e.

Discussion

The present results suggest that synergistic interplay between oxidative and hydrolytic enzymes in crystalline cellulose degradation reflects a distinct gain in efficiency of the hydrolytic enzyme as result of the oxidative counterpart's action. Mechanistically, the efficiency enhancement involves two components. One is an increase in the number of CBH I adsorption sites on the cellulose surface, particularly in areas hardly attacked by the cellulase in the absence of LPMO. The other is enhanced dynamics in elementary steps of CBH I action. The frequency of adsorption and desorption events is increased and the bound cellulases show enhanced processive mobility. Each of these steps is considered to be potentially rate-limiting for hydrolysis.[6,31,32] The results also reveal a time scale for the action of adsorbed LPMO much longer (min compared to seconds) than that of CBH I. An important problem, made evident by the current study, is therefore to ensure efficient coupling of oxidative and hydrolytic action over an extended course of cellulose saccharification.

Online methods

Materials

Unless stated, all chemicals were of the highest purity available from Carl Roth + Co KG (Karlsruhe, Germany).

Preparation of cellulose nanocrystals

Cellulose nanocrystals were produced according to literature.[33] Whatman® qualitative filter paper (Grade 1; Sigma-Aldrich) was cut into squared pieces of 2 × 2 mm size. About 4 g of cellulose were hydrolyzed in 70 mL of 64 % (w/w) of sulfuric acid for 45 minutes at 45°C. The reaction was stopped by 10-fold dilution with deionized water. Repeated centrifugation and washing with deionized water was used to bring the suspension to a final pH of 1.5 or higher. Finally, a colloidal cellulose preparation was obtained by repeated 1 min-long sonification (Sonoplus; Bandelin electronic GmbH & Co. KG, Berlin, Germany) of the suspension cooled on ice. Concentration of the solution was determined to be 15 g L^{-1} by weighing of the dry mass. The colloidal cellulose nanocrystal suspension was stored at 4 °C until further use.

Characterization of cellulose nanocrystals

The crystallinity index (C_i) of the obtained cellulose nanocrystal preparation was calculated to be ≥ 90% using wide angle X-ray scattering (WAXS) as described previously.[34] Raman spectroscopy, conducted as described elsewhere[34], was used to identify the cellulose allomorph as I_β by comparison with corresponding reference spectra from Whatman® qualitative filter paper. Transmission electron microscopy (TEM) and atomic force microscopy (AFM) were used to determine the morphology of the cellulose nanocrystals. Image data was fitted as normal distribution and average values of 127 ± 45 nm in length and 17 ± 6 nm in width were calculated for the more or less rod-shaped cellulose nanocrystals. The detailed experimental setup and staining procedure for TEM investigations were reported previously.[34] A FT-Raman-based method developed by Zhang and coworkers[35] was used to assess the amount of sulfate half-ester groups on the surface of the cellulose nanocrystals quantitatively. A calculation based on the normalized areas under the Raman bands between 843 and 825 cm^{-1} indicated a degree of surface substitution (DS_s) below 0.2 (supplementary Fig. 4). Data fitting and peak deconvolution were performed using Origin 9 (OriginLab cooperation, Northampton, USA). Raman data was analyzed using using LabSpec 6 (Horiba, Tulln an der Donau, Austria).

Sample preparation for AFM observations

Highly oriented pyrolytic graphite (HOPG) grade I wafers (SPI Supplies, West Chester, PA, USA) were used for fixation of the cellulose nanocrystals.[22,23] The HOPG wafer surface (10 × 10 mm) was prepared by removing the top graphite layer with adhesive tape ("adhesive tape cleaving") followed by immediate incubation with 500 µL of a cellulose nanocrystal suspension diluted to a concentration of 0.6 g L^{-1} with deionized water. Note that concentration and volume of the cellulose nanocrystal suspension were selected to avoid aggregation of nanocrystals on the HOPG wafer. After 10 minutes of incubation, the HOPG wafer was rinsed with 10 mL of deionized water and dried via CO_2 spraying. A vacuum chuck was used to mount the HOPG wafer for succeeding AFM observations.

Enzyme preparations

CBH I was isolated from a cellulase preparation obtained from *T. reesei* SVG17 using a slightly modified ion-exchange protocol as published elsewhere.[36] Purification was done at room temperature. Cellulase was applied to a 6-mL pre-packed Resource Q column (GE Healthcare, United Kingdom) equilibrated with 20 mM triethanolamine, pH 7.0. Elution was done with a linear gradient of 0 - 300 mM NaCl over 10 column volumes. CBH I elutes in a discrete protein peak at about 180 mM salt, clearly separated from other known cellulase activities. Enzyme was gel-filtered to remove salt and stored in 50 mM sodium citrate buffer, pH 5.0 at 4 °C. Purity of CBH I was confirmed by SDS PAGE where isolated enzyme migrated as single Coomassie-stained protein band. Specific activity of CBH I assayed with methylumbelliferyl-β-D-cellobioside according to an earlier published procedure[37] was comparable to that of a commercial enzyme preparation (Megazyme).

Purified preparations of two LPMOs, one C1' (*Nc*LPMO9F) and the other C4' (*Nc*LPMO9C) oxidizing, were obtained through reported procedures.[18] The production of hydrogen peroxide by the purified enzymes was assayed with a fluorimetric assay using L-ascorbic acid as reducing agent as published elsewhere.[18]

The production of oxidized cello-oligosaccharides was measured using cellulose nanocrystals (0.5 g L^{-1}) as substrate. Reactions were conducted in 50 mM sodium acetate, pH 5.0, supplemented with 500 µM L-ascorbic acid, in a total reaction volume of 1 mL at 25°C in Eppendorf tubes sealed with oxygen-permeable Parafilm. Enzyme concentration was 16 µg mL^{-1}. The samples were shaken at 400 rpm in an Eppendorf Thermomixer comfort (Eppendorf AG, Hamburg, Germany). The reaction was stopped by adding an equal volume of 100 mM sodium hydroxide to the reaction mixture after 45 minutes or 90 minutes, respectively. The samples were centrifuged (× 10, 000 g) for 5 min at 8 °C, and the cleared

supernatant was assayed for oxidized cello-oligosaccharides as shown in supplementary Fig. 5.

Aliquots of the LPMOs were stored at -70 °C using a protein concentration of either 8 g L^{-1} (*Nc*LPMO9F) or 55 g L^{-1} (*Nc*LPMO9C) in 20 mM TrisHCl buffer, pH 8.0. Concentrations of purified enzyme preparations were determined via UV absorbance at 280 nm using molar extinction coefficients calculated from their protein sequence on Uniprot using Protparam (CBH I) or taken from literature (LPMOs).[18] (ε_CBH I = 86,760 M^{-1} cm^{-1}; ε_ *Nc*LPMO9F = 51,130 M^{-1} cm^{-1}; ε_ *Nc*LPMO9C = 46,910 M^{-1} cm^{-1})

AFM observations

AFM observations were carried out using a FastScan Bio Atomic Force Microscope (Bruker AXS, Santa Barbara, CA, U.S.A.) operated by a Nanoscope V controller. All experiments were conducted in a small-volume (60 µL) flow cell (Bruker AXS, Santa Barbara, CA, U.S.A.) and FastScan D cantilevers were used in tapping mode with a nominal spring constant and tip radius of 5 nm and 0.3 N m^{-1}, respectively.

Prior to image acquisition the small volume cell covering the HOPG wafer was carefully rinsed with reaction buffer (50 mM sodium acetate, pH 5.0, supplemented with 500 µM L-ascorbic acid) using an in-house build syringe driven injection system until the system was devoid of macroscopic air bubbles. The system was allowed to equilibrate for 30 minutes at 25 °C and multiple reference images of varying size were recorded. Continuous image acquisition was started by the carefully rinsing the cell with 200-250 µL pre-warmed buffer solution containing a C1' oxidizing LPMO (*Nc*LPMO9F) (16 µg mL^{-1}) or CBH I (8 µg mL^{-1}). Scan rate was either 40 or 3.5 seconds per frame for high-speed observations or imaging for multiple cellulose nanocrystals, respectively.

Synergy experiments using CBH I and the C1' oxidizing LPMO were conducted using the same enzyme concentrations as described above at 25°C. The cellulose nanocrystal preparation fixed on the HOPG wafer was incubated with LPMO for 45 minutes prior to the addition of CBH I. Subsequently, 200-250 µL pre-warmed buffer solution containing CBH I was added and continuous image acquisition continued as soon as possible.

Experiments with a C4' oxidizing LPMO (*Nc*LPMO9C) were conducted in a similar fashion except for the temperature, which was set to 40°C and a prolonged equilibration phase of one hour.

Set points and drive amplitudes were selected in order to obtain stable scanning with the lowest energy dissipation possible and adapted if required.

AFM image processing and analysis was performed using Gwyddion 2.31 (released 02/21/2013) and Nanoscope Analysis 1.50 (Build R2.103555, Bruker AXS, CA, USA). All images were plane fitted at 1st order and a median filter was applied unless otherwise stated. Digital movies were constructed using an automated MATLAB routine (developed in Version 7.11.1.866 (R2010b) service pack 1) for drift correction in x, y and z dimension, respectively, and Fiji (ImageJ 1.51g) (National Institute of Health, USA). Tracking of individual particles was done with the TrackMate v3.4.2 plugin in Fiji.

Synergy between LPMO and CBH I

Synergy of CBH I and LPMO (*Nc*LPMO9F) was studied in 50 mM sodium acetate, pH 5.0, supplemented with 500 µM L-ascorbic acid, in a total reaction volume of 1 mL at 40°C in Eppendorf tubes sealed with oxygen-permeable Parafilm. The samples were shaken at 400 rpm in an Eppendorf Thermomixer comfort (Eppendorf AG, Hamburg, Germany). Substrate concentration was 1 g L^{-1} of cellulose nanocrystals. The reaction was started by adding a negligible volume of buffer containing CBH I (8 µg mL^{-1}) supplemented with or without LPMO (16 µg mL^{-1}) as control, respectively. Sampling was performed at suitable time points (2.5, 5, 24 and 60 hours). In brief, 150 µL of the well-mixed suspension was withdrawn and mixed with 150 µL of 100 mM sodium hydroxide to stop the reaction. Subsequently, the samples were centrifuged (× 10, 000 g) for 5 min at 8 °C, and the cleared supernatant was subjected to sugar quantification.

Analytics

Glucose and cellobiose and higher oligosaccharides were analyzed with high performance anion exchange chromatography coupled to pulsed-amperometric detection (HPAEC-PAD) (Dionex BioLC, Thermo Fisher Scientific, Waltham, MA) as described elsewhere.[34]

The production of oxidized cellulose-oligosaccharides was monitored with the same HPAEC-PAD system equipped with a CarboPac® PA10 column (4 × 250 mm) and a CarboPac PA10 guard column (4 × 50 mm) at 30 °C. Elution of uncharged saccharides was performed at 0.7 mL min^{-1} using 50 mM sodium hydroxide and 20 mM sodium acetate in the mobile phase for 16 minutes followed by a sodium acetate gradient. Aldonic acids were eluted by a linear gradient from 40 mM up to 400 mM sodium acetate at a flow of 0.7 mL min^{-1} over 20 minutes. Afterwards the column was re-equilibrated for nine minutes with 50 mM sodium hydroxide and 20 mM sodium acetate.

D-Glucose, D-cellobiose and D-gluconic acid were used as authentic standards. Identification or quantification of oxidized products was not pursued.

References

1. Sheldon, R. A. Green chemistry, catalysis and valorization of waste biomass. *J. Mol. Catal. A Chem.* **422,** 3–12 (2016).
2. Albers, S. C., Berklund, A. M. & Graff, G. D. The rise and fall of innovation in biofuels. *Nat. Biotechnol.* **34,** 814–821 (2016).
3. Himmel, M. E. *et al.* Biomass Recalcitrance: Engineering Plants and Enzymes for Biofuels Production. *Science* **315,** 804–807 (2007).
4. Donohoe, B. S. & Resch, M. G. Mechanisms employed by cellulase systems to gain access through the complex architecture of lignocellulosic substrates. *Curr. Opin. Chem. Biol.* **29,** 100–107 (2015).
5. Müller, G., Várnai, A., Johansen, K. S., Eijsink, V. G. H. & Horn, S. J. Harnessing the potential of LPMO-containing cellulase cocktails poses new demands on processing conditions. *Biotechnol. Biofuels* **8,** 187 (2015).
6. Payne, C. M. *et al.* Fungal Cellulases. *Chem. Rev.* **115,** 1308–1448 (2015).
7. Bommarius, A. S., Sohn, M., Kang, Y., Lee, J. H. & Realff, M. J. Protein engineering of cellulases. *Curr. Opin. Biotechnol.* **29,** 139–145 (2014).
8. Vaaje-Kolstad, G. *et al.* An oxidative enzyme boosting the enzymatic conversion of recalcitrant polysaccharides. *Science* **330,** 219–222 (2010).
9. Hemsworth, G. R., Johnston, E. M., Davies, G. J. & Walton, P. H. Lytic Polysaccharide Monooxygenases in Biomass Conversion. *Trends Biotechnol.* **33,** 747–761 (2015).
10. Beeson, W. T., Vu, V. V., Span, E. a., Phillips, C. M. & Marletta, M. a. Cellulose Degradation by Polysaccharide Monooxygenases. *Annu. Rev. Biochem.* **84,** 923–946 (2015).
11. Horn, S. J., Vaaje-Kolstad, G., Westereng, B. & Eijsink, V. G. Novel enzymes for the degradation of cellulose. *Biotechnol. Biofuels* **5,** 45 (2012).
12. Harris, P. V, Xu, F., Kreel, N. E., Kang, C. & Fukuyama, S. New enzyme insights drive advances in commercial ethanol production. *Curr. Opin. Chem. Biol.* **19,** 162–170 (2014).
13. Walton, P. H. & Davies, G. J. On the catalytic mechanisms of lytic polysaccharide monooxygenases. *Curr. Opin. Chem. Biol.* **31,** 195–207 (2016).
14. Kracher, D. *et al.* Extracellular electron transfer systems fuel cellulose oxidative degradation. *Science* **352,** 1098–1101 (2016).
15. Cannella, D. *et al.* Light-driven oxidation of polysaccharides by photosynthetic

pigments and a metalloenzyme. *Nat. Commun.* **7,** 11134 (2016).

16. Vermaas, J. V., Crowley, M. F., Beckham, G. T. & Payne, C. M. Effects of Lytic Polysaccharide Monooxygenase Oxidation on Cellulose Structure and Binding of Oxidized Cellulose Oligomers to Cellulases. *J. Phys. Chem. B* **119,** 6129–6143 (2015).
17. Eibinger, M. *et al.* Cellulose surface degradation by a lytic polysaccharide monooxygenase and its effect on cellulase hydrolytic efficiency. *J. Biol. Chem.* **289,** 35929–35938 (2014).
18. Kittl, R., Kracher, D., Burgstaller, D., Haltrich, D. & Ludwig, R. Production of four *Neurospora crassa* lytic polysaccharide monooxygenases in *Pichia pastoris* monitored by a fluorimetric assay. *Biotechnol. Biofuels* **5,** 79 (2012).
19. Levasseur, A., Drula, E., Lombard, V., Coutinho, P. M. & Henrissat, B. Expansion of the enzymatic repertoire of the CAZy database to integrate auxiliary redox enzymes. *Biotechnol. Biofuels* **6,** 41 (2013).
20. Cantarel, B. I. *et al.* The Carbohydrate-Active EnZymes database (CAZy): An expert resource for glycogenomics. *Nucleic Acids Res.* **37,** 233–238 (2009).
21. Crouch, L. I., Labourel, A., Walton, P. H., Davies, G. J. & Gilbert, H. J. The Contribution of non-catalytic Carbohydrate Binding Modules to the Activity of Lytic Polysaccharide Monooxygenases. *J. Biol. Chem.* **291,** 7439–7449 (2016).
22. Igarashi, K. *et al.* Traffic Jams Reduce Hydrolytic Efficiency of Cellulase on Cellulose Surface. *Science* **333,** 1279–1282 (2011).
23. Igarashi, K. *et al.* High speed atomic force microscopy visualizes processive movement of Trichoderma reesei cellobiohydrolase I on crystalline cellulose. *J. Biol. Chem.* **284,** 36186–90 (2009).
24. Zhang, Y., Zhang, M., Alexander Reese, R., Zhang, H. & Xu, B. Real-time single molecular study of a pretreated cellulose hydrolysis mode and individual enzyme movement. *Biotechnol. Biofuels* **9,** 85 (2016).
25. Nakamura, A. *et al.* Trade-off between processivity and hydrolytic velocity of cellobiohydrolases at the surface of crystalline cellulose. *J. Am. Chem. Soc.* **136,** 4584–4592 (2014).
26. Frandsen, K. E. H. *et al.* The molecular basis of polysaccharide cleavage by lytic polysaccharide monooxygenases. *Nat. Chem. Biol.* **12,** 298–303 (2016).
27. Loose, J. S. M., Forsberg, Z., Fraaije, M. W., Eijsink, V. G. H. & Vaaje-Kolstad, G. A rapid quantitative activity assay shows that the *Vibrio cholerae* colonization factor GbpA is an active lytic polysaccharide monooxygenase. *FEBS Lett.* **588,** 3435–3440

(2014).

28. Hu, J., Arantes, V., Pribowo, A. & Saddler, J. N. The synergistic action of accessory enzymes enhances the hydrolytic potential of a 'cellulase mixture' but is highly substrate specific. *Biotechnol. Biofuels* **6,** 112 (2013).
29. Arfi, Y., Shamshoum, M., Rogachev, I., Peleg, Y. & Bayer, E. a. Integration of bacterial lytic polysaccharide monooxygenases into designer cellulosomes promotes enhanced cellulose degradation. *Proc. Natl. Acad. Sci. U. S. A.* **111,** 9109–14 (2014).
30. Selig, M. J. *et al.* Modified cellobiohydrolase–cellulose interactions following treatment with lytic polysaccharide monooxygenase CelS2 (*Sc*LPMO10C) observed by QCM-D. *Cellulose* **22,** 2263–2270 (2015).
31. Jalak, J. & Väljamäe, P. Mechanism of initial rapid rate retardation in cellobiohydrolase catalyzed cellulose hydrolysis. *Biotechnol. Bioeng.* **106,** 871–83 (2010).
32. Cruys-Bagger, N., Tatsumi, H., Ren, G., Borch, K. & Westh, P. Transient kinetics and rate-limiting steps for the processive cellobiohydrolase Cel7A: effects of substrate structure and carbohydrate binding domain. *Biochemistry* **52,** 8938–8948 (2013).
33. Lu, P. & Hsieh, Y.-L. Preparation and properties of cellulose nanocrystals: Rods, spheres, and network. *Carbohydr. Polym.* **82,** 329–336 (2010).
34. Ganner, T. *et al.* Tunable Semicrystalline Thin Film Cellulose Substrate for High-Resolution, In-Situ AFM Characterization of Enzymatic Cellulose Degradation. *ACS Appl. Mater. Interfaces* **7,** 27900–27909 (2015).
35. Zhang, K., Brendler, E. & Fischer, S. FT Raman investigation of sodium cellulose sulfate. *Cellulose* **17,** 427–435 (2010).
36. Medve, J., Lee, D. & Tjerneld, F. Ion-exchange chromatographic purification and quantitative analysis of Trichoderma reesei cellulases cellobiohydrolase I, II and endoglucanase II by fast protein liquid chromatography. *J. Chromatogr. A* **808,** 153–165 (1998).
37. Eibinger, M., Bubner, P., Ganner, T., Plank, H. & Nidetzky, B. Surface structural dynamics of enzymatic cellulose degradation, revealed by combined kinetic and atomic force microscopy studies. *FEBS J.* **281,** 275–290 (2014).

Acknowledgements

R. Ludwig (University of Natural Resources and Life Sciences) kindly provided *Nc*LPMO9C and *Nc*LPMO9F. H. Fitzek (Graz University of Technology) performed Raman spectroscopy

analysis. This work was supported by the Austrian Science Funds (FWF Project P-24156-B21 to B.N.).

Author contributions

H.P. and B.N. designed the research. M.E., J.S. and T.G. performed experiments. M.E., J.S. and H.P. analyzed data. M.E. and B.N. wrote the paper.

Competing Financial Interests Statement

The authors declare no competing financial interest.

Materials & Correspondence

Correspondence and material requests should be addressed to B.N or H.P.

Figures

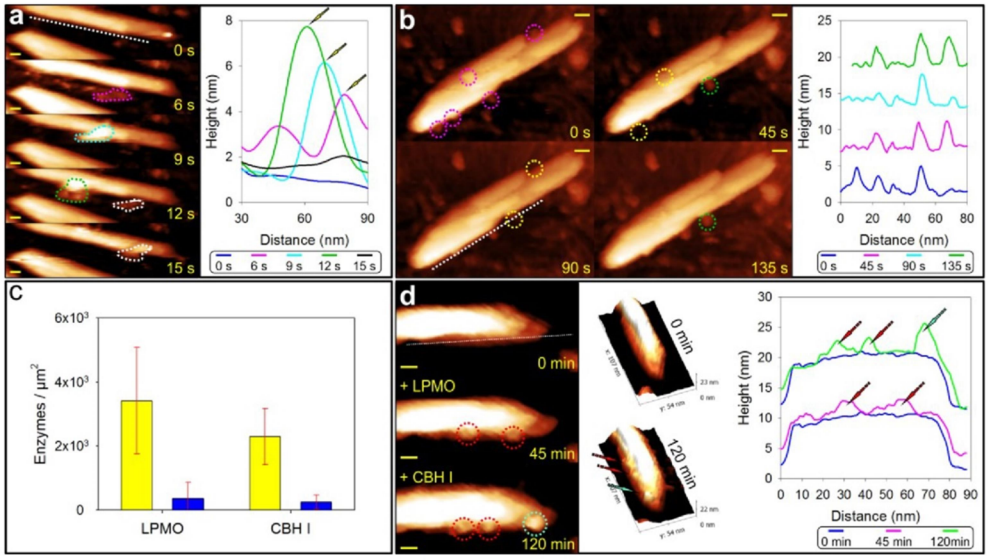

Figure 1: Single molecule observations on cellulose nanocrystals. (a) Real-time AFM observation of CBH I molecules (outlined in color) on a cellulose nanocrystal. Images were recorded at 0.3 s^{-1} and the ones depicted are from supplementary movie 1. Enzyme movements were extracted from individual images along the dashed line next to the crystal's edge as representatively shown via height profiles (correlate with individual colors). The yellow arrow indicates the enzyme's center moving sideways and slightly upwards. The CBH I molecule in white becomes adsorbed but does not move in the relevant timespan. (b) LPMO molecules on a cellulose nanocrystal visualized in real time (1.3 AFM frames min^{-1}). Colored frames indicate enzymes present initially (magenta), adsorbing (green) or desorbing (vacated position; yellow) in the relevant timespan. The height profile along the dashed line shows multiple stationary LPMO molecules bound on the side wall of the cellulose nanocrystal. (c) Individual enzyme adsorption to the side walls (yellow bars) and the top (blue bars) surfaces of cellulose nanocrystals. (d) Visualization and cross section analysis of LPMO (circled red, red arrows) and CBH I (circled turquois, turquoise arrow) along the dashed line showed successive adsorption to the same cellulose nanocrystal. As enzymes differ in height, LPMOs (~2 nm) are clearly distinguished from CBH I molecules (~4 nm). All scale bars are 10 nm.

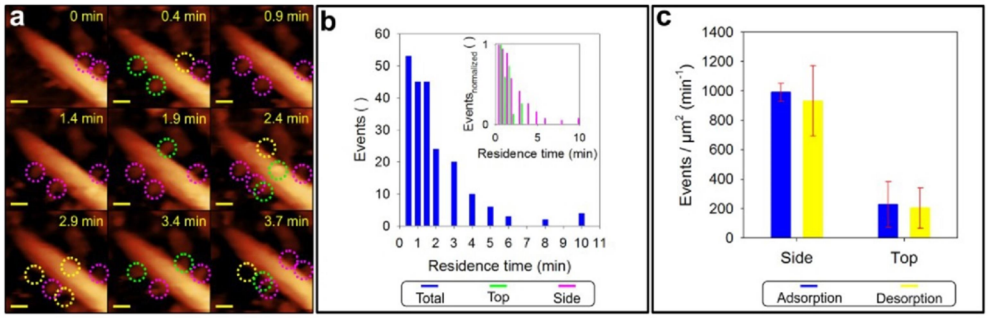

Figure 2: Adsorption/desorption of LPMO. (a) Real-time observation of LPMO molecules adsorbing to and desorbing from cellulose nanocrystals. Images are taken from supplementary movie 2 and 3. Colored frames show enzymes present initially (magenta), adsorbing (green) or desorbing (vacated position; yellow) in the relevant timespan. (b) The residence time of LPMO on the surface of nanocrystals. The distribution was fit by an exponential decay, yielding a dissociation rate constant of 1.6 ± 0.2 min^{-1}. Qualitative analysis showed similar distributions for LPMOs independent of their adsorption site. (c) Adsorption and desorption events on the top and side surfaces of cellulose nanocrystals revealed by analyzing ~250 individual enzymes bound to 8 different nanocrystals. Scale bars are 10 nm.

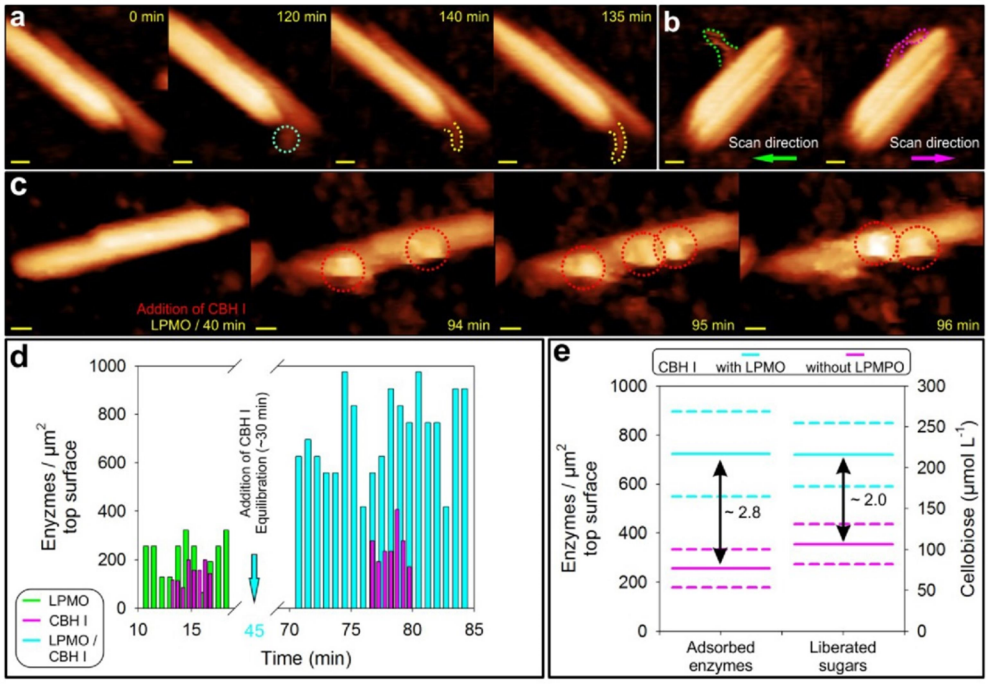

Figure 3: Real time observations of LPMO activity on cellulose nanocrystals and its effect on CBH I. (a) Partial detachment of cellulose fibrils from nanocrystals as result of LPMO activity. An LPMO molecule adsorbs (blue circle) to an intact crystal and after its desorption, a fibril loosened from the crystalline material (yellow frame) becomes visible. (b) By comparing forward (trace; green frames) and backward direction (retrace; blue frames) of AFM line scans, the loosened parts of the fibrils are shown to be moveable by the AFM tip. The fibril part associated with the cellulose nanocrystal, by contrast, was not moveable. Further examples of cellulose nanocrystal fibrillation by LMPO are shown in Fig. S2. (A,B,C) (c) LPMO enhances the adsorption of CBH I to cellulose nanocrystals, as shown in AFM images (compare panel C and Fig. 1A) and quantitative single-molecule analysis (panel D). (d) Enzyme molecules/surface area on the top surface of 16 nanocrystals are shown for LPMO alone and after the addition of CBH I. A control using CBH I alone is also shown. Real-time observations are also shown in supplementary movies 4 and 5. Besides enhancement of adsorption, the movies also show an increased fraction of mobile enzymes on the cellulose surface when LPMO and CBH I act together. (e) Synergy between CBH I and LPMO on cellulose nanocrystals. LPMO addition stimulated the CBH I adsorption and resulted in an increase of liberated sugars eventually. Solid lines represent mean values and standard error is indicated by dashed lines. All scale bars are 10 nm.

Supplementary information

Single molecule study of oxidative enzymatic deconstruction of cellulose

Manuel Eibinger[1], Jürgen Sattelkow[2], Thomas Ganner[2], Harald Plank[2,3]*, Bernd Nidetzky[1,4]*

[1]Institute of Biotechnology and Biochemical Engineering, Graz University of Technology, Petersgasse 10-12/1, 8010 Graz, Austria.

[2]Institute for Electron Microscopy and Nanoanalysis, Graz University of Technology, Steyrergasse 17, 8010 Graz, Austria.

[3]Graz Centre for Electron Microscopy, Steyrergasse 17, A-8010 Graz, Austria.

[4]Austrian Centre of Industrial Biotechnology, Petersgasse 14, 8010 Graz, Austria.

*Correspondence to: bernd.nidetzky@tugraz.at (B.N.); harald.plank@felmi-zfe.at (H.P.)

Supplementary Results

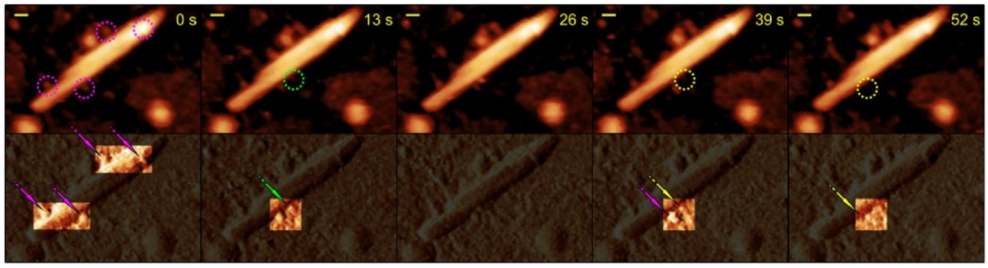

Supplementary Figure 1: Real-time observation of C4' oxidizing LPMO molecules adsorbing and desorbing from cellulose nanocrystals. Colored frames indicate enzymes present initially (magenta), adsorbing (green) or desorbing (vacated position; yellow) in the depicted timespan. Amplitude images of the corresponding time points are shown along the bottom panel. LPMO molecules are indicated by arrows using the same color code as described above. All scale bars are 10 nm.

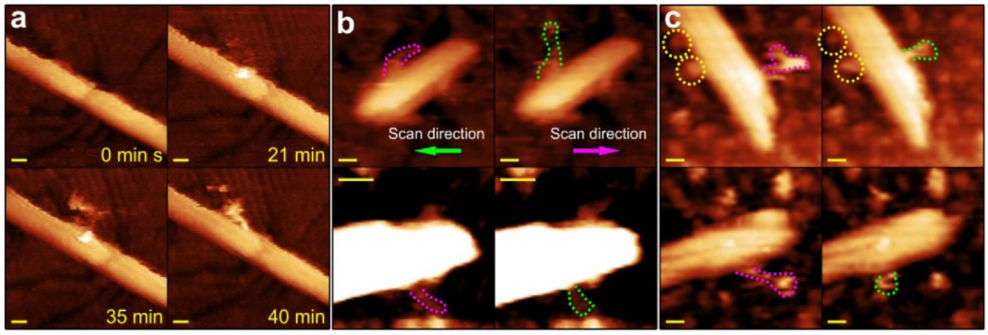

Supplementary Figure 2: Real time observations of LPMO and its effect on cellulose nanocrystals (a) Real-time observation of partial detachment of cellulose fibrils from nanocrystals as result of LPMO (*Nc*LPMO9F) activity. An LPMO molecule adsorbs to an intact crystal and a fibril loosened from the crystalline material becomes visible contemporaneous. The frame recording rate is 1 min^{-1} to provide high resolution images. (b) By comparing forward (trace; magenta) and backward direction (retrace; green) of AFM line scans, the loosened parts of the fibrils are shown to be often moveable by the AFM tip. The fibril part associated with the cellulose nanocrystal, by contrast, was not moveable. (c) Similar AFM observations concerning fibrillation were made using a C4' oxidizing LPMO (*Nc*LPMO9C) at elevated temperature (40°C). Note that intact LPMO molecules (yellow frames) have a similar shape and position in trace and retrace unlike detached fibers.

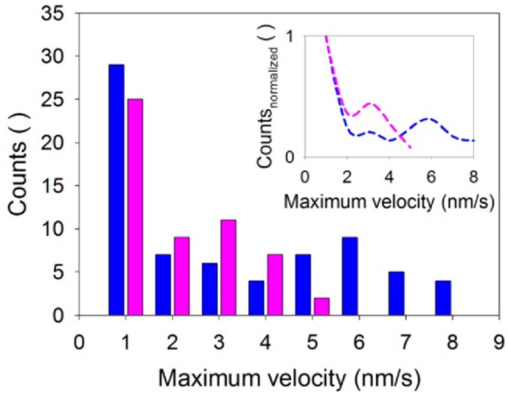

Supplementary Figure 3: LPMO affects the apparent maximum velocity of CBH I. Distribution of the maximum velocity of CBH I molecules in the presence (blue bars) or absence of a C1' oxidizing LPMO (magenta bars). The apparent maximum velocity of CBH I molecules ($n \geq 50$) in the presence of LPMO was increased at least 1.5-fold as compared to CBH I ($n \geq 50$) acting without LPMO. Analysis was based on experiments with a frame-recording rate of 0.2 s^{-1} or 0.3 s^{-1}. Tracking of individual particles and calculation of the maximum velocity was done with the TrackMate v3.4.2 plugin in Fiji.

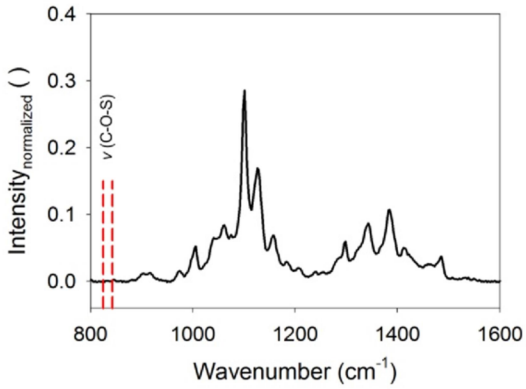

Supplementary Figure 4: Raman spectroscopy of cellulose nanocrystals. The degree of surface substitution (DS_s) can be calculated based on the normalized areas under the Raman bands between 843 and 825 cm^{-1}, which correspond to the C–O–S stretching vibration, ν(C-O-S). No clear bands were resolved and thus the DS_s is below the detection limit (~ 0.2) of the method. Baseline correction and a vector-normalization were done using LabSpec 6 (Horiba, Tulln an der Donau, Austria).

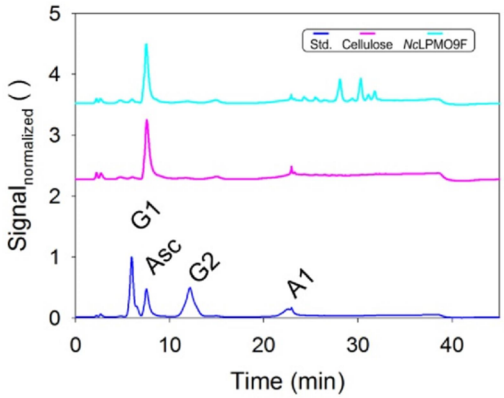

Supplementary Figure 5: HPAEC-PAD chromatogram of LPMO incubated with cellulose nanocrystals. HPAEC-PAD chromatogram of C1' oxidizing LPMO incubated with cellulose nanocrystals for 45 minutes in the presence of 500 µM L-ascorbic acid. The identity of D-glucose (G1), D-cellobiose (G2), L-ascorbic acid (Asc) and D-gluconic acid (A1) were assigned using authentic standards.

Supplementary Movie 1: Real-time AFM observation of a CBH I molecule sliding along a cellulose nanocrystal. The enzyme's center is moving sideways and slightly upwards as shown in Fig. 1a. CBH I is outlined in color and scale bar is included in the images. The grey scale corresponds to heights between 1 and 12 or 14 nm, respectively.

Supplementary Movie 2: Real-time observation of LPMO molecules adsorbing to and desorbing from cellulose nanocrystals. Enzymes outlined in color (sidewall: green; top surface: magenta) were present in the previous image. Vacated positions are indicted with a '×' mark. Scale bar is included in the images. The grey scale corresponds to heights between 0 and 20 nm.

Supplementary Movie 3: Real-time observation of LPMO molecules adsorbing to and desorbing from multiple cellulose nanocrystals. Note that microscopic air bubbles (outlined in blue) were present throughout the whole experiment. Color coding of enzymes is as described for supplementary movie 2. Scale bar is included in the images. The grey scale corresponds to heights between 0 and 20 nm.

Supplementary Movie 4: Real-time AFM observation of LPMO preincubation enhances the adsorption of CBH I to cellulose nanocrystals. Adsorbed enzymes are outlined in color. Scale bar is included in the images and the grey scale covers a height of 15 nm.

Supplementary Movie 5: High-speed AFM observation of LPMO enhances the adsorption/desorption of CBH I to cellulose nanocrystals. Note that all images were contrast enhanced for clarity by setting gamma to 0.4 using CorelDrawX8. Scale bar is included in the images.

Complete list of peer reviewed publications & oral presentations

Complete list of peer reviewed publications

Dissecting and Reconstructing Synergism: In situ visualization of cooperativity among cellulases
Ganner T, Bubner P, Eibinger M, Mayrhofer C, Plank H & Nidetzky B (2012) *J. Biol. Chem.* **287**, 43215–43222.

Surface structural dynamics of enzymatic cellulose degradation, revealed by combined kinetic and atomic force microscopy studies
Eibinger M, Bubner P, Ganner T, Plank H & Nidetzky B (2014) *FEBS J.* **281**, 275–290.

Tunable mixed amorphous–crystalline cellulose substrates (MACS) for dynamic degradation studies by atomic force microscopy in liquid environments
Ganner T, Aschl T, Eibinger M, Bubner P, Meingast A, Chernev B, Mayrhofer C, Nidetzky B & Plank H (2014) *Cellulose* **21**, 3927–3939.

Cellulose Surface Degradation by a Lytic Polysaccharide Monooxygenase and Its Effect on Cellulase Hydrolytic Efficiency
Eibinger M, Ganner T, Bubner P, Rošker S, Kracher D, Haltrich D, Ludwig R, Plank H & Nidetzky B (2014) *J. Biol. Chem.* **289**, 35929–35938.

Tunable Semicrystalline Thin Film Cellulose Substrate for High-Resolution, In-Situ AFM Characterization of Enzymatic Cellulose Degradation
Ganner T, Roŝker S, Eibinger M, Kraxner J, Sattelkow J, Rattenberger J, Fitzek H, Chernev B, Grogger W, Nidetzky B & Plank H (2015) *ACS Appl. Mater. Interfaces* **7**, 27900–27909.

Direct-Write Fabrication of Cellulose Nano-Structures via Focused Electron Beam Induced Nanosynthesis
Ganner T, Sattelkow J, Rumpf B, Eibinger M, Reishofer D, Winkler R, Nidetzky B, Spirk S & Plank H (2016) *Sci. Rep.* **6**, 32451.

Cellular automata modeling depicts degradation of cellulosic material by a cellulase system with single-molecule resolution
Eibinger M, Zahel T, Ganner T, Plank H & Nidetzky B (2016) *Biotechnol. Biofuels* **9**, 56.

The micromorphology of *Trichoderma reesei* analyzed in cultivations on lactose and solid lignocellulosic substrate, and its relationship with cellulase production
Novy V, Schmid M, Eibinger M, Petrasek Z & Nidetzky B (2016) *Biotechnol. Biofuels* **9**, 169.

Functional characterization of the native swollenin from *Trichoderma reesei*: study of its possible role as C1 factor of enzymatic lignocellulose conversion
Eibinger M, Sigl K, Sattelkow J, Ganner T, Ramoni J, Seiboth B, Plank H & Nidetzky B (2016) *Biotechnol. Biofuels* **9**, 178.

Single molecule study of oxidative enzymatic deconstruction of cellulose
Eibinger M, Sattelkow J, Ganner T, Plank H & Nidetzky B (2017) *Nat. Commun.*, in revision

Active-site His^{85} of *Pasteurella dagmatis* sialyltransferase facilitates productive sialyl transfer and so prevents futile hydrolysis of CMP-Neu5Ac
Schmölzer K, Eibinger M & Nidetzky B (2017) *ChemBioChem*, in revision

Oral presentations

In situ visualization of cooperativity among cellulases
Eibinger M, Bubner P, Ganner T, Aschl T, Dohr J, Mayrhofer C, Plank H & Nidetzky B (2013) 10th Carbohydrate Bioengineering Meeting, Prague, Czech Republic

Visualizing cellulase activity on the cellulose surface
Eibinger M, Ganner T, Plank H & Nidetzky B (2014) 36th Symposium on Biotechnology for Fuels and Chemicals, Clearwater Beach, USA

Visualizing cellulase activity on the cellulose surface
Eibinger M, Ganner T, Plank H & Nidetzky B (2015) 13th Doc Day, Graz, Austria

Visualizing cellulase activity on the cellulose surface
Eibinger M, Ganner T, Plank H & Nidetzky B (2015) 19th Austrian Carbohydrate Workshop, Graz, Austria

Dynamic, localized high-resolution methods in biology: a missing link!
Eibinger M, Ganner T, Plank H & Nidetzky B (2015) Atomic Force Microscopy Workshop on Advanced Bio- and Materials Characterisation & Industrial Applications, Graz, Austria

Action of an AA9 - type lytic polysaccharide monooxygenase on the cellulose surface and its effect on cellulase hydrolytic efficiency
Eibinger M, Ganner T, Plank H & Nidetzky B (2015) 18th European Carbohydrate Symposium, Moscow, Russian Federation

Enzymatic deconstruction of cellulose
Eibinger M, Novy V, Ganner T, Sattelkow J, Petrasek Z, Plank H & Nidetzky B (2016) EPNOE Minisymposium on Carbohydrate Technology, Graz, Austria

Action of lytic polysaccharide monooxygenase on the cellulose surface and its impact on cellulase efficiency
Eibinger M, Ganner T, Plank H & Nidetzky B (2016) LPMO Symposium, Copenhagen, Denmark

Auxiliary Activities and their Effect on the Cellulosic Surface: Swollenin and Lytic Polysaccharide Monooxygenase
Eibinger M, Sigl K, Sattelkow J, Ramoni J, Ganner T, Seiboth B, Plank H & Nidetzky B (2017) 12th Carbohydrate Bioengineering Meeting, Vienna, Austria